Development of tomographic PIV for the study of turbulent flows

Adam Cheminet

NNT : 2016 SACLX020

THESE DE DOCTORAT
DE
L'UNIVERSITE PARIS-SACLAY
PREPAREE A
L'OFFICE NATIONALE D'ÉTUDES ET DE RECHERCHE AERONAUTIQUE

ECOLE DOCTORALE N° 579
Sciences Mécaniques et Energétiques, Matériaux et Géosciences

Spécialité : Mécanique des fluides

Par

M. Adam Cheminet

Développement de la PIV tomographique pour l'étude d'écoulements turbulents

Thèse présentée et soutenue à l'ONERA-DAFE (Meudon), le 19 Mai 2016 :

Composition du Jury :

M., Scarano, Fulvio	Professeur, Technical University Delft	Président
M., David, Laurent	Professeur, Universités de Poitiers, Institut Pprime	Rapporteur
M., Heitz, Dominique	Chef d'unité IRSTEA, HdR	Rapporteur
M., Lecordier, Bertrand	Chargé de recherches CNRS, CORIA	Examinateur
M., Andreas Schröder	Chercheur, DLR Göttingen	Examinateur
M., Leclaire, Benjamin	Chercheur ONERA, Pr. chargé de cours Ecole Polytechnique	Examinateur
M., Jacquin, Laurent	Professeur Ecole polytechnique	Directeur de thèse
M., Champagnat, Frédéric	Chercheur ONERA, HdR	Co-directeur de thèse

Remerciements

Ma thèse n'aurait jamais pu voir le jour ni aboutir sans l'aide de nombreuses personnes, qui m'ont aidé, soutenu et que je souhaite remercier.

Je tiens tout d'abord à remercier mes deux directeurs de thèse pour leur soutien, leurs encouragements, leur recul réflexif. Merci à Frédéric Champagnat pour nos conversations téléphoniques Palaiseau-Meudon passionnantes et pour toutes les remarques et réflexions qui m'ont ouvert un monde que je ne connaissais pas. Merci à Laurent Jacquin pour son enthousiasme débordant.

Je tiens particulièrement à remercier Benjamin Leclaire qui m'a suivi, soutenu et encouragé pendant ces années de thèse. Son sens de l'analyse et du détail, sa rigueur exigeante mais aussi sa bienveillance, sa patience, et son écoute m'ont guidé et fait progresser pendant toute ma thèse.

J'ai aussi grand plaisir à remercier Guillaume Blanquart avec qui j'ai travaillé à Caltech, et qui a encouragé mon goût pour la recherche. Il a ouvert la voie en m'accueillant dans son laboratoire.

Mes remerciements vont également à toute l'équipe DTIM-DAFE, la « startup PIV-3D », Frédéric Champagnat, Philippe Cornic, Guy Le Besnerais, Aurélien Plyer, Yves Le Sant, et Benjamin Leclaire. Nos réunions foisonnantes d'idées et de rires vont me manquer.

Je souhaite remercier l'ensemble du Département d'Aérodynamique Fondamentale et Expérimentale à l'ONERA Meudon. Gilles Losfeld et Cédric Illoul m'ont offert un soutien indéfectible dans la création d'un dispositif expérimental nouveau et complexe. Mes remerciements vont aussi à Dominique Grandson et Claire Planchard pour leur aide chaleureuse et leur attention, et aussi à Denis Sipp, Reynald Bur, Philippe Geoffroy, Florence Bouvier, Jean-Pierre Tobeli et Philippe Reijasse.

Je tiens à remercier Xavier Amandolèse, qui m'a ouvert les portes de la mécanique des fluides expérimentale et du monde des souffleries.

Mes remerciements vont également aux doctorants du DAFE, soeurs et frères d'armes, Fulvio, Clauddio, Sami, Laurence, Juanito, Holly, Samir, Nicolas, Damien, Ye-Bonne, Robin, Carlos, Jean-Lou et tout particulièrement Romain, avec qui je partageais beaucoup pendant ces trois années.

Je tiens à remercier mes amis de toujours Marie, Alexie, François, Christophe, et Médéric, mes amis musiciens des orchestres du COGE, d'Oya Kephale, des Clés d'Euphonia, sans oublier les musiciens de l'Ensem(le Parenthèse.

Enfin, ma famille proche sans laquelle rien n'aurait été possible.

Abstract

Dissertation summary

This research dissertation focuses on the developments of tomographic PIV (tomo-PIV) for the measurement of turbulent flows (Elsinga et al. 2006). It is based on the tomographic reconstruction of a volumic intensity distribution of tracer particles from projections recorded on cameras. The corresponding volumic distributions are correlated to obtain 3D displacement fields. The present work surveys the state of advancement of the research conducted on this technique and the main issues it has been confronted with so far. The main research focus was on tomographic reconstruction. Indeed, its main limitation is the appearance of ghost particles, ie reconstruction noise, which occurs when high tracer concentrations are required for high spatial resolution measurements.

For a thorough understanding of tomographic noise, we carried out a numerical study of experimental factors impacting the quality of tomographic reconstruction. Geometric considerations quantified the impact of "added particles" lying in the Union volume but not in the Intersection volume, between the camera fields of view and the illumination area. This phenomenon was shown to create ghost particles. The decrease in signal-to-noise ratio in the image was investigated, considering Mie scattering and defocusing effects. Particle image defocusing mainly results in the loss of real particles in reconstruction. Mie scattering's main impact is also the loss of real particles due to the polydisperse nature of the seeding.

This study of imaging conditions for tomo-PIV led us to propose an alternative approach to classical tomographic reconstruction. It seeks to recover nearly single voxel particles rather than blobs of extended size using a particle-based representation of image data. We term this approach Particle Volume Reconstruction (PVR). PVR underlies a more physical, sparse volumic representation of point particles, which lives halfway between infinitely small particles, and voxel blobs commonly used in tomo-PIV. From that representation, it is possible to smooth it to 2 voxel diameter blobs for a 3D-PIV use of PVR incorporated in a SMART algorithm. Numerical simulations showed that PVR-SMART outperforms tomo-SMART (Atkinson et al. 2009) on a variety generating conditions and a variety of metrics on volume reconstruction and displacement estimation, especially in the case of seeding density greater than 0.06 ppp.

We introduce a cross-correlation technique for 3D-PIV (FOLKI-3D) as an extension to 3D of the FOLKI-PIV algorithm (Champagnat et al. 2011). The displacement is searched as the minimizer of a sum of squared differences, solved iteratively by using volume deformation. Numerical tests confirmed that spatial frequency response is similar to that of standard iterative deformation algorithms. Numerical simulations of tomographic reconstruction characterized the robustness of the algorithm to specific

tomographic noise. FOLKI-3D was found more robust to coherent ghosts than standard deformation algorithms, while gains in accuracy of the high-order deformation scheme were obtained for various signal noises.

The application of PVR-SMART on experimental data was performed on a turbulent air jet. Several seeding density conditions were used to compare the performance of tomo-SMART and PVR-SMART on the near field region of the jet. With the given image pre-processing, PVR-SMART was found to yield velocity fields that are about 50

Finally, conclusions are drawn from the main results of this dissertation and lead to potential research perspectives of our work with respect to the future of tomographic PIV.

Résumé de thèse

Cette thèse porte sur le développement de la PIV tomographique (tomo-PIV) pour la mesure d'écoulements turbulents. Elle se fonde sur la reconstruction tomographique d'une distribution volumique d'intensité de particules traceuses, à partir de projections enregistrées par des caméras. Les distributions volumiques sont corrélées, fournissant ainsi un champ de déplacement 3D.

Les principales avancées de la recherche sur cette technique sont présentées ainsi que les points bloquants. Les efforts ont principalement été portés sur la reconstruction tomographique. La principale difficulté est le bruit dit tomographique (particules fantômes) qui croît exponentiellement lorsqu'une forte densité de traceur est requise pour obtenir une résolution spatiale fine de la mesure, particulièrement pour les écoulements turbulents.

Afin de mieux appréhender ce bruit de reconstruction, nous avons étudié numériquement les facteurs expérimentaux nuisant à la qualité de la reconstruction. Des considérations géométriques ont permis de quantifier l'impact de « particules ajoutées », qui se trouvent dans le volume de l'union mais pas dans le volume de l'intersection entre la zone laser et les champs de vue des caméras. La diminution du ratio signal-à-bruit dans les images, due à la diffusion de Mie et l'astigmatisme des optiques, a pour principal effet la perte de vraies particules dans la reconstruction.

Etudier les conditions optiques de la tomo-PIV nous a permis de proposer une approche alternative à la reconstruction tomographique classique, qui vise à reconstruire une particule presque sur un unique voxel, plutôt que comme un agrégat de voxels de taille étendue, en se fondant sur une représentation particulaire des images. Nous nommons cette méthode Reconstruction Volumique de Particules (PVR). Après avoir été incorporée à un algorithme de reconstruction (SMART), il est possible d'élargir la représentation particulaire de PVR, afin d'obtenir des blobs de 2/3 voxels de diamètre requis par les algorithmes de corrélation de 3D-PIV. Des simulations numériques sur un large spectre de conditions génératrices, ont montré qu'utiliser PVR-SMART permettait des gains de performance par rapport à un algorithme classique comme tomo-SMART (Atkinson 2009).

L'aspect vélocimétrie par corrélation de la méthode a aussi été pris en compte avec une extension sur GPU à la 3D (FOLKI-3D) de l'algorithme FOLKI-PIV (Cham-

pagnat et al. 2011). Le déplacement y est cherché en minimisant itérativement une fonctionnelle, du type des moindres carrés, par déformation de volume. Les tests synthétiques confirment que la réponse fréquentielle d'espace est semblable à celle d'autres algorithmes classiques itératifs de déformation de volume. Les simulations numériques de reconstruction tomographique ont permis de caractériser la robustesse de l'algorithme au bruit spécifique de la tomographie. Nous avons montré que FOLKI-3D était plus robuste aux particules fantômes cohérentes que les algorithmes classiques de déformation volumique. De plus, des gains de performance ont été observés en utilisant des schémas d'ordre élevé pour différents types de bruit.

L'application de PVR-SMART sur des données expérimentales a été effectuée sur un jet d'air turbulent. Différentes densités de particules ont été utilisées pour comparer les performances de PVR-SMART avec tomo-SMART sur la région proche buse du jet. Avec le pré-traitement d'image utilisé, nous avons montré que les champs de vitesse de PVR-SMART étaient près de 50 % moins bruités que ceux de tomo-SMART. L'analyse sur les champs de vitesse comporte l'étude de quantités statistiques, de peak-locking, de divergence, du tenseur des gradients ainsi que de structures cohérentes.

Enfin, nous concluons avec une synthèse des résultats obtenus au cours de cette étude, en envisageant de nouvelles perspectives de recherche dans le contexte de la PIV tomographique.

Résumé étendu de thèse

0.1 Introduction

La Turbulence est l'un des grands problèmes non résolus de la Physique, au sens où une théorie prédictive complète des écoulements turbulents n'a pas encore été établie. Les écoulements turbulents sont caractérisés par des mouvements instationnaires, irréguliers, qui semblent aléatoires et chaotiques, aussi bien dans l'espace que dans le temps [Pope, 2000]. La turbulence est donc par essence, un phénomène tri-dimensionnel, ce qui pose la question de notre capacité à mesurer avec précision les déplacements 3D instationnaires d'écoulements turbulents.

Au cours du XX^{ime} siècle, nos capacités expérimentales de mesure se sont considérablement améliorées grâce au développement des technologies optiques, digitales et grâce à l'augmentation de nos capacités de calcul. Les premiers instruments de mesures permettaient une mesure uni-dimensionnelle du champ de vitesse (tube de pitot, fil chaud). Les visualisations planes d'écoulements utilisant des colorants ou de la fumée ont permis à la recherche sur les structures cohérentes de se développer. Grâce à l'amélioration des lasers à haute fréquence, des caméras digitales et des ordinateurs, le développement de la Vélocimétrie par Imagerie de Particules (PIV) a permis d'accéder à des mesures quantitatives de champs bi-dimensionnels (2D/2C). Cette mesure utilise la corrélation entre deux images de particules ensemençant l'écoulement et qui sont éclairées par un plan laser. De nombreuses avancées, aussi bien algorithmiques que technologiques, ont permis d'améliorer la précision spatiale et temporelle de la mesure. [Elsinga et al., 2005] ont introduit cette technique permettant d'étendre la PIV à la 3D, appelée PIV tomographique ou tomo-PIV. Le dispositif expérimental est étendu à la 3D, en utilisant plusieurs caméras (typiquement 4 [Scarano, 2013]) La PIV tomographique

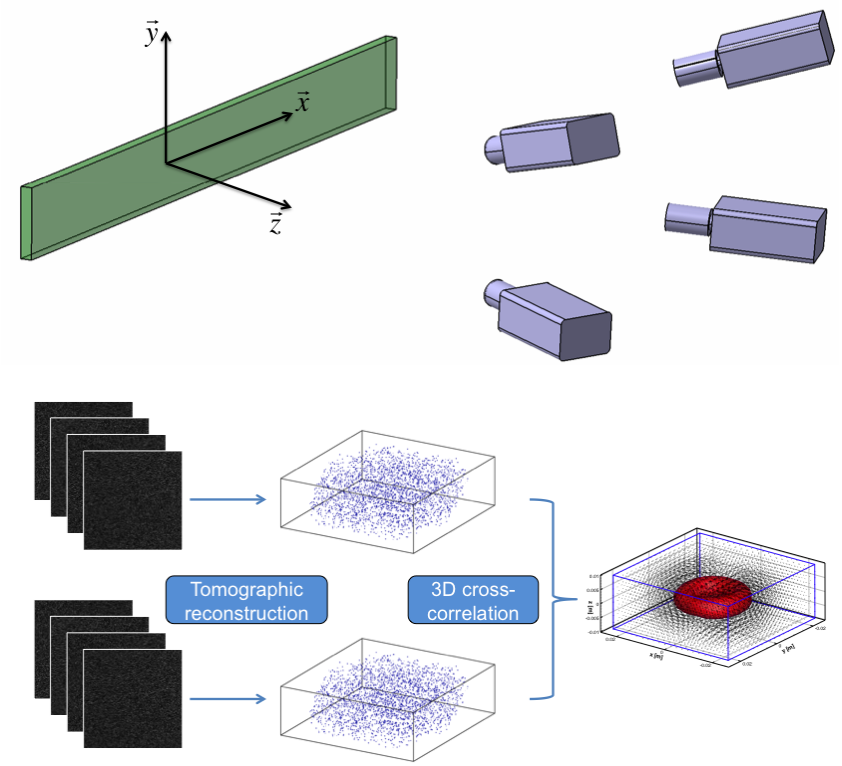

Figure 0.1.1: Principe du dispositif expérimental (**haut**) et des étapes algorithmiques (**bas**) de la PIV tomographique .

se fonde sur la reconstruction tomographique d'une distribution volumique d'intensité de particules traceuses, à partir de projections enregistrées par des caméras (voir figure 1.3.1). Les distributions volumiques sont ensuite corrélées, fournissant ainsi un champ de déplacement 3D. Cette étape de corrélation est une extension à la 3D de l'étape déjà existante dans la PIV 2D/2C.

C'est sur le développement de la PIV tomographique (tomo-PIV) pour la mesure d'écoulements turbulents que porte ma thèse.

La nouvelle étape de reconstruction tomographique est celle sur laquelle les efforts de la recherche se sont principalement portés. Cette étape a été vue historiquement ([Elsinga et al., 2006]) comme une inversion de système linéaire d'équations du type :

$$I(x_i, y_i) = \sum_{j=1:N} w_{i,j} E(x_j, y_j, z_j) \tag{0.1.1}$$

où I est l'ensemble des données des projections, E est le champ volumique d'intensité discrétisé que l'on essaye de reconstruire et w un modèle linéaire liant l'inconnue à la donnée, qui historiquement a été pris comme un modèle tomgraphique géométrique liant l'unité de discrétisation du volume (voxel) et le pixel de la donnée Elsinga et al. [2006]. La principale difficulté est le bruit de la reconstruction (particules fantômes) qui croît exponentiellement lorsqu'une forte densité de traceur est requise pour obtenir une résolution spatiale fine de la mesure [Scarano, 2013], particulièrement pour les écoulements turbulents. La plupart des efforts de la communauté scientifique se sont donc focalisés sur l'amélioration de la qualité de la reconstruction tomographique afin d'augmenter la densité de particules traceuses et donc la résolution spatiale de la mesure.

Des algorithmes comme MART ([Elsinga et al., 2006]) ou SMART ([Atkinson and Soria, 2009]) sont particulièrement bien adaptés aux caractéristiques de ce problème qui reconstruit un volume assez creux. Des techniques d'initialisation de ces algorithmes comme MFG [Worth and Nickels, 2008] puis plus important encore Multiplicative-line-of-sight (MLOS) [Atkinson and Soria, 2009], permettant de réduire la taille du problème, ont été introduites. Certaines améliorations se concentrent sur la sparsité de la solution pour améliorer la précision et le temps de calcul comme [Petra and Schnörr, 2009] et [Barbu et al., 2011]. Une amélioration significative a été apportée par les méthodes dites "multi-exposure" [Scarano, 2013] qui utilisent l'information cachée ans la cohérence temporelle de vraies particules, comme l'algorithme MTE de [Novara et al., 2010]. Cet algorithme a été étendu à la tomo-PIV résolue en temps [Lynch and Scarano, 2015].

Cependant, même si ces méthodes sont applicables pour un large panel de conditions expérimentales, elles ne prennent pas en compte la défocalisation optique, l'astigmastime ou d'autres abbérations optiques, qui changent la forme de l'image de la particule (Point Spread Function, PSF) et qui détériorent la qualité de la reconstruction [Elsinga et al., 2006]. Pour surmonter ces difficultés, [Scarano, 2013] ont proposé de prendre en compte ces variations tout en conservant la forme de la particule reconstruite comme un blob gaussien standard qui est adapté aux algorithmes de corrélation classiques.

Plus récemment, un ensemble de méthodes ont combiné des aspects de la 3D-PIV avec le tracking de 3D-PTV (Particule Tracking Velocimetry). [Wieneke, 2013] a introduit un algorithme itératif (Iterative Particle Reconstruction, IPR) qui détermine les coordonnées 3D des particules pour une densité supérieure à celle de la 3D-PTV. Dans le contexte de la 3D-PIV résolue en temps, où les particules peuvent être suivies sur de multiples snapshots, [Schanz et al., 2013b] ont utilisé le principe de IPR et "tracker" des particules sur plusieurs instants, permettant de trouver un critère clair d'élimination des particules fantômes dans la reconstruction. [Schanz et al., 2016] montrent des gains de performance aussi bien sur données synthétiques qu'expériemntales.

0.2 Objectifs de la thèse

C'est dans ce contexte très évolutif de la recherche que ma thèse se situe. Nous venons de voir les nombreuses avancées effectuées pour améliorer la qualité de la reconstruction tomographique, qui se concentrent principalement sur les méthodes algorithmique d'inversion. Le modèle d'inversion tomographique a été relativement peu étudié dans la littérature, surtout considérant le fait que la distribution 3D d'intensité n'est pas une quantité physique. Est-il possible de trouver un modèle d'inversion plus physique ? Un modèle de projection fondé sur une représentation plus physique de l'image PIV peut-il améliorer les performances de la reconstruction ?

A l'ONERA, un algorithme rapide et précis de cross-corrélation a été développé pour la 2D-PIV (FOLKI-PIV) et la stéréo-PIV (FOLKI-SPIV) [Champagnat et al., 2011]. Il est naturel de penser à étendre cet algorithme à la 3D. Comment cet algorithme résistera-t-il au bruit spécifique de la reconstruction tomographique ?

Ma thèse va tâcher de répondre à ces deux questions. Les avancées de ma thèse ainsi que les principaux résultats répondant à ces problématiques sont ici résumés en trois points différents : Tout d'abord un ensemble d'études numériques m'ont permis

d'étudier les conditions optiques de la 3D-PIV et leurs influences sur la qualité de la reconstruction tomographique. Dans un second temps, j'ai étudié les performances de notre algorithme de cross-corrélation 3D (FOLKI-3D) et sa robustesse vis-à-vis du bruit spécifique tomographique. Enfin, grâce à une meilleure compréhension des conditions optiques, nous introduisons un nouveau modèle de reconstruction tomographique utilisant une représentation particulaire de la création d'image PIV, que nous appelons Particle Volume Reconstruction (PVR). Des tests numériques ainsi qu'une validation expérimentale sur jet turbulent montrent des gains significatifs sur les approches classiques de reconstruction utilisant un modèle géométrique d'inversion.

0.3 Etudes numériques des conditions expérimentales dans la PIV-3D

Afin de mieux appréhender le bruit de reconstruction et comprendre l'impact des conditions expérimentales, nous avons effectué une étude numérique sur les facteurs expérimentaux nuisant à la qualité de la reconstruction. Cette étude est effectuée en simulant numériquement le processus expérimentale de la PIV-3D. La simulation numérique est particulièrement bien adaptée pour l'étude de la qualité de la reconstruction tomographique puisque cela requiert la connaissance de la vérité terrain, c'est-à-dire, la localisation des particules ainsi que leur intensités. Dans nos images de synthèse, différents bruits ou détériorations d'images ont été généré pour évaluer leurs impact sur la qualité de la reconstruction. Nous avons considéré ici les conditions d'images que l'on trouve dans les écoulements incompressibles d'air.

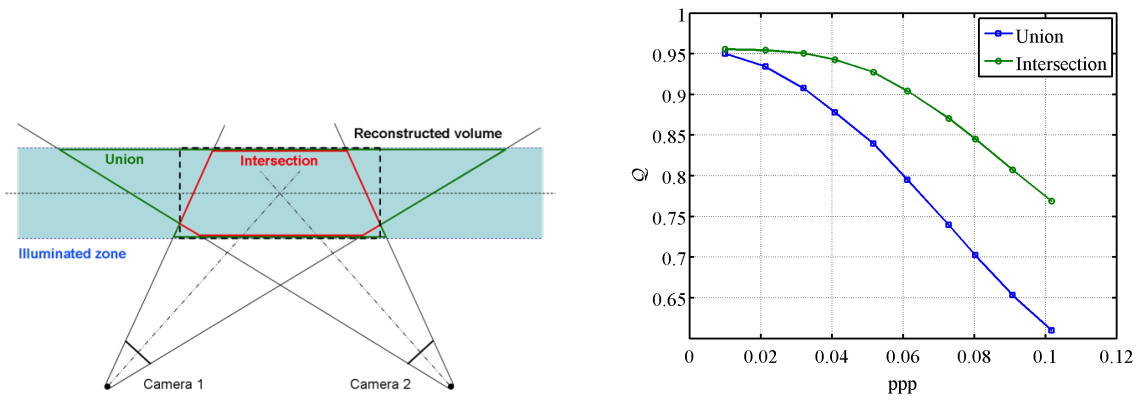

Figure 0.3.1: (**Gauche**) Dispositif expérimental typique avec 2 caméras pour simplifier la compréhension, montrant la difference entre le volume reconstruit (traits noirs discontinus), l'union et l'intersection (rouge) des champs de vue des caméras et de la zone laser. (**Droite**) Influence de la densité des traceurs lorsque les particules ne sont que dans l'intersection (vert) ou dans l'union (bleu).

La première dégradation d'images que nous avons étudiée peut être vue comme un bruit additionnel dans les images. A partir de considérations géométriques nous avons pu quantifier l'impact des "particules ajoutées", qui se trouvent dans la zone de l'Union entre le champ de vue des caméras et de la zone illuminée (voir figure 2.3.1, gauche). A partir de cela, un facteur géométrique a pu être déduit, permettant de quantifier le niveau de bruit introduit dans la reconstruction : c'est le ratio entre l'Intersection et l'Union défini par les champs de vue des caméras et la zone illuminée. On nomme ce facteur $R_{I/U}$. Les critères de qualité utilisés sont le critère $\mathcal{Q}$ classique [Elsinga et al., 2006] ainsi que

des critères de détection, Précision et Rappel construits sur les quantités TP (lorsqu'une détection est une vraie particule), FP (la détection est une particule fantôme, FN (pas de détection là où une vraie particule est). On a alors $Precision = TP/(TP + FP)$ et $Rappel = TP/(TP + FN)$. L'impact principal sur la reconstruction de $R_{I/U}$ est l'augmentation du nombre et de l'intensité des particules fantômes figure 2.3.3. Nous démontrons qu'effectuer des simulations numériques sans prendre en compte ces effets revient à surestimer drastiquement la précision de l'algorithme de reconstruction (voir figure 2.3.1, droite).

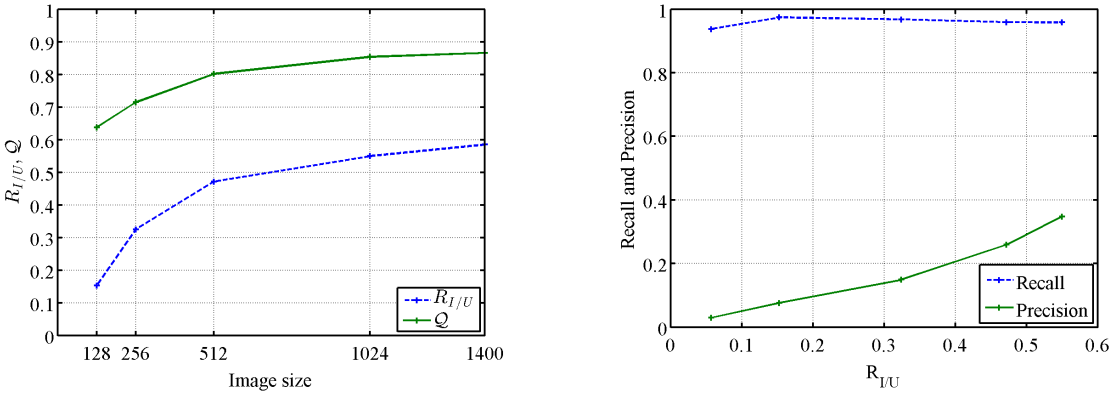

Figure 0.3.2: (**Gauche**) Impact de la taille de l'image sur le ratio $R_{I/U}$ et sur la qualité de la reconstruction $\mathcal{Q}$ et influence du ratio $R_{I/U}$ sur la Précision et le Rappel (**Droite**).

L'autre aspect de détérioration des images que j'ai étudié est la diminution du ratio signal-à-bruit dans les images, en considérant particulièrement la diffusion de Mie ainsi que les effets de défocalisation. Les résultats (figure 2.3.6) suggèrent que l'impact principal qu'a la délocalisation des particules dans les images sur la reconstruction est la perte des vraies particules. Cette perte est due à la baisse de l'intensité maximale de la particule dans l'image lorsque la taille de la PSF augmente (quand les particules deviennent de plus en plus floues).

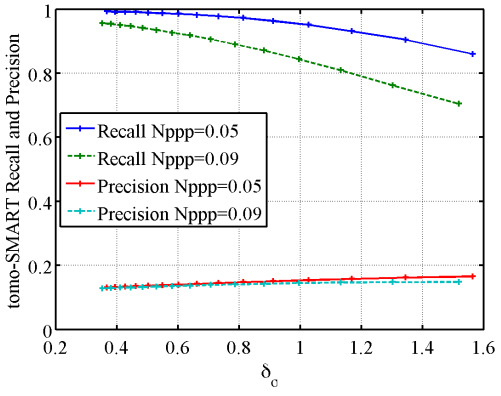

Figure 0.3.3: Rappel et Précision pour différentes densité ($ppp = 0.055$ and $ppp = 0.098$) en fonction d'une intensité variable de défocalisation δ_σ.

Pour l'étude des effets de la diffusion de Mie où l'intensité d'une particule est fonction de son diamètre et de l'angle entre la direction de la lumière qui l'impacte et la caméra figure 2.3.7, j'ai classé les effets en trois phénomènes physiques : une différence d'intensité entre les images, la dispersion d'intensité à l'intérieur même d'une image, et la dépendance de l'intensité d'une particule sur son diamètre. Nous avons montré que

ne pas prendre en compte le véritable modèle de la diffusion de Mie dans une simulation sur-estime drastiquement la qualité de la reconstruction. De plus, la source principale de détérioration de la qualité de la reconstruction est, comme pour la délocalisation, la perte des vraies particules, causée par la nature polydisperse de l'ensemencement dispersant les intensités des particules de façon drastique.

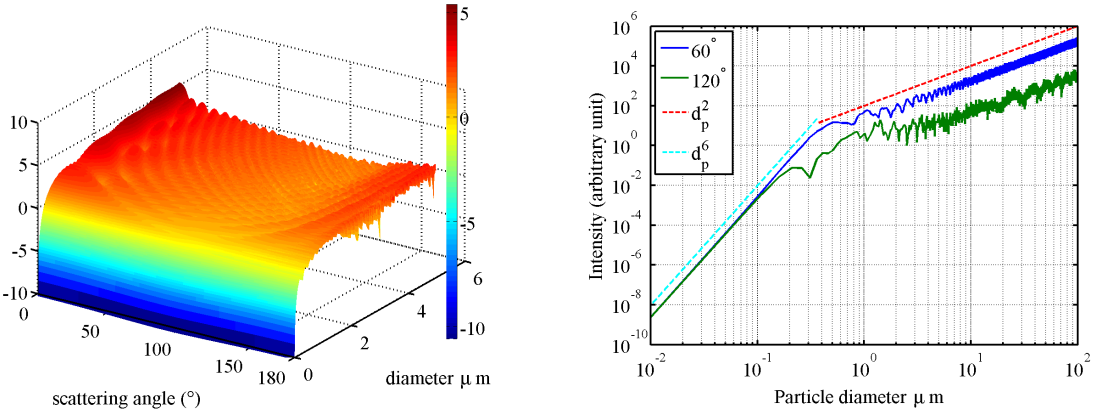

Figure 0.3.4: (**Gauche**) Logarithme de la fonction de diffusion de Mie $\mathcal{S}_{11}$ qui dépend de deux paramètres : le diamètre de la particule d_p ainqi que l'angle de diffusion θ. (**Droite**) Logarithme de la fonction de diffusion de Mie pour deux angles de diffusion fixés.

Ces raffinements de la simulation augmentent le réalisme de la simulation et révèlent l'importance des conditions optiques lors de la prise d'image en PIV-3D. Ces conditions sont tout particulièrement déterminantes quand le ratio signal-à-bruit dans les images est bas, ce qui est souvent le cas lorsque l'on effectue une expérience de PIV-3D résolue en temps dans l'air. De plus, nous avons montré qu'une fois les caméras positionnées, optimiser leur orientation n'avait qu'un apport peu significatif sur le ratio $R_{I/U}$.

0.4 Une nouvelle méthode de correlation 3D utilisant un paradigme de Lucas-Kanade

Nous introduisons une méthode de cross-corrélation pour la PIV-3D (FOLKI-3D) comme une extension sur GPU à la 3D de l'algorithme FOLKI-PIV [Champagnat et al., 2011]. Comme dans le cas plan, le déplacement y est cherché en minimisant itérativement une fonctionnelle equation (4.2.1), du type des moindres carrés, par déformation de volume. Cette déformation est faite soit par un schéma linéaire soit par un schéma d'ordre plus élevé, dit B-Spline cubique.

Voici une description de la fonctionnelle que l'on minimise : Si l'on considère un volume physique discrétisé, on appelle k l'indice du voxel de la grille. Comme dans une approche traditionnelle de PIV utilisant la correlation d'image, notre objectif est de déterminer le déplacement $u(k)$ d'un motif de particules 3D contenues dans le volume d'interrogation (IV), $V(k)$ centré autour d'un voxel k. Cependant, l'objectif mathématique n'est pas le même et appartient à la famille algorithmique de Lucas-Kanade [Baker and Matthews, 2004], car cela revient à minimiser une somme des différences au carré.

$$u(k) = \textbf{arg min} \sum_m v(m-k) \left[E_1\left(m - \frac{u(k)}{2}\right) - E_2\left(m + \frac{u(k)}{2}\right)\right]^2 \qquad (0.4.1)$$

Les tests synthétiques confirment que la réponse fréquentielle d'espace est semblable à celle d'autres algorithmes classiques itératifs de déformation de volume aussi bien pour des fenêtres de poids "top-hat" ou gaussienne figure 4.3.1. De plus, des gains de performance similaire à la littérature ont été observés en utilisant l'interpolation B-Spline plutôt que la simple interpolation linéaire.

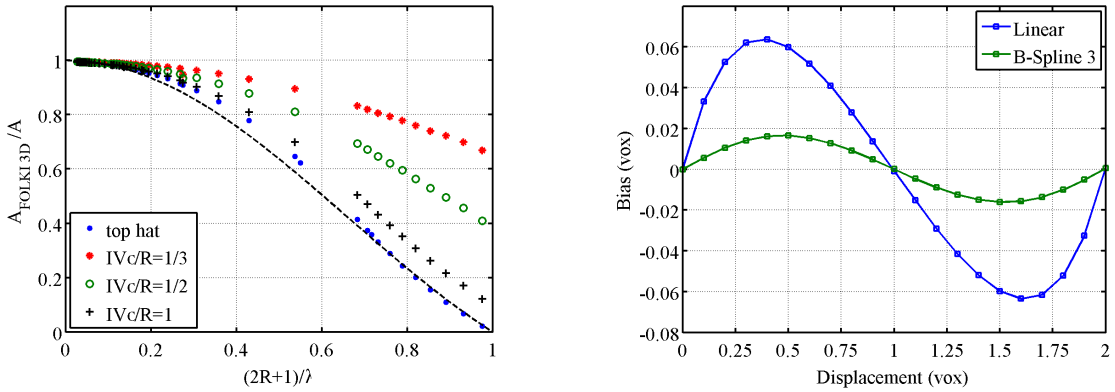

Figure 0.4.1: (**Gauche**) Réponse fréquentielle d'espace de l'algorithme pour différentes fonctions de poids : top-hat (en noir) ou gaussien, avec différentes paramétrisations de l'écart type de la gaussienne par rapport au rayon de la fenêtre (rouge, bleu, vert). (**Droite**) Biais d'erreur de l'algorithme à un déplacement unidimensionnel pour une interpolation linéaire (bleu) ou d'ordre plus élevé B-Spline (vert).

Des simulations numériques de reconstruction tomographique nous ont alors permis de caractériser la robustesse de l'algorithme au bruit spécifique de la tomographie, c'est-à-dire aux particules fantômes, ainsi que les gains obtenus par une interpolation d'ordre plus élevé dans des configurations caméras plus réalistes. Nous avons montré que FOLKI-3D était plus robuste aux particules fantômes cohérentes qu'un algorithme classique de déformation volumique figure 4.4.3. Pour montrer cela, nous avons comparé les performances de notre algorithme à celles du corrélateur de LaVision Davis 8.2 utilisant le mode de corrélation directe et les mêmes paramétrages de volumes d'interrogation. Le déplacement utilisé est une déplacement de cisaillement le long des lignes de vues des caméras, où le déplacement est de l'ordre de grandeur de la taille de la particule. Dans ce cas [Elsinga et al., 2011] ont montré que des particules fantômes cohérentes entre deux instants apparaissaient et détérioraient le calcul du déplacement. De plus des gains en précision pour des schémas d'interpolation d'ordre plus élevé ont été confirmés pour différentes quantités de particules fantômes ainsi que différentes formes des particules reconstruites qui dépendent des configurations caméras.

0.5 Particle Volume Reconstruction

0.5.1 Principes et tests synthétiques

Les études portant sur les conditions optiques de la tomo-PIV nous a permis de proposer une approche alternative à la reconstruction tomographique classique. Nous nommons cette méthode Reconstruction Volumique de Particules (PVR). Le but de cette approche est de reconstruire une particule presque sur un unique voxel, plutôt que comme un agrégat de voxels de taille étendue, en se fondant sur une représentation particulaire des im-

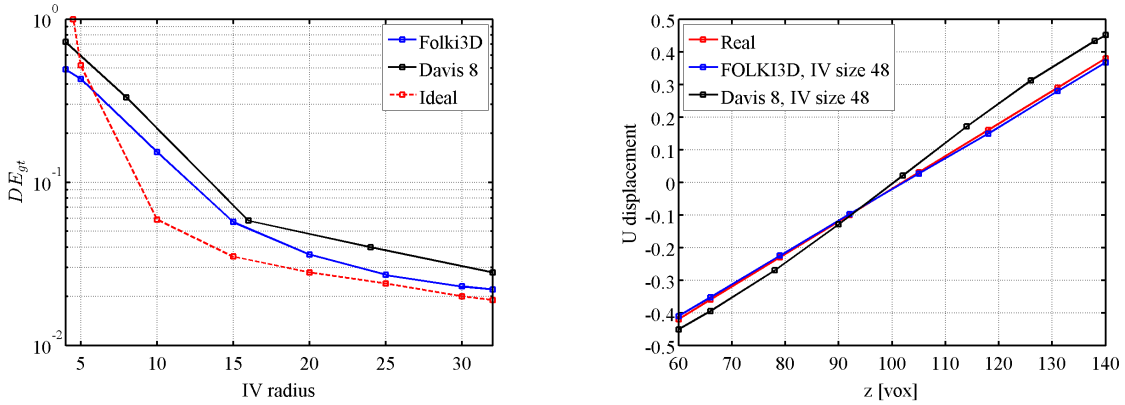

Figure 0.4.2: (**Gauche**) Erreur moyenne de déplacement pour le déplacement de cisaillement, en fonction de la taille du volume d'interrogation, IV radius, et (**Droite**) profiles de déplacement le long de Z (profondeur du volume) moyenné sur les directions X et Y avec la même taille de volume d'interrogation obtenus par notre algorithme FOLKI-3D et Davis 8.2 sur des reconstructions tomographiques ainsi qu'un déplacement idéal obtenus avec FOLKI-3D sur une reconstruction parfaite de particules. Remarque : le déplacement "real" dans le graphique de droite correspond au profil du vrai déplacement imposé.

ages. En effet, l'image d'une particule peut être vue comme la projection d'une particule ponctuelle sur la caméra, qui s'étend sur les pixels par la PSF ou comme l'intégration le long de la ligne de vue des pixels d'une intensité volumique (voir figure 0.5.1. La seconde approche est celle qui historiquement a été choisie, préférant une vision tomographique du volume.

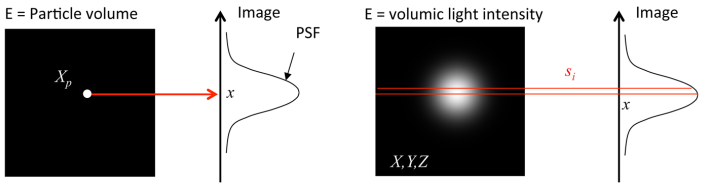

Figure 0.5.1: Formation de l'image à partir de la projection d'un volume: soit un volume particulaire (**Gauche**) soit un modèle de blob (**Droite**)

PVR suppose une représentation creuse du volume où la particule est presque vue comme un point, à mi-chemin entre un point infinitésimalement petit (ce qu'en réalité elles sont presque) et un blob plus large de 2 à 3 voxles de diamètre, utilisé traditionnellement en tomo-PIV. De cette représentation, il est possible de faire deux choses : soit on raffine la position de la particule pour privilégier une approche particulaire de la détection de mouvement et donc faire du tracking comme en PTV-3D; soit on ré-élargit les particules par un filtrage gaussien pour reconstruire des blobs de 2/3 voxels de diamètre requis par les algorithmes de corrélation de 3D-PIV. Nous utiliserons ici la seconde possibilité comme méthode de reconstruction, en incorporant PVR dans un algorithme classique de reconstruction SMART [Atkinson and Soria, 2009].
Les performances de la méthode de reconstruction PVR-SMART ont été étudiées sur données synthétiques, aussi bien sur la reconstruction que sur des champs de vitesses reconstruits. Nous montrons que PVR-SMART a de meilleures performances que tomo-SAMRT [Atkinson and Soria, 2009] sur un large spectre de conditions génératrices et pour

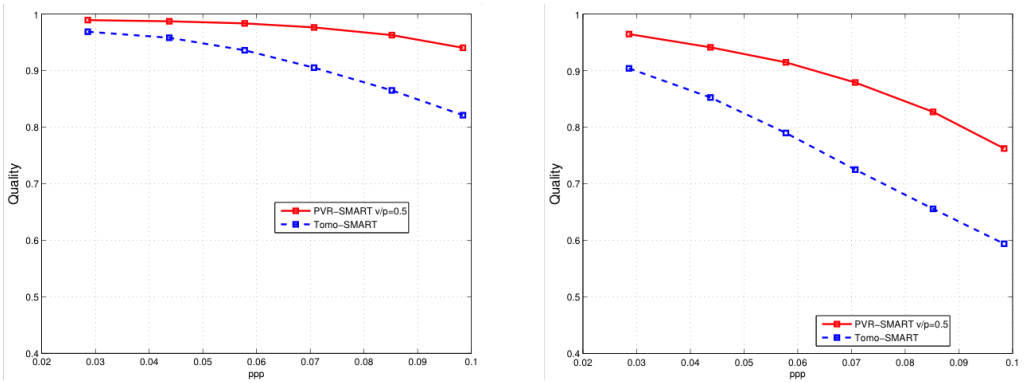

Figure 0.5.2: Critère $\mathcal{Q}$ de qualité de reconstruction en fonction de la densité *ppp* dans le cas où les particules ne sont disposées dans le volume de l'Intersection (**Gauche**) ou dans le volume de l'Union (**Droite**)

diverses critères de qualité sur le volume reconstruit et sur des champs de déplacements, particulièrement pour des densités supérieures à 0.06 *ppp*. Nous montrons également que PVR-SMART était moins impacté par le bruit généré par "les particules ajoutées" qui a fait l'objet d'études résumées dans la section 0.3. La chute de performance impliquée par les particules dans le volume de l'Union est plus forte pour tomo-SMART que pour PVR-SMART (voir figure 0.5.2). De plus, nous avons caractérisé le comportement de PVR-SMART pour différentes tailles de PSF : PVR-SMART est particulièrement plus performant que tomo-SMART pour des écarts types de PSF supérieurs à 0.8. Nous avons également vérifié la robustesse de PVR-SMART à une mauvaise connaissance de la taille de la PSF, ce qui est souvent le cas dans une expérience.

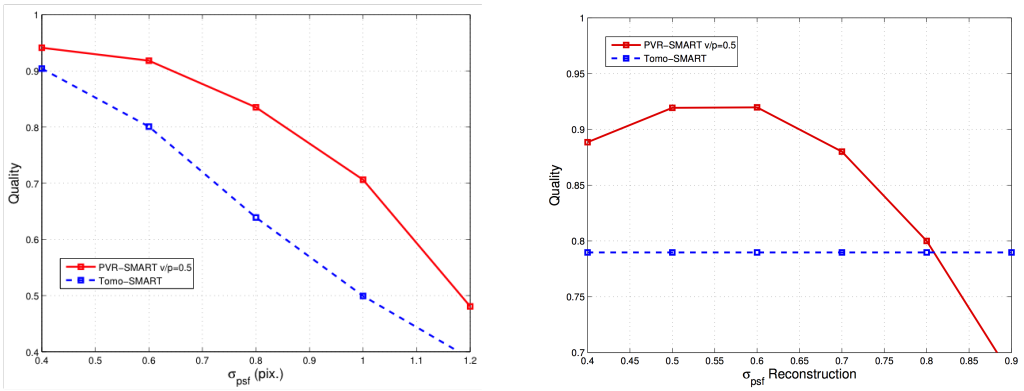

Figure 0.5.3: Critère $\mathcal{Q}$ de qualité de reconstruction en fonction pour différentes valeurs de PSF dans les images à densité constante (**Gauche**) et dans le cas où l'on ne connait pas la taille de la PSF, fixée ici à $\sigma_{PSF} = 0.6$ (**Droite**).

Les tests montrent que les gains de performance sur les champs de vitesse reconstruits sont systématiquement obtenus avec PVR-SMART par rapport à tomo-SMART quelle que soit la valeur de la PSF dans le cas de l'indétermination et que ces gains persistent dans le cas d'une sur-estimation de plus de 10 % de la vraie valeur de la PSF.

0.5.2 Validation expérimentale de PVR sur Jet turbulent

Tout est maintenant prêt pour effectuer une validation expérimentale de PVR. Le but de cette validation est de comparer différentes quantités physiques (statistiques, structures cohérentes entre autres) issues de reconstructions PVR-SMART ou tomo-SMART

et corrélées avec notre algorithme FOLKI-3D. L'écoulement étudié est un jet d'air rond turbulent à un nombre de Reynolds basé sur le diamètre D de $Re_D \approx 4300$ et $D = 12\ mm$. De plus, afin de disposer d'une mesure de référence, nous avons synchronisé au système PIV-3D, un système de mesure PIV-2D classique. De plus, ce dispositif nous permettra une estimation de la densité de particules.

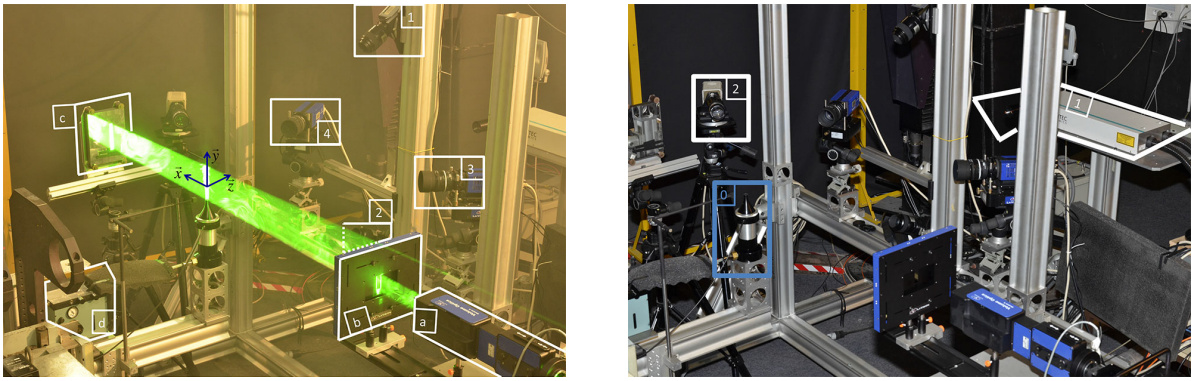

Figure 0.5.4: **Gauche :** Photo du dispositif de PIV-3D avec a = générateur de volume laser, b = diaphragme, c = miroir, d = générateur d'ensemencement interne, $\{1/2/3/4\}$ = numéros des caméras. **Droite :** Dispositif de PIV-2D avec *0* = buse du jet turbulent, *1* = laser 2D, *2* = caméra de la PIV-2D.

Le dispositif expérimental de PIV-3D est composé de 4 caméras 2048×2048 pixels, disposées en croix, d'un laser de 120 mJ basse fréquence de 14.5 mm d'épaisseur, d'un miroir permettant de minimiser les effets de la diffusion de Mie, ainsi que de deux systèmes d'ensemencement (interne et externe au jet), voir figure 5.2.3. Le système de PIV-2D est composé d'un laser de 200 mJ ainsi que d'une caméra 4000×2672. Les deux systèmes ont été synchronisé pour acquérir alternativement une mesure 3D et une mesure 2D, toutes les deux à la même fréquence de 2 Hz. Les procédures de calibration sont effectuées pour la PIV-3D en utilisant un modèle explicite sténopé de caméra avec 2 angles de Scheimpflug. Les détails peuvent être trouvés dans [Cornic et al., 2015b]. De plus, nous utilisons une procédure de self-calibration [Wieneke, 2008] afin de minimiser les erreurs de calibration, qui doivent être inférieurs à 0.1 pixels pour une bonne reconstruction [Wieneke, 2008]. La procédure de calibration de la PIV-2D est effectuée utilisant un code maison [Le Sant et al., 2007].

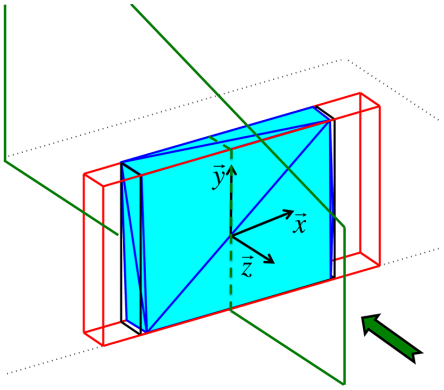

Figure 0.5.5: Visualisation des volumes de PIV-3D avec en bleu, le volume de l'Intersection, en noir, le plus petit parallélépipède rectangle contenant l'Intersection, et en rouge le plus petit parallélépipède rectangle contenant l'Union. En vert, nous avons représenté le plan de mesure de la PIV-2C.

Le dispositif de PIV-3D permet de reconstruire un volume de $112 \times 86 \times 14.5$ mm avec une résolution de 18. vox/mm. Pour la PIV-2D, le plan de mesure est de 128×86 mm dans le plan $x = 0$ (voir figure 5.2.4), et la résolution est de 29.7 pix/mm.

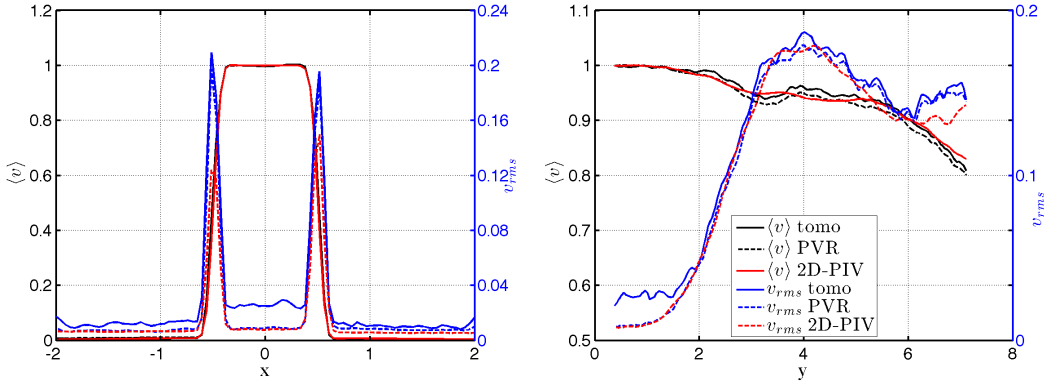

Figure 0.5.6: **Gauche :** Profil de vitesse axiale moyenne et de fluctuations rms à $z = 0$ and $y = 0.46 * D$ **Droite :** Profils de vitesse axiale et fluctuations rms le long de l'axe central du jet.

Une étude intensive a été effectuée afin de déterminer les meilleurs paramétrages possibles des algorithmes de reconstruction et de corrélation. Un soin tout particulier a été porté au choix des valeurs de seuillage utilisées dans la reconstruction PVR-SMART et tomo-SMART pour juguler les effets néfastes du bruit de capteur. Le choix de la taille de la PSF de reconstruction pour PVR a été effectué a-posteriori à une valeur de $\sigma_{PSF} = 0.2$. Les tailles de la fenêtre d'interrogation en PIV-2D et du volume d'interrogation en PIV-3D ont également été fixé a-posteriori, en fonction d'un compromis entre le nombre de particules par fenêtre d'interrogation et le bruit de mesure.

Différentes densités de particules ont été utilisées pour comparer les performances de PVR-SMART et de tomo-SMART sur la région proche buse du jet, de 0 à 7 diamètre D. Nous ne montrons dans ce résumé que les résultats comportant 300 snapshots de PIV-3D dont la densité de particules traceuses a été estimée à près de 0.15 ppp (quoique que nous montrions dans le manuscrit complet que cette estimation est sur-évaluée).

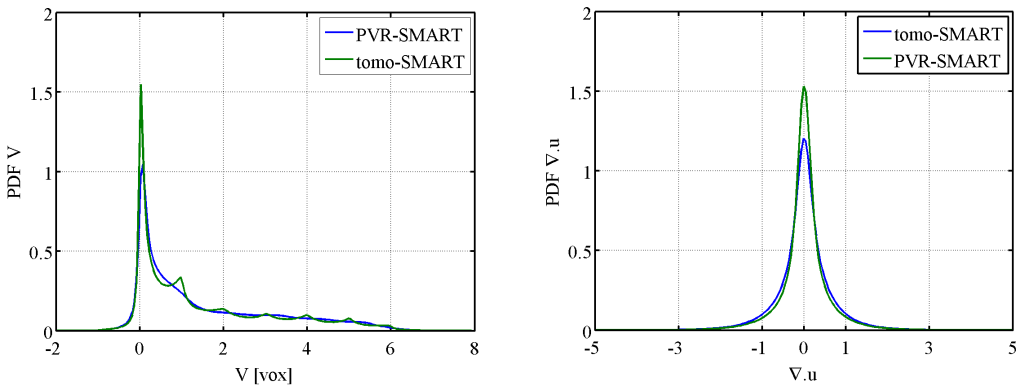

Figure 0.5.7: **Gauche :** Fonction de densité de probabilité des déplacements sur Y en voxels pour PVR-SMART et tomo-SMART **Droite :** Fonction de densité de probabilité de la divergence pour PVR-SMART et tomo-SMART.

Avec le pré-traitement des images utilisé, nous montrons que les champs de vitesse de PVR-SMART sont près de 50 % moins bruités que ceux de tomo-SMART. Cela est visible lorsque l'on compare le profils moyens et les fluctuations rms en sortie de buse ainsi que le long de l'axe principal du jet figure 6.3.4. On observe que dans les zones de faibles fluctuations physiques, les courbes de fluctuations rms de PIV-2D et PVR-SMART se superposent, alors que tomo-SMART a de plus fortes valeurs de fluctuations rms, ce qui implique que tomo-SMART a plus de bruit de mesure que PVR-SMART.

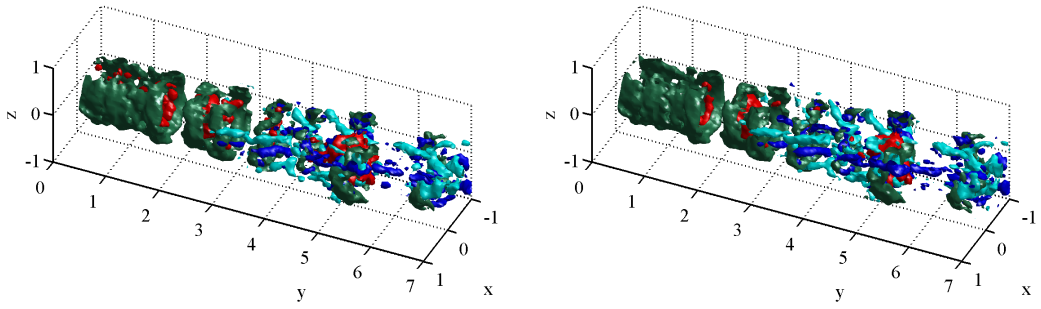

Figure 0.5.8: Isovaleur de la vitesse axiale à $1.05V_0$ (en rouge), où V_0 est la vitesse de sortie du jet, isovaleur de la composante azimuthale de la vorticité $\omega_\theta = 2$ (vert), isovaleurs de la composante axiale de la vorticité $\omega_z = 1.2$ (cyan) et $\omega_z = -1.2$ (bleu) pour tomo-SMART (**Gauche**) et pour PVR-SMART (**Droite**).

Cette différence de bruit de mesure peut être expliquée en partie par le fait que PVR-SMART reconstruit mieux les particules avec moins de particules fantômes, cela étant démontré dans nos tests synthétiques. Mais une étude statistique des valeurs de déplacement en voxels montre aussi que tomo-SMART souffre de peak-locking, due certainement à la petite taille de la PSF dans les images, et les pré-traitements qui ne comportaient pas de filtrage gaussien (voir figure 6.3.5). Tomo-SMART semble avoir plus d'erreurs de mesure que PVR-SMART. Cela est confirmé par l'analyse statistique de la divergence. En effet, pour un écoulement incompressible, la divergence de l'écoulement étant nulle, celle-ci peut être vue comme une estimation de l'erreur de mesure. La figure 6.3.5 montre que PVR-SMART a une divergence plus petite que tomo-SMART.

La PIV-3D permet de visualiser les structures cohérentes de l'écoulement puisqu'elle donne accès au champ 3D de vitesse. La comparaison de la structure de l'écoulement mesurée par tomo-SMART ou PVR-SMART confirme que tomo-SMART est plus bruité que PVR-SMART. La figure 6.3.9 visualise des isovaleurs des composantes azimuthales et axiales de vorticité du jet. Cette visualisation permet de montrer les anneaux de vorticité issus de l'instabilité de Kelvin-Helmotz convectés le long du jet, le développement des instabilités azimuthales sur ces anneaux ainsi que l'apparition de paires de tourbillons axiaux. Une visualisation zoomée entre 2.5 et 4.5 diamètres permet de voir que les structures de vorticité de tomo-SMART sont plus bruitées, moins bien définies et moins lisses que PVR-SMART. De plus, on peut associer les patchs rouges de sur-vitesse axiale visibles sur tomo-SMART au peak-locking, alors que PVR-SMART n'a que très zone de sur-vitesse axiale.

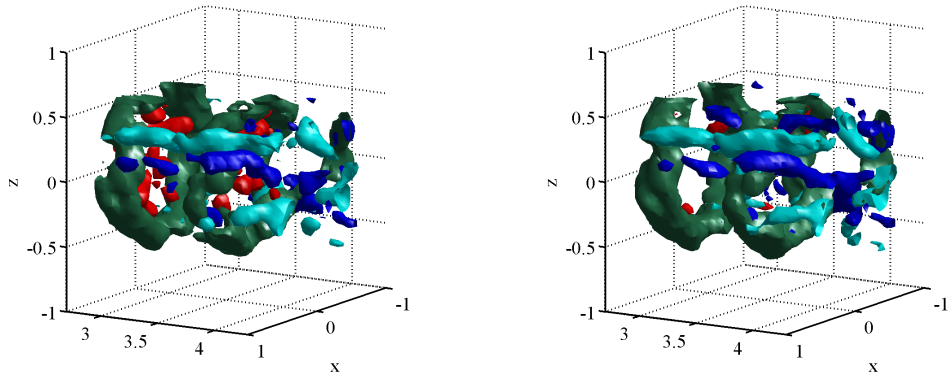

Figure 0.5.9: Isovaleur de la vitesse axiale à $1.05V_0$ (en rouge), où V_0 est la vitesse de sortie du jet, isovaleur de la composante azimuthale de la vorticité $\omega_\theta = 2$ (vert), isovaleurs de la composante axiale de la vorticité $\omega_z = 1.2$ (cyan) et $\omega_z = -1.2$ (bleu) pour tomo-SMART (**Gauche**) et pour PVR-SMART (**Droite**) entre 2.5 et 4.5 diamètres D.

0.6 Conclusions et perspectives :

Une étude initiale sur les conditions optiques présentes lors d'une expérience de PIV-3D résolue en temps dans l'air nous a permis d'appréhender l'impact de facteurs expérimentaux sur la qualité de reconstruction tomographique. Cela nous a mené à proposer un nouveau modèle de reconstruction tomographique (appelé PVR) fondé sur une vision particulaire physique des images de PIV, permettant également une conception particulaire du volume reconstruit où une particule est reconstruite sur très peu de voxels. Nous avons étendu à la 3D notre algorithme de cross-corrélation utilisant le paradigme de Lucas-Kanade, et évalué ses performances face au bruit spécifique de la reconstruction tomographique. La dernière partie de ma thèse est la validation expérimentale de PVR sur un jet turbulent de Reynolds $Re_D = 4300$, où nous montrons que notre méthode de reconstruction permet de mesurer des champs de vitesses moins bruités que les méthodes de reconstruction classiques.

La méthode de reconstruction PVR est le développement principal de ma thèse. PVR a besoin de la connaissance de la taille de la PSF dans les images. Une des perspectives principales est l'utilisation de méthodes de calibration de la PSF dans les images, qui permettraient de prendre en compte une PSF variable, et ainsi améliorer les performances de la reconstruction dans le cas de volumes de larges tailles où la défocalisation des particules dans les images est inévitable. De plus, de part sa représentation sparse spécifique du volume, PVR est particulièrement bien adapté à des algorithmes de reconstructions sparses [Cornic et al., 2013], avec pour but final d'estimer le déplacement par tracking.

Enfin, dans le contexte de la PIV résolue en temps appliquée aux jets turbulents étudiés au DAFE (ONERA) et après les travaux de [Davoust et al., 2014] et [Courtier, 2015], je pense que les méthodes développées lors de ma thèse seront des outils puissants d'étude des structures cohérentes et de leur développements.

Contents

1 Introduction

"If it disagrees with experiment, it's wrong. In that simple statement is the key to science. It doesn't make any difference how beautiful your guess is, it doesn't matter how smart you are, who made the guess, or what his name is... If it disagrees with experiment, it's wrong. That's all there is to it."

Richard Feynman, 1964

This quote from Richard Feynman's Messenger Lectures on "The Character of Physical Law" originally delivered at Cornell University in November 1964, underlines the importance of experimental sciences in physics. The ability to measure physical quantities with accuracy and precision is crucial to all areas of research in physics. Turbulence is one of the great unsolved problems in physics in the sense that a complete predictive theory of turbulent flow has not yet been established. Turbulent flows are characterized by unsteady, irregular, seemingly random and chaotic motions both in time and space [Pope, 2000]. Turbulence is inherently a three-dimensional phenomenon raising the issue of our ability to accurately measure the unsteady three-dimensional motions of turbulent flows.

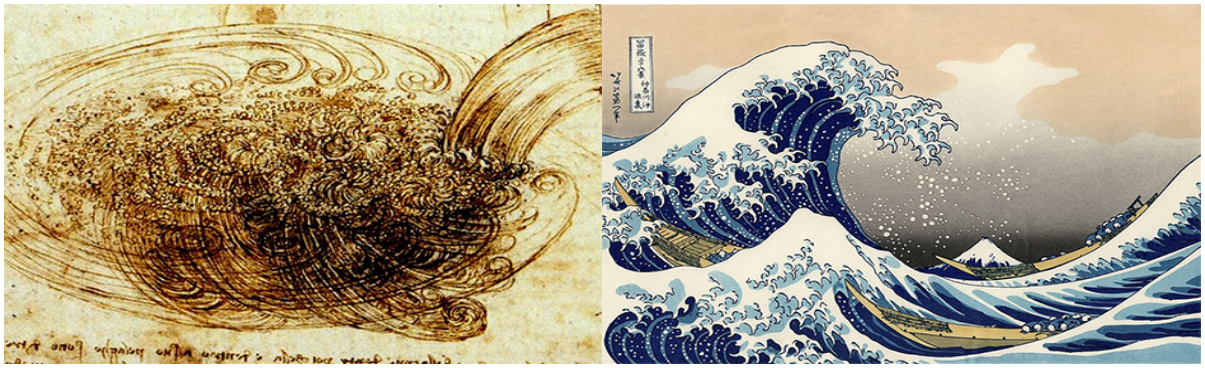

Figure 1.0.1: Representations of turbulent flows : from a Leonardo Da Vinci sketch of a free water jet issuing from a square hole into a pool in the 16th century (left), to the famous Great Wave off Kanagawa of Katsushika Hokusai in 1830 (right).

During the 20th century up to today, with the development of numerous optical, digital and computational technologies, our experimental capabilities have increased. The perception of turbulence and its understanding evolved along these measurement improvements as recalled in [Elsinga, 2008]. The initial perception of turbulence was through a statistical description : turbulent flows were seen as the superimposition of random fluctuations with a mean flow, stemming from the unsteady decomposition of Osbourne Reynolds [Reynolds, 1895]. Turbulence was considered through fluctuation statistical analysis, studying statistical moments and correlation functions. This conception of turbulence was influenced and confirmed by the existing experimental

measurement at the time, which were point-wise measurements (of one to three velocity components), such as pressure probes, hot-wire velocimetry and laser-Doppler anemometry.

Flow visualization has always been used in fluid mechanics since the very start of research in this field. In 1904 Ludwig Prandtl used a suspension of mica particles on the surface of the water to study the steady and unsteady flow structures around two-dimensional models such as cylinders, prisms, or wings. In the 1950's, planar flow visualizations in turbulent flows, using dye or smoke as flow markers (figure 1.0.2), were responsible for the rise of the concept of coherent structures [Hussain, 1986]. Thanks to those visualizations, two-dimensional flow patterns were identified as being non-random, spatially coherent structures. However, those visualizations were only qualitative data. Thanks to the improvements of high repetition rate lasers, digital cameras and computational power, the development of Particle Image Velocimetry (PIV) led to quantitative data, by measuring two components of the velocity field in a plane (also called 2C/2D PIV). This technique strengthened research on coherent structures in turbulent flows where they were shown to play a dominant role. PIV became widely used in the community since it was the only measurement that offered such a dense quantitative data while being quite accurate, thanks to the algorithmic development of image post-processing. However, like turbulence, those structures are inherently three-dimensional. A development towards 3D was needed.

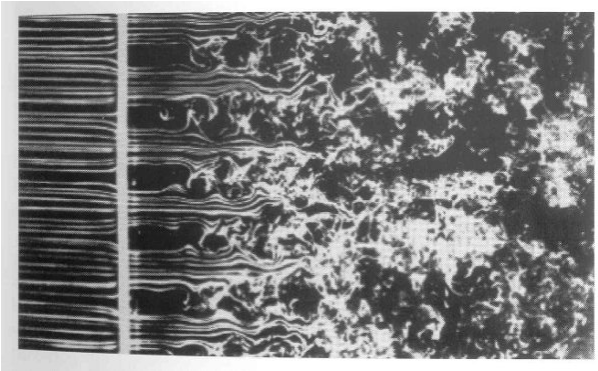

Figure 1.0.2: Smoke wires visualization of grid turbulence [Dyke, 1982]

Historically, three-dimensional quantitative data on turbulent flows became available with the development in the 1980's of Direct Numerical Simulation (DNS). It aims at solving the governing equations of the flow, ie Navier-Stokes equations, by resolving all the scales of the flow, both in space and in time, with initial and boundary conditions fitted to the flow under study. Though DNS full three-dimensional aspect of physical data and precision is quite unparalleled, its major limitation resides in its very definition, since all the scales are required to be solved. In turbulent flows, timescales and lengthscales have a very broad range, with a $Re^{-1/2}$ dependence for the Kolmogorov timescale and a $Re^{-3/4}$ dependence for the Kolmogorov lengthscale. This means that the computational cost of DNS significantly increases with the Reynolds number. Most turbulent flows in every day life or of practical industrial interest, have Reynolds numbers which are still inaccessible to DNS, the only hope being that the ever-increasing computational power catches up one day. To bypass this issue, turbulence modeling appeared in the form of Reynolds-Averaged Navier-Stokes (RANS) simulations or Large Eddy Simulations (LES). Both methods are based on a decomposition of the velocity field, either using ensemble decomposition from [Reynolds, 1895] for RANS, or

space-wise averages for LES. RANS simulations aim at solving the mean velocity field and LES aim at solving the large scales of the motions. However, when incorporating the decomposition in Navier-Stokes equations, both methods need a closure model to account for an unknown term of the equations. As the introducing quote pointed out, it is therefore crucial to compare those models to experimental results. This also drove the existing measurement methods to expand to 3D.

In the next section, we will present the main features of PIV, as well as different techniques that developed towards the measurement of 3D velocity fields. Finally, we will recall the main principles of tomographic PIV whose development and improvement is the subject of this research dissertation.

1.1 Particle Image Velocimetry

1.1.1 PIV Principles

PIV was introduced as an almost non intrusive planar velocity measurement technique using images of illuminated tracer particles in the flow to compute the flow displacement field. It can be seen as the improvement of a visualization technique, based on tracer images, towards a quantitative measurement technique. Figure 1.1.2 illustrates the basic experimental setup used in PIV along with its main working principle. A thorough review of this technique, working principle, limitations and evolution is explained in [Raffel et al., 2007].

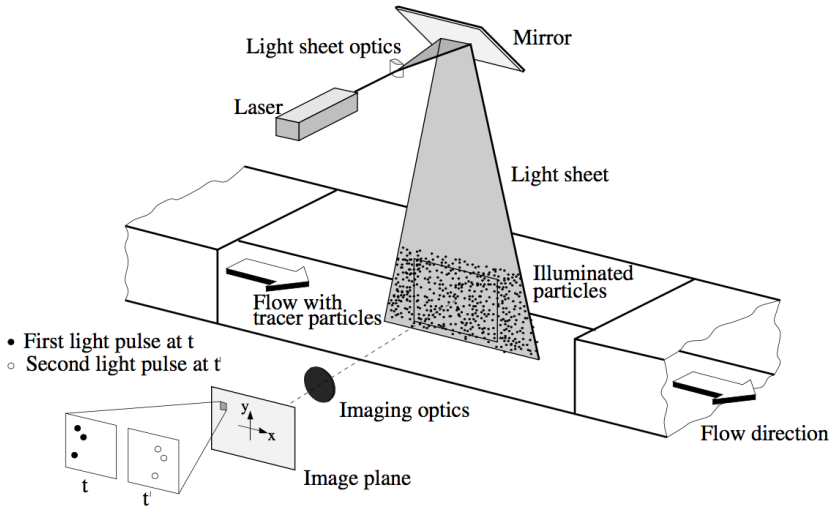

Figure 1.1.1: Representation of a classical 2D-PIV setup. This illustration comes from [Raffel et al., 2007]

We consider a flow seeded with passive tracer particles. They are illuminated by a pulsed laser which is mounted with an optical system resulting in a planar laser sheet. This planar laser sheet defines the measurement plane which is viewed by a single camera, synchronized with the laser pulses. The measurement plane is visualized on the camera focus plane, and consecutive images of tracer particles are recorded. The consecutive images, separated by a time interval Δt, show tracer particles 2D fields, exhibiting a 2D displacement field between the two images. Through image cross-correlation, based on image sub-domains pattern matching, one is able to compute an image displacement field, which is directly linked through camera calibration to the displacement flow field $\Delta \mathbf{x}$. One thus computes the velocity :

$$\mathbf{V} = \frac{\Delta \mathbf{x}}{\Delta t} \tag{1.1.1}$$

More precisely, the velocity field measured is an approximation of the real flow field, and through the investigation of this statement, one will understand some of the limitations and constraints that PIV has to face. Let us consider the Lagrangian description of velocity. In the first image I_0 taken at an time instant t, a fluid particle is $\xi(\mathbf{x_0}, t)$. In the next image I_1, the same fluid particles traveled to $\xi(\mathbf{x_0}, t + \Delta t)$. The Lagrangian description of the velocity ($\mathbf{V}_{\mathcal{L}}$) states that :

$$\mathbf{V}_{\mathcal{L}}(\mathbf{x_0}, t) = \frac{\mathrm{d}\xi(\mathbf{x_0}, t)}{\mathrm{d}t} = \lim_{\Delta t \to 0} \frac{\xi(\mathbf{x_0}, t + \Delta t) - \xi(\mathbf{x_0}, t)}{\Delta t} = \mathbf{V}_{\mathcal{E}}(\mathbf{x}, t)|_{\mathbf{x}=\xi(\mathbf{x_0},t)} \tag{1.1.2}$$

with $\mathbf{V}_{\mathcal{E}}$, the Eulerian description of the velocity flow field. PIV tries to approximate this limit at best. For an accurate measurement, the interval time between two pulses Δt has to be smaller than the smallest characteristic time of the flow. However, the displacement between two pulses must be large enough so as to be reconstructed with the cross-correlation algorithm. The image cross-correlation algorithm aims at tracking a particle ensemble pattern from one instant to the next. This results in an averaged estimation of the displacement field over the particle patterns, which determines the spatial resolution of the method. The measured velocity field is both time-averaged over the pulse time interval Δt and space-averaged over the particle pattern ensemble on which the cross-correlation is made.

Another issue resulting from the velocity definition is the fact that the velocity is time dependent. To take this into account, laser double pulses have to be as close as possible to one another. This was made possible by high repetition pulsed lasers which allow the PIV to be time-resolved. This allowed to track the coherent structures of the flow.

1.1.2 Tracer particles

Tracer particles are required to be small enough to follow all the scales of the flow. Furthermore, since their density is usually greater than that of the fluid (solid particles in water flow, or liquid particles in gas flows), inertial forces acting on the particles can create a lag of the particle motion. To follow the flow, the particle's lag must be smaller than the smaller characteristic timescale of the flow. In the air, where the denstiy of the particle is much higher than the density of the flow, the previous statement is verified using the particle's relaxation time τ_s resulting from the Stokes drag [Raffel et al., 2007] :

$$\tau_s = d_p^2 \frac{\rho_p}{18\mu} \tag{1.1.3}$$

where, d_p is the particle diameter, ρ_p the particle density, μ is the fluid dynamic viscosity. Depending on the fluid under study, a range of particle sizes and densities are possible. For air flows, tracer particles are often oil particles of about typical $1\mu m$ diameter.

1.1.3 Imaging particles

Once we are sure that the particles faithfully follow the flow, we must obtain a visualization of the tracer particles in the flow. This is done by illuminating the particles with the laser sheet. The two features that define a particle's image recorded on the CCD sensor of the camera are its intensity and its shape.

The intensity of a particle is directly proportional to the scattered light power [Raffel et al., 2007]. Particles scatter the incident light received from the laser, this scattering being thus observed by the cameras. The light scattering depends on different parameters, the refractive index of the particles to that of the surrounding medium, the particle size, its shape and orientation, light polarization and the observation angle. Considering spherical particles, if their diameter d_p is larger than the wavelength of the incident light λ, Mie's scattering theory can be applied. In that case, the light scattered depends mainly on two parameters : their diameter and the angle between the incident light and the viewing camera. For simplified conditions [Bohren and Huffman, 1983] computed the field of intensity resulting from the Mie regime. This particular subject will be a discussed topic in chapter 2.

The shape of the particle image is defined by its geometrical size on the focus plane of the camera as well as by the response function of the lens to a point particle. Indeed, considering the typical size of the particles, the wavelength of the illuminating laser, diffraction of the light occurs. [Hecht and Zajac, 2001] showed that a distant point source forms a Fraunhofer diffraction pattern through an aberration-free lens. The obtained pattern is called an Airy disk whose diameter is [Raffel et al., 2007] :

$$d_{diff} = 2.44 f_{\#}(M+1)\lambda \tag{1.1.4}$$

with $f_{\#}$, the ratio of the lens focal length f and the optics aperture diameter, and M the magnification factor. This response function of the optical system to a light source point is also called the optical system's Point Spread Function (PSF). [Adrian and Yao, 1985] showed that the particle final image shape is the combination of the particle geometric shape and the Airy function, with a final image size such as :

$$d_i = \sqrt{(M d_p)^2 + d_{diff}^2} \tag{1.1.5}$$

In classical PIV optical settings (in the air, and not in a microscopic setting where M is large), diffraction effects are dominant with the geometric size $M d_p$ being negligible compared to d_{diff}. The size the PSF function is often approximated by a Gaussian function defined by its standard deviation σ_{PSF} such as $\sigma_{PSF} = f_{\#}(1+M)\lambda\sqrt{2}/\pi$, [Raffel et al., 2007].

To avoid image blur and defocusing effects, the optics are set so that the focus plane coincides with the measurement plane. The blur effects appear when the geometrical size of the particles is comparable to the size of the PSF function. The depth of focus is the distance over which the particles stay sharp in the images. It is estimated with the following formula :

$$\delta z = 4.88\lambda f_{\#}^2 (1 + \frac{1}{M})^2 \tag{1.1.6}$$

Further details are available in chapter 5 of this dissertation especially for the estimation of the particle size when defocusing effects are predominant.

1.1.4 Displacement estimation

Displacement estimation is a research topic that is not restricted to PIV and fluid dynamics. This issue can be found for instance in solid mechanics where deformation fields are measured using target markers glued on the surface of the deforming solid. Displacement estimation in PIV is done using cross-correlation algorithms. In PIV community, the most widely adopted approach relies on the concept of Interrogation Window (IW).

Each consecutive image I_0 and I_1 is divided into sub-domains, i. e. IW. Each interrogation window, $\mathcal{W}_{\mathbf{k}}$ is centered around a pixel $\mathbf{k}$. Usually, $\mathcal{W}_{\mathbf{k}}$ is a square or a rectangle. From this definition, it is possible to compute a correlation function, centered around $\mathbf{k}$ between the two consecutive images :

$$C(\mathbf{k}, \Delta\mathbf{x}(\mathbf{k})) = \sum_{m \in \mathcal{W}_{\mathbf{k}}} w(m-\mathbf{k}) I_0(m) I_1(m - \Delta\mathbf{x}(\mathbf{k})) \tag{1.1.7}$$

with $w(m - \mathbf{k})$ a weighting function such as a Box or a Gaussian function. The idea is to find the displacement field $\Delta\mathbf{x}(\mathbf{k})$ which maximizes the correlation function. This will determine the displacement which moves the particle pattern $\mathcal{W}_\mathbf{k}$ centered around pixel $\mathbf{k}$ from one image I_0 to the next I_1. Most classical PIV algorithms tend to

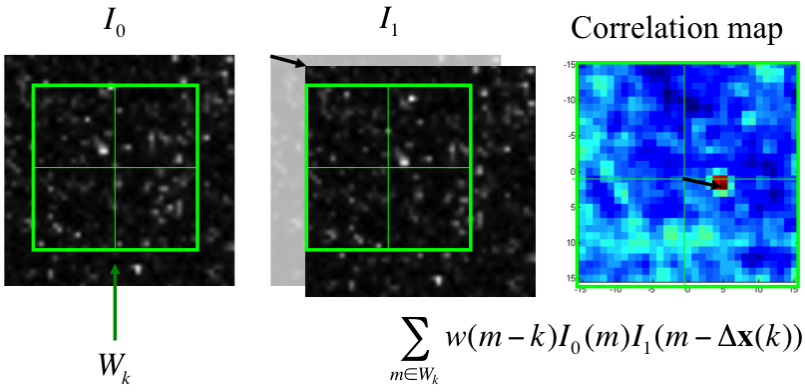

Figure 1.1.2: Zoomed representation of the correlation process : (left) : I_0 with Interrogation Window W_k centered around k, (middle) : I_0 and (right) : correlation map exhibiting a peak. This illustration comes from [Davoust, 2011].

compute the correlation function using Fast Fourier Transforms (FFT) and to find the maximum of the correlation function through a Gaussian peak-fitting process which yields sub-pixel accuracy. The main limitations of this method are the fact that the searched displacement has to be small compared to the size of the interrogation window. To improve the correlation accuracy, iterative image algorithms were developed [Scarano and Riethmuller, 2000] which use multigrid window deformation technique. A review of the iterative deformation technique is found in [Scarano, 2002], and the main features are summed up in chapter 4 of this dissertation.

More recently, at ONERA, [Champagnat et al., 2011] introduced a new approach to determine $\Delta\mathbf{x}(\mathbf{k})$. Based on a Lucas-Kanade paradigm [Baker and Matthews, 2004], it aims at minimizing a sum of squared differences :

$$SSD(\mathbf{k}, \Delta\mathbf{x}(\mathbf{k})) = \sum_{m\in\mathcal{W}_\mathbf{k}} w(m - \mathbf{k}) \left[I_0(m) - I_1(m - \Delta\mathbf{x}(\mathbf{k}))\right]^2 \tag{1.1.8}$$

The minimization process is done by a Gauss-Newton gradient descent algorithm, without having to do a peak-fitting step. More details are available in chapter 4 of this dissertation.

The accuracy of the displacement estimation step depends on different parameters. The number of tracer per IW is crucial. 10 particles were shown to yield good results [Raffel et al., 2007]. The size of the tracers in the images is also important so as to avoid peak-locking (measurement bias towards integer values). An optimized size of $2 - 3$ pixels in diameter was found [Raffel et al., 2007] depending on the size of the IW.

1.2 Towards 3D

In this section, we will present a quick survey of the main measurement techniques used to measure 3D flows.

To overcome PIV limitations to 2D velocity fields, a technique known as Stereoscopic PIV (Stereo-PIV) [Willert, 1997] [Arroyo and Greated, 1991] was introduced. It measures the 3D displacement field in the 2D plane defined by a laser light sheet using two cameras viewing the tracer particle motions from different directions. The two cameras see different projections from different angles : Using the camera calibration, we are able to reconstruct the three components of the displacement field in the laser sheet plane. It is referred to as a 2D-3C PIV method.

Another method directly issuing from 2D-PIV and Stereo-PIV is Scanning PIV [Brucker, 1995] with a light sheet scanning through the measurement volume. The volume is sliced by the laser sheet at different depth positions where images are recorded. This technique yields planar velocity fields obtained at the different recorded positions. The main benefit is that the relatively high spatial resolution from PIV is maintained since no requirement on the seeding density is made. However, the underlying assumption is that the scanning velocity must be very high compared to the flow velocities in order to yield an actual volumic measurement, which means that this technique cannot be used for high velocity flows such as commonly found in turbulent air flows.

Holographic-PIV (HPIV) is a full 3D technique [Zhang et al., 1997],[Hinsch, 2002]. It uses the interference pattern of a reference light beam with light scattered by a particle, which is recorded on a on a photographic plate or, more recently, directly on CCD camera sensors (Digital Holographic PIV, DHPIV). The interference pattern is then used to determine the particle location in depth. The main difficulty is to extract quantitative measurements from film photography. To bypasss this issue, DHPIV was developed. However, this technique comes with volume limitations (and thus, is limited to low seeding densities), which corresponds to configurations with an optimal optical system accuracy-wise [Meng et al., 2004]. A full review of the different techniques can be found in [Meng et al., 2004].

One of the main 3D measurement technique is Three-dimensional Particle Tracking Velocimetry (3D-PTV) [Maas et al., 1993]. Like Defocusing PIV [Pereira et al., 2000], it is based on the identification of individual particles in the PIV image recordings using several cameras. For 3D-PTV, from the different viewing directions, the particles 3D locations in space are found using epipolar geometry : the intersection of the lines of sight corresponding to a particle image in the recordings from several viewing directions. In Defocusing PIV, a different implementation is used to find the particle location using the defocused blur of the seeding particles, see [Pereira et al., 2000] for more details. Once the particles are found in space in different frames, they are tracked from one frame to the next [Malik et al., 1993] yielding Lagrangian motion and Eulerian velocities by interpolation of the Lagrangian velocities on a mesh. However, the main limitation is relative low seeding density. Indeed, when the seeding density increases, the epipolar geometry is not discriminating enough to eliminate false particle detections. [Maas et al., 1993] suggested to use a seeding density of typically 0.005 particles per pixel for a three cameras system. However, recent developments combining iterative reconstruction algorithm and particle tracking (such as the Shake-The-box algorithm [Schanz et al., 2013b]) have shown promising results in term of seeding density (see section 1.3.2.4).

1.3 Tomographic PIV

Tomographic PIV (tomo-PIV) or 3D-PIV was introduced in 2006 [Elsinga et al., 2006] as an extension of PIV for three-dimensional measurements. A thorough review of the method, its principles, limitations, practice advice as well as a survey of its major applications can be found in [Scarano, 2013]. The overall idea behind tomo-PIV is that it combines a simple optical setup with a quite robust particle volume reconstruction procedure. This process does not use particle identification as does 3D-PTV which allows for an increase in the seeding density up to around 0.05 particles per pixel. The robustness of the velocimetry technique is further increased by applying particle pattern matching instead of particle tracking. Furthermore, it is well suited to measure high speed flows, which Scanning-PIV can not do. Its relatively high spatial resolution makes it an ideal 3D measurement technique for turbulent flows. This is one of the reasons why the fluid dynamics community takes such an increasing interest in this measurement technique.

1.3.1 Principles and general remarks

1.3.1.1 Working principles

The main idea behind the method is to use the principle of PIV, i. e. image correlation of seeded flows, and to extend it to 3D. In PIV, the displacement is found by correlating two objects, more precisely by reconstructing the motion that transformed an object from one recorded state to another recorded state. To obtain a 3D displacement field by a cross-correlation method, one needs a 3D object that represents the state of the system at a given time. In 2D-PIV, the state of the system (the flow) is represented by a 2D image of particles. Therefore, to expand it to 3D, one needs a pseudo 3D image of the particles.

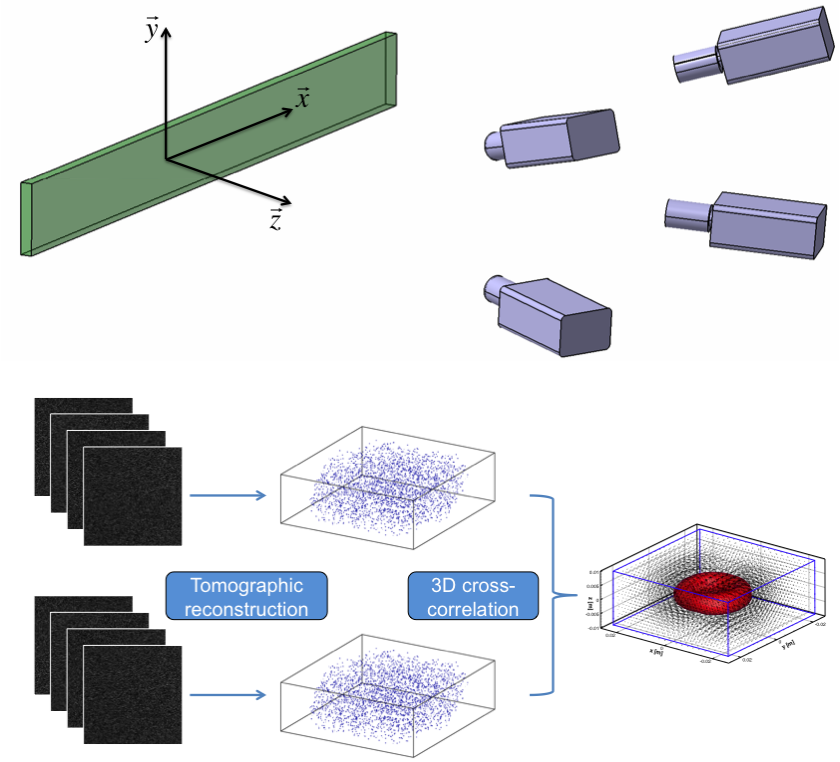

Figure 1.3.1: Simplified experimental setup (top) and main working principles of tomographic PIV (down).

In practice, this 3D intensity distribution is obtained by tomography. Tomography is a well known concept in the medical imaging or in materials sciences. It consists in reconstructing an object based on recorded projections. This is an inverse problem. Most of the time, the number of projections is quite high, as the non-moving object can be viewed by a recording device numerous time. 3D-PIV uses this concept of tomography to reconstruct 3D images of the particles from recorded 2D projections. In a fluid dynamics context (typically in the air), where the flow velocities are high, the recorded devices are high speed cameras. Furthermore, the optical accesses in a wind or hydrodynamic tunnel are usually scarce in number, not to mention expensive. Therefore, the number of projection is limited from 3 to 6 in the literature. This feature is one of the main limitations of the method, as detailed later, for it means that the reconstruction algorithm has to be able to reconstruct the 3D intensity distribution with little information available. This means that the inverse problem in our case is underdetermined.

A seeded flow is illuminated by a light source. Thanks to the increasing power of high frequency lasers, it is possible to expand the laser sheet to a volume, using adapted optics without losing too much energy for the particles to be detected. A 3D region of the flow is thus lighted and viewed by several cameras. Once two consecutive 3D intensity distributions are reconstructed from the 2D recorded images, the corresponding volumes are correlated to obtain a 3D displacement field as depicted in figure 1.3.1. To obtain discretized 3D images of the particles, the reconstructed volumes are discretized into a mesh of volumic pixels (voxels).

1.3.1.2 Calibration step

For the reconstruction step, as in Stereo-PIV, camera calibration is needed : it links the image coordinates and the physical space of the reconstruction volume. Calibration procedures are common in stereo-PIV, and the same methods are used in tomo-PIV. The usual procedure relies on the viewing of a calibration target at several positions in the volume. The calibration process returns the calibration functions of the cameras. There are two models of calibration functions : camera pinhole model or third-order polynomial functions [Soloff et al., 1997]. Furthermore, the tomographic reconstruction is based on the triangulation of particles from the projection. Therefore, there is a great need for calibration accuracy. [Wieneke, 2008] showed that projection errors should be smaller than a 1/10 of pixel. To increase the calibration accuracy, a process known as volume self-calibration was introduced [Wieneke, 2008] using the matching of 3D particles by triangulation. The residual triangulation error ('disparity') is then used to update and correct the mapping functions of all cameras.

1.3.1.3 Remarks on tomo-PIV main limitations

From its main principles, one understands that tomo-PIV is a succession of different steps : from the imaging of a volume of tracer particles, then to the tomographic reconstruction on to the cross-correlation. Each step has a direct impact on the following one, and ultimately on the displacement measured. To understand the issue regarding the accuracy of tomo-PIV, one must understand each of the step's main limitations.

We introduced tomo-PIV in the practical order of the method : from the experimental setup, to the displacement estimation. In order to better grasp one of tomo-PIV main limitations, it is interesting to invert our perception of the method. We have

shown that the spatial resolution of a cross-correlation method depends on the size of the interrogation window (in 2D), Interrogation Volume (IV) in 3D. In turbulent flows, the lengthscales have a very broad band. In an ideal world, the IV size has to be smaller or comparable to the smaller lengthscale of the turbulent flow, referred to as the Kolmogorov lengthscale $\eta = (\nu^3/\epsilon)^{1/4}$, with ν the kinematic viscosity of the fluid and ϵ the energy dissipation rate. Furthermore, there is a constraint on the number of tracers per IV for the cross-correlation to work. Therefore, for a good spatial resolution of the correlation, one needs an appropriate seeding density. However, those considerations do not take into account the intrinsic limitations due to tomography.

In their seminal paper, Elsinga et al. [2006] showed that the quality of reconstruction is highly dependent on the seeding density, more precisely on a non-dimensional number which is a projected representation of the seeding density : the number of particles per pixel (*ppp*) recorded on the camera CCD sensor. The more tracers there are, the more noise in the reconstruction appears (ghost particles). This noise is detrimental to the correlation. A trade-off between measurement noise due to low seeding densities and measurement errors due to inaccurate reconstruction must be found. A seeding range centered around 0.05 *ppp* was found to be optimal for tomo-PIV.

Most research efforts have focused on increasing the quality on the tomographic reconstruction to increase the seeding density and therefore, the spatial resolution of the measurement. Pushing the boundaries of the seeding density in the reconstruction will also help enlarge the volume of the measurement. Indeed, increasing the laser volume size leads to an increase in the number of particles in the images, therefore decreasing the quality of the reconstruction. However, when large volume are considered, experimental limitations become predominant, as the laser intensity decreases, and optical issues arise due to defocusing effects. This statement is the starting point of our dissertation (chapter 2) as we will investigate the impact of experimental factors when considering increasing the size of the volume.

The next section is devoted to the tomographic reconstruction problem and algorithms developed for the inversion problem.

1.3.2 On the tomographic reconstruction

In this section, we will investigate the inversion problem and the inversion model that is commonly used in 3D-PIV as well as different inversion algorithms. We will recall the main principles as introduced in [Elsinga et al., 2006] as well as some improvements regarding the accuracy of tomographic reconstruction.

1.3.2.1 Inversion problem

The inversion problem has to reconstruct an intensity distribution from recorded projections. The number of projections is small (from 3 to 6) and the reconstructed volume is relatively sparse. These features are the reasons why algebraic reconstruction technique [Herman and Lent, 1976] are better suited for this problem than analytical reconstruction techniques which are widely used in medical imagery. Algebraic reconstruction techniques iteratively solve a set of linear equation. The volume is discretized into a mesh of N cubic elements called voxels $E(x, y, z)$. The projections are also discretized into arrays of M pixels $I(x, y)$. A linear link (W) is assumed between the projections

and the volume which reads :

$$I(x_i, y_i) = \sum_{j=1:N} w_{i,j} E(x_j, y_j, z_j) \tag{1.3.1}$$

The size of the volume discretization was chosen so that the size of a voxel is the same as the size of a projected pixel in the volume. In these conditions, using 4 classical 2048×2048 CCD cameras, and a volume containing $2048 \times 2048 \times 200$ voxels, the W matrix dimensions are about $10^7 \times 10^9$. The inversion problem is therefore heavily underdetermined.

1.3.2.2 Classical tomographic model

The tomographic model is the model chosen to link the volume voxel to the pixel projections. The model describes the weighting coefficient $w_{i,j}$ which is the j^{th} voxel contribution to the i^{th} pixel. [Elsinga et al., 2006] used a geometrical model of varying complexity, as the light integration is performed over a cone having the optical center as apex and a square pixel trace on the focal plane. In this context, building the weighting matrix W linking the voxel and pixel spaces results in computing the volume intersecting this 'pixel cone' and a voxel. As reviewed by [Thomas et al., 2010], several techniques were suggested in the literature to simplify this geometrical model. Among them, [Elsinga et al., 2006] and later [Atkinson and Soria, 2009] proposed approximating the cubic voxel by a sphere and the 'pixel cone' by a cylinder [Lamarche and Leroy, 1990].

As a consequence, the particles will be reconstructed as 3D Gaussian blobs of voxels which are the geometrical explication of the diffracted particle image which spread on several pixels. This reconstructed blob is well suited for cross-correlation method used in PIV as mentioned previously in section 1.1.4.

Another consequence illustrated in figure 1.3.2 is the fact that W is a sparse matrix since a line of the W matrix (a pixel line of sight) only intersects a small amount of the total voxels. This is of particular importance considering the computational cost of tomographic reconstruction. The tomographic problem can be simplified to :

$$I(x_i, y_i) = \sum_{j=1:N_i} w_{i,j} E(x_j, y_j, z_j) \tag{1.3.2}$$

where N_i is the number of voxel which intersect the i^{th} pixel line-of-sight.

1.3.2.3 Inversion algorithms

Since the beginning of tomo-PIV, several reconstruction algorithms have been used and studied in the literature. We will focus here on the main algorithms classically used in tomo-PIV. Those algorithms belong to a family called "Row-Action Methods" [Barbu, 2014]. They consist in iteratively projecting the current guess or estimate of the solution onto convex subsets defining the set of feasible solutions by comparing it to the recorded projections. Here, we will present only two of the most common reconstruction algorithms for tomo-PIV, which were shown to provide the best results in the context sparse reconstruction.

MART : Multiplicative Algebraic Reconstruction Technique [Herman and Lent, 1976]. This algorithm is based on a global entropy maximization [Thomas et al., 2014].

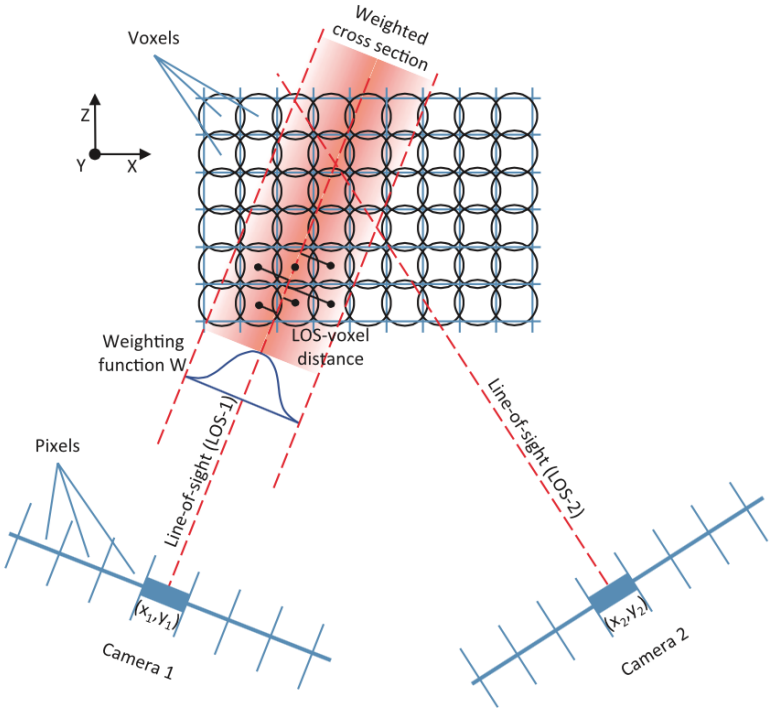

Figure 1.3.2: 2D representation of the tomographic model : a pixel line-of-sight is represented as a cone and the voxel element as a sphere. This illustration is taken from [Scarano, 2013]

For each pixel i, the intensity of every voxel along its line of sight (N_i) is updated such as :

$$E_j^{k+1} = E_j^k \left(\frac{I_i}{\sum_{N_i} w_{i,j} E_j^k} \right)^{\mu w_{i,j}} \tag{1.3.3}$$

where μ is a relaxation parameter. MART was shown to be perfectly suited for reconstruction of 3D particles distribution due to its multiplicative nature and the sparse nature of the solution [Elsinga et al., 2005] and [Elsinga et al., 2006].

SMART : Simultaneous Multiplicative Algebraic Reconstruction Technique solves linear systems under non-negative constraints [Byrne, 2008], and is a popular choice for tomographic PIV reconstruction following the work of [Atkinson and Soria, 2009].

$$E_j^{k+1} = E_j^k \left(\Pi_i \left(\frac{I_i}{\sum_{N_i} w_{i,j} E_j^k} \right)^{\mu w_{i,j}} \right)^{1/N} \tag{1.3.4}$$

1.3.2.4 On the improvement of tomographic reconstruction

When both algorithms were introduced in the tomo-PIV community, the main issue was the computational cost of such techniques, especially considering the classical dimension of a typical tomographic reconstruction problem. To address this issue, initialization techniques such as multiplicative first guess (MFG) [Worth and Nickels, 2008] and more importantly Multiplicative-line-of-sight (MLOS) [Atkinson and Soria, 2009] were introduced. They select voxels on which the iterative process will occur, and the remaining voxels have a zero intensity.

From this, many developments occurred. Some focused on the sparse nature of

the solution to improve both accuracy and computational time such as the work by [Petra and Schnörr, 2009] or [Barbu et al., 2011]. Others focused on increasing the seeding density by using the information hidden in the time coherence of the real particles, and the time incoherence of the ghost particles. Those methods are referred to as multi-exposure methods [Scarano, 2013]. [Novara et al., 2010] introduced a novel method that exploits the information taken at two (or more) different time instants. Gains in accuracy were shown to be quite significative. This method was expanded to time-resolved 3D-PIV [Lynch and Scarano, 2015].

Although such approaches have proven wide practical utility, their domain of use is restricted to favorable viewing conditions, this point being linked to the uncertain physical nature of the reconstruction itself. In difficult experimental conditions, for instance when in the presence of defocusing or in the presence of compressible flows, it is known that the shape of the PSF, *ie* of the particle images, can vary dramatically, leading to accuracy losses in the estimation, since geometry cannot account for these perturbations. In order to overcome these difficulties, [Schanz et al., 2013a] recently proposed accommodating for variations of the PSF through the definition of an adapted weight matrix. In their approach, this matrix is built from a dedicated processing of PSF samples which is specifically designed to yield reconstructed volumes made of particle blobs suited to 3D cross-correlation. Their study indeed showed increased reconstruction quality and more accurate displacement estimations, in particular in the case of astigmatism and defocus.

More recently, a trend known as "return to the particle" appeared which aims at combining the iterative reconstruction process used in tomo-PIV and 3D-PTV. The reconstructed particle is not seen as a 3D blob but as a set of 3D coordinates in space combined with an unknonwn intensity. [Wieneke, 2013] introduced an iterative algorithm (Iterative Particle Reconstruction, IPR) which reconstructs 3D particles coordinates for a density higher than classical 3D-PTV. It consists in generating particle hypothesis using PTV techniques, then in removing their predicted image from the acquired image. From these cleaned images, one can expect to extract more reliable predictions of particle locations. In the context of time-resolved 3D-PIV, where particles can be tracked on multiple frames, [Schanz et al., 2013b] used the previous IPR algorithm [Wieneke, 2013] and tracked particles in 3D space over multiple frames providing a clear elimination criteria for the ghost particles from reconstructions. Application on experimental data showed a great potential for measuring turbulent flows [Schröder et al., 2015].

It is in this highly changing and evolving context that the following dissertation takes place.

1.4 Objective and outline of the thesis

The improvement of tomographic reconstruction quality is a strong research topic nowadays for tomographic reconstruction is the main barrier regarding the accuracy of tomo-PIV. As mentioned in the previous section, many efforts focused on the inversion process and algorithm, either trying other types of algorithms or using multi-exposure methods. However, to the best of our knowledge, the study of the tomographic model did not receive much attention especially since the reconstructed 3D intensity distribution is not a real physical quantity. Is it possible to find a more physical inversion model ?

Could a projection model based on a more physical understanding of the PIV image generation process lead to increased performances ?

At ONERA, as mentioned previously, an effective and fast cross-correlation algorithm was developed [Champagnat et al., 2011] for 2D-PIV (FOLKI-PIV) and Stereo-PIV (FOLKI-SPIV). Its robustness towards PIV image noises was tested. It seems natural to expand it to 3D for a tomo-PIV use. How will this algorithm behave in a 3D-PIV context with specific tomographic noise which deteriorates the displacement estimation step (Elsinga et al. [2011]) ?

To answer both questions, chapter 2 starts by investigating imaging conditions for tomo-PIV, especially focusing on difficult experimental conditions such as time-resolved tomo-PIV in the air evolving towards large volumes. A better understanding of imaging conditions in tomo-PIV has led us to rethink the classical geometrical tomographic model. In chapter 3, we introduce a new reconstruction approach using a particle-based representation of image referred to as Particle Volume Reconstruction (PVR). Numerical simulations show significant gains over classical reconstruction technique. In chapter 4, we assess the performance of our 3D-cross correlation algorithm (FOLKI-3D) towards tomographic noise through numerical simulations. An experimental application of a tomo-PIV measurement combining the reconstruction approach PVR and our cross-correlation algorithm FOLKI-3D is now possible. This experimental validation is done on a turbulent air jet setup. This includes a tomo-PIV setup of 4 cameras as well as 2D-PIV setup synchronized with the tomo-PIV setup working as a reference measurement. The experimental setup and the jet are described in chapter 5. Finally, experimental results of both tomographic reconstructions and velocity fields are investigated in chapter 6. An accuracy assessment of PVR methods for tomo-PIV is done using a comparison with classical tomographic reconstruction algorithms and 2D-PIV measurements.

2 Experimental factors and tomographic PIV

2.1 Introduction

In its most common form, the three-dimensional measurement of flow velocity by PIV relies on a two-step process, in which one first seeks to reconstruct a volumic intensity distribution from several camera images at two time instants, and then correlates the corresponding volumic distributions [Elsinga et al., 2006]. The first step, i.e. tomographic reconstruction, is entirely new compared to traditional plane PIV, and is known to have a strong impact on the final measurement quality. Its optimization is crucial to ensure the accuracy of the vector fields, and has received much attention since the introduction of the technique. In past studies, the influence of various experimental factors have been studied, in order to assess their effect, both on the reconstruction quality in itself, and on the displacements. The number and position of the cameras, their calibration, the particle image diameter in the images and the seeding density have been recognized as the most influential ones [Elsinga et al., 2006] & [Scarano, 2013], and corresponding ranges of operation which guarantee a good measurement quality have been derived.

While they have managed to provide useful guidelines and directions for designing more efficient reconstruction strategies, some of these studies have limitations, in the sense that they have partly oversimplified some experimental problems. This has recently led [De Silva et al., 2012] to propose a refined view, by considering 3D instead of 2D synthetic experiments, and introducing a simplified model for Mie scattering, among others. The present contribution proceeds from the same motivation, and aims at providing further landmarks and optimization guidelines for the experimentalists, by taking a step forward in the physical model complexity. As an expected by-product, our characterizations should also provide foundations for further refinement of the reconstruction algorithms, if possible. The influential parameters investigated in this chapter are mostly of geometrical nature, in a direct or indirect way. We consider ranges of variations for these parameters which roughly match the case of high repetition rate measurements in air flows, raising specific constraints and challenges. We conduct synthetic reconstruction tests using MLOS-SMART [Atkinson and Soria, 2009], which we assess with the usual quality criterion initially proposed by [Elsinga et al., 2006], and also introduce new performance measures adapted to detection problems. Here, we focus on the reconstruction only.

Four parameters are varied. The first parameter is seeding density, whose impact we will simply mention in order to provide a comparison with the following ones. Then, we will show that when choosing the angular positions of the cameras relative

to the illuminated volume, a new parameter should be considered, which is the ratio between the intersection and the union volumes of the cameras' fields of view. As briefly mentioned in [Elsinga et al., 2006], the fact that some particles are not seen by all cameras acts as a source of noise and degrades the reconstruction. We show that this ratio is the adapted control parameter to quantify this phenomenon. We thirdly investigate the impact of out-of-focus particles in the images. Here as well, we build a tuning parameter to control the degree of defocusing. Such a test is important in practice, as depth of field limitations are frequently encountered in tomo-PIV. In particular, these tests will allow to quantify the amount of degradation obtained if one tries to extend the size of the illuminated volume beyond the cameras depth of field, but when this defocusing is not taken into account. In other words, this may help define a boundary beyond which it is necessary to model it, such as in the approach of [Schanz et al., 2013a], or in [Cornic et al., 2013] & [Champagnat et al., 2014]. Finally, we will consider images synthesized using the full Mie theory, and compare the reconstruction results with reconstructions from images built with different approximations classically found in the literature. We will quantify the resulting differences in reconstruction quality. This will help us determine the degree of realism of these approximations depending on the setup geometry and nature of the seeding.

This chapter is outlined as follows: section 2.2 describes the principles of the synthetic tests, in terms of image generation and of choice in quality criteria. The results of the parametric studies are then exposed in section 2.3. Finally, concluding remarks are given in section 2.4.

2.2 Principle of the tests

In this section, we explain and describe the principles of the synthetic tests that we performed to assess the impact of several factors on the reconstruction quality. We will focus on the description of our image generating process, the reconstruction algorithm used as well as the measurement quality criteria that we will consider.

2.2.1 Image generation

We here describe the setup and parameters defining the synthetic test cases that will be used throughout the chapter.

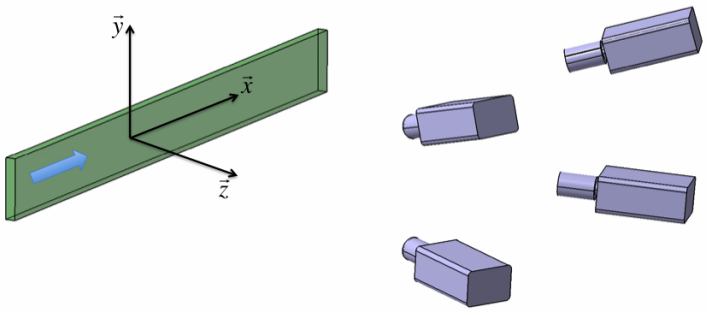

Figure 2.2.1: Typical camera and laser setup for synthetic experiment: the setup is made of 4 cameras, a laser sheet whose light direction is along the $\vec{x}$ axis.

2.2.1.1 Optical Setup

All our simulations involve four cameras, which are positioned on a single side of the laser sheet at the vertices $\left(\pm 1/2, \pm 1/2, \pm 1/\sqrt{2}\right)$ of a square of 1 m side. They are positioned at a distance of 1 m from the center of the reconstructed volume, the latter defining the origin $(0, 0, 0)$ and point at it. A pinhole model is assumed for the cameras, without Scheimpflug adapter for simplicity, and calibration is supposed to be perfectly known and to obey a pinhole model. The focal length is 100 mm, thus the magnification factor M is equal to 0.1, and the pixel size is 10 μm with a fill factor of 100%. The images' size, and hence the field of view, depends on the test cases and will be specified for each simulation.

The laser sheet is modeled as a 20 mm thick parallelepiped. Its intensity profile is assumed to be Gaussian in the z direction with a standard deviation σ_L. However, in this study the dependence in z will be very weak as we will consider the laser sheet as an almost perfect top hat with $\sigma = 0.05$ m. The direction of the light is taken as the $\vec{x} = (1, 0, 0)$ axis. Its wavelength is $\lambda = 532$ nm. In all the tests below, we will consider the horizontal and vertical extensions of the laser sheet to be infinite.

The reconstructed volume, also 20 mm thick, is always the smallest parallelepiped including the illuminated volume seen by all the cameras. Thus it depends on the field of view and is given for each experiment. The voxel-to-pixel ratio is set to one.

2.2.1.2 Tracer particles

Tracer particles are uniformly distributed in the light sheet volume. The density is controlled by the particle per voxel count (ppv). This volumic density dictates the image density also referred to as the number of particles per pixels in the tomo-PIV literature [Elsinga et al., 2006]. We will call this parameter as 'ppp' for the remaining of the thesis. Horizontal and vertical extensions of the laser sheet are larger than the field of view covered by all the cameras. Thus, all illuminated particles cannot be seen by all cameras, a fact that always occurs in real dataset but is nonetheless often overlooked in synthetic experiments.

The particles are assumed to be spheres with diameters small enough (a few microns, i.e. we focus on experiments in air flows) to neglect the size of their geometric image $M.d_p$. Given the size of particles typically used in a real experiment, emitted intensity is governed by Mie scattering which applies to a sphere of diameter $d_p \approx \lambda$.

Unless otherwise specified, we will consider a traditional approximation which considers the scattered light as proportional to the square of the particle physical diameter d_p and determines the intensity of a particle by its diameter and its depth only via:

$$E \propto d_p^2 e^{-\frac{z^2}{2{\sigma_L}^2}} \tag{2.2.1}$$

Here, the particles physical diameters are randomly drawn in the $\left[min_{d_p}\ ,\ max_{d_p}\right]$ segment, according to a Gaussian distribution law with mean m_{d_p} and standard deviation σ_{d_p}, with $min_{d_p} = 0.5\ \mu m$, $max_{d_p} = 2.5\ \mu m$ and $m_{d_p} = 1.5\ \mu m$. The distribution is controlled by σ_{d_p} , $\sigma_{d_p} = 0.15\ \mu m$ yielding medium-low diameter scattering and $\sigma_{d_p} = 0.5\ \mu m$ high scattering.

As [De Silva et al., 2012] already noted, and as we will further confirm it in this chapter, accounting more finely for Mie scattering may lead to significant changes in algorithms performance. In another series of synthetic experiments, we will thus introduce a complete model for this scattering in the generated images, contrary to [De Silva et al., 2012] who rely on an approximation. Assuming the light to be non-polarized, [Bohren and Huffman, 1983] show that the scattered intensity of a sphere particle is proportional to a scattering function $\mathcal{S}_{11}(d_p, \theta)$ which depends on d_p and θ, the scattering angle being defined as the angle between the light source direction and the detector direction in the scattering plane of the particle. Figure 2.2.2 shows a typical scattering function for a particle of 2 μm in diameter. The refractive index of the particles in the air is taken as $n = 1.47$. An algorithm developed by [Bohren and Huffman, 1983] was used to compute the scattering function based on d_p, λ and n. Within this exact model, the particles' diameter are still randomly drawn in $\left[min_{d_p}\ ,\ max_{d_p}\right]$ according to a Gaussian distribution law with mean m_{d_p} and standard deviation σ_{d_p}, this time with physical, dimensional values of d_p. In particular, one considers $min_{d_p} = 0.2\ \mu m$ and $max_{d_p} = 2\ \mu m$.

In our camera setup, described in section 2.2.1.1, 2 cameras are in a forward scatter configuration (with a 60° scattering angle) and 2 cameras are placed in a backward scatter configuration (with a 120° scattering angle).

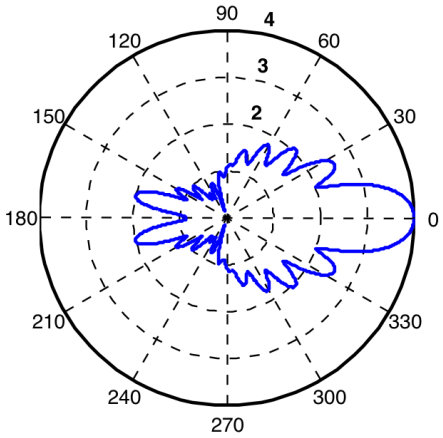

Figure 2.2.2: Logarithmic representation of the scattering function ($log_{10}[\mathcal{S}_{11}(d_p, \theta)]$), as a function of the scattering angle (shown here in degrees). The function was computed for a 2 μm diameter particle with a refractive index $n = 1.47$.

2.2.1.3 Final image intensities

Considering P particles with intensity E_p located at point $\mathbf{X_p}$ in 3D-space, the intensity distribution in the image is given by :

$$I(\mathbf{x}) = \sum_{p=1}^{P} E_p.h(\mathbf{x} - F(\mathbf{X}_p)) \tag{2.2.2}$$

where $\mathbf{x} = (x, y)$ denotes any location in the image plane, F is the geometric projection function in the image, and h the so-called Point Spread Function (PSF) which models the aperture limited diffraction and pixel integration.

For the tests presented in this chapter, we assume an integrated Gaussian PSF function. Apart from section 2.3.3 where we account for defocusing effects in the reconstruction, the standard deviation σ_{PSF} is set to 0.6 pixels, averaged on the pixel surface, with a 100% fill factor so that h is :

$$h(x,y) = \frac{1}{4}\,[erf(\,\frac{x+1/2}{\sqrt{2}\sigma_{PSF}}\,) - erf(\,\frac{x-1/2}{\sqrt{2}\sigma_{PSF}}\,)] \times [erf(\,\frac{y+1/2}{\sqrt{2}\sigma_{PSF}}\,) - erf(\,\frac{y-1/2}{\sqrt{2}\sigma_{PSF}}\,)] \tag{2.2.3}$$

Unless otherwise specified, we assume an image dynamic range of 8 bit, and a Gaussian noise with $\mu_{Noise} = 5$ and standard deviation $\sigma_{Noise} = 2$ is added to the images. Its amplitude is set at about 10% relative to the maximum particle intensity.

2.2.2 Reconstruction and Quality measurement

2.2.2.1 Reconstruction algorithm

To reconstruct the volume, we build a first guess using an MLOS step, and then refine the reconstruction using a SMART algorithm [Atkinson and Soria, 2009] that we implemented in a GPU frame. In the rest of the thesis, this algorithm (MLOS followed by SMART iterations using a reconstruction model as described in [Atkinson and Soria, 2009]) will be referred to as tomo-SMART. In the context of our study, it is useful to recall some fundamentals of this algorithm, and what can be expected in some of the situations we consider. However, for more details on the algorithm, the reader is advised

to go to chapter 3.

SMART iteratively inverts the linear system :

$$I = W.E \tag{2.2.4}$$

which links the image and volume intensities, I and E, through the sensing matrix W. Each iteration combines a projection from the volume, and then a back-projection from the images. Matrix W is here built in the exact same way as initially proposed by [Elsinga et al., 2006] and [Atkinson and Soria, 2009], as widely done in the literature. It is now well-known that since this system is highly underdetermined, reconstruction is affected by the presence of ghost particles which act as a source of noise during the subsequent velocity estimation by cross-correlation. Aside from this lack of unicity, another, more fundamental issue is the existence problem, i.e. how ill-posed the problem is. Indeed, any linear system such as equation (2.2.4) is at least mildly ill-posed, as approximations cannot be avoided; however, the approximation can be more or less relevant depending on the situations. In the present formalism, W is built on the basis of geometrical considerations, and does not include any angular variation due to Mie scattering, for instance. Thus, in the hypothesis of significant scattering differences, the projection step of SMART will consist in projecting a single voxel intensity with the same weight on all images, whereas the actual images will have different intensities. In such a situation, the problem will be all the more ill-posed than when scattering differences are negligible. In this chapter, we used 20 SMART iterations, with a relaxation parameter of 1.1.

An additional comment must be made regarding thresholds when confronted to noisy images. As explained in section 2.2.1.3, unless otherwise specified, we used a Gaussian noise with $\mu_{Noise} = 5$ and standard deviation $\sigma_{Noise} = 2$ on the images. For the MLOS step, the images were thresholded : only the pixels of intensity greater than 8 were kept. The images are thresholded at 93 % with regards to the noise distribution. When we did not use any noise in the images, the images are not thresholded.

2.2.2.2 Reconstruction quality measurement

The quality of the reconstruction is assessed by several means, the first being the well-known $\mathcal{Q}$ criterion [Elsinga et al., 2006]:

$$\mathcal{Q} = \frac{\sum_{x,y,z} E_0(x,y,z).E_1(x,y,z)}{\sqrt{\sum_{x,y,z} E_0^2(x,y,z).E_1^2(x,y,z)}} \tag{2.2.5}$$

where $E_1(x,y,z)$ is the reconstructed intensity field and $E_0(x,y,z)$ is an ideal reconstruction intensity field (considered as the ground truth), in which a particle is seen as a 3D isotropic volume of Gaussian intensity whose standard deviation is the same as the standard deviation of the PSF in the images [Elsinga et al., 2006] & [Scarano, 2013]. This quality factor $\mathcal{Q}$ is very well suited for classical tomographic reconstruction analysis where a particle is seen with the same intensity in every camera, i.e. when the scattered light is considered to depend only on the particle diameter and depth. However, taking Mie scattering into account means that the intensity of a particle differs from one camera to the other. In that case, the question of building a volumic ground truth becomes less obvious, as one cannot associate a single intensity value to a given particle. Computing a $\mathcal{Q}$ criterion then necessitates a choice for this intensity (e.g., for each particle, the highest intensity among all images), which diminishes its meaning as

an objective quality criterion. In our study of Mie scattering, we will restrict our use of this quantity to the most relevant cases, and indicate precisely how we approximate the ground truth. The same remark can be made when considering defocusing effects when the image diameter of a particle depends on a geometrical variable for every camera (see section 2.3.3).

Another performance diagnosis is thus required, which should bring another perspective on the quality of the reconstruction and be compatible with all the experimental nuisance factors we consider here. We propose to introduce a metric suited to measure the detection performance of the reconstruction. Detection performance measurements are well known features in pattern recognition and information retrieval. This method is based on the classification of a "detection". A "detection" is defined here as a local maximum voxel, whose intensity is greater than a threshold level set to 8 in order to eliminate local maxima created by noise.

A detection is declared a True Positive (TP) if it is in the neighborhood of a true particle. Unless otherwise specified, the neighborhood is here a $3 \times 3 \times 3$ voxels cube centered on the voxel of the true particle. A detection is a False Positive (FP), ie. a ghost, if it is not in the neighborhood of a true particle. A particle is recorded as False Negative (FN) if there is no detection in its neighborhood. Precision quantifies the fraction of true particles among all detected particles, and Recall is defined as the number of true positive divided by the total number of true particles, ie:

$$\text{Precision} = \frac{\#TP}{\#TP + \#FP} \quad , \quad \text{Recall} = \frac{\#TP}{\#TP + \#FN} \tag{2.2.6}$$

where # stands for “number of”. The best achievable performance is given by Recall = 1 (# FN=0, every particle is detected) and Precision=1 (# FP=0, all the detected particles are true). Note that whatever the quality criterion considered, and in all the simulations below, the ground truth will consist of the particles that are seen by all the cameras exclusively, which is consistent with the fact that all reconstructions are initialized with MLOS.

2.3 Experimental factors

2.3.1 Seeding density

The effects of image seeding density (ppp) on the quality of the reconstruction has been widely explored in the literature, as the concentration of participle tracers is directly linked to the spatial resolution of the Tomographic PIV technique. [Elsinga et al., 2006] showed that an increased particle density produces a larger amount of ghost particles, consequently decreasing the reconstruction quality and so the velocity measurement. Ultimately, a compromise must be reached between high spatial resolution and the accuracy of the technique.

As this dependence is a well-known landmark to tomo-PIV users, we will here simply mention its amplitude, as a reference enabling us to assess the relative impact of the other experimental parameters which we will consider in the following. Figure 2.3.2 shows the decrease in quality of the tomo-SMART reconstruction with respect to the seeding density ppp. When the density increases, as the ambiguities in the images increase, the number of ghost particles increases, an energy transfer arises between real particles and ghost particles, which decreases the intensity of the real particles, altering their shape and sometimes delocalizing their center ultimately decreasing the signal-to-noise ratio in the reconstruction.

2.3.2 Geometric considerations on the reconstructed volume

2.3.2.1 Intersection and Union volumes

In this paragraph, we focus on geometry-related considerations. In one of the conclusions of their study, [Elsinga et al., 2006] recommended that the reconstructed volume should include all illuminated particles, since particles which lie outside this volume but are still visible by the cameras act as an important source of noise. Those were referred to as "added background particles" in [Elsinga et al., 2006], arguing that this situation occurs due to either the laser sheet Gaussian profile or uncontrolled light reflections.

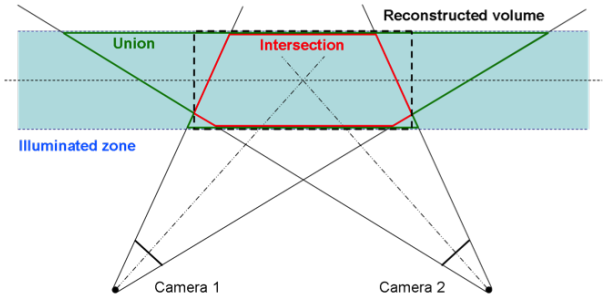

Figure 2.3.1: Typical setup with two cameras for simplicity, showing the difference between reconstructed volume (dashed black rectangle), union (green) and intersection (red) of the camera field of views and illuminated area.

However, it turns out that this situation inevitably occurs, partially due to the reconstruction algorithms used. Indeed, common algorithms such as MART or SMART are multiplicative in nature, so that they only reconstruct particles seen by all cameras and automatically eliminate the others. Geometrically, actually reconstructed particles lie in the Intersection volume between the cameras' fields of view and the laser sheet, as depicted in figure 2.3.1. As seen in this figure, the image recorded by each camera

also includes particles which are not seen by the remaining cameras. These "added" particles lie in the Union between the cameras' fields of view and the laser volume, but do not lie in the Intersection volume.

Figure 2.3.2 shows the influence of the seeding density *ppp* on two tests : in one case, the particles were randomly spread in the Union volume, in the second case, the particles lie in the Intersection only. The cameras sensor size was set to 800×800. In order only to assess the specific noise, introduced by particles lying in union volume and not in the intersection, we did not introduce any additional noise in the images contrary to section 2.2.1.3. We used the $\mathcal{Q}$ factor [Elsinga et al., 2006] to assess the reconstruction quality. We can observe the quality difference between the two cases which increases along with the particle density. Because it is not possible in practice to overcome this situation due to the extension of the laser volume, this source of noise should be quantified.

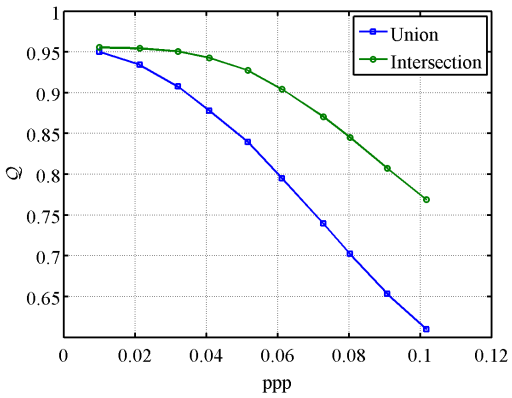

Figure 2.3.2: Influence of the seeding density ppp for the two synthetic cases, using 800×800 sensor size.

2.3.2.2 Ratio between Intersection and Union volumes of the camera's fields of view

We designed a synthetic test which accounts for the above mentioned phenomenon. A natural choice for the associated control parameter is then the ratio between Intersection and Union volumes equation (2.3.1). $R_{I/U}$ is varied without changing other experimental parameters by varying the sensor sizes (ie varying the number of pixels while keeping the size of each pixel constant), and thereby the solid angles of the cameras' fields of view. In practice, this ratio will more probably vary with the cameras' angular positions. We used the same synthetic setup as in section 2.2.1.1, only using camera pixel sizes ranging from 128×128 to 1400×1400. The seeding density was set to $ppp \approx 0.05$.

$$R_{I/U} = \frac{\text{Vol(Intersection)}}{\text{Vol(Union)}} \tag{2.3.1}$$

The reconstructed volume is systematically chosen as the smallest parallelepiped containing the Intersection volume. Figure 2.3.3 right shows that this parameter is indeed of utmost importance, as both $R_{I/U}$ and $\mathcal{Q}$ follow the same evolution with image size, with a decrease in quality with decreasing $R_{I/U}$. Besides, the amplitude of this decrease within the present range of variation is comparable to the typical variation due to ppp (figure 2.3.2). These "added" particles, lying in the Union but not in the Intersection,

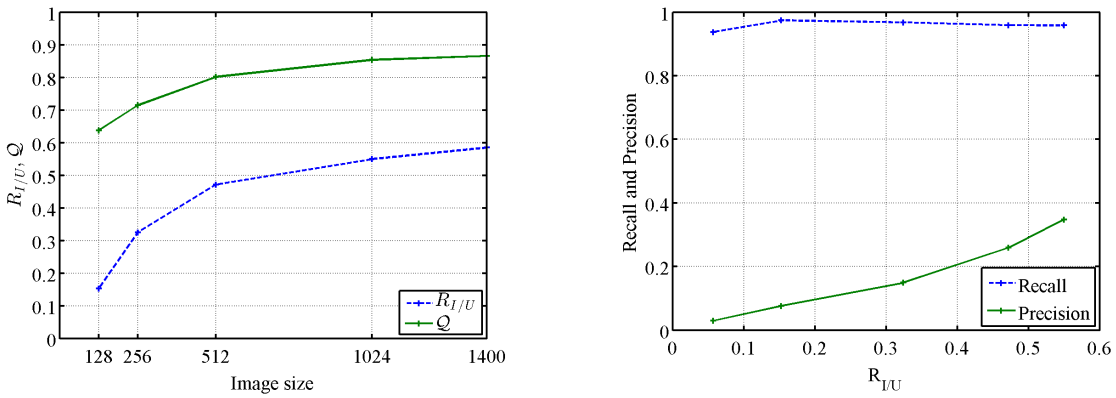

Figure 2.3.3: Influence of the image size on the $R_{I/U}$ ratio and on the reconstruction quality (left) and influence of the $R_{I/U}$ ratio on the Precision and Recall performance measures (right).

act as a strong source of noise in the reconstruction: indeed, the inversion algorithm will try to explain the particle detected in the image as a particle in the Intersection volume, where it is not. This will lead to an increase in the number of ghost particles. This phenomenon is clearly seen in figure 2.3.3 (right) where it is shown that the Precision increases with the $R_{I/U}$ ratio.

2.3.2.3 Optimizing the $R_{I/U}$ factor

In the two previous sections we introduced and characterized the specific noise created by particles lying in the Union volume but not in the Intersection. This phenomenon cannot be avoided in a real life experiment, but can anything be done to improve $R_{I/U}$ within a given experiment ? What experimental parameters can be used to optimize ?

In this paragraph we will try to understand the issue at stake and give guidelines to optimize the $R_{I/U}$ factor. The $R_{I/U}$ is directly linked to the camera setup used and the choice of the camera setup depends on several parameters :

1. Optical access in the wind tunnel.

2. Distance between the camera and the measurement volume : the choice of this parameter along with the choice of the optical lens of the cameras will determine the magnification of the imaging system which is directly linked to the spatial resolution of the measurement. This will also determine the angular field of view of the cameras. Furthermore, this will determine the optical depth of focus which is a crucial parameter since the particles in the illuminated region must be in focus [Scarano, 2013] for a good reconstruction. This is further investigated in section 2.3.3.

3. The system angular aperture [Scarano, 2013] [Thomas et al., 2014] is a well-known parameter whose choice is critical to the quality of the reconstruction. This stems from the fact that the projections of the volume on the images must be as little collinear as possible to one-another to invert the linear system equation (2.2.4).

4. The Scheimpflug adapter : to ensure that the whole of the volume is in focus, Scheimpflug adapters are mounted on the cameras. Usually the Scheimpflug adapters are mounted so that the $z = 0$ plane is in focus (in the middle of the

laser illumination volume). If the Scheimpflug adapter is a "simple Scheimpflug adapter", i.e. there is only one angle to adjust, realizing the Scheimpflug condition will set the camera rolling angle (the angle of the camera around its optical axis). In that case there is no more parameter to adjust, the cameras are set and so is the $R_{I/U}$ factor. If the Scheimpflug adapter has two angles to adjust, then it is possible to adjust the rolling angle to optimize $R_{I/U}$.

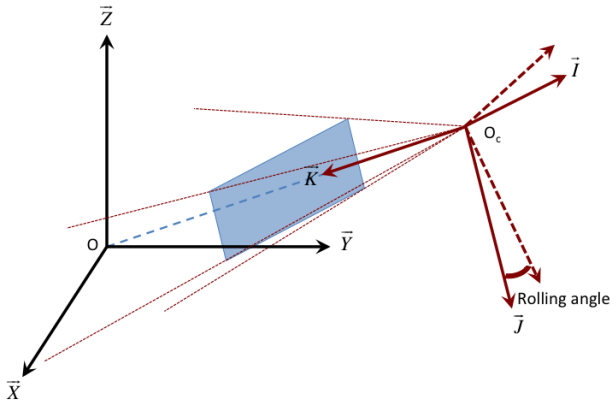

Figure 2.3.4: Coordinate reference system of the camera in a pinhole model, visualization of the rolling angle of the camera. $(O, \vec{X}, \vec{Y}, \vec{Z})$ is the world coordinate system and $(O_c, \vec{I}, \vec{J}, \vec{K})$ is the camera coordinate system.

The rolling angle is defined as the angle of camera around its optical axis as illustrated in figure 2.3.4. The coordinate system of the camera was defined as following : $\vec{K}$ is the direction vector of the optical axis of the camera pointing at the world origin. We defined the $\vec{I}$ vector as being orthogonal to $\vec{K}$ in the $(O, \vec{K}, \vec{X})$ plane and $\vec{J}$ as being the cross-product of $\vec{K}$ and $\vec{I}$. The rolling angle is the angle controlling the rotation of camera system around its $\vec{K}$ axis.

In the case of a two angles Scheimpflug adapter, it is possible to tune the rolling angle of the camera in order to optimize the $R_{I/U}$ factor, assuming the intersection volume is always big enough to contain the desired measurement volume. To illustrate this idea, using our experimental setup section 2.2.1.1, with 2048×2048 sensor size, we performed an optimization of the 4 rolling angles called $\mathbf{Roll} = (roll_1, roll_2, roll_3, roll_4)$ of the 4 cameras, using a non linear least-square optimization process of the cost functional $f(\mathbf{Roll}) = \| \ 1 - R_{I/U}(\mathbf{Roll}) \ \|^2$. The idea is to find the 4 rolling angles that optimize the $R_{I/U}$ in a non linear least-square paradigm. The algorithm used to minimize the cost functional was the Levenberg-Marquardt algorithm. The initialization we used was $\mathbf{Roll}_0 = (0°, 0°, 0°, 0°)$. The iterative optimization process was stopped when the relative square of the cost functional was changed by less than 10^{-6}. The optimal solution found is $\mathbf{Roll}_1 = (9.50°, -9.54°, -9.54°, 9.58°)$. The $R_{I/U}$ factor was increased from 0.51 to 0.53. Figure 2.3.5 shows the Union volumes and Intersection volumes of the initialization case and the optimal case.

The gain in $R_{I/U}$ is small. In order to check if it also leads to small gains in performance, we performed two 3D reconstruction synthetic tests using the two camera

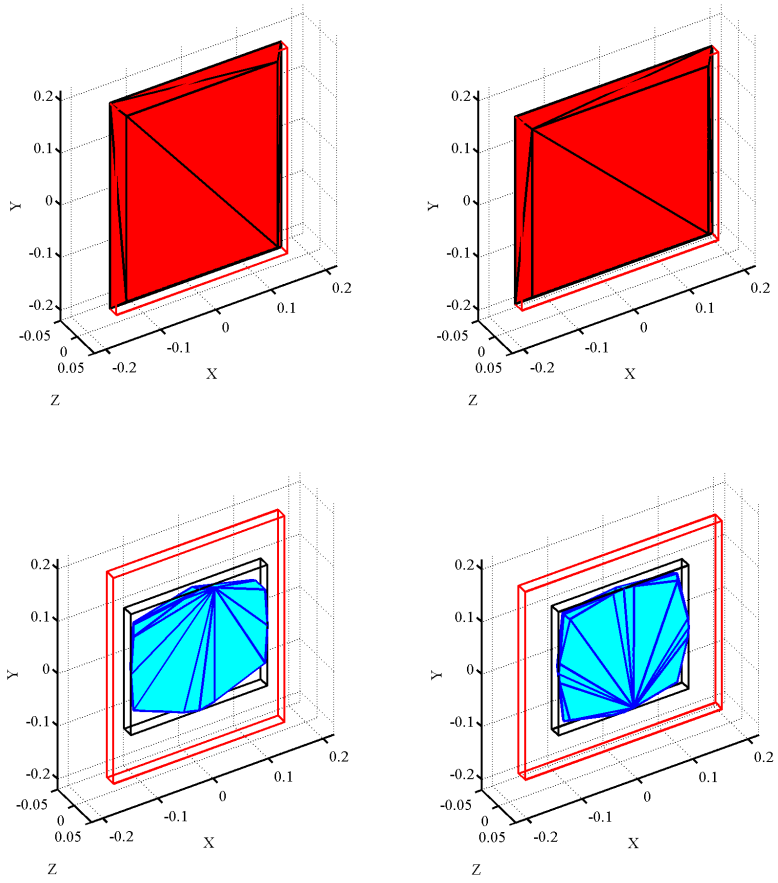

Figure 2.3.5: 3D visualization of the Union in red (up) and Intersection volumes in cyan (down) for the **Initialization case** (left) and for the **Optimized case** (right). The red cuboid are smallest cuboid containing the Union volume. The black cuboid is the smallest cuboid containing the Intersection volume.

calibrations obtained from the above optimizing process. The four cameras have 2048 × 2048 pixels, we did not use any camera noise, the volumic tracer density was set so that in both cases the image seeding density is close to $ppp \approx 0.05$. The tracer particles were randomly spread in the Union volume in both cases. The results are summed up in table 2.3.1. We used the above mentioned quality measurements section 2.2.2.2 as well as the normalized intensity variance σ_E^* which is used in [Lynch and Scarano, 2014] as an alternative reconstruction quality measurement.

	Initialization case	**Optimized case**
$\mathcal{Q}$	0.8742	0.8762
Precision	0.435	0.440
Recall	0.998	0.998
σ_E^*	12.90	12.96

Table 2.3.1: Performance measurements of the reconstruction: one case without $R_{I/U}$ optimization process, (**Initialization case**), the other obtained after $R_{I/U}$ optimization (**Optimized case**).

The different performance indexes shown in table 2.3.1 agree on the fact that the gains resulting from optimization of camera orientation are negligible. Thus within a classic tomo-PIV setup which favors isotropic resolution reconstruction within the depth of field, there is little room to optimize $R_{I/U}$.

2.3.3 Defocusing effects

When considering larger volumes than currently obtained when restricting the camera depth of fields, a defocusing of particle images will be observed. Some aspects of this issue have already been tackled in a recent study by [Schanz et al., 2013a]; in particular, these authors have considered one instance of defocusing and varying seeding densities. [Cornic et al., 2013] & [Champagnat et al., 2014] (see chapter 3) also proposes a complete "particle" approach, where this varying Point Spread Function can be accounted for. As a first quantifying step, we propose a systematic point of view in which the degree of defocusing is varied. This is equivalent to the progressive increase in the laser volume thickness (z direction in figure 2.2.1).

In order to account for the limited depth of field, each camera is given a defocusing function $\sigma_{PSF}(\tilde{z})$ where $\tilde{z}$ is the space variable along the camera's optical axis. We did not simulate a Scheimpflug adapter on the cameras. The defocusing function was inspired from [Olsen and Adrian, 2000]. The level of defocusing is determined by the camera aperture diameter, the laser sheet thickness remaining constant. The only parameter that we changed is the size of the PSF. A corresponding control parameter was built as the difference between the standard deviation σ_{PSF} of the particle with the largest image diameter among all cameras and that of in-focus particles, i.e. $\delta_\sigma = \sigma_{max} - \sigma_{focus}$. The defocusing function was adapted so as to have the same in-focus image diameter for all cameras. For all cameras, we have $\sigma_{PSF}(\tilde{z} = 0) = \sigma_{focus} = 0.6$ [pixels]. An important remark is that the intensity (E_p in equation (2.2.2)) given to each particle was kept constant in all the defocusing tests. This means that as the σ_{PSF} increases, the image peak intensity of the particles decreases due to the integration in the PSF function. Moreover, since each camera has its own defocusing function, the photometric consistency between the cameras is lost, namely a particle does not have the same peak image intensity and shape in every camera. Simulations are run for two seeding densities, at $ppp = 0.055$ and at $ppp = 0.098$.

In his study, [Scarano, 2013] showed that the quality of the reconstruction depends on the image diameter and consequently on the image source density. The $\mathcal{Q}$ factor was used to show the quality dependence on the image diameter, with an optimal image diameter found for $d_\tau^* = 1.5$ [pixels] for a given seeding density. In this study, only the particles diameter changes, the image intensity remaining the same. This means that for small image diameter, the quality decrease comes from discretization errors and for big particle image diameters, the quality decrease comes from overlapping particles, the images becoming more and more full, the reconstruction process becomes more difficult for the algorithm. This has the same effect as an increase of seeding density : the number of ghosts particles increases, the real particles lose their shape and intensity to the ghosts particles.

In our simulations, we expect to witness a decrease in the reconstruction quality. However a question remains : does this quality drop come from an increase in the number of ghost particles, or does this come from a decrease in the number of real reconstructed particles ?

Since every camera has its own defocusing function, it is irrelevant to construct a $\mathcal{Q}$ quality factor since the particle ground truth is not the same for each camera. We will use the detection performance measurements. Results are shown in figure 2.3.6 for

a simple MLOS reconstruction and a tomo-SMART reconstruction. Both results exhibit the same behavior, namely that the Precision quantity does not seem to be impacted by the defocusing parameter, but the Recall quantity decreases with δ_σ. The drop is even more significative for tomo-SMART than for MLOS. At a given δ_σ, the drop increases in magnitude with the seeding density. The main effects of defocusing seems to be the loss of real particles in the reconstruction.

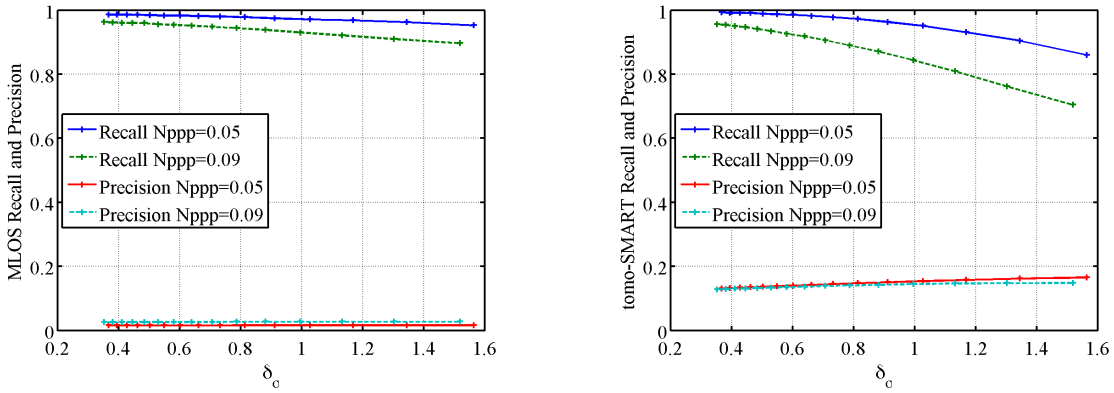

Figure 2.3.6: Recall and Precision obtained at varying intensity of defocusing in the images, for $ppp = 0.055$ and $ppp = 0.098$, 512×512 images. MLOS (left), tomo-SMART (right).

This can be partially explained by thresholds applied to the image during the MLOS step. Increasing the defocusing parameter leads to a decrease in the particle image intensity, as explained above. The threshold value applied on the images before the MLOS step was kept constant (equal to 8). Particles whose image intensities are lower than the threshold value, in at least one of the cameras, are eliminated from the reconstruction. This trend increases with the SMART iterations. The number of ghost particles remains constant compared to the number of real particles which drastically decreases.

Therefore, the main effect of defocusing in the images is the loss of particles in the reconstruction, due to low image intensity levels of the defocused particles. Furthermore, in our simulation, only the shape (h in equation (2.2.2)) of the particle in the image was a function of a space variable ($\tilde{z}$), the full model [Olsen and Adrian, 2000] states that the peak intensity (E_p in equation (2.2.2)) is also a function of a state variable ($E_p \approx 1/\tilde{z}^2$). This means that the intensity loss is worsened when compared to our simulation. This will lead to lower signal-to-noise ratio in the reconstruction volumes. Contrary to the precedent conclusion referring to $R_{I/U}$, this stems mainly from a decrease in the number of true particles detected, the number of ghost remaining comparable.

2.3.4 Polydisperse seeding and Mie scattering

2.3.4.1 General remarks

In this section, we analyze the influence of both the effects of Mie scattering and the dispersion in particle physical diameter d_p, which is common in practical seeding. Both factors are indeed closely related to one another: taking Mie scattering into account means that the intensity of a particle image depends on two parameters: θ the scattering angle, and d_p the particle diameter (the refractive index n and laser wavelength λ are

constant throughout the whole section). Figure 2.3.7 (left) shows the scattering function $\mathcal{S}_{11}$, as a function of both variables, while figure 2.3.7 (right) focuses on the dependence on the particle diameter at chosen scattering angles. Both plots show $log_{10}(\mathcal{S}_{11})$.

The scattering function has a complex behavior with respect to both d_p and θ, which raises several issues that will be addressed now. To do so, we will investigate the effects of each scattering function variable separately. First, we will consider the effects due to angular variations in space (θ) while having a fixed monodisperse seeding; then we will investigate the effects due to polydisperse seeding. In the remaining chapter, the PSF size of the particles in the images is set to $\sigma_{PSF} = 0.6$.

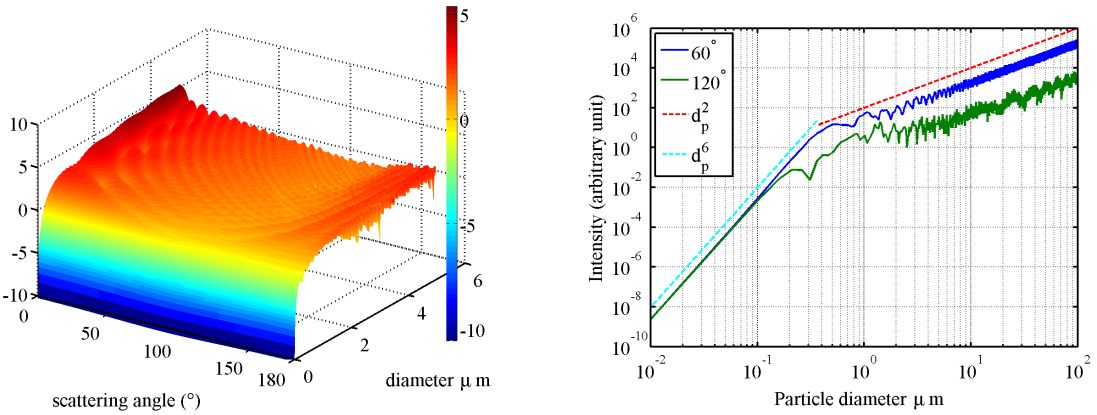

Figure 2.3.7: Logarithm of the scattering function $\mathcal{S}_{11}$ as a function of d_p and θ (left) and as a function of d_p for given θ (right).

First, assuming a fixed diameter d_p, the immediate consequence of Mie scattering regime is expectedly that the intensity difference between backward and forward scatter may be of several orders of magnitude, i.e. one may observe important differences in the average intensity levels of the images. A simple way to compensate for them could be to determine the relative values of $\mathcal{S}_{11}$, and to rescale the darkest images in order to reach the level of the brightest images. This could be done as a pre-processing, or even be included in the construction of matrix W, and would simply lead to images with different signal-to-noise ratio, as one would amplify the noise in the same way as the particles. However, this operation is only made possible if, within a given image, the variation in scattering angle and diameter remains moderate enough to avoid strong variations of $\mathcal{S}_{11}$ between different particles, or at different locations in the camera sensor for a fixed value of d_p.

Our second interest will be to determine, still for a given particle diameter d_p, under which conditions significant intensity variations should be expected within an image, due to the variation of $\mathcal{S}_{11}$ with θ, i.e. due to the variations in viewing angle from one end of the camera sensor to the other. To the best of our knowledge, this point has not been discussed or accounted for in past studies.

Finally, in a third step, we will then consider the issue regarding a polydisperse seeding, by assuming a dispersion in d_p, which may also prevent the simple intensity compensation mentioned above. This corresponds to a very frequent situation, since even in well-controlled experiments, a finite degree of dispersion is inevitably present, especially when working with seeding for airflows. In that respect, we will particularly compare the usual approximation, where the scattered intensity is assumed to vary as d_p^2

with no dependence with θ, to the exact physical situation. Given the behavior observed in figure 2.3.7 (right), this approximation may be a strong one, especially in air flows where small particles are frequently used. For instance, the d_p^2 behavior corresponds to the largest particles, while for the smallest a variation as d_p^6 is observed. The transition occurs roughly at 0.3 microns, which is among the typical values for seeding in the air. In this realistic situation, simple methods for compensating the illumination variations, or models accounting for them, should be very difficult to derive. Thus our goal will be to quantify the error which one makes when synthetic tests only consider a partial modelling of Mie scattering and physical diameter dispersion.

2.3.4.2 Intensity difference between cameras

As mentioned above, the intensity difference between two cameras in backward and forward scatter configuration is the most obvious setback for tomo-PIV technique due to Mie scattering behavior. Indeed, it may lead to a practical situation where a particle seen in the forward scatter camera is missed on the backward scatter camera because its intensity is too low or comparable to that of the CCD noise and thus cannot be reconstructed, ultimately leading to a decrease in reconstruction and velocity field quality. Understanding the mechanism of such a phenomenon is therefore crucial.

For the sake of simplicity, and to clarify ideas, we introduce a first experiment in which a pure mono-disperse seeding is considered, with a simplified account of Mie scattering and not the full model. The particle intensities are computed through equation (2.2.1), without any angular dependence at first. Two cameras ($x > 0$) are considered in forward scattering configuration and the remaining two ($x < 0$) in backward scatter configuration. To account for this difference in scatter and corresponding intensity loss, the particle's intensity (E in equation (2.2.1)) in the images of the cameras ($x < 0$) are multiplied by an attenuation coefficient α so that,

$$E_{x<0} = \alpha \; E_{x>0} \tag{2.3.2}$$

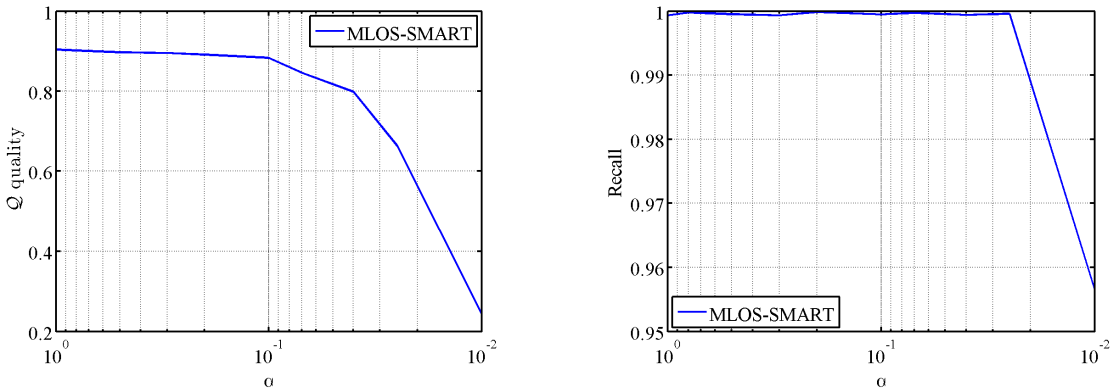

Figure 2.3.8: Influence of the attenuation parameter α between backward and forward scatter cameras on the $\mathcal{Q}$ reconstruction quality and on the Recall parameter.

By doing so, we break the photometric consistency between the cameras, meaning that the particles do not have the same intensity for every camera. The range of α values, that we investigated, was from 1 (no Mie scattering) to 10^{-2}. Note that in practice, such a coefficient can be determined theoretically, by reading for instance the values of $\mathcal{S}_{11}$

(figure 2.3.7) for both sets of cameras. The seeding density was such that $ppp = 0.024$ and we used 512×512 camera sensor size. In this experiment, the reconstruction was done using 16 bit images for better dynamics and the signal-to-noise ratio was increased in all four cameras compared to previous test, in order to have a better understanding of the issue and avoiding too many particle detection losses in the backward scatter cameras due to thresholds in the images during the MLOS step. However, once the noise level is set in all four cameras, it remains constant while α decreases. The signal-to-noise ratio in the back scattering cameras therefore decreases with α.

Figure 2.3.8 (left) shows the effect of this coefficient on the $\mathcal{Q}$ criterion. To build the ground truth corresponding to this case, we attributed to each particle the intensity corresponding to that observed on the brightest camera. As discussed in section 2.2.2.2, this is a first case in which the ill-posedness of the problem is increased. The observed drop in quality evidenced in figure 2.3.8 (left) is firstly due to an associated reconstruction intensity decrease; indeed, given the different intensities on the camera images for a same particle, the solution with minimal error consists in averaging these intensities, which is what SMART will converge to. Figure 2.3.9 illustrates this effect: the probability density function of the real particles shifts to the left and becomes more peaked. By contrast, the intensities of the ghost particles are almost not altered. A second effect explaining this quality drop is the slight increase in detection loss: figure 2.3.8 (right) of the Recall parameter indeed shows that this inevitably occurs when α increases. This phenomenon will amplify when considering wider ranges of intensity differences between the cameras.

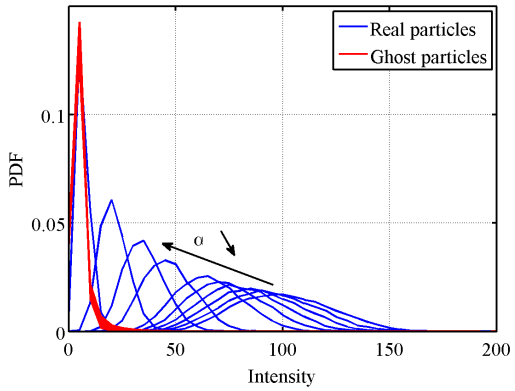

Figure 2.3.9: Intensity PDFs of real and ghost maxima in the reconstructed volume for decreasing α.

To sum up, the intensity difference between forward and backward scatter cameras will lead to two combined effects which decrease the reconstruction quality and may be detrimental to the cross-correlation step. The first effect is the decrease in intensity of the reconstructed particles which leads to a decrease in the signal-to-noise ratio in the reconstruction. Then, depending on the signal-to-noise ratio in the images and the values of thresholds in the reconstruction, a second effect appears : real particles whose intensity is too weak are no longer reconstructed. This effect appeared in our simulation for $\alpha < 0.1$.

2.3.4.3 Intensity differences within an image

We still consider a mono-disperse seeding, and seek now to determine if some angular settings may lead to significant variations of the particle image intensities within a given

camera image. To do so, we simply need to consider a one-dimensional image whose size allows to span the scattering angle variation of a real image. For each pixel along the obtained line, we compute the corresponding value of $\mathcal{S}_{11}$, which yields an intensity distribution along the image. We then compute the average μ_I and root mean square σ_I of this distribution. This finally yields a convenient way to quantify the "intra-image" variation, by considering the relative fluctuation σ_I/μ_I.

Results are presented in figure 2.3.10. As could be expected, the dependence in d_p and θ is rather complex. Logically, for the smallest diameters, σ_I/μ_I remains very low, whatever the angle, due to the high regularity of S_{11} in that case. For larger diameters, three zones can be distinguished. A common point to all these zones is the high-frequency and regular alternation of peaks and valleys. Close to forward and backward scattering (i.e., respectively, for $120° < \theta < 180°$ and $0° < \theta < 20°$, approximately), high values of σ_I/μ_I can be reached with an order of magnitude of 1. For intermediate values $20° < \theta < 120°$, the maximum values are smaller with an order of magnitude of 0.2.

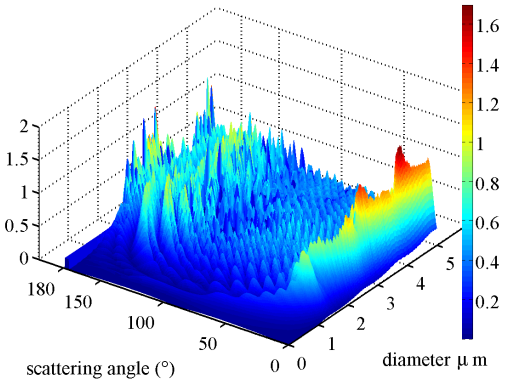

Figure 2.3.10: Level of intensity fluctuation σ_I/μ_I observed in the camera images as a function of the particle diameter and scattering angle. See the text for the definition of σ_I/μ_I.

To model the impact of this phenomenon on the reconstruction, we again consider a simplified framework which allows faster processing but contains the entire problem complexity. As in section section 2.3.4.2, we consider a test case with pure mono-disperse seeding whose intensities are simply computed with equation (2.2.1), i.e. still with no exact account of Mie theory angular. For each camera and for each particle, dispersion intensity coefficients (E_p in equation (2.2.1)) are randomly drawn from a Gaussian law, (of mean I_0 and mean root square σ_{I_0}) leading to an equivalent intensity dispersion in the image. The photometric consistency between the cameras is thus broken. Results in term of True detection and False detection are plotted in figure 2.3.11 as a function of the control parameter of the intensity image dispersion σ_{I_0}/I_0. The seeding density was such that $ppp = 0.024$. One does not observe a significant decrease in missed detections, since there is only a 0.4% decrease, but the number of ghost increases significantly up to 20 %.

The level of intensity distribution that we investigated ranges from $\sigma_{I_0}/I_0 = 0$ to $\sigma_{I_0}/I_0 = 0.5$. This range is comparable to the range exhibited in figure 2.3.10 for scattering angles ranging 30° to 130°, which is a usual angular range used in real tomo-PIV experiment. Considering this intensity distribution level, the results in figure 2.3.11 show that this issue has a limited impact on the reconstruction. Only the

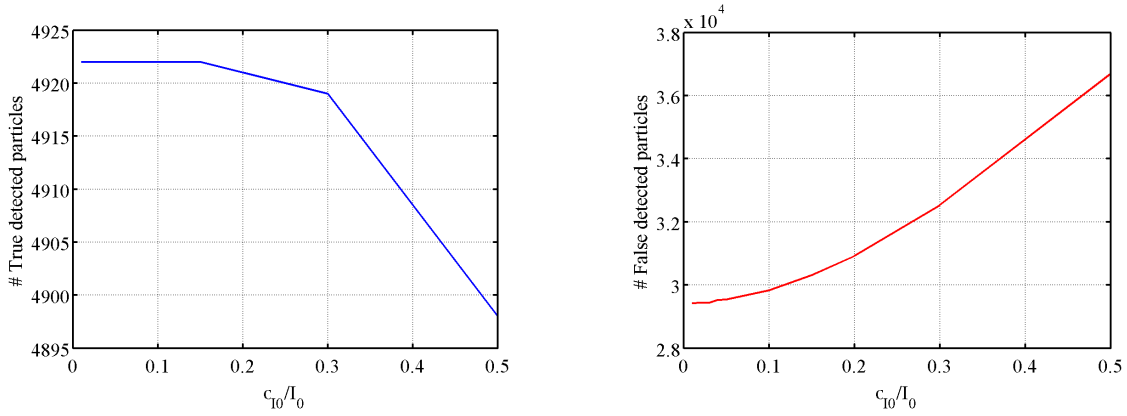

Figure 2.3.11: True (left) and False (right) detected particles in the volume as a function of the image intensity dispersion σ_{I_0}/μ_{I_0}.

number of ghosts increases due to excessive image intensity levels on some particles which transfer their intensity to the ghosts because of the ill-posed reconstruction problem.

2.3.4.4 Polydisperse seeding

We finally turn to the most difficult case of a polydisperse seeding. To understand the effects of a real Mie scattering function when dealing with polydisperse seeding, we will compare it to the classical model which considers a squared dependence of the intensity on the particle's diameter. Therefore, we designed two test cases of increasing complexity : the first one (***Case 1***) is the classically adopted approximation where particle intensities vary as d_p^2, following equation (1). The second one (***Case 2***) is the exact computation of Mie scattering function $\mathcal{S}_{11}(d_p, \theta = 60°)$ [Bohren and Huffman, 1983].

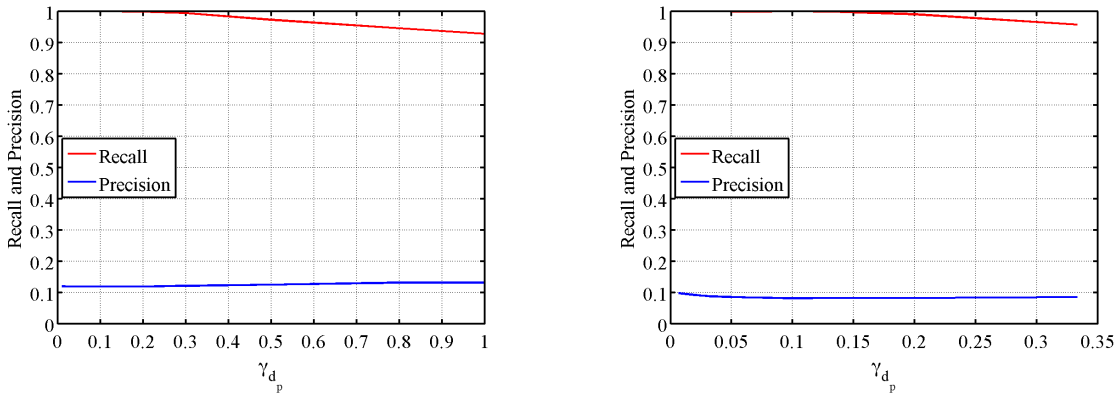

Figure 2.3.12: Influence of the particles diameter distribution (γ_{d_p}) on Recall and Precision quantities, for a simple scattering model, ***Case 1*** (left), and for a more complex Mie scattering model ***Case 2*** (right).

In order to discriminate between the angular effects (which were investigated in sections above) and particle diameter distribution effects of Mie scattering, we consider a different camera setup than that of figure 2.2.1. We will now consider that all the cameras are in forward scatter positions with a scattering angle fixed at 60°. As a consequence, there is no difference in the average intensities of the cameras, the photometric consistency between cameras is restored. Therefore in this context the only observed effects will

be caused by to the polydisperse character of the seeding where a particle's intensity is function of its diameter with the dependency shown in figure 2.3.7 (right).

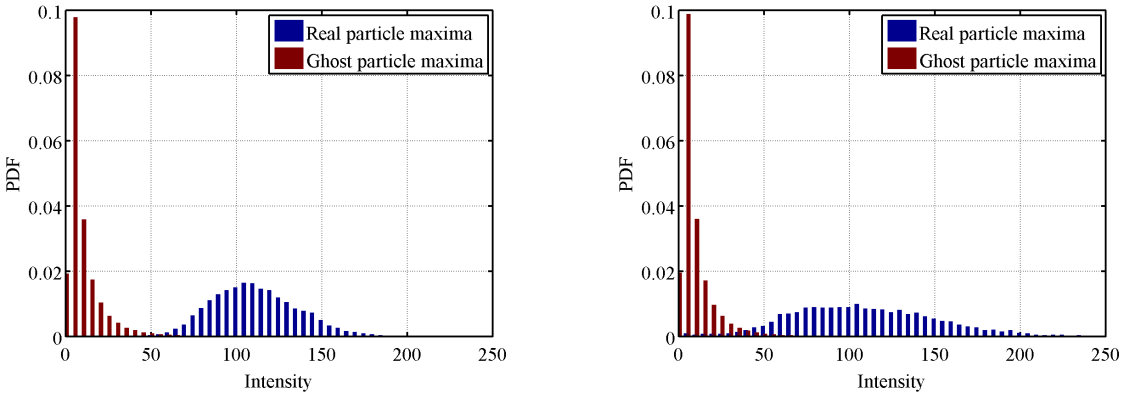

Figure 2.3.13: Simple scattering model, ***Case 1***: for $\gamma_{d_p} = 0.01$ (left) and $\gamma_{d_p} = 0.3$ (right).

For both models, we consider a Gaussian distribution of d_p, with variable standard deviation σ_{d_p}. The diameters are randomly drawn from the segment $\left[min_{d_p}\ ,\ max_{d_p}\right]$, according to a Gaussian distribution law with mean $\mu_{d_p} = 0.5\ \mu m$ and standard deviation σ_{d_p}, with $min_{d_p} = 0.1$, $max_{d_p} = 1$. In both cases, the control parameter is defined as the ratio between the standard deviation and the mean diameter called $\gamma_{d_p} = \sigma_{d_p}/\mu_{d_p}$. We increased the σ_{d_p} from 0 to 0.5 for ***Case 1*** and from 0 to 0.165 for ***Case 2***. For ***Case 2***, we did not investigate for wider diameter distribution because of the dramatic loss of particles due to the d_p^{-6} regime of the Mie scattering function (see figure 2.3.7). The seeding density was set to $ppp = 0.024$ in both cases.

Similar results between the two models are obtained in terms of TP and FP, and therefore in terms of Recall and Precision, as shown by figure 2.3.12, right and left. One notices that as γ_{d_p} increases, the Precision does not vary much, and the Recall tends to decrease. Both quality measures progressively drop. ***Case 2*** 's recall parameter drops faster than ***Case 1***'s recall parameter. Indeed, taking into account the real diameter dependency due to Mie scattering increases the intensity dispersion in the volume compared to ***Case 1***, thus increasing the number of missed detection due to a very low intensity level on certain particles. This detection loss can be seen in the

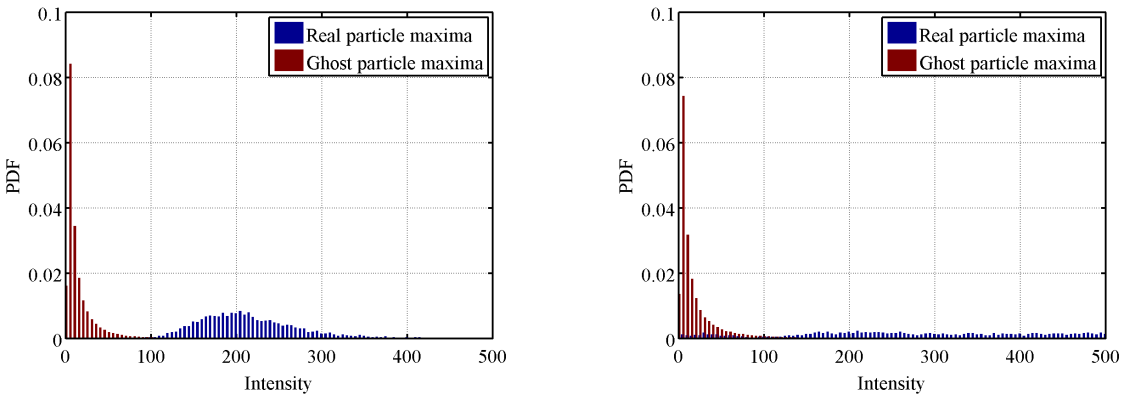

Figure 2.3.14: Mie scattering model, ***Case 2***: for $\gamma_{d_p} = 0.01$ (left) and $\gamma_{d_p} = 0.3$ (right).

PDFs in figure 2.3.13 and figure 2.3.14. The PDFs show that for a same $\gamma_{d_p} = 0.3$,

the reconstructed intensities in ***Case 2*** are widely scattered compared to ***Case 1***. Distinguishing between a real particle and a ghost particle becomes more difficult. The signal-to-noise ratio in the reconstruction volume is thus lowered in ***Case 2***.

This shows that a proper modeling of the Mie function is crucial for an accurate prediction of accuracy loss in the reconstruction and ultimately in the velocity field. The classical model whith a d_p^2 dependency of the intensity drastically underestimate the intensity dispersion.

2.4 Conclusions

In this chapter, our aim was to assess the influence of experimental factors on the quality of tomographic reconstruction for 3D-PIV. By investigating experimental factors through numerical simulations, we increased the level of complexity and physical realism of those simulations. To do so, we degraded the quality of the images using geometrical and optical considerations (Mie scattering and defocusing effects) and studied the effects of those deteriorations on the reconstruction quality.

We identified a new factor built on geometric considerations. This parameter, $R_{I/U}$, is the ratio between the Intersection and union Volume determined by the camera fields of view and the laser volume. The "added" particles, which lie in the union but are not in the intersection, act as a strong source of noise, degrading the reconstruction quality from a resulting increase in the number of ghost particles. However, we showed that in a classical 3D-PIV setup, optimizing the camera angle to increase the $R_{I/U}$ factor had only marginal gains in terms of reconstruction accuracy.

By analyzing the influence of limited depth of field of the cameras, we showed that conducting an experiment with a degree of defocusing but without accounting for it in the reconstruction, will be at the cost of signal-to-noise ratio in the volumes used in the correlation. Contrary to the earlier conclusion referring to $R_{I/U}$, this loss results from an increase in missed detections, while the number of ghost remains comparable.

Finally, we studied the effects of Mie scattering on the reconstruction. We classified the effects of light scattering in three physical phenomena: an intensity difference between images, intensity dispersion within an image and the dependency of intensity on the particle diameter. We showed that all three phenomena tend to decrease the signal-to-noise ratio in the reconstruction volume. The main concluding comment is the fact that not taking into account for the real Mie model leads to an over-estimation of the reconstruction quality. The main source of quality loss does not come from the angular variation of the Mie model, but rather does come from the intensity dispersion due to a polydisperse seeding which leads to missed detections in the reconstruction.

The investigation of the geometry of the reconstructed volume showed us that the $R_{I/U}$ has a strong impact on the reconstruction quality. For a more realistic simulation of the tomographic reconstruction, particles should be spread inside the whole illumination volume and not only inside the intersection volume. This added source of noise in the reconstruction helps further characterize the reconstruction algorithm and its robustness to ghost particles. In chapter 3, we introduce a new approach for the tomographic reconstruction based on a particle paradigm. The algorithm behavior is characterized using numerous imaging conditions, including the image noise generated by the $R_{I/U}$ factor.

3 Particle Volume Reconstruction

3.1 Introduction

As mentioned in the introduction of this dissertation, many research efforts focused on the tomographic reconstruction to improve the overall quality of the 3D-PIV measurement. To do so, different reconstruction algorithms were investigated from algebraic reconstruction methods (ART, MART, SMART, Bi-SMART [Thomas et al., 2014]) to multi-exposure algorithms such as MTE-MART [Novara et al., 2010]. However, all those inversion algorithms use an inversion model which aims at reconstructing particles as 3D blobs of intensity distribution. This is far from physical reality since the particles are even smaller than a voxel most of the time.

In chapter 2, we generated synthetic PIV images using a particle-based representation of the images where a particle is defined by a given intensity, its location in space and its PSF function associated with a given camera.

Our idea now is to use this more physical representation as an inversion model for the tomographic reconstruction. If one knows or even estimates the PSF function, it is possible to use well-known algebraic reconstruction algorithms to reconstruct "particles" in a discretized space. Such an approach requires only a few voxels to explain the image appearance, therefore it favors much more sparsely reconstructed volumes than classic tomo-PIV. Furthermore, this method, as [Schanz et al., 2010] is well adapted to difficult viewing conditions where defocusing effects and astigmatism are present. This approach is referred to as Particle Volume Reconstruction (PVR).

In chapter 3, we now will investigate this inversion model and its implications on the reconstruction volume. Numerical simulations of tomographic reconstruction and displacement estimation will be used to test PVR behavior on a large variety of generating conditions (seeding density, PSF size) and its robustness to an uncertainty of the PSF knowledge.

3.2 PVR : working principles and numerical assessment

IOP Publishing Measurement Science and Technology

Meas. Sci. Technol. **25** (2014) 084002 (14pp) doi:10.1088/0957-0233/25/8/084002

Tomographic PIV: particles versus blobs

Frédéric Champagnat[1], Philippe Cornic[1], Adam Cheminet[2], Benjamin Leclaire[2], Guy Le Besnerais[1] and Aurélien Plyer[1]

[1] Department of Information Processing and Modelization, ONERA, Chemin de la Hunière, Palaiseau, France
[2] Department of Fundamental and Experimental Aerodyanmics, ONERA, 8 rue des Vertugadins, Meudon, France

E-mail: frederic.champagnat@onera.fr

Received 13 December 2013, revised 30 April 2014
Accepted for publication 2 June 2014
Published 14 July 2014

Abstract

We present an alternative approach to tomographic particle image velocimetry (tomo-PIV) that seeks to recover nearly single voxel particles rather than blobs of extended size. The baseline of our approach is a particle-based representation of image data. An appropriate discretization of this representation yields an original linear forward model with a weight matrix built with specific samples of the system's point spread function (PSF). Such an approach requires only a few voxels to explain the image appearance, therefore it favors much more sparsely reconstructed volumes than classic tomo-PIV. The proposed forward model is general and flexible and can be embedded in a classical multiplicative algebraic reconstruction technique (MART) or a simultaneous multiplicative algebraic reconstruction technique (SMART) inversion procedure. We show, using synthetic PIV images and by way of a large exploration of the generating conditions and a variety of performance metrics, that the model leads to better results than the classical tomo-PIV approach, in particular in the case of seeding densities greater than 0.06 particles per pixel and of PSFs characterized by a standard deviation larger than 0.8 pixels.

Keywords: 3D PIV, tomography, volume reconstruction, imaging, sparsity, point spread function

(Some figures may appear in colour only in the online journal)

1. Introduction

In numerous particle image velocimetry (PIV) (Adrian and Westerweel 2010) and tomo-PIV (Elsinga *et al* 2006) experiments, particles have a very small physical size, so that their images on the camera sensors are mostly controlled by the aperture diffraction, and are thus essentially a characteristic of the imaging system. Optimization in plane PIV developments has led to the seeking of a resulting point spread function (PSF) in the images having a 3×3 pixel square shape in order to guarantee good subpixel accuracy in the displacement estimation. Later pioneering works on tomo-PIV sought to maintain a similar rule-of-thumb by considering geometrical models, as those used in x-ray tomography. Conventional multiplicative algebraic reconstruction technique (MART)/ simultaneous multiplicative algebraic reconstruction technique (SMART)-based tomo-PIV methods (Atkinson and Soria 2009, Elsinga *et al* 2006) have indeed aimed at reconstructing volumic 'particle blobs', i.e., aggregates of several voxels width, rather than the actual particles, which would lie in a single voxel (and, usually, be much smaller than the voxel size). This discrepancy, compared to the actual image formation physics, is depicted in figure 1. A particle whose geometrical image is much smaller than the PSF produces an Airy-like image, as in the left part, whereas in the above cited tomo-PIV methods, this image is modeled as the integration of a 3D bell-shaped volumic distribution of particle intensity (or 'blob') in the volume, along a thin pixel-sized pencil elongated in the direction of the line of sight (right part).

Such approaches naturally rely on geometric considerations of varying complexity, as the light integration is performed over a cone having the optical center as apex and a square pixel trace on the focal plane. In this context, building the weighting matrix W linking the voxel and pixel spaces amounts to computing the volume intersecting this 'pixel cone' and a voxel. As reviewed by Thomas *et al* (2014), several techniques have been proposed in the literature to simplify this geometrical model. Among them, Elsinga *et al* (2006) and later Atkinson and Soria (2009) have proposed approximating the cubic voxel by a sphere and the 'pixel cone' by a cylinder

Meas. Sci. Technol. **25** (2014) 084002 F Champagnat *et al*

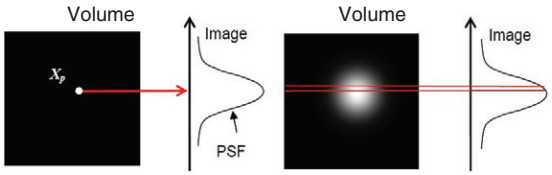

Figure 1. Image formation from a volumic projection: particle model (present approach, left) and blob model (right).

of the same surface in the vicinity of the voxel in order to maintain tractable computation times.

Although such approaches have proven wide practical utility, their domain of use is restricted to favorable viewing conditions, this point being linked to the uncertain physical nature of the reconstruction itself. In difficult experimental conditions, such as when viewing through curved walls, in the presence of defocusing or in compressible flows, it is known that the shape of the PSF, i.e. of the particle images, can vary dramatically, leading to accuracy losses in the estimation, since geometry cannot account for these perturbations. In order to overcome these difficulties, Schanz *et al* (2013) recently proposed accommodating for variations of the PSF through the definition of an adapted weight matrix. In their approach, this matrix is built from a dedicated processing of PSF samples, which is specifically designed in order to yield reconstructed volumes made of particle blobs suited to 3D cross-correlation. Their study indeed showed increased reconstruction quality and more accurate displacement estimations, in particular in the case of astigmatism and defocus.

We propose here a different and novel approach called *particle volume reconstruction* (PVR), which consists of a direct discretization of the image formation model from optics depicted in figure 1, left. The two most salient new features of PVR, which are tightly linked to one another, are that, firstly, it uses a weight matrix W *directly made up of PSF samples*, i.e., the construction of W requires information from the calibration of the imaging set-up only. The second specificity is that, consequently, it reconstructs point-like particles rather than blobs. As such, the PVR result can be the basis of either a particle tracking velocimetry (PTV) technique or a correlation based PIV, with post-processing adapted to each case. This is summarized in the flow chart of figure 2, which considers the three usual steps of an experiment. The first one is calibration, which provides the geometric projection functions of the cameras and, thanks to dedicated techniques, the PSF, which enables one to directly build the weight matrix. The second one is reconstruction, which can be based on a conventional MART or SMART approach, and provides a near punctual particle volume. The last one is velocity estimation, which can be done by PTV or correlation based PIV, after a post-processing step adapted to each case. Indeed PVR underlies a sparse volumic representation of point particles, which lives halfway between infinitely small particles and larger two to three voxel blobs usually used in tomo-PIV. From that representation, it is possible to go further and sharpen the particle to its essential features, which is the aim of performing PTV (intensity and 3D position, by using subvoxel refinement), or

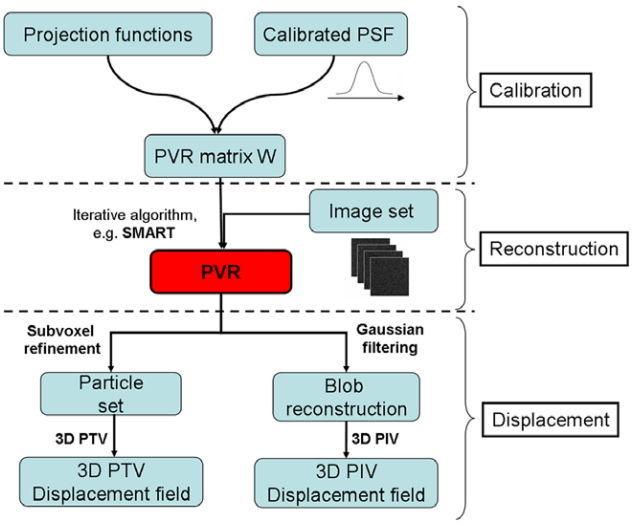

Figure 2. Flow-chart of a typical experiment using the particle volume reconstruction (PVR) method.

to smooth it to the ubiquitous two voxel diameter blob, which is the gold standard of correlation for PIV, thanks to Gaussian post-filtering.

In this paper, regarding velocity estimation, we will focus mostly on the use of PVR for correlation-based 3D PIV. As mentioned above, the second processing choice of PVR volumes, 3D PTV, requires a dedicated subvoxel refinement, which in our opinion should be directly combined with the estimation of motion. This is an ongoing and separate axis of work in itself, and will thus not be presented here. However, the potential of the PVR result for 3D PTV will still be accounted for in this paper, first by showing that the model converges to the true particle position in the case of an increasingly refined discretization grid and, second, by evaluating the reconstructed volume using detection metrics, i.e., by evaluating the fraction of true detected particles and of ghosts.

As the weight matrix W is constructed by directly incorporating the calibrated PSFs, the PVR model is designed to offer a simple systematic approach for dealing with spatially varying PSF due, for instance, to defocussing and astigmatism, which are commonly encountered if the illuminated volume is larger than the camera's depth of field, in the presence of interfaces or in compressible flows. Thanks to synthetic tests we will show that, indeed, PVR-SMART behaves quasi-systematically better than the classical geometrical approach, hereafter referred to as tomo-SMART, whatever the performance metric considered (reconstruction or displacement estimation).

Thus, similar to Schanz *et al* (2013), PVR is expected to lead to significant gains in accuracy in the difficult experimental situations mentioned above. However, in contrast to Schanz *et al* (2013), PVR uses the calibrated PSF directly so as to obtain a reconstruction of point-like particles instead of blobs, and then applying a post-processing suited either to PTV or to PIV.

Note that our approach has similarities with the iterative particle reconstruction (IPR) recently introduced by Wieneke (2013). Indeed, IPR directly works on the same image formation as we do, but does not discretize it and directly tackles

the non-linear problem of fitting the particle parameters of the image model to observed images. The logic of IPR is to remove from observed images the additive contribution of a tentative particle in order to enhance the detectability of particles being otherwise hidden by that particle. Implementation of this idea relies on a complex iterative procedure that cyclically adds, refines or removes particles. In the proposed PVR approach, the discretization of the image formation model provides a linear forward model, which allows us to use classical and well-behaved algorithms such as MART or SMART by simply using the weight matrix derived from the PSF.

Our approach is also well suited to sparsity-based techniques (Barbu *et al* 2011, Cornic *et al* 2013, Petra *et al* 2009). For instance, Cornic *et al* (2013) managed to obtain dramatic reductions of the problem size, and thus of the processing time, for the same set of particles compared to classical tomographic reconstruction techniques.

The outline of this paper is as follows. Section 2.1 recalls the basic image formation model for particle images. Then the main contribution of this paper is introduced in section 2.2, that is, a discretization of the image model that justifies the classic expression of image data in terms of an appropriate weight matrix and a voxelized intensity field. The usefulness of such a representation is demonstrated for tomographic reconstruction in section 3, then for velocity estimation in section 4.

2. Model description

In our approach, the weighting matrix W is built directly by following the physical model depicted in the left part of figure 1. This model is briefly reviewed in section 2.1, then its discretization is derived in section 2.2.

2.1. Imaging

Our imaging model is based on the concept of PSF. Any source point located at $\boldsymbol{X}$ in 3D-space has a geometrical image located at $F(\boldsymbol{X})$ in the focal plane of a given camera (in practice, the 3D to 2D projection function F results from the camera calibration procedure, see for instance Wieneke (2008)), and the source intensity E is shared between the impacted pixel and its immediate neighbors according to weights given by the so-called PSF $h_{\boldsymbol{X}}(\boldsymbol{x})$. As implied by index $\boldsymbol{X}$, the PSF is dependent on the location of the source point $\boldsymbol{X}$; this enables us for instance to model defocussing and astigmatism, which lead to distortions of the PSF compared to standard, in-focus imaging. Such variations of $h_{\boldsymbol{X}}(\boldsymbol{x})$ can be determined by an adequate calibration procedure.

To the best of our knowledge, the only PSF calibration published in the PIV community is that of Schanz *et al* (2013). This is based on a self-calibration step (Wieneke 2008) followed by a particle-by-particle least-squares fitting of a Gaussian PSF template. To build the so-called optical transfer function used for reconstruction by Schanz *et al* (2013), PSF parameters are then smoothed and resampled on a Cartesian voxel grid. In practice, one could also alternatively resort to simpler PSF calibration procedures used in computer vision, such as the slanted-edge method of Reichenbach *et al* (1991). This relies on the imaging of a black–white step, captured by the camera with a small but non-zero angle w.r.t. pixel alignment. The maximum slope of the transition separating the purely white and black zones can then be related to the σ of a Gaussian PSF model. During the PSF calibration process, such slanted-edge charts are swept in the z-dimension of the volume in order to capture the PSF variation with respect to depth. Recently, Delbracio *et al* (2012) have proposed a more elaborate chart and non-parametric PSF calibration techniques that have been used in the context of depth from defocus techniques (Trouvé *et al* 2013). It can thus be expected that in practice such calibration techniques should allow accurate determinations of the PSF $h_{\boldsymbol{X}}(\boldsymbol{x})$ in the entire experimental volume. Note that, whatever the calibration procedure, a fundamental property is that the PSF is a feature of the camera system, not of the source.

We consider a set of P particles, each of which is denoted by index p and located at $\boldsymbol{X}_p$ in 3D space. If we assume that the geometrical image of these particles is much smaller than the PSF at $\boldsymbol{X}_p$, then the intensity distribution in the image plane reads

$$I(\boldsymbol{x}) = \sum_{p=1}^{P} E_p h_{\boldsymbol{X}_p}(\boldsymbol{X} - F(\boldsymbol{x}_p)), \tag{1}$$

where $\boldsymbol{x}=(x, y)$ denotes any location in the image plane and E_p is the intensity of particle p. In practice, camera sensors consist of an array of pixels $\boldsymbol{k}=(k_1, k_2)$, each gathering a single intensity value $I(\boldsymbol{k})$. In order to alleviate the following derivations, we will omit the dependence in $\boldsymbol{X}_p$ of the PSF h, i.e., denote it by $h(\boldsymbol{x})$.

2.2. Discretization

Based on (1), an estimation of the number of particles, their 3D positions and intensities is a difficult non-linear problem, which has been tackled for instance within the IPR approach of Wieneke (2013). IPR fits the nonlinear model (1) for imaging data using a complex procedure that iteratively adds or removes particles, as does the CLEAN algorithm in astronomy (Hogbom 1974). Our approach builds on a simpler linear relationship between images and an intermediate representation of particles on a regular 3D grid associated with a voxel space representation, encoding simultaneously the particles' locations and intensities.

An important parameter of such a grid is its scale Δ, i.e., the voxel physical size. Without loss of generality, any node of this grid (the center of a voxel) can be indexed with a triplet of signed integers $\boldsymbol{n}=(n_x, n_y, n_z)$ such that the 3D position of the node is $\boldsymbol{n}\,\Delta$.

We look for a matrix–vector counterpart of (1)

$$\boldsymbol{I} = \mathrm{W}\widetilde{\boldsymbol{E}}, \tag{2}$$

where

- $\boldsymbol{I}$ is a vector that collects image pixels indexed by $\boldsymbol{k}$,
- $\widetilde{\boldsymbol{E}}$ is a vector of intensities located at discrete nodes $\boldsymbol{n}\,\Delta$, encoding both location and intensity of particles,
- the weight matrix W has entries denoted by $\mathrm{W}_{\boldsymbol{kn}}$.

Meas. Sci. Technol. **25** (2014) 084002 F Champagnat *et al*

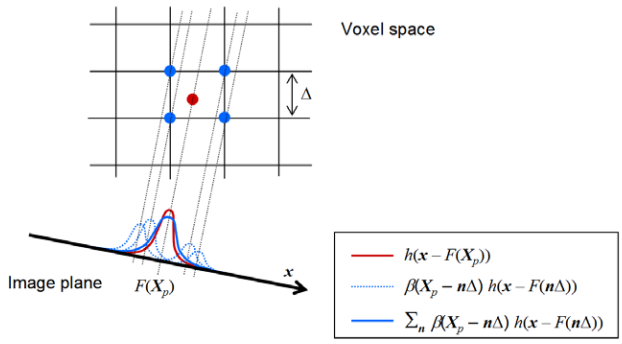

Figure 3. Approximation of the projection + PSF function, exemplified on 2D geometry.

Discretization of (1) requires a volumic approximation of the projection + PSF function $\boldsymbol{X} \mapsto h(\boldsymbol{x} - F(\boldsymbol{X}))$ based on grid node values near $\boldsymbol{X}$, i.e.,

$$h(\boldsymbol{x}-F(\boldsymbol{X})) \approx \sum_{\boldsymbol{n}} h(\boldsymbol{X}-F(\boldsymbol{n}\Delta))\,\beta(\boldsymbol{X}-\boldsymbol{n}\Delta). \tag{3}$$

This approximation is illustrated in figure 3 for a 2D case.

β can be any interpolation kernel, but for the sake of particle reconstruction we advocate that this kernel should be as compact as possible; thus in this paper we will use a trilinear interpolation. Using (3) for each particle position $\boldsymbol{X}_p$, and plugging into (1), we get

$$\begin{aligned} I(\boldsymbol{x}) &\approx \sum_{p=1}^{P} E_p \left(\sum_{\boldsymbol{n}} h(\boldsymbol{x} - F(\boldsymbol{n}\Delta)) \beta(\boldsymbol{X}_p - \boldsymbol{n}\Delta) \right), \\ &\approx \sum_{\boldsymbol{n}} h(\boldsymbol{X} - F(\boldsymbol{n}\Delta)) \left(\sum_{p=1}^{P} E_p \beta(\boldsymbol{X}_p - \boldsymbol{n}\Delta) \right), \end{aligned} \tag{4}$$

where the last equality is obtained by swapping the summations. The last expression enables us to introduce a discrete 3D field

$$\widetilde{E}_{\boldsymbol{n}} = \sum_{p=1}^{P} E_p \beta(\boldsymbol{X}_p - \boldsymbol{n}\Delta). \tag{5}$$

Evaluating (4) at the pixel index $\boldsymbol{k}$ and introducing (5) we get:

$$I(\boldsymbol{k}) \approx \sum_{\boldsymbol{n}} h(\boldsymbol{k} - F(\boldsymbol{n}\Delta)) \widetilde{E}_{\boldsymbol{n}}. \tag{6}$$

This is the matrix-vector representation sought (2). The entries of the weight matrix W have a straightforward expression in terms of the PSF and the geometric projection function:

$$\mathrm{W}_{\boldsymbol{k}\boldsymbol{n}} = h(\boldsymbol{k} - F(\boldsymbol{n}\Delta)). \tag{7}$$

This remarkable property stems from the fact that we are considering the reconstruction of point-like particles. Indeed, in works which are based on blob reconstruction, such as (Schanz *et al* 2013), the components of W are derived from a dedicated processing of the PSF.

For all the synthetic experiments performed in this paper we assume an 'optics + pixel' PSF made of a Gaussian with standard deviation σ_{psf} for optics averaged on the pixel surface, assuming a 100% fill factor:

$$\begin{aligned} h(x, y) = \frac{1}{4} &\left(\mathrm{erf}\left(\frac{x + 0.5}{\sqrt{2}\,\sigma_{\mathrm{psf}}} \right) - \mathrm{erf}\left(\frac{x - 0.5}{\sqrt{2}\,\sigma_{\mathrm{psf}}} \right) \right) \\ &\times \left(\mathrm{erf}\left(\frac{y + 0.5}{\sqrt{2}\,\sigma_{\mathrm{psf}}} \right) - \mathrm{erf}\left(\frac{y - 0.5}{\sqrt{2}\,\sigma_{\mathrm{psf}}} \right) \right). \end{aligned} \tag{8}$$

It is important to note here that the accuracy of the approximation in (6) depends on the accuracy of the original approximation (3), which, in turn, depends on the voxel-to-pixel (v/p) ratio. Typically, a PSF $\sigma_{\mathrm{psf}} = 1$ can be accurately sampled using $v/p = 1$, but for a sharply focused particle with $\sigma_{\mathrm{psf}} = 0.4$ it will be shown to be insufficiently accurate, $v/p = 0.5$ being more appropriate in this case. Further examples of this dependence will be given in section 3.4.

According to equation (5), the 3D field $\widetilde{E}_{\boldsymbol{n}}$ can be seen as a discrete approximate representation of the original Dirac-like particle field. Conversely, given $\widetilde{E}_{\boldsymbol{n}}$, one can recover unambiguously the intensity and position of particles with subvoxel accuracy within this 3D representation, if they do not overlap. Note that the occurrence of the overlapping of blobs in 3D space is extremely rare given the typical values of the number of particles per volume N_{ppv} in 3D PIV. Thus, it is expected that the reconstructions $\widetilde{E}_{\boldsymbol{n}}$ will most often represent truthfully the particle distribution. Refinements to this approach may also be found in the case of overlapping, should the case arise in practice.

In this paper, we will however not try to recover the original particle field, but rather correlate $\widetilde{E}$, as we will use a 3D cross-correlation algorithm to estimate the displacement. As we will show, this correlation process will provide 3D vectors with subvoxel accuracy. This is due to the fact that the reconstruction of a particle is not strictly contained in a single voxel, but has a slightly larger extent. Thus, the shape of $\widetilde{E}$ depends on the subvoxel position of the particles, which can be retrieved by this correlation.

3. Single volume reconstruction using PVR

We now turn to an assessment of the efficiency of representation (6) based on synthetic image data. We first specify the parameters used and the quantities of interest considered for this evaluation. We then consider the relative performances of PVR-SMART and of the classical geometry-based tomo-SMART (Atkinson and Soria 2009, Elsinga *et al* 2006) in several experimental conditions, obtained by varying the number of particles per pixel N_{ppp} and σ_{psf}. In the latter case, we first explore the ideal case where the PSF size σ_{psf} is known by the experimentalist, but allow this factor to vary. Such a situation mimics for instance the situation where variations of the PSF, for instance due to the presence of defocused particles or of astigmatism, have been evaluated during calibration. Then we test the robustness of PVR-SMART w.r.t. inaccuracy in this parameter, in order to quantify the robustness of the method to situations where the PSF calibration was difficult or impossible in a direct way (such as in the presence of shocks in the flow, for instance).

3.1. Synthetic setup

All our simulations involve four cameras, which are positioned on a single side of the laser volume at the vertices $\left(\frac{\pm 1}{2}, \frac{\pm 1}{2}, \frac{1}{\sqrt{2}}\right)$ of a square of 1 m side. These are positioned 1 m from the center of the reconstructed volume, the latter defining the origin (0, 0, 0), and point at it. The pin-hole model is assumed for the cameras (without a Scheimpflug adapter for simplicity) and calibration is supposed to be perfectly known. The focal length is 100 mm, thus the magnification factor M is equal to 0.1 and the pixel size is 10 μm with a 100% fill factor. Thus a voxel-to-pixel ratio $v/p = 1$ leads to voxels of 0.1 mm side. The image size is set to 512 × 512; hence, the field of view is fixed for each simulation. The dynamic range of the images is chosen to equal 8 bits.

The laser volume is modeled as a 20 mm thick parallelepiped. The reconstructed volume, also 20 mm thick, is the portion of the illuminated volume seen by all the cameras. The tracer particles are uniformly distributed in the light sheet volume. The density is controlled by the particle per voxel count (ppv). Horizontal and vertical extension of the sheet are larger than the field of view covered by all the cameras. As particles are present all over the laser sheet, it is important to notice that this leads to the fact that all the illuminated particles cannot be seen by all cameras, which is systematically the case in real datasets, and is however not often taken into account in synthetic experiments. As shown in Cheminet *et al* (2013) and Cornic *et al* (2013) the parameter that measures the impact of neglecting this factor (i.e., considering that only the particles seen by all cameras are illuminated) is the ratio I/U of the volume formed by the intersection of the camera fields of view with the volume formed by the union of their fields of view. It turns out that a large number of studies in the literature consider only particles within the intersection volume, which amounts to considering $I/U = 1$. Thus, to enable easier comparisons and to address situations more directly relevant to experiments, we will present results both for $I/U = 1$ and $I/U < 1$.

The scattered light is proportional to the square of the particle diameter d_p. Note that Mie scattering is not taken into account in this study. Since the laser sheet profile is considered uniform, the intensity of a particle depends only on its diameter. This is given by $I_0 d_p^2 / 4$, where I_0 is a constant. The particle diameters are supposed to be small enough (a few microns) to neglect the size of their geometric image Md_p. A monodisperse seeding is considered with $I_0 d_p^2 / 4 = 170$.

The images are synthesized according to (1) with a PSF given by (8). Unless otherwise specified, we take $\sigma_{\text{psf}} = 0.6$. With this value, a particle has a 4 × 4 pixel image pattern.

We will consider different synthetic tests with increasing but uniform values of σ_{psf}, ranging between 0.4 and 1.2. This will allow us to evaluate the ability of PVR to deal with defocussing. Indeed, processing the corresponding images using the exact value of σ_{psf} will provide a first-order account of situations where variations of σ_{psf} have been successfully calibrated, whereas processing them with a different value will evaluate situations where these variations could not be quantified.

Unless otherwise specified, a zero-mean Gaussian noise with standard deviation 2 is added to the images, with negative image values thresholded to zero. Its amplitude is thus about 5% relative to the maximum particle intensity.

3.2. Reconstruction algorithm

SMART solves linear systems under non-negative constraints (Byrne 2008), and is a popular choice for tomographic PIV reconstruction following the work of Atkinson and Soria (2009). It is considered here because of its parallel structure (compared to MART, which is highly sequential). Applying SMART in order to solve (2) yields the following update equation (in logarithmic form in order to emphasize parallelism):

$$\log E^{k+1} = \log E^k + \mu \widetilde{\mathrm{W}} (\log I - \log \mathrm{W} E^k). \tag{9}$$

$\widetilde{\mathrm{W}}$ is obtained by normalizing W over the columns and μ is a relaxation parameter. In our simulations μ is set to 1 in order to guarantee convergence (Byrne 2008).

Our simulations consider a reference algorithm, referred to as tomo-SMART, and a new algorithm derived from the present framework referred to as PVR-SMART. Both algorithms start with a multiplicative line-of-sight (MLOS) step (Atkinson and Soria 2009) that aims to reduce the number of voxels that have to be considered in the reconstruction. The MLOS volume is thresholded: only the voxels of intensity greater than 4 are retained for further refinement. Then, 25 iterations of SMART are performed. In both cases, the iteration is defined by (9), though the matrix W is different. Tomo-SMART builds W by computing the volume intersected by a cylinder and a sphere centered on the voxel as described in Elsinga *et al* (2006) and Atkinson and Soria (2009). PVR-SMART computes W using PSF samples and geometric projection functions with (7). As discussed below equation (6), the model is parameterized by the scale of the voxel selected in the discretization of the image formation model, i.e., the voxel to pixel ratio v/p. As will be shown in section 3.4, $v/p = 0.5$ constitutes a good trade-off between processing times and the degree of refinement necessary to account for a large range of PSFs. As the optimal setting of v/p for tomo-SMART is known to be around 1 (Thomas *et al* 2014), this value will be retained in the tests for this algorithm.

Note that in the following, in order to allow a consistent comparison between the methods, all lengths or diameters given in voxel units will refer implicitly to $v/p = 1$ voxels, unless otherwise specified. This simply translates into applying a change of units to the results of PVR-SMART reconstructions, which are performed at $v/p = 0.5$, in order to be consistent with the sampling of tomo-SMART reconstructions.

The MLOS, tomo-SMART and PVR-SMART algorithms have been coded in CUDA in order to take advantage of their intrinsic parallelism and of the massively parallel capacities of GPUs. The matrix W is not stored, its entries being computed on the fly for projection and backprojection, and recomputed at the next SMART iteration.

In order to characterize the PVR-SMART reconstruction w.r.t. tomo-SMART we have performed 50 independent reconstructions of a single particle with random locations.

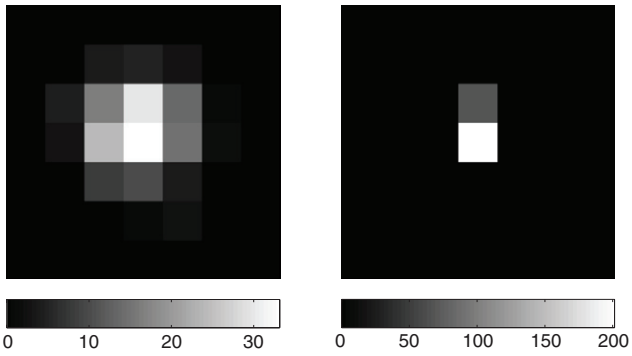

Figure 4. Zoom on a slice of reconstructed volume using tomo-SMART (left) and PVR-SMART with $v/p=1$ (right). $\sigma_{psf}=0.9$. PVR-SMART shows more spiky results than tomo-SMART; note also the larger dynamic of the PVR-SMART reconstruction.

Table 1. Averaged σ ($v/p=1$ voxel unit) in each direction extracted from a $7 \times 7 \times 7$ voxel volume around a maximum reconstructed intensity.

	σ_x	σ_y	σ_z
tomo-SMART	0.83	0.82	0.84
PVR-SMART	0.19	0.23	0.35

The total intensity of each particle equals 450 counts, which is spread on images with $\sigma_{psf}=0.9$. Figure 4 shows a close-up on a 7×7 slice around the maximum reconstructed intensity voxel.

We have also computed the dispersion of reconstructed blobs using the standard deviation in each direction, then averaged this quantity on the 50 particle samples. The result is displayed in table 1. Figure 4 and table 1 clearly indicate more spiky results for PVR-SMART than tomo-SMART. Note that spikiness is obtained here without using sparsity-enhancing techniques such as Petra *et al* (2009), Barbu *et al* (2011) and Cornic *et al* (2013). MART/SMART techniques are indeed already sparsity techniques in themselves and are exploited here by using our weight matrix W built from PSF samples.

3.3. Performance metrics for volume reconstructions

The difference between the particle approach considered here and the classical tomographic approach initially introduced by Elsinga *et al* (2006) raises the question of which ground truth to consider for building performance criteria for the algorithms. Indeed, for the same set of physical particles, the former will aim at providing essentially the list of voxels containing a particle together with its corresponding intensity, while the latter will reconstruct volumetric blobs of approximately the back-projected particle image size, centered around these physical particles. In this tomographic framework in particular, Elsinga *et al* (2006) built the ground truth by expanding locally the physical particles to a 3D Gaussian blob, usually of the order of two to three voxels size, according to the idea of having volumetric distributions well adapted to the subsequent correlation step that yields the 3D displacement field.

A natural quality measure is then the Q criterion, which indicates the degree of correlation between the reconstruction and this ground truth. In the case of PVR-SMART, the Q criterion cannot be applied directly, as the particle reconstructions generated by PVR-SMART have nearly one voxel size. Therefore, to compute this criterion in the following, we expand the PVR-SMART reconstruction using the same method as for building the ground truth, i.e., filter the voxel volume using a 3D Gaussian kernel. The standard deviation of this Gaussian is σ_{psf}, which is also the standard deviation of the Gaussian that expands locally the physical particles to 3D Gaussian blobs, leading to the ground truth volume. In this way, as usually performed in the literature (see, for instance, Elsinga *et al* 2006), the ground truth volume accounts for the fact that the blobs reconstructed by tomo-SMART have approximately the size σ_{psf}. An important point to mention here is that, whatever the v/p ratio chosen, the quality factor Q is computed in a $v/p=1$ discretized space. In the case where $v/p \neq 1$, the reconstructed volume is considered as a set of particles: any voxel with non-zero intensity is considered as a particle with the center of the voxel as a 3D location. This set of particles is then converted to an intensity volume of scale $v/p=1$ in the same way as the set of true particles is converted to the ground truth volume for quality factor Q.

We also introduce a metric adapted to measure the detection performance of the methods. A detection is here a local maximum in the reconstructed volume. It is termed a true positive (TP) if it is in the neighborhood of a true particle. The neighborhood of any particle is the $2 \times 2 \times 2$ voxel cube whose center has a chessboard distance from the particle lower than one voxel. A detection is a false positive (FP), i.e., a ghost, if it is not in the neighborhood of a true particle. A particle is recorded as a false negative (FN) if there is no detection in its neighborhood. A first useful metric is then the Recall, i.e., the fraction of detected particles found, e.g., in Wieneke (2013), defined by

$$\frac{\#TP}{\#TP+\#FN}. \tag{10}$$

A second metric has to be considered for a complete account of the detection performance. This quantity is the Precision and quantifies the fraction of ghosts among all detected particles. In order to simplify the presentation of results, we will restrict the set of detected particles and only retain the S brightest of them, with $S=\#TP+\#FN$ equal to the actual number of true particles. Such a choice is shown in Champagnat *et al* (2013) to be a good landmark for assessing the relative performance of algorithms. With such a choice, one can easily check that Precision and Recall are equal, so that one parameter enables us to quantify both the fraction of detected particles and the fraction of ghosts among the detections. In the following, we will refer to this quantity as Recall in the figures. Here as well, even when the reconstruction has been performed using $v/p \neq 1$, the Recall metric is computed in order to correspond to a $v/p=1$ discretized space.

3.4. Selection of v/p

As shown in section 2.2, the accuracy of the approximation in the PVR reconstruction model (6) depends on the accuracy of the original approximation of the projection+PSF function (3), which in turn depends on the v/p ratio: the lower, the finer the

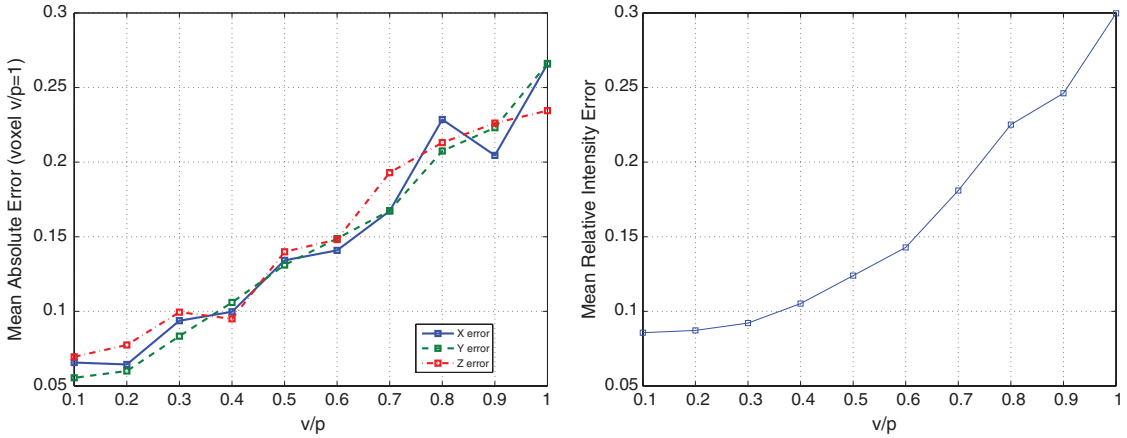

Figure 5. Evolution as a function of v/p of PVR localization error in the case of a single particle with $\sigma_{psf}=0.6$ and random location. Left: absolute location error ($v/p=1$ voxels). Right: relative intensity error (counts). Averaged on 50 samples.

approximation. Therefore, the accuracy of PVR reconstruction is expected to grow for increasingly refined voxel grids.

In order to measure the gain in accuracy provided by varying v/p, we perform a Monte Carlo experiment that involves the reconstruction of a single particle using PVR-SMART. At each run a single particle is generated with random location within a voxel, and its image is computed according to the PSF model (1) with $\sigma_{psf}=0.6$. Then, PVR-SMART is run with a given v/p, the voxel of maximum intensity is extracted and the coordinates of its center are taken as the particle location estimate. The mean absolute location error is then computed.

This procedure is performed for v/p varying from 0.1 to 1 by steps of 0.1. The resulting mean absolute location error averaged over 50 runs is drawn in figure 5, left. Figure 5, right, presents the mean relative intensity error between the true particle intensity and the sum of the reconstructed intensity.

Despite the crude estimation for particle location and intensity (as no subvoxel interpolation is performed), figure 5 shows a decrease of both mean errors from $v/p=1$ to $v/p=0.1$, the slope of the error being approximately constant for the location estimate. These curves indicate converging behavior of PVR toward the true location and intensity of the particle as v/p decreases to zero.

An increase of detection and velocity estimation performance can thus indeed be expected as v/p decreases to zero. Conversely, the computational complexity and memory requirement grow as $(v/p)^{-3}$: a trade-off between accuracy/performance and computational complexity must thus be found. In order to help this choice, figure 6 shows the evolution of the Q-factor w.r.t. v/p for different values of N_{ppp}.

Clearly, for $N_{ppp} \geqslant 0.07$, a gain greater than 0.05 in quality can be expected from a decrease of v/p down to 0.5. Note also that the slope of the Q-factor decreases gradually as v/p decreases, so that the gain between $v/p=0.6$ and $v/p=0.5$ is rather modest. Meanwhile, at $v/p=0.5$ the computational complexity and memory requirement are already about 8 times higher than that required for $v/p=1$. Going even further down to $v/p=0.4$ would require twice as much memory and flops with a negligible expected gain in quality. Consequently, $v/p=0.5$ appears a reasonable trade-off and will be the recommended value for PVR.

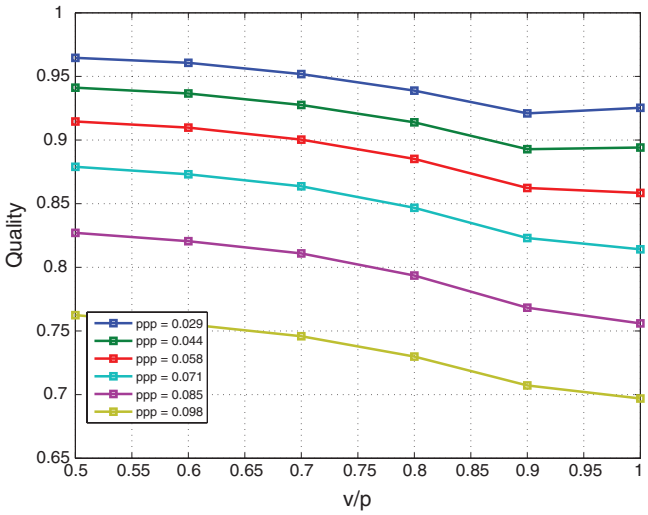

Figure 6. Quality criterion Q w.r.t. v/p. $\sigma_{psf}=0.6$ and $I/U=0.47$.

As mentioned in section 3.2, for tomo-SMART, the optimal value of v/p has been shown on the contrary to be slightly larger than 1 (as seen in figure 2 of Thomas *et al* (2014)). In particular, this study showed that refining the voxel grid, i.e., using a value of v/p lower than 1, is counter-productive as it leads to decreased quality criteria. Therefore, in order to use each method at its optimal performance in the comparative tests, we will choose $v/p=1$ for tomo-SMART.

3.5. Behavior w.r.t. N_{ppp}

The image particle density N_{ppp} is known to be one of the major factors that drives the reconstruction performance in tomo-PIV.

Figures 7 and 8 present a comparison of a classical tomographic reconstruction (tomo-SMART) and PVR (PVR-SMART) for $\sigma_{psf}=0.6$. This PSF size corresponds to a good balance between signal-to-noise ratio in the images and peak-locking in the displacement estimation. Figure 7 corresponds to a setting where only particles in the common field of view of each camera are illuminated particles (case $I/U=1$), whereas figure 8 corresponds to the more realistic setting where some

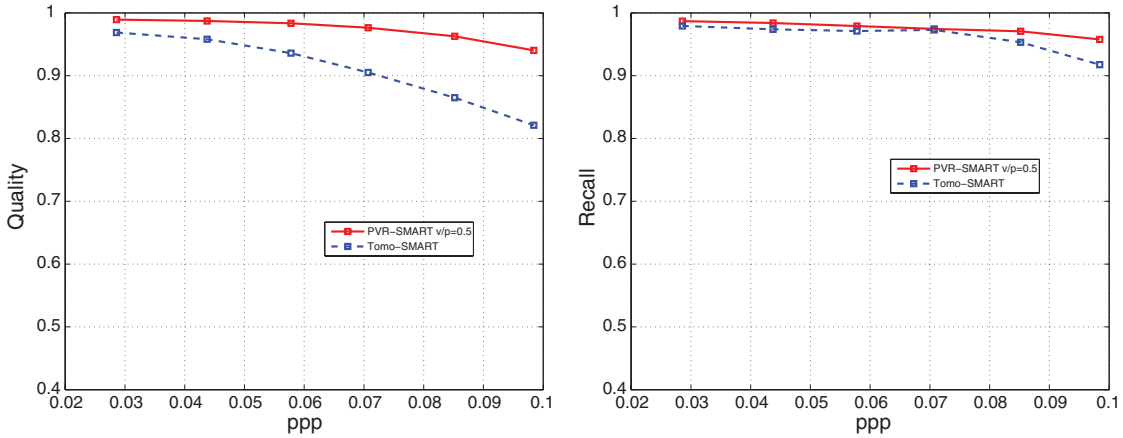

Figure 7. Comparison between conventional tomographic reconstruction and the proposed PVR approach, using the SMART algorithm, $\sigma_{psf}=0.6$, for varying N_{ppp}. $I/U=1$. Left: Q criterion. Right: fraction of detected true particles. Note that in all parts of this section, each method is operated at its optimal v/p value, i.e., $v/p=0.5$ for PVR-SMART and $v/p=1$ for tomo-SMART.

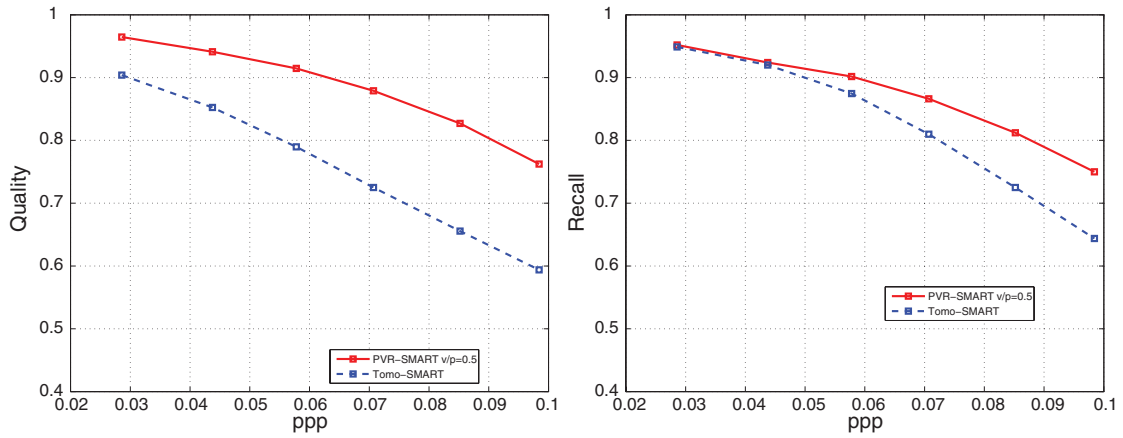

Figure 8. Comparison between conventional tomographic reconstruction and the proposed PVR approach, using the SMART algorithm, $\sigma_{psf}=0.6$, for varying N_{ppp}. $I/U=0.47$. Left: Q criterion. Right: fraction of detected true particles.

illuminated particles are seen by at least one camera but not by all (case $I/U=0.47$).

First, one observes in both figures 7 and 8 the expected decrease of performance for Q and Recall as N_{ppp} grows, which corresponds to the increasing ambiguity in image data. The comparison of figures 7 and 8 also shows the sensitivity of performances to the I/U factor. The level of reconstruction performance (Q and Recall) drops consistently with lower I/U. The effect of lowering I/U is most seen at the highest N_{ppp}, causing tomo-SMART to cross the 0.75 Q-factor level at $N_{ppp}=0.065$. Overall, the performance of PVR-SMART is systematically higher than that of tomo-SMART, and the advantage of PVR-SMART over tomo-SMART grows with increasing N_{ppp} and with decreasing I/U. In particular, in the realistic case where I/U is less than unity, the Q-factor obtained with PVR-SMART remains above 0.75 for all values of N_{ppp} considered.

3.6. Behavior w.r.t. σ_{psf}

PVR tends to produce spiky results whatever the size of the PSF, thus a better robustness than tomo-SMART to the change of shape and size of PSF is expected. The goal of this section is to investigate this prediction: image sets are synthesized for $N_{ppp}=0.07$ and different σ_{psf}, then PVR-SMART is run on each set using the value of σ_{psf} used during synthesis, while tomo-SMART is run in standard conditions as described above. Figures 9 and 10 compare the performance of both approaches on these data. Note that, as explained in section 3.3, computation of the quality factor Q is done by considering a ground truth made of Gaussian blobs defined by σ_{psf}. Thus in figures 9 (left) and 10 (left), as well as in figure 11 (left), each value of σ_{psf} corresponds to a different ground truth.

A quick look at figures 9 and 10 shows a global decrease of performance as σ_{psf} grows. This is a global impact of the particle image signal-to-noise ratio: indeed, the particle intensity is kept constant while the PSF spreads over more pixels as σ_{psf} grows, thus the peak intensity decreases, whereas noise remains constant. Another noticeable trend, visible in the Recall, is that the fraction of ghost particles also grows with σ_{psf}, due to the increase in particle image area (Elsinga *et al* 2011). As mentioned above, the performance indices drop significantly when one compares $I/U=1$, figure 9, and a lower $I/U=0.47$, figure 10. In particular,

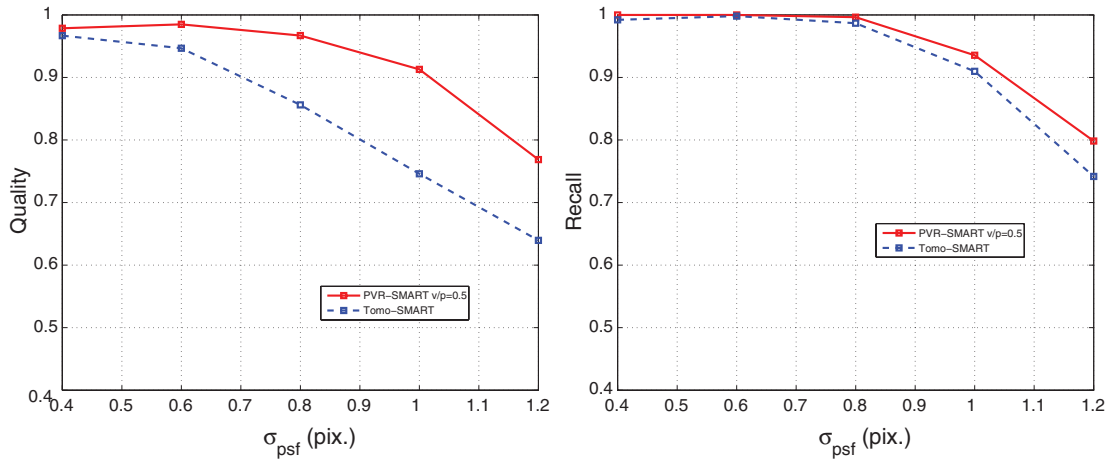

Figure 9. Comparison between conventional tomographic reconstruction and the proposed PVR approach, using the SMART algorithm, $I/U=1$, $N_{ppp}=0.07$, for varying σ_{psf}. Left: Q criterion. Right: fraction of detected true particles, or Recall.

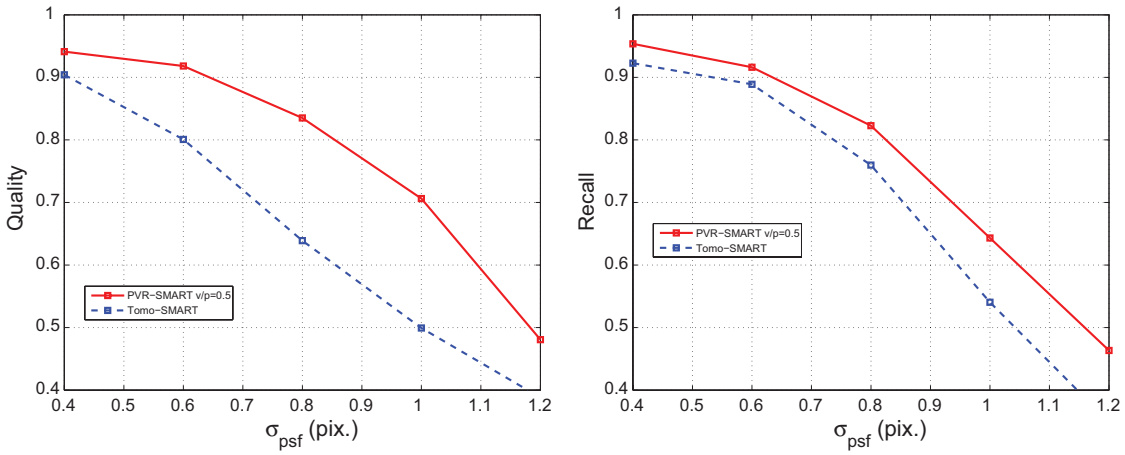

Figure 10. Comparison between conventional tomographic reconstruction and the proposed PVR approach, using the SMART algorithm, $I/U=0.47$, $N_{ppp}=0.07$, for varying σ_{psf}. Left: Q criterion. Right: fraction of detected true particles, or Recall.

Recall remains nearly optimal until $\sigma_{\text{psf}}=0.8$ at $I/U=1$, but drops more rapidly at $I/U=0.47$. Q for PVR-SMART has also a better robustness to the increase of σ_{psf} at $I/U=1$ than at $I/U=0.47$.

All performance metrics are in favor of PVR-SMART in the whole range of variation of σ_{psf} and the advantage of PVR-SMART is even larger for the more difficult configuration $I/U=0.47$. Thus PVR-SMART is expected to work consistently better in the presence of spatially varying PSF, for instance if the illuminated volume is larger than the focus zone of the cameras.

3.7. Robustness w.r.t. inaccurate PSF knowledge

In practice, in order to achieve these reconstruction estimation gains in situations of defocus, PVR-SMART needs PSF inputs, which result from an adapted calibration procedure. Depending on the context, a family of models can be fitted to experimental data, as explained in section 2.1. This means that situations may occur where PVR-SMART will use an approximate PSF model, for instance because of residual errors in the calibration process. We thus propose investigating the robustness of PVR-SMART to such imperfect knowledge by conducting experiments where the true PSF is given by (8) with $\sigma_{\text{psf}}=0.6$, while the value of σ_{psf} used for the reconstruction varies between 0.4 and 0.9.

In figure 11, tomo-SMART has constant behavior since σ_{psf} is not a parameter of the method. One observes that PVR-SMART is fairly tolerant to inaccurate knowledge of σ_{psf}. In particular, Q obtained with PVR-SMART remains above that of tomo-SMART for $0.40\leqslant\sigma_{\text{psf}}\leqslant0.81$, and is lower for larger values. When considering Recall, the domain of valid σ_{psf} reconstruction parameters ranges from 0.48 to 0.85. In both cases, PVR-SMART remains thus robust to deviations from the true PSF of up to 20%.

4. PVR for PIV velocity estimation

We now turn to an assessment of the efficiency of representation (6) for 3D PIV using correlation. We first specify the parameters used and the quantities of interest considered for this evaluation. Then we compute and analyze the relative performances of PVR-SMART and tomo-SMART in several

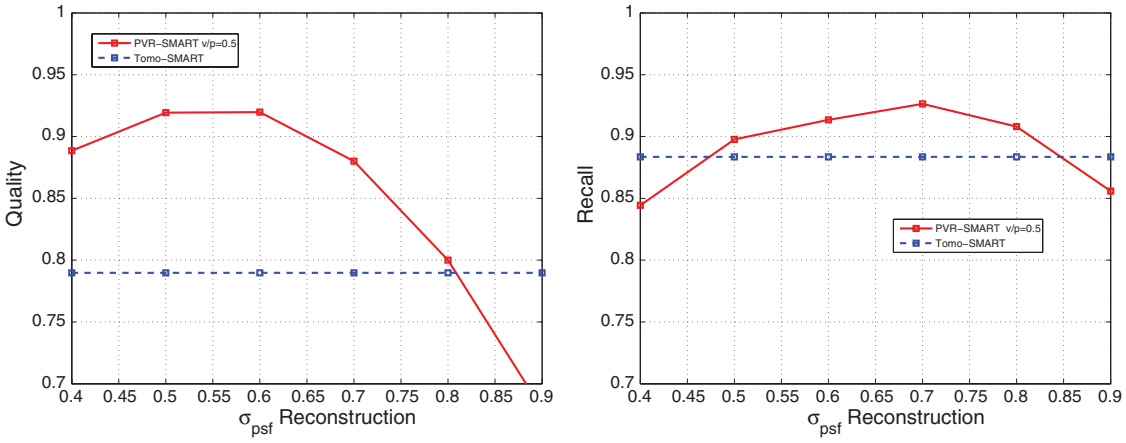

Figure 11. Robustness of PVR-SMART to inaccurate knowledge of the image PSF σ_{psf}. The different metrics are drawn as a function of the σ_{psf} used in PVR-SMART, whereas the image σ_{psf} equals 0.6. $N_{ppp}=0.07$, $I/U=0.47$. The level of performance of tomo-SMART is recalled in the blue solid line. Left: Q criterion. Right: fraction of detected true particles, or Recall.

experimental conditions, obtained by varying the two parameters N_{ppp} and σ_{psf} as in the previous section.

4.1. Ground truth velocity field

The displacement field considered is a vortex ring, similar to that considered by Elsinga *et al* (2006), whose main section lies in the $z=0$ plane. The radius of the ring is equal to 197 voxels and the maximum displacement is equal to 2.94 voxels (in $v/p=1$ unit). Figure 12 shows the corresponding vector field, together with the $\omega=0.05$ vox/vox vorticity contour (depicted in red) of the vortex ring.

4.2. Displacement estimation

In order to maintain realistic processing times, 3D PIV evaluation is chosen to be performed at $v/p=1$ voxel size. Indeed, the finer $v/p=0.5$ choice would have required 8 times more memory and flops. Correlation can thus be performed directly on the output of tomo-SMART, while that of PVR-SMART has to be sampled from the $v/p=0.5$ to the $v/p=1$ discretization grid. This transfer must include an anti-aliasing filter in order to preserve the $v/p=0.5$ information of PVR. We therefore choose the post-processing of PVR-SMART (as outlined in the flow chart of figure 2) using the two following steps: first, the $v/p=0.5$ voxel volume is filtered using a 3D Gaussian kernel with standard deviation σ_{blob}, then the result is down-sampled using a factor of two in each direction. In practice, it is known from plane PIV that a favorable PSF total width for accurate processing is around 2 × 2 to 3 × 3 pixels. Therefore, in the following, we will choose σ_{blob} equal to 0.6, this value being expressed in $v/p=1$ voxels. The sensitivity of measurement quality to this choice will be assessed in more detail at the end of this section.

Displacement estimation from both tomo-SMART and the post-processed PVR-SMART volumes is then performed with FOLKI3D, an extension to 3D PIV of the iterative

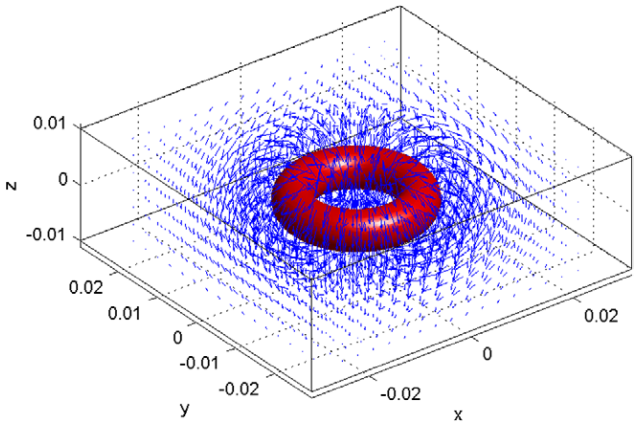

Figure 12. Vector field of the vortex ring used in the synthetic tests. The red contour corresponds to $\omega=0.05$ vox/vox.

image deformation algorithm introduced by Champagnat *et al* (2011). Cross-correlation is maximized using an iterative gradient-based approach, in the spirit of Lucas–Kanade methods. The algorithm has a highly parallel structure and is implemented on a graphics processing unit (GPU). Similar to the 2D version, the main parameter of FOLKI3D is the size of the interrogation volume, which determines the spatial resolution of the result. This parameter has been set here to 39 × 39 × 39 voxels. During the iterative process, volume deformation is achieved using a cubic B-spline interpolation.

Displacement fields obtained with FOLKI3D are then assessed using, firstly, the averaged norm of error between estimated and ground truth displacement, defined as

$$VE_{gt} = \frac{1}{K}\sum_{k=1}^{K} \|\hat{v}(X_k) - v^*(X_k)\|; \qquad (11)$$

where $\hat{\boldsymbol{v}}(\boldsymbol{X}_k)$ is the value of displacement estimated at grid node $\boldsymbol{X}_k$, $\boldsymbol{v}^*(\boldsymbol{X}_k)$ is the ground truth displacement at $\boldsymbol{X}_k$ and the sum is performed on all the displacement vectors retained

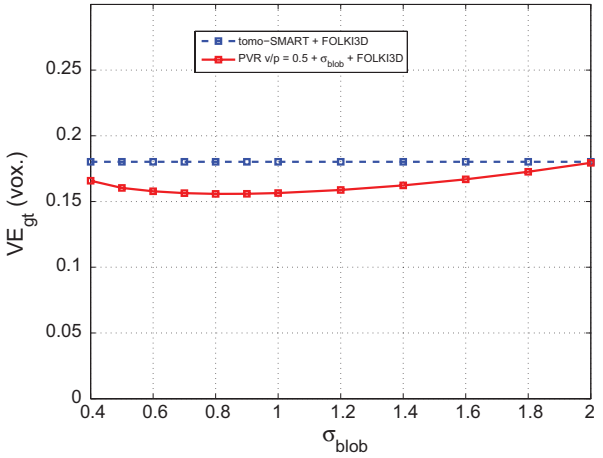

Figure 13. Sensitivity of displacement error w.r.t. the post-processing Gaussian filter size σ_{blob}. Images correspond to $\sigma_{\text{psf}}=0.6$, $N_{ppp}=0.07$. $I/U=0.47$. The displacement error for tomo-SMART is drawn as a reference.

after the estimation. We also found it interesting to complement this index with a metric that reflects the error w.r.t. an estimated displacement using a perfectly reconstructed volume. We denote this quantity

$$VE_{\text{blob}} = \frac{1}{K}\sum_{k=1}^{K} \|\hat{v}(X_k) - v^{\circ}(X_k)\|; \qquad (12)$$

where $\boldsymbol{v}^{\circ}$ is the displacement field obtained from the 'ground truth volumes', which are built by expanding locally the point particles to a 3D Gaussian blob, as described in section 3.3. This index was proposed by Schanz *et al* (2013), who considered that correlation of a perfectly reconstructed volume is a more realistic goal for displacement estimation. We observed that this index is more discriminating than the previous one. However, it does not quantify the overall accuracy of the displacement measurement, and thus both metrics are informative. All displacement errors are expressed in $v/p=1$ voxel units, as this is the discretization choice for correlation.

As a first assessment, we proposed to investigate whether the choice for the value of σ_{blob} used in the post-processing of PVR-SMART might have an impact on the quality of the estimation. To do so, we performed a basic PVR-SMART $v/p=0.5$ reconstruction from images generated with $N_{ppp}=0.07$ and $\sigma_{\text{psf}}=0.6$. We then applied the scale transfer down to $v/p=1$ using values of σ_{blob} varying between 0.4 and 2. Finally, we processed the obtained volumes with FOLKI3D and computed the displacement error. Volumes obtained from tomo-SMART were also processed with FOLKI3D and their error computed, to serve as a reference. As figure 13 shows, the choice of σ_{blob} is indeed a very mild choice, as the displacement error varies only slightly within the range considered. In particular, the value $\sigma_{\text{blob}}=0.6$, which we decided to choose in practice, is close to the broad minimum observed at around $\sigma_{\text{blob}}=0.8$. As in the following, the volumes obtained with PVR-SMART will be systematically post-processed with $\sigma_{\text{blob}}=0.6$, so we will omit this precision for conciseness, and simply refer to them as the PVR-SMART volumes (or PVR-SMART).

4.3. Behavior w.r.t. N_{ppp}

Figures 14 and 15 present a comparison of displacement errors obtained with tomo-SMART and PVR-SMART, using the processing and evaluation chain described in the previous section, for images generated with $\sigma_{\text{psf}}=0.6$. Figure 14 corresponds to a setting where only particles in the common field of view of each camera are illuminated (case $I/U=1$), whereas figure 15 corresponds to the more realistic setting where some illuminated particles are seen by at least one camera but not by all (case $I/U=0.47$).

Plots of VE_{gt} in the left parts of figures 14 and 15 are a good illustration of the fundamental trade-off of tomo-PIV: N_{ppv} grows with N_{ppp}, and should all the particles be perfectly reconstructed, one would observe a continuous decrease of displacement error (as in the curves of the 'true particles'). In practice, though, ambiguity also grows in the form of ghost particles, which perturb 3D correlation and which take over so that the error grows. In this respect, PVR-SMART shows better robustness than tomo-SMART, with an error VE_{gt} almost constant for $N_{ppp}>0.07$ in figures 14 and 15.

As in the case of reconstruction quality, the comparison of figures 14 and 15 also shows the sensitivity of performances to the I/U factor. Figures 14 and 15 show that PVR-SMART leads to significantly lower displacement errors than tomo-SMART for N_{ppp} higher than 0.06. The gain brought by PVR-SMART increases consistently with N_{ppp}, and is more important for the realistic situation of $I/U=0.47$, shown in figure 15.

4.4. Behavior w.r.t. σ_{psf}

A first account of the better behavior of PVR to the change of shape and size of the PSF was formerly given in section 3.6. This section investigates further this observation with displacement performance measures: different image sets are synthesized with $N_{ppp}=0.07$ and different σ_{psf}, then both algorithms are run on each set. For PVR-SMART, the value of σ_{psf} chosen for image synthesis is used in the reconstruction.

Figures 16 and 17 compare tomo-SMART and PVR-SMART on these data: all performance metrics are in favor of PVR-SMART in the range of variation of σ_{psf}. In particular, the difference in displacement error VE_{blob} stays approximately constant until $\sigma_{\text{psf}}=0.6$, and then gradually grows, reaching a difference of 0.15–0.18 voxel at $\sigma_{\text{psf}}=1.2$, depending on the value of I/U. The left sides of figures 16 and 17 show a global decrease of performance as σ_{psf} grows. As noted previously in section 3.6, this is a consequence of the decrease of particle image signal-to-noise ratio and of the increase of ghosts as σ_{psf} grows. Besides, as mentioned above, the performance indices again drop when one compares $I/U=1$, figure 16, and a lower $I/U=0.47$, figure 17.

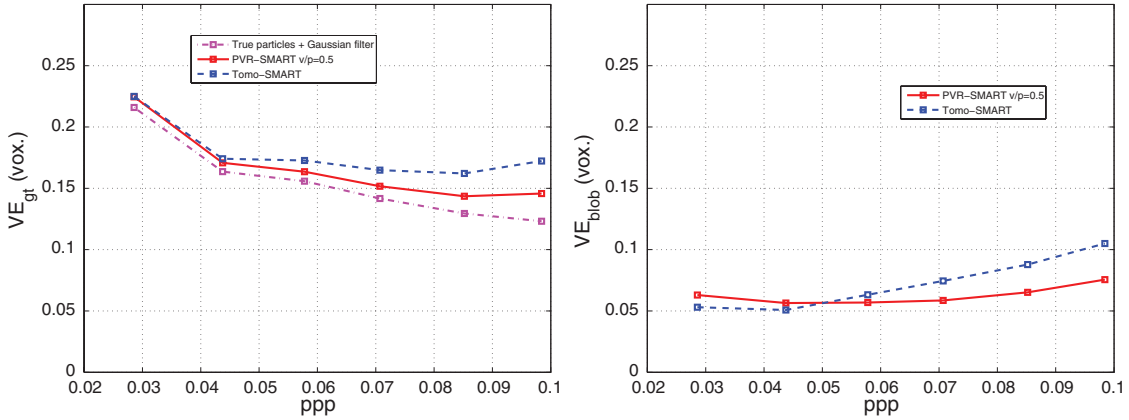

Figure 14. Comparison between conventional tomographic reconstruction and the proposed PVR approach, using the SMART algorithm, $\sigma_{\text{psf}}=0.6$, for varying N_{ppp}. $I/U=1$. Left: displacement error w.r.t. ground truth $\boldsymbol{v}^*$. Right: displacement error w.r.t. $\boldsymbol{v}^\circ$.

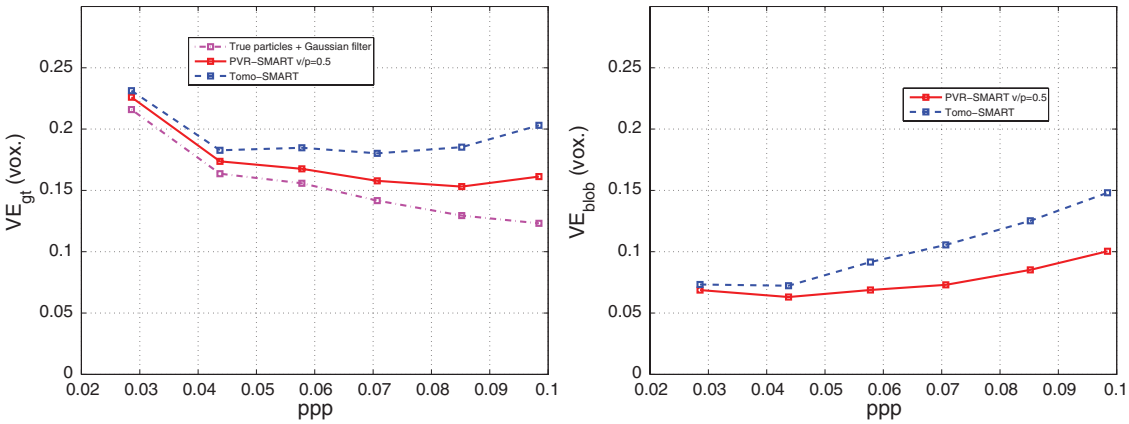

Figure 15. Comparison between conventional tomographic reconstruction and the proposed PVR approach, using the SMART algorithm, $\sigma_{\text{psf}}=0.6$, for varying N_{ppp}. $I/U=0.47$. Left: displacement error w.r.t. ground truth $\boldsymbol{v}^*$. Right: displacement error w.r.t. $\boldsymbol{v}^\circ$.

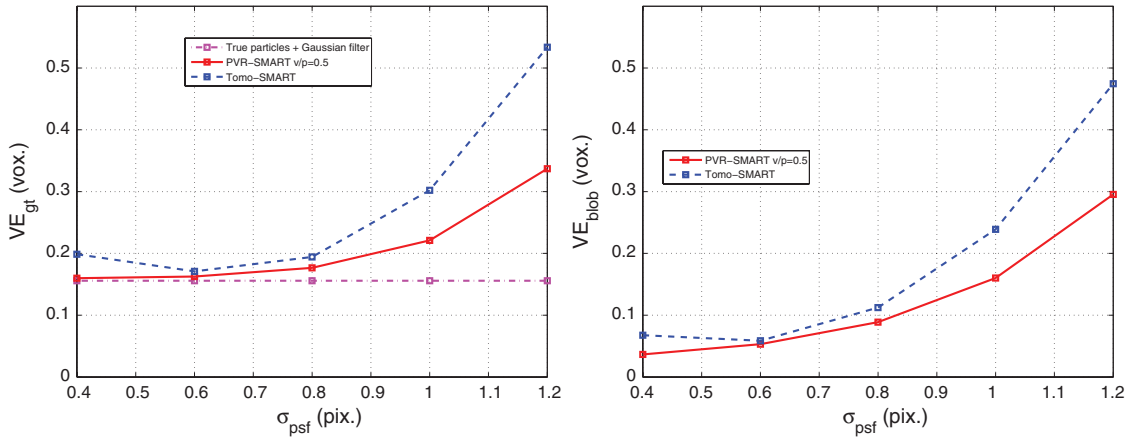

Figure 16. Comparison between conventional tomographic reconstruction and the proposed PVR approach, using the SMART algorithm, $I/U=1$, $N_{ppp}=0.07$, for varying σ_{psf}. Left: displacement error w.r.t. ground truth $\boldsymbol{v}^*$. Right: displacement error w.r.t. $\boldsymbol{v}^\circ$.

According to these experiments, PVR-SMART is thus expected to work consistently better in the case of spatially varying PSF, for instance that due to defocussing.

4.5. Robustness w.r.t. inaccurate PSF knowledge

In the same spirit as in section 3.7, we consider the case where only an imperfect PSF calibration was available. We investigate the robustness of PVR-SMART to this imperfect knowledge by conducting experiments where the true PSF is given by (8) with $\sigma_{\text{psf}}=0.6$, while σ_{psf} used for reconstruction varies between 0.4 and 0.9.

In figure 18, tomo-SMART has constant behavior since σ_{psf} is not a parameter for the method. One observes that the domain of validity of PVR-SMART ranges from 0.40 to 0.70 for VE_{gt} and from 0.40 to 0.67 for VE_{blob}. The latter results

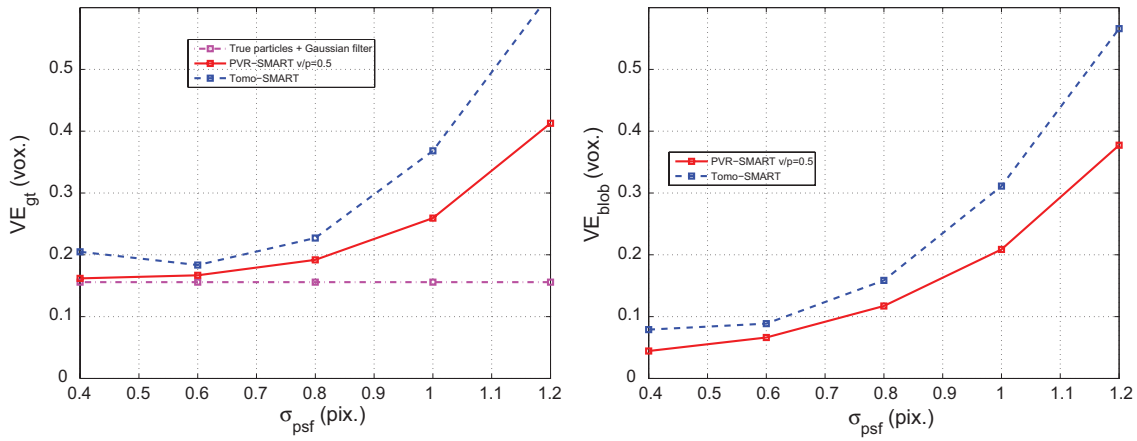

Figure 17. Comparison between conventional tomographic reconstruction and the proposed PVR approach, using the SMART algorithm, $I/U=0.47$, $N_{ppp}=0.07$, for varying σ_{psf}. Left: displacement error w.r.t. ground truth $\boldsymbol{v}^*$. Right: displacement error w.r.t. $\boldsymbol{v}^\circ$.

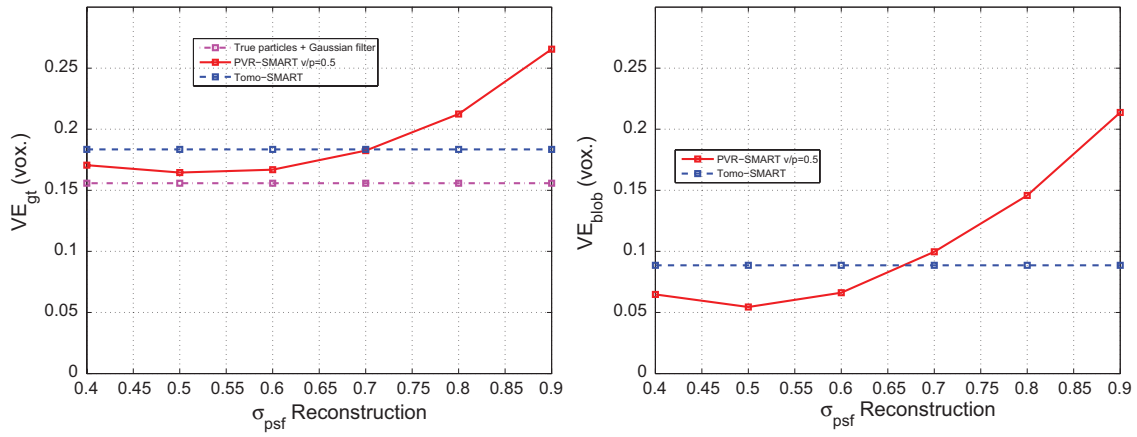

Figure 18. Robustness of PVR-SMART to inaccurate knowledge of the image PSF σ_{psf}. The displacement error metrics are drawn as a function of the σ_{psf} used in PVR-SMART, whereas the image σ_{psf} equals 0.6. $N_{ppp}=0.07$, $I/U=0.47$. The level of performance of tomo-SMART, which does not depend on σ_{psf}, is recalled for reference. Left: displacement error w.r.t. ground truth $\boldsymbol{v}^*$. Right: displacement error w.r.t. $\boldsymbol{v}^\circ$.

and the quality factor of figure 11 indicate a better robustness to underestimation than to overestimation. Such behavior can be explained by the fact that it is easier to fit a large particle image with a smaller PSF than the converse. In the case of favorable SNR we are confident that a calibration procedure such as described in section 2.1 should meet the 10–15% accuracy required to achieve the expected gain. However, if experimental conditions during calibration cannot guarantee a sufficient SNR, a backup solution will then be to bias the estimated PSF diameter to a lower value.

5. Discussion and concluding remarks

This paper has dealt with the first step of tomo-PIV, volume reconstruction. We have presented an alternative approach to the classical tomographic reconstruction that seeks to recover nearly single voxel particles rather than blobs of extended size, an approach referred to as PVR. The baseline of our approach is a particle-based representation of image data. The image model is discretized in order to yield a rigorous representation of image data in terms of voxelized particle intensity and a weight matrix built with PSF samples. As such an approach requires only a few voxels to explain the image appearance, it favors much more sparse reconstructed volumes than classic tomo-PIV.

PVR underlies a sparse volumic representation of point particles, which lives halfway between infinitely small particles, and larger two to three voxel diameter blobs usually used in tomo-PIV. From that representation, it is possible to go further and sharpen the particle to its essential features in the idea of performing PTV (intensity and 3D position, by using subvoxel refinement) or to smooth it to the 2 voxel diameter blob, which is the gold standard of correlation for PIV.

The degrees of freedom of this representation were analyzed, in particular the voxel-to-pixel ratio. It has been shown that the model converges to true particle position as the voxel-to-pixel ratio decreases to zero. A voxel-to-pixel ratio equal to 0.5 has been shown to be a good trade-off between accuracy and numerical complexity. PVR-SMART has been shown to outperform tomo-SMART on a large domain of generating conditions and a variety of metrics on volume reconstruction

and displacement estimation, in particular in the case of seeding density greater than 0.06 ppp and of PSFs characterized by a standard deviation larger than 0.8 pixel. Robustness to inaccurate knowledge of the PSF size has also been checked. Tests showed that displacement estimation performance gains with PVR are systematically obtained whatever the value of the PSF in the case of underestimation, and they persist in the case of an overestimation of up to 10% of the PSF value.

As PVR directly builds the weight matrix from samples of the PSF, PSF calibration techniques as proposed by Reichenbach *et al* (1991), or more recently by Delbracio *et al* (2012) and Schanz *et al* (2013), can readily be used in practice to benefit from the obtained improvements.

More generally, PVR provides a principled approach for dealing with spatially varying PSF due to defocussing and astigmatism. It can be easily expanded in order to deal with non-conventional single lenses, single cameras (Cierpka *et al* 2011) and new optical devices such as plenoptic cameras (Thurow and Fahringer 2013).

To us, one of the most promising perspectives of this work is to use the proposed model with sparsity based reconstruction algorithms (Barbu *et al* 2011, Cornic *et al* 2013, Petra *et al* 2009), with the final aim of estimating the displacement by PTV. As demonstrated by Cornic *et al* (2013), in such a context, the PVR approach can lead to dramatic reductions of computational complexity while maintaining good detection rates. Since PVR is oriented to detection at the voxel scale, particle location refinement schemes will have to be developed in order to enable accurate tracking of the particles with time. Work is in progress along these lines.

References

Adrian R J and Westerweel J 2010 *Particle Image Velocimetry* (Cambridge: Cambridge University Presss)

Atkinson C and Soria J 2009 An efficient simultaneous reconstruction technique for tomographic particle image velocimetry *Exp. Fluids* **47** 553–68

Barbu I, Herzet C and Mémin E 2011 Sparse models and pursuit algorithms for PIV tomography *Forum on Volumic Reconstruction (Poitiers, France)*

Byrne C L 2008 *Applied Iterative Methods* (Wellesley: Peters)

Champagnat F, Cornic P, Cheminet A, Leclaire B and Le Besnerais G 2013 Tomographic PIV: particles versus blobs *Proc. PIV13 (Delft, The Netherlands)*

Champagnat F, Plyer A, Le Besnerais G, Leclaire B, Davoust S and Le Sant Y 2011 Fast and accurate PIV computation using highly parallel iterative correlation maximization *Exp. Fluids* **50** 1169–82

Cheminet A, Leclaire B, Champagnat F, Cornic P and Le Besnerais G 2013 On factors affecting the quality of tomographic reconstruction *Proc. PIV13 (Delft, The Netherlands)*

Cierpka C, Rossi M, Segura R and Kähler C J 2011 On the calibration of astigmatism particle tracking velocimetry for microflows *Meas. Sci. Technol.* **22** 015401

Cornic P, Champagnat F, Cheminet A, Leclaire B and Le Besnerais G 2013 Computationally efficient sparse algorithms for tomographic PIV reconstruction *Proc. PIV13 (Delft, The Netherlands)*

Delbracio M, Musé P, Almansa A and Morel J M 2012 The Non-parametric sub-pixel local point spread function estimation Is a well posed problem *Int J. Comput. Vis.* **96** 175–94

Elsinga G E, Scarano F, Wieneke B and van Oudheusden B W 2006 Tomographic particle image velocimetry *Exp. Fluids* **41** 933–47

Elsinga G E, Westerweel J, Scarano F and Novara M 2011 On the velocity of ghost particles and the bias errors in tomographic-PIV *Exp. Fluids* **50** 825–38

Hogbom J A 1974 Aperture synthesis with a non-regular distribution of interferometer baselines *Astron. Astrophys. Suppl.* **15** 417–26

Petra S and Schnörr C 2009 TomoPIV meets compressed sensing *Pure Math. Appl.* **20** 49–76

Reichenbach S E, Park S K and Narayanswamy R 1991 Characterizing digital image acquisition devices *Opt. Eng.* **30** 170–7

Schanz D, Gesemann S, Schröder A, Wieneke B and Novara M 2013 Non-uniform optical transfer functions in particle imaging: calibration and application to tomographic reconstruction *Meas. Sci. Technol.* **24** 024009

Thomas L, Tremblais B and David L 2014 Optimization of the volume reconstruction for classical tomo-PIV algorithms (MART, BIMART and SMART): synthetic and experimental studies *Meas. Sci. Technol.* **25** 035303

Thurow B S and Fahringer T 2013 Recent development of volumetric PIV with a plenoptic camera *Proc. PIV13 (Delft, The Netherlands)*

Trouvé P, Champagnat F, Sabater J, Le Besnerais G, Avignon T and Idier J 2013 Passive depth estimation using chromatic aberration and a depth from defocus approach *Appl. Opt.* **52** 7152–64

Wieneke B 2008 Volume self-calibration for 3d particle image velocimetry *Exp. Fluids* **45** 549–56

Wieneke B 2013 Iterative reconstruction of volumetric particle distribution *Meas. Sci. Technol.* **24** 024008

3.3 Conclusion

This chapter has provided a numerical assessment of a novel approach to tomographic particle image velocimetry which was shown to outperform classical reconstruction algorithm [Atkinson and Soria, 2009] in a variety of conditions.

The next logical step is to perform an experimental validation of this method. This is the subject of the last two chapters of this dissertation. Chapter 4 is dedicated to the assessment of our in-house displacement code in the context of tomographic noise. Since both reconstruction step and estimation step have been investigated, we can perform a full experimental validation in chapter 5 and chapter 6.

4 Accuracy assessment of FOLKI-3D for 3D-PIV

4.1 Introduction

Tomographic PIV offers a tremendous potential for the characterization of complex flows, as it enables the instantaneous measurement of three-dimensional velocity fields. In terms of accuracy, much effort has been devoted to characterizing the specific noise introduced by the reconstruction step which is specific to the 3D context and may have a significant impact on the final result. The second chapter of this dissertation was dedicated to the impact of experimental factors on the reconstruction accuracy and noise. The third chapter presented a new reconstruction model based on a particular paradigm and on the modeling of the optical system in the reconstruction. We showed through numerical analysis that this new reconstruction technique increases the reconstruction performances with respect to several experimental parameters. The focus of this chapter is placed on the second step of the 3D-PIV technique, namely the displacement estimation step.

This step can be seen as a simple extension to the third dimension of classical PIV correlation algorithms. However with this added dimension new questions and challenges come up. Many researchers have directed their work towards reducing the problem complexity (see, e.g., [Scarano, 2013]). Indeed, handling 3D volumes represents a huge amount of data, and thus potentially prohibitive processing times. This may also constrain algorithmic choices, as approaches which were proven successful and accurate in 2D-PIV may be prohibitive in 3D with the current computational capacities.

In this chapter, we now present a new approach for 3D cross-correlation consisting in a gradient-based iterative volume deformation method, in the Lucas-Kanade framework. It is the extension to 3D of the approach proposed in [Champagnat et al., 2011] and, due to its highly parallel structure, it is also implemented on GPU. Volume deformation may be performed with a simple, linear interpolation as in most algorithms, or, thanks to an efficient implementation, with a higher-order cubic B-Spline scheme, while maintaining reasonable processing times. Our purpose in this chapter is to characterize this algorithm with a particular emphasis on its response to specific 3D noise sources. Focus will also be placed on the possible gains arising from high-order interpolation in this context.

Thos chapter is structured as follows : First, we mention the principle of the displacement estimation method with an emphasis on the useful parameters and their influence. We then use synthetic tests to characterize the algorithm in terms of spatial resolution and to assess the impact of the interpolation scheme on bias and

rms errors in the subvoxel displacement estimation. Finally, we assess the algorithm robustness to noise, especially tomographic PIV noise, *i.e.* ghost particles, by using synthetic simulations of 3D-PIV experiments. The final assessment of this algorithm on experimental data will be the subject of chapter 6.

4.2 General principle

The present implementation is the extension to 3D of the FOLKI-PIV algorithm described in [Champagnat et al., 2011]. In this section we present the main characteristics only and refer the reader to their paper for more details.

4.2.1 Iterative scheme

Considering a discretized physical volume, let k denote the index of a voxel in the grid. As in traditional correlation-based PIV, our objective is to determine the displacement $u(k)$ of a particle pattern contained in the interrogation volume (IV), $V(k)$ centered around voxel k. The mathematical objective differs however and belongs to the Lucas-Kanade paradigm (see [Baker and Matthews, 2004] for a review), as it amounts to minimizing the sum of squared differences (SSD).

$$u(k) = \mathbf{arg\ min} \sum_m v(m-k) \left[E_1\left(m - \frac{u(k)}{2}\right) - E_2\left(m + \frac{u(k)}{2}\right)\right]^2 \tag{4.2.1}$$

Here E_1 and E_2 respectively denote the volume intensity distributions reconstructed at the illumination instants t and $t + dt$, and function v is the support of interrogation volume $V(k)$. Note that this criterion is symmetrical, i.e. it leads to a second order estimate of $u(k)$ in time, at $t + dt/2$. In practice, we use either a top-hat cubic IV, parameterized by its radius R, or a Gaussian cubic IV, defined by two parameters: the radius R and its standard deviation σ.

The minimization of equation (4.2.1) is performed using Gauss-Newton iterations. Supposing that a predictor $u_0(k)$ is available, one then replaces $u(k)$ by $u(k)-u_0(m)+u_0(m)$, so that

$$u(k) = \mathbf{arg\ min} \sum_m v(m-k) \left[E_1^{-u_0/2}\left(m - \frac{u(k)-u_0(m)}{2}\right) - E_2^{u_0/2}\left(m + \frac{u(k)-u_0(m)}{2}\right)\right]^2 \tag{4.2.2}$$

Here, one has introduced the deformed (or warped) intensity distributions

$$\left.\begin{aligned} E_1^{-u_0/2} &= E_1\left(m - \frac{u_0(m)}{2}\right) \\ E_2^{u_0/2} &= E_2\left(m + \frac{u_0(m)}{2}\right) \end{aligned}\right\} \tag{4.2.3}$$

The following step then consists in linearizing equation (4.2.2), assuming that the displacement increment to be found is weak, i.e. $u(k) - u_0(m) \approx 0$, so that

$$u(k) = \mathbf{arg\ min} \sum_m v(m-k) \left[E_1^{-u_0/2}(m) - E_2^{u_0/2}(m) - \frac{\nabla E_1^{-u_0/2}(m) + \nabla E_2^{u_0/2}(m)}{2}\left(u(k) - u_0(m)\right)\right]^2 \tag{4.2.4}$$

Finally, after some algebra, deriving the SSD in equation (4.2.3) leads to finding $u(k)$ as the solution of a 3×3 linear system

$$H(k)u(k) = c(k) \tag{4.2.5}$$

where matrix H and left-hand-side c involve the predictor u_0, the deformed volumes, and their gradients.

4.2.2 Processing flow-chart and control parameters

Similarly to the plane approach of FOLKI-PIV, the guess-value is obtained by implementing a multi-resolution Gaussian pyramid of intensity volumes. A pyramid contains J levels, including the raw intensity volume (level 0). Level $j+1$ is formed by applying a low-pass filter on level j, and then retaining one pixel out of a cube of $2 \times 2 \times 2$ voxels. Thus, volumes at level $j+1$ are eight times smaller than at level j, and displacements are divided by two in each direction. The number of levels J has then to be chosen according to the maximum displacement expected. Indeed, a condition for the Gauss-Newton iterations (equation (4.2.4)) to converge is that the predictor be close to the exact displacement. Considering enough levels will thus allow this convergence when choosing a zero displacement field as the predictor for level $J-1$. Gauss-Newton iterations are then run at this level until convergence. The final estimate is interpolated at level $J-2$ and serves as the first predictor for the Gauss-Newton iterations at this level. The process is then repeated until convergence is reached at level 0.

To ensure robustness with respect to variations in intensity in the volumes, a mean and standard deviation normalization is applied at each pyramid level prior to the Gauss-Newton iterations (see [Champagnat et al., 2011] for more details). Also, similarly to FOLKI-PIV, FOLKI-3D produces a dense output (one displacement per voxel) with no computational overload, while its resolution remains tied to the IV size (see the tests below). To sum up, FOLKI-3D is tuned by three main parameters:

1. The number J of pyramid levels which depends on the maximum displacement expected in the volumes.

2. The number N of Gauss-Newton iterations performed at each level. Usually, 3 to 10 iterations are enough to reach convergence, the exact number usually depending on the signal-to-noise ratio of the volumes.

3. The size of the interrogation volume which controls the spatial resolution of the result, as in traditional cross-correlation PIV and will be shown below.

4.2.3 Comments

One of the PIV algorithms currently acknowledged in the literature as a state-of-the art is an iterative image or volume deformation method (IDM), whether the estimation is done on planar or volumic data (see, for instance, [Scarano, 2002] and [Scarano, 2013]). In a 3D framework, supposing that a predictor displacement field is available, the 3D intensity fields are first deformed with this displacement value, requiring a subvoxel interpolation scheme. Then the subvoxel increment allowing to maximize the cross-correlation from these deformed volumes is determined by using a three-point Gaussian fit. This results in a new estimate of the displacement. As pointed out by several authors in the literature, it is necessary to smooth this displacement field in order to prevent a divergence of the iterative scheme; choosing an adapted filter kernel may also enable to improve the algorithm transfer function, as studied in detail by [Schrijer and Scarano, 2008]. Once this filtering is done, the data may be used again for deformation, and so forth.

Though FOLKI-3D belongs to a Lucas-Kanade paradigm, it also belongs to the IDM family with similarities to the above described flow-chart. Firstly, the global objective, formulated as the minimization of a Sum of Squared Differences (equation (4.2.1)),

becomes identical to maximizing a Cross-Correlation score as soon as the mean and standard deviation pre-processing is performed. When transposed in an iterative context, FOLKI-3D also uses volume deformation at the subvoxel level before each iteration, as shown by equations 4.2.2 and 4.2.3. However, the following steps differ from traditional IDM algorithms: indeed, instead of computing the whole cross-correlation map on a given domain by FFT or direct correlation, and then refining the maximum by a Gaussian fit, FOLKI-3D determines the minimum of the SSD by iteratively using a gradient method, directly at a subvoxel level. Also, as described in [Leclaire et al., 2011], the displacement increment is defined in a slightly different way as in traditional IDM algorithms, which guarantees stability with the number of iterations and renders unnecessary the intermediate filtering step of the displacement before deformation.

The next section will present the response of FOLKI-3D to traditional tests used in the literature, which will enable us to further situate it among the IDM framework.

4.3 Spatial resolution and Interpolation schemes

In this section, we introduce a first series of synthetic tests to assess the performances of FOLKI-3D. This is done on ideal 3D blob-like particle distributions (i.e. supposing ideal tomographic reconstructions), in order to determine the spatial resolution of the algorithm and the influence of the interpolator choice on the bias and random errors.

4.3.1 Spatial wavelength response

Following [Scarano and Riethmuller, 2000] the frequency response of a PIV algorithm can be evaluated using a sinusoidal shear displacement test :

$$(U, V, W) = \left(A \ sin(2\pi \frac{Y}{\lambda}), 0, 0 \right) \tag{4.3.1}$$

where X,Y and Z are the 3D coordinates and U, V, W the associated displacement components. For this test, 3D ideal particles randomly distributed in the correlation volume are generated by locally expanding a physical point particle to a 3D Gaussian blob with $\sigma = 0.6$ voxel (thus a diameter of 2.4 voxel) in order to have a volumetric distribution well adapted to the correlation algorithm. The particle density is high compared to real tomo PIV experiments densities in order to have at least 20 to 30 particles per IV for the smaller IV size. We then use this displacement field equation (4.3.1) with amplitude A set to 2 voxels and the wavelength λ varied from 20 to 400 voxels. FOLKI-3D interrogation volume (IV) size is varied from 11 to 63 voxels. As the displacement is rather close to zero, we use $J = 1$ level and $N = 3$ iterations. B-Spline interpolation scheme was used for the volume deformation step. For each volume corresponding to a given (λ, R) couple, we compute the ratio between the estimated amplitude of the sinusoid $A_{\text{FOLKI-3D}}$ and the ground truth value $A = 2$ voxels.

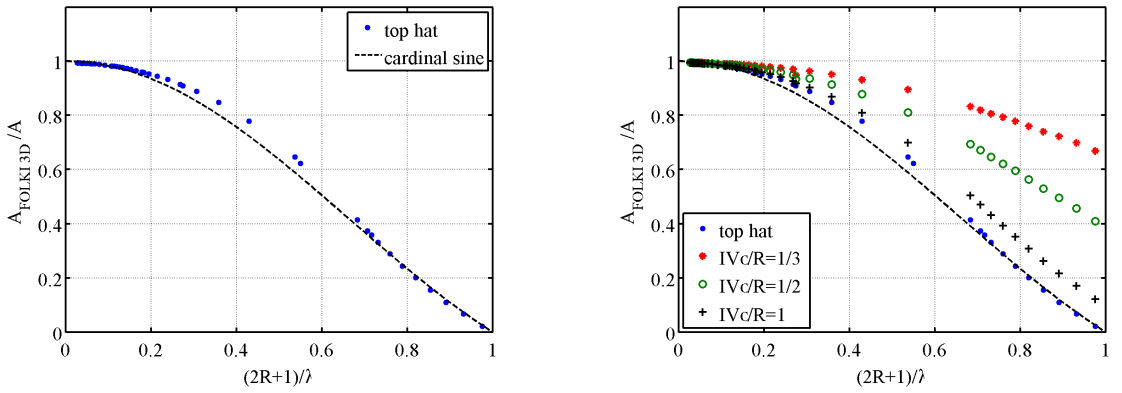

(a) Saptial wavelength response for top hat IV

(b) Saptial wavelength response for Gaussian IV

Figure 4.3.1: Amplitude ratio $A_{\text{FOLKI-3D}}/A$ as a function of the normalized volume interrogation size for (left) top hat IVs and (right) Gaussian IVs. The dashed line is the response of a $[-R, R]$ sliding average (cardinal sine function).

The evolution of this ratio as a function of the normalized IV size $2R/\lambda$ is plotted in figure 4.3.1. In figure 4.3.1 (left), we used a cubic top-hat interrogation volume and in figure 4.3.1 (right) we used Gaussian IVs with a given σ/R ratio. In figure 4.3.1 (left), all values of $A_{\text{FOLKI-3D}}/A$ nearly collapse on a cardinal sine curve which is the frequency response to a $[-R, R]$ sliding average, as usual in correlation based methods [Scarano and Riethmuller, 2000]. In particular, this means that the spatial resolution of FOLKI-3D is

also directly linked to the size of the IV. The fact that a dense output (one vector per voxel) is obtained is an algorithmic specificity, and retaining all voxels in the final results corresponds to over-sampling.

4.3.2 Interpolation schemes and Peak-locking

It is known from several studies on planar PIV that the choice of the interpolation scheme used to deform the images may have an important effect on the displacement precision at a subpixel level. This has been studied in detail by [Astarita and Cardone, 2005], in particular. In their work, an important number of schemes is introduced, and the accuracy is logically found to be inversely linked to the computational cost of the interpolator, i.e. the cheaper the interpolator (e.g., linear), the less precise the result. As the performance of the algorithms and hardware has evolved rapidly, some of the advanced interpolation methods (such as with cubic B-Splines, or even more precise using a cardinal sine basis) are now commonly used in planar PIV. In the 3D context however, domain sizes are much larger so that the question of using more advanced interpolation schemes than the linear one may come with a dramatic increase in the computational cost. Thus, as mentioned by [Scarano, 2013], linear interpolation remains the standard.

Building on optimizations began during works on planar PIV [Champagnat et al., 2011]. [Champagnat and Le Sant, 2013] recently proposed an implementation for cubic B-Spline interpolation which is particularly optimized for GPU, and may be used in FOLKI-3D. In practice, this optimization guarantees that the increase in computational time compared to linear interpolation remains reasonable, with a significative increase in accuracy. As in section , we consider perfect volumic blob-like synthetic distributions. In figure 4.3.2, we monitor the bias and rms error for increasing values of a unidimensional displacement $(U, 0, 0)$, with U ranging from 0 to 2 voxels, and the standard deviation of the Gaussian blob set to $\sigma = 0.625$ (2.5 voxels wide blob). As shown in [Astarita and Cardone, 2005], for symmetric IDM algorithms such as FOLKI-3D, this range is sufficient to explore, as the response is periodic. Note that we chose the seeding density so as to have the same number of tracers in an IV as the number of particles in the IWs chosen by [Astarita and Cardone, 2005] (ie of the order of 20).

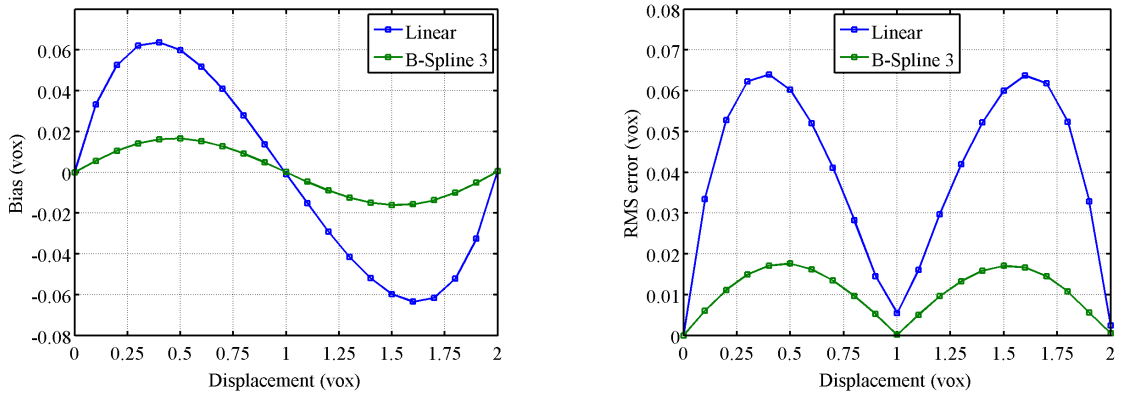

(a) Bias error **(b)** rms error

Figure 4.3.2: Bias (a) and rms error (b) for both linear and cubic B-Spline interpolators, for increasing values of the unidirectional displacement (U,0,0).

When using a cubic B-Spline interpolation, the maximum bias error for this particle size is roughly equal to 0.017 voxel, compared to 0.064 for the linear scheme (gain of a factor larger than three). This gain is similar in terms of maximum rms error, with respectively 0.018 and 0.064 voxel. These curves and their maxima are in excellent agreement with the results of [Astarita and Cardone, 2005], confirming the similarity of FOLKI-3D with standard IDM algorithms. The slight differences observed may stem from the fact that we consider a monodisperse seeding, whereas [Astarita and Cardone, 2005] allowed a variation of the particle diameter in their images, and also from the difference in the final subvoxel/pixel estimation (i.e. minimization vs. Gaussian fit, see section 2.3)

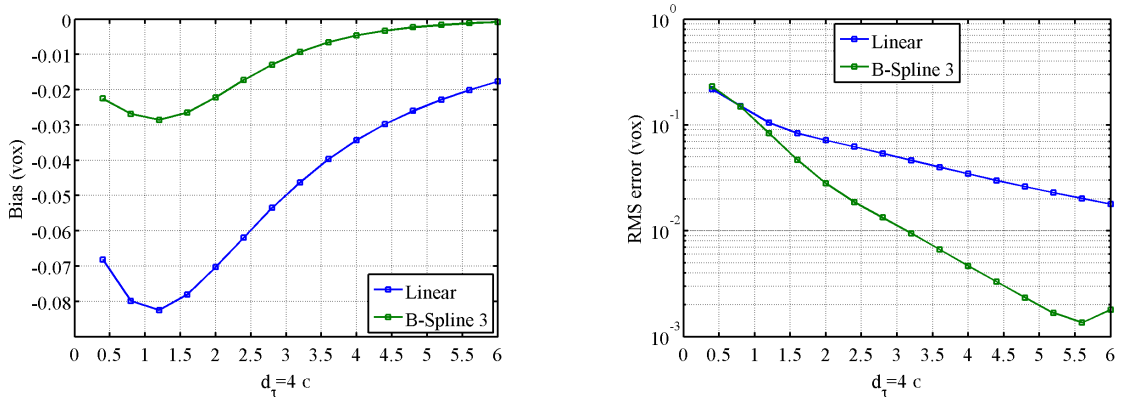

(a) Bias error **(b)** rms error

Figure 4.3.3: Bias (a) and rms error (b) for both linear and cubic B-Spline interpolators, as a function of the 3D particle diameter d_τ, for a displacement (U,V,W) = (1.5,0,0) voxel.

As the shape and size of the particles produced by the tomographic reconstruction depend on the size of their image on the camera sensors, but also on the geometrical arrangement, it is even more important than in plane PIV to assess the accuracy of the algorithm to different particle sizes. This is done in figure 4.3.3 where the plots represent the bias and rms errors corresponding to a uniform displacement (U,V,W) = (1.5,0,0) (for which the rms error is maximum, see figure 4.3.2), for varying values of the particle diameter $d_\tau = 4\sigma$. Here again, results are in very good agreement with those of[Astarita and Cardone, 2005], with a systematic reduction in bias and a quasi-systematic reduction in rms error for the B-Spline scheme. The gain in rms error increases with increasing particle diameter. However, compared to [Astarita and Cardone, 2005], the B-Spline scheme of FOLKI-3D is slightly less efficient for very small particles compared to the linear scheme. However, the minimum level of rms error reached with the B-Spline scheme is smaller. As the synthetic conditions should be close to identical between our study and that of [Astarita and Cardone, 2005] for this second test, these differences are most likely ascribed to the subpixel estimation approach.

4.4 Robustness versus tomographic reconstruction noise

We now turn to more realistic conditions, using the complete 3D-PIV setup and tomographic reconstructions. Our objective in this section is to assess the robustness of the algorithm to specific noise sources encountered in the 3D framework, i.e. to the influence of various effects linked to the presence of ghost particles.

Similar to traditional sources of noise in planar PIV, the ghost particles play a key role in the accuracy of the result, and in the choice of the experimental parameters (see for instance [Elsinga et al., 2006]). Indeed, the number of ghosts is known to increase with seeding density, whereas the accuracy of motion estimation increases with seeding density. Therefore, while increasing the rms error, they also play a key role in the spatial resolution of the result, as the choice of the IV size has to result from a trade-off between spatial resolution (small IV requiring a high seeding) and noise (which decreases when the IV size increases). Besides, as shown by [Elsinga et al., 2011] depending on the setup and displacement field, a proportion of ghosts may be coherent between the two laser pulses, thereby adding a bias to the result.

In the following, we will assess the response of FOLKI-3D to these sources of noise and bias, and, for some of them we will compare its response to state-of-the-art LaVision Davis 8.2 software. In Addition to the bias due to coherent ghosts, we will also consider the influence of viewing conditions, and, in that respect, assess the differences obtained for the two interpolation schemes of FOLKI-3D. These conditions may play a significant role; firstly, [Cheminet et al., 2013], [Cornic et al., 2013] (see chapter 2 for more details) recently showed that the ratio between the intersection and the union of the camera fields of view directly influences the proportion of ghosts, while it is also known that different directions result in different shapes of the reconstructed particles, as for instance summed up in [Scarano, 2013].

4.4.1 Tomographic synthetic setup

3D particle distributions reconstructed from PIV images are generated from a classical 3D-PIV setup. The synthetic setup is very similar to the one presented in chapter 2. Our simulations involve four cameras which are positioned on a single side of a laser volume. Their positions depend on the tests and will be addressed further down in this paper. A pinhole model is assumed for the cameras, without Scheimpflug adapter for simplicity, and calibration is supposed to be perfectly known and to obey a pinhole model. The pixel size is 10 μm with a fill factor of 100%.

The laser sheet is modeled as a 20 mm thick parallelepiped. Its intensity profile is assumed to be uniform. The reconstructed volume, also $20mm$ thick, is taken as the smallest parallelepiped including the illuminated volume seen by all the cameras. Thus it depends on the field of view and is given for each experiment. The voxel-to-pixel ratio is in this paper always set to one. We use 512×512 pixels cameras which lead to typical reconstruction sizes of the order of $600 \times 600 \times 200$ voxels. Unless otherwise specified, the cameras are positioned on a single side of the laser sheet at the vertices $(\frac{1}{2}, \frac{1}{2}, \frac{1}{\sqrt{2}})$ of a square of 1 meter side. They are positioned at 1 meter from the centre of the reconstructed volume located at $(0, 0, 0)$ and point at it. The focal length is 100 mm, thus the magnification factor M is equal to 0.1.

Tracers particles are uniformly distributed in the light sheet volume. The density is controlled by the particle per voxel count (ppv) and is set so that the particle density image (ppp) is equal to 0.056. Horizontal and vertical extension of the laser sheet are larger than the field of view covered by all the cameras. Thus all illuminated particles cannot be seen by all cameras, a fact that always occurs in real datasets and is however often overlooked in synthetic experiments ([Cheminet et al., 2013], [Cornic et al., 2013]). Unless otherwise specified, the illuminated particles lie in the union of the laser sheet and the cameras fields on view (Union) and the reconstruction process is done on the intersection of those volumes (Intersection). For simplicity sake, the scattered light is taken as uniform and we will consider a monodisperse seeding.

Considering P particles with intensity E_p located at point X_p in 3D-space, the intensity distribution in the image is given by :

$$I(x) = \sum_{p=1}^{P} E_p.h(\mathbf{x} - F(\mathbf{X}_p)) \tag{4.4.1}$$

where $\mathbf{x} = (x, y)$ denotes any location in the image plane, F is the geometric projection function in the image, and h the so-called Point Spread Function (PSF), which models the aperture limited diffraction and pixel integration. For the tests presented in this paper, we assume a Gaussian PSF with standard deviation σ_{PSF} set to 0.6, with a 100% fill factor. We assume an image dynamic range of 8 bit, and a Gaussian noise with mean=0 and standard deviation 2 is added to the images. Its amplitude is set at about 10% relative to the maximum particle intensity.

Tomographic reconstruction is then performed using an MLOS-SMART algorithm similar to that of [Atkinson and Soria, 2009], with 25 iterations and the relaxation parameter μ set to 1. This algorithm is called tomo-SMART in the rest of the thesis.

4.4.2 Robustness versus coherent ghost particles

4.4.2.1 Displacement field

[Elsinga et al., 2011] showed that under certain conditions displacement errors arise due to the coherent motion of ghost particles. This occurs when a given ghost particle is formed from the same set of actual particles and is found in both reconstructed volumes used in the 3D correlation analysis. Indeed, for a given set of particles, whenever the displacement normal to the viewing direction between two exposures is nearly equal to the particle image diameter, ghost particles are formed in both exposures and are coherent time-wise. Their displacement is approximately the average displacement of the particle set responsible for the ghost particle. This results in an underestimation of the displacement gradients. To illustrate this, [Elsinga et al., 2011] used a shear layer type displacement field in a 2D synthetic simulation,

$$(U, V) = (5 + \alpha z, 0) \tag{4.4.2}$$

where α is a linear displacement gradient. They showed that for a small α gradient, the coherent motion of ghost particles strongly impacted the displacement field and that this phenomenon tends to disappear when α increases.

To determine FOLKI-3D behavior with respect to the coherent motion of ghost particles we performed 3D synthetic simulations, reconstructing particle distribution from 2D PIV images using a similar displacement field,

$$(U, V, W) = (5 + \alpha z, 0, 0) \tag{4.4.3}$$

for $\alpha = 0.01$ and $\alpha = 0.05$ voxel/voxel. Estimated displacement fields can be assessed using the averaged norm of the error between estimated and ground truth displacement (Displacement Error), defined as

$$DE_{gt} = \frac{1}{N} \sum_{n=1}^{N} ||\mathbf{v}(\mathbf{X}_n) - \mathbf{v}_{GT}(\mathbf{X}_n)|| \tag{4.4.4}$$

Here, $\mathbf{v}$ and $\mathbf{v}_{GT}$ respectively denote the estimated and ground truth displacements. It is also possible to base our quality measurement on the velocity $v_{\mathbf{Ideal}}$ estimated by using Ideal Gaussian blob reconstructions, as considered in section 4.3. The displacement overlap is chosen to be 75%, and the averaged displacement error is computed at points $\mathbf{X}$ which are included in a parallelepiped contained within the intersection volume of both the laser sheet and the cameras fields of view (Intersection). In order to achieve statistical convergence of this quantity, we performed the tests on typially three to five different initial particle distributions depending on the tests, each leading to different reconstructed volumes and displacement fields. In this section, only top hat weighted interrogation volumes are considered. The interpolation scheme used is the cubic B-Spline, unless otherwise specified. The number of levels is $J = 3$ and we used $N = 7$ iterations.

4.4.2.2 Results

Figure 4.4.1 shows displacement profiles along Z, averaged in the X and Y directions, for $\alpha = 0.01$ and $\alpha = 0.05$. Results are plotted for both an ideal particle distribution, and for reconstructed volumes from 2D images. We also compute the displacement of ghost particles by removing the real particles from the SMART reconstruction. The results show a clear underestimation of the displacement gradient for small α, similar to [Elsinga et al., 2011], and this effect decreases as α increases. For $\alpha = 0.05$ both ideal and reconstructed mean displacement curves overlap. [Elsinga et al., 2011] showed that this underestimation for small gradients is due to the coherent motion of ghost particles which appear in the reconstruction process, as a result of small displacement gradients orthogonal to the line of sight of the cameras.

Following [Elsinga et al., 2006], [Cheminet et al., 2013] and [Cornic et al., 2013], (see chapter 2 for details) further quantified the impact of 'added particles', *i.e.* particles that lie in the Union, as a source of noise on the reconstruction quality. To further understand the impact of this effect on the displacement measurement, we computed PIV images with particles only in the Intersection on the one hand, and particles in the Union on the other hand, and determined the displacements in the case of the $\alpha = 0.01$ shear displacement.

Figure 4.4.2 shows the impact on the average velocity errors of particles which lie in the Union, but not in the Intersection, leading to a strong increase in the rms measurement errors (left figure). Indeed, those particles are responsible for an increase in the number of ghost particles in the reconstructed volume: the reconstruction

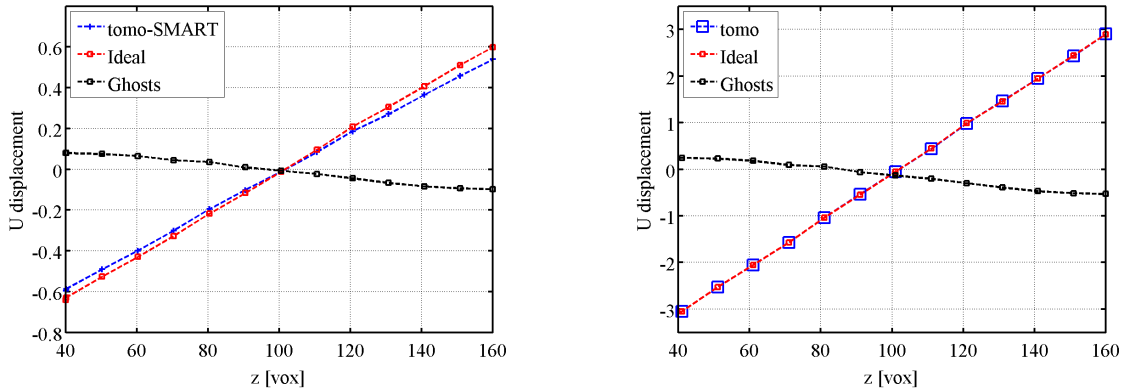

(a) $\alpha = 0.01$ **(b)** $\alpha = 0.05$

Figure 4.4.1: Profiles along Z of the displacement averaged over X and Y for shear displacements with $\alpha = 0.01$ (a) and $\alpha = 0.05$ (b). Results shown here are obtained with an IV side of 41 voxels (radius of 20 voxels).

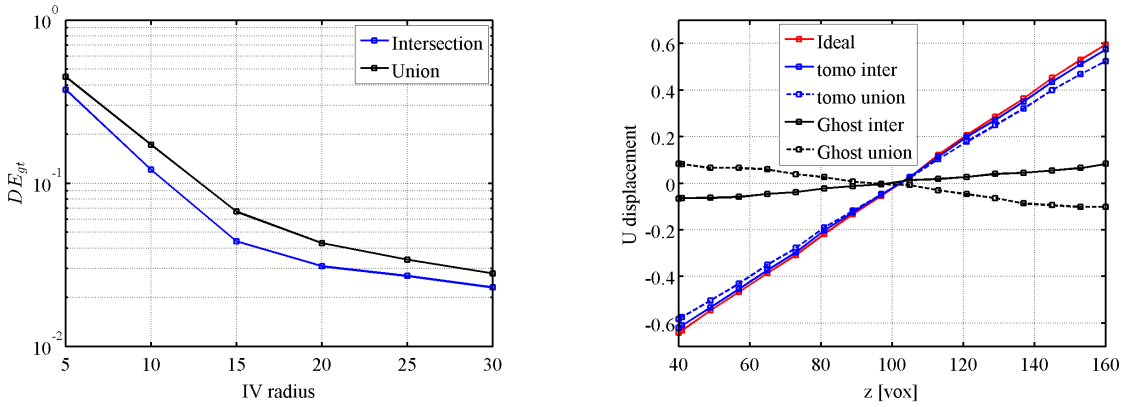

(a) Displacement error **(b)** Displacement for IV = 40 vox

Figure 4.4.2: Average velocity errors for $\alpha = 0.01$ (a) as a function of the IVs radius R. Velocity profiles along Z, averaged in the X and Y directions (b) for ideal reconstruction, SMART reconstruction and ghost particles. Cases where particles lie only in the Intersection, or in the Union. On the right subfigure, the IV side is set to 41 voxels (radius of 20 voxels).

quality Q [Elsinga et al., 2006] for the Intersection case is 0.94 and drops to 0.79 for the Union case. Figure 4.4.2 (right) compares the average displacement profiles of the reconstruction and of the ghost particles in both cases. It is interesting to see that the ghost particles average velocity in the Union case is of opposite sign to the reconstruction displacement, thus impacting strongly the overall velocity estimation through a clear underestimation of the velocity gradient. These ghost particles lead to an increase in the rms errors as well as an increase in bias errors. To minimize their impact, experiments should thus be designed so as to maximize the ratio $R_{I/U}$ between Intersection and Union, as long as this does not increase other noise sources.

In order to further situate FOLKI-3D among other VDM algorithms, we performed a comparison with LaVision Davis 8.2, using the direct correlation setting, and with top hat interrogation volumes for both algorithms. Further parameters for Davis 8.2 include an intermediate rejection step using the universal outlier detection method [Westerweel and Scarano, 2005], and smoothing between the iterations with a $3 \times 3 \times 3$ Gaussian

filter. The test case chosen for this comparison is the $\alpha = 0.01$ shear displacement with illuminated particles lying in the Union volume, which was shown to be a particularly noisy case for the correlation. Firstly, we performed a tomographic reconstruction from the synthetic PIV images using our implementation of MLOS-SMART. Then, the same resulting reconstructed volumes were processed both by FOLKI-3D and Davis. This operation was repeated with 3 different particles sets to achieve statistical convergence of the average displacement error. Figure 4.4.3 shows this quantity as well as the displacement profiles, for both algorithms.

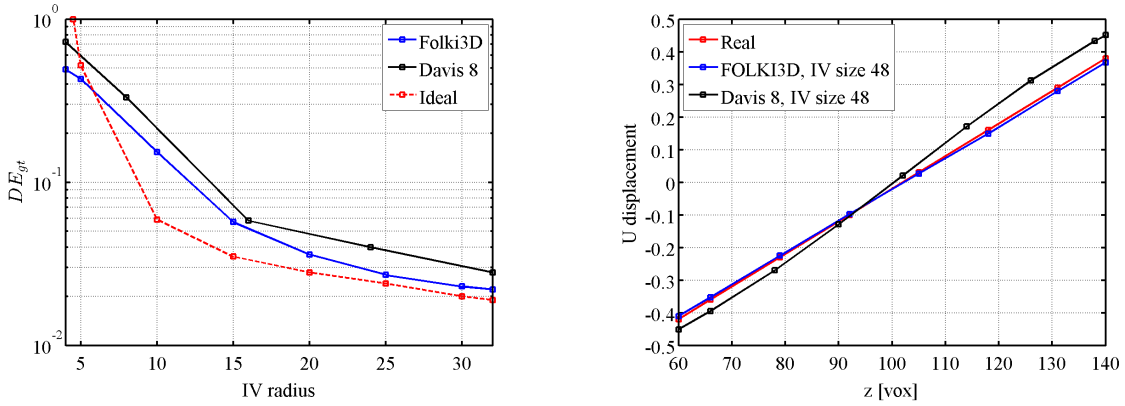

(a) Averaged norm of the displacement error **(b)** Bias error

Figure 4.4.3: Average displacement errors for $\alpha = 0.01$ (a) as a function of the IVs radius R, and displacement profiles along Z, averaged in the X and Y directions (with an IV side of 48 - radius of 24 voxel), obtained with FOLKI-3D and Davis 8.2 on the same tomographic reconstructions, and with FOLKI-3D on ideal volumic distributions.

In figure 4.4.3, FOLKI-3D's rms displacement error VE_{gt} is compared to Davis's for different IVs sizes, and averaged velocity profiles are also compared for an IV side of 48 voxels. FOLKI-3D and Davis have a similar behavior, the rms error rising as the IV size decreases. It turns out that FOLKI-3D performs equally or better than Davis while it does not involve any data post-processing between two successive iterations. This is especially true for small IV sizes. [Champagnat et al., 2011] showed the same results on the 2D version of the algorithm.

4.4.3 Interpolators and shape of the reconstructed particles

As studied by [Elsinga et al., 2006] and [Scarano, 2013] among others, the reconstruction quality is strongly dependent on the global aperture angle of the cameras. Indeed, small values of the aperture will lead to reconstructed particles with an elongated shape in the Z direction, whereas larger apertures will lead to more isotropic blobs. In this section, we further consider the impact of this parameter on the corresponding velocity fields, and also investigate the influence on the result of the interpolation scheme used during deformation. We choose a camera arrangement in the form of a cross (or '+' sign), parameterized by its aperture angle β, similar to that considered in [Scarano, 2013], and vary β between 20 and 100°. For each angle value, as in the previous sections, we generate two sets of synthetic images, corresponding to particles lying either in the Intersection only, or in the Union. Besides, since the voxel-to-pixel ratio is chosen equal to 1 in all situations, choosing the same ppv for all angles results in images with the same *ppp*. Thus, varying the angle β will amount to varying the Intersection to Union ratio $R_{I/U}$, thereby varying the proportion of ghosts as well as the shape of the reconstructed

particles.

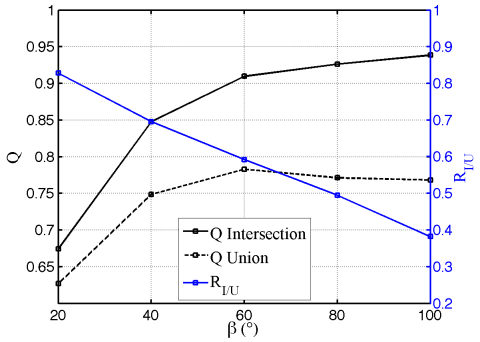

Figure 4.4.4: Reconstruction quality as a function of the camera aperture angle β, for synthetic images generated with particles contained only in the Intersection, or in the Union. The value of the Intersection to Union ratio $R_{I/U}$ is also indicated.

Figure 4.4.4 shows the evolution of the reconstruction quality as a function of β in the Intersection and Union cases. Similarly to [Scarano, 2013], one logically observes an important drop in Q for decreasing β, due to the elongation of the reconstructed particles in the Z direction. In the realistic Union case, the quality does not increase strictly with β contrary to the Intersection case, but reaches a plateau from $\beta \approx 60°$, close to a $0.75 - 0.8$ level. This is due to the fact that as β increases, the $R_{I/U}$ ratio increases. Therefore, even if the shape of the reconstructed particles is closer to ideal, the corresponding gain in quality is cancelled by an increase in the number of ghosts due to added particles.

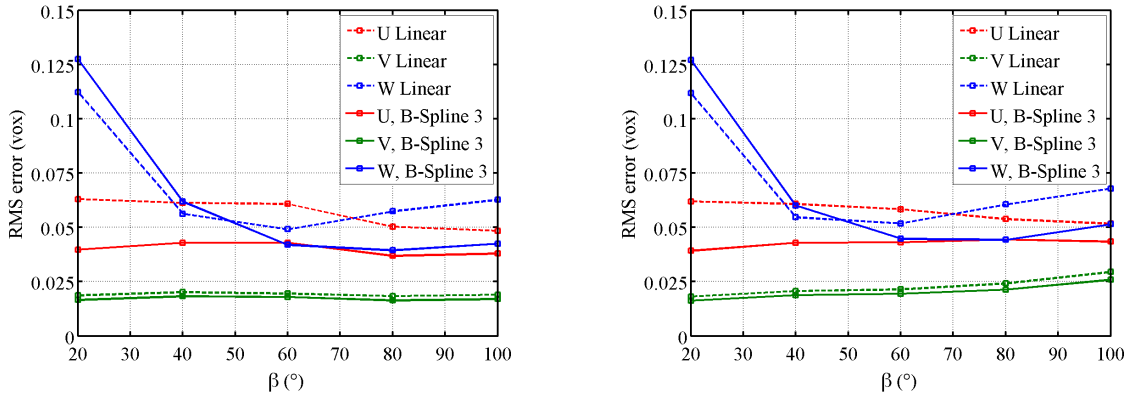

(a) Particles in Intersection **(b)** Particles in Union

Figure 4.4.5: Component-wise RMS error for linear and cubic B-Spline interpolators as a function of the camera aperture angle β, for synthetic images generated with particles contained only in the Intersection (a), or in the Union (b). The displacement field is a shearing motion with $\alpha = 0.01$, as in section 4. The IV size in FOLKI-3D is of 41 voxels (radius of 20)

In figure 4.4.5, the corresponding displacement rms errors are represented separately for each component, for fields obtained using either the linear or the cubic B-Spline interpolators in FOLKI-3D. In all cases, the IV size has been set to 41 voxels. The ground truth displacement considered here is made up of the superposition of shearing motions along both U and W, with the same strength $\alpha = 0.01$ More precisely:

$$(U, V, W) = (\alpha z, 0, \alpha x) \tag{4.4.5}$$

The resulting velocity field is thus a hyperbolic point in the XZ plane. Starting with the Intersection case (figure 4.4.5 left), one observes that, logically, the rms error on W increases for the smaller value of β and becomes comparable to that on U and V for values equal or larger to 40°. Another important result is that fields with the B-Spline interpolator have quasi-systematically lower rms errors than with the linear interpolator for all components. The exception is precisely the rms error on W for the smaller values of β. However, these angles correspond to small apertures which are rarely considered in practice, as they have a large rms error also with the linear interpolator. Therefore, we can conclude that in a more complex situation than the ideal distribution considered in section 4.3.2 (that is, actual reconstructions with noise in the images), the use of a B-Spline interpolator for deformation allows a significant increase in accuracy. Going one step further in complexity, when particles lie in the Union field (figure 4.4.5 right), one observes that this gain is robust with overall comparable results for both interpolators. A slight difference is observed in the form of higher rms values for all components and interpolators for the largest values of β (80 and 100°). This can probably be ascribed to the large number of ghost particles due to the low value of the $R_{I/U}$ ratio.

4.5 Conclusion

In this chapter, we introduced an extension to 3D of the algorithm FOLKI-PIV [Champagnat et al., 2011]. As in the planar context, the displacement is searched as the minimizer of a sum of squared differences which is solved iteratively by using volume deformation. The latter can be performed using a simple, linear scheme or a higher-order cubic B-Spline scheme. Numerical tests performed on synthetic 3D particle distributions have confirmed that the spatial frequency response is similar to that of standard iterative deformation algorithms for both top-hat and Gaussian weightings, while similar gains as reported in the literature are obtained by choosing the cubic B-Spline interpolation rather than the linear one. Tests on volumes reconstructed from projected images have then allowed us to characterize the robustness of the algorithm to specific tomographic noise (i.e. ghost particles), as well as the gain brought by the higher-order interpolation in a more realistic configuration. FOLKI-3D has been found in particular more robust to coherent ghosts, while the gain in accuracy of the high-order deformation has been confirmed for various quantities of ghosts in the reconstructions, and for various shapes of the reconstructed particles.

This accuracy assessment was carried out using numerical simulations of 3D-PIV reconstruction and synthetic flow fields. The final assessment on experimental data will be performed on our free round jet facility, presented in chapter 5. The choice of FOLKI-3D parameters as well as the experimental velocity results are described in chapter 6.

5 Description of the experimental setup and jet flow

5.1 Introduction

In the three previous chapters of this thesis, the explorations of experimental factors impacting the quality of the 3D-PIV measurement, the investigations of a new reconstruction algorithm (using the PVR paradigm) and the assessment of our 3D correlation algorithm, numerical simulations of 3D-PIV experiments were used. The remaining two chapters of this thesis are now dedicated to the experimental application of the algorithmic developments made in earlier chapters. More precisely, our aim is to perform an experimental validation of PVR reconstruction methods and compare it to classical tomographic reconstruction methods. We chose to carry out the validation on a free round air jet. At DAFE (ONERA), much research on turbulent jet has been carried out [Davoust et al., 2012]. We believe that the development of time-resolved 3D-PIV at ONERA will help us further understand the structure of turbulence in the mixing layer and the organization of coherent structures in the jet flow that were investigated using Stereo-PIV in [Davoust et al., 2014].

The focus of this chapter is twofold: first, we describe the experimental setup. Then, we describe the jet flow on which the measurements are made.

We will describe the jet facility and the seeding particles used for the PIV measurements. Two measurements systems are used for validation : a 3D-PIV setup and a 2D-PIV setup which is used as a measurement reference. For both measurement systems, illumination and configuration of the imaging system are covered. The synchronization between the two systems is explained as well as the calibration methods. From the calibration step of both measurement systems, two main influential parameters in 3D-PIV can be estimated : the particle image size and the particle volume density. The theoretical estimation of the particle image size is particularly helpful for the choice of PSF size in the PVR-SMART algorithm. Particle density is a crucial quantity on which the measurement quality depends. Our seeding density estimation method based on 2D-PIV images is explained.

For the physical description of the flow, we start by introducing the theoretical background related to free round jet flows. Finally, the jet flow in our setup and its properties are described using 2D-PIV measurements.

5.2 Experimental setup

This section is devoted to the description of the jet facility, the experimental instrumentation as well as the arrangements used for the experimental validation of PVR.

5.2.1 Jet facility

Experiments are conducted in DAFE laboratories at ONERA (Meudon). The flow on which measurements are made is the near field region of an round turbulent air jet, shown in figure 5.2.1. The jet consists of a cylindrical aluminum tube (120 mm in diameter) with an entrance for pressurized air on one side and an exit nozzle with a $D = 12$ mm diameter outlet on the other side, which yields a contraction ratio of $100 : 1$. Inside the nozzle at $z = 20$ mm of the exit nozzle plane, a small step of diameter $D = 17$ mm was placed to trigger turbulence. The air is supplied by the pressurized

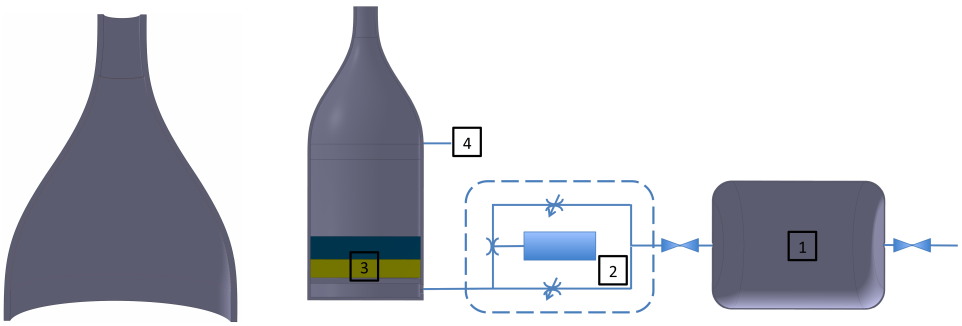

(a) Jet nozzle **(b)** Air suply diagram

Figure 5.2.1: Jet nozzle (**a**-left). Air supply diagram (**b**-right) with (**1**) settling chamber, (**2**) seeding generator, (**3**) Honeycomb and grids, (**4**) pressure tap.

air system at ONERA yielding a 30 bar pressure. A settling chamber or pressure tank (**1**, in figure 5.2.1) was installed just before a seeding generator to yield a stationary flow rate (**2**, in figure 5.2.1). The air flow rate is set by two valves, one controlling the seeding density, the other controlling the non-seeded air flow. Honeycomb and grids are fitted in the duct upstream of the nozzle contraction to reduce the flow turbulence (**3**, in figure 5.2.1). Finally a pressure tap just before the final contraction was used to monitor and control the output velocity (**4**, in figure 5.2.1).

Static pressure difference (Δp) between the pressure hole and the outside air was measured through a KIMO AMI 300 multi-manometer. Using Bernoulli's theorem and considering that temperature variations are negligible, one can compute the output velocity :

$$V_0 = \sqrt{\frac{2\Delta p}{\rho\left[1 - \left(\frac{D_{input}}{D_{output}}\right)^4\right]}} \tag{5.2.1}$$

The velocities used ranged from 5 $m.s^{-1}$ to 30 $m.s^{-1}$ yielding a Reynolds number range based on the nozzle diameter ($Re_D = V_0 D/\nu$) of $Re_D = [3800, 23000]$ considering the kinematic viscosity of the air at 20° Celsius , $\nu = 15.6 \times 10^{-5}$ $m^2.s^{-1}$. Finally the jet nozzle was mounted on a three axes traverse system that enabled accurate positioning of the jet exit in the three space directions.

5.2.2 Seeding particles

To ensure a good seeding homogeneity throughout the whole measurement volume, especially in the shear layer and non turbulent areas, we used two seeding generators. The first seeding generator is the Dantec seeding generator 55L18 (see figure 5.2.1) directly linked to the jet stream. We will call it the "internal" seeding generator. It generates DEHS (Di-Methyl-Hexyl-Sebacate) droplets. The estimation of the diameter distribution this generator creates varies in the literature from a mean diameter of $0.65\mu m$ with a standard deviation of $0.16\mu m$ [Albrecht et al., 2003], to a mean geometric diameter of $1.65\mu m$ with a standard deviation of $0.3\mu m$ [Borys et al., 2002]. The DEHS density is $\rho \approx 0.9 \times 10^3 kg.m^{-3}$. Considering the mean diameter, one can compute the relaxation time of the particle's response to a velocity perturbation [Raffel et al., 2007].

$$\tau_p^i = \frac{d_p^2}{18\nu}.\frac{\rho_p}{\rho} \approx 10^{-11}s \tag{5.2.2}$$

The second seeding generator, using DEHS particles of similar diameter as previously, was used to seed the ambient air of the experimentation room, non-turbulent areas of the flow, as well as the shear layer. For this generator, we did not have any means to adjust the seeding density, we only had a on/off switch button to create smoke. Its relaxation response time is, as previously:

$$\tau_p^e = \frac{d_p^2}{18\nu}.\frac{\rho_p}{\rho} \approx 10^{-11}s \tag{5.2.3}$$

This ensures us that particles from both seeding generators follow every flow scale since Kolmogorov time scale is given by

$$\tau_K = \sqrt{\nu\frac{D}{U_0^3}} \approx 10^{-5}s \qquad , \qquad \text{for } U_0 = 6\ m/s \tag{5.2.4}$$

The external seeding seeding generator was located 5 meters back of the jet ($z < 0$) in the $\vec{z}$ direction (see figure 5.2.3 for the definition of the axis coordinate system). For the seeding particles to be homogeneously spread in the measurement volume, we had to seed the whole experimental room. Once the room was filled with particles in high density, we had to wait for the external seeding to settle down and reach the density of the internal seeding which is set by a valve and is steady compared to the external seeding. Thus, during any image acquisition, external seeding is always decreasing and internal seeding is constant.

5.2.3 Measurement Setup

Our measurement setup is made of two different measurement systems . The first system is a classical 3D-PIV system composed of 4 cameras, a pulsed laser and a mirror and the second system is a standard 2D-PIV setup with a camera and a pulsed laser as shown below in figure 5.2.2. The main characteristics of the two measurement systems are summed up in table 5.2.1 below.

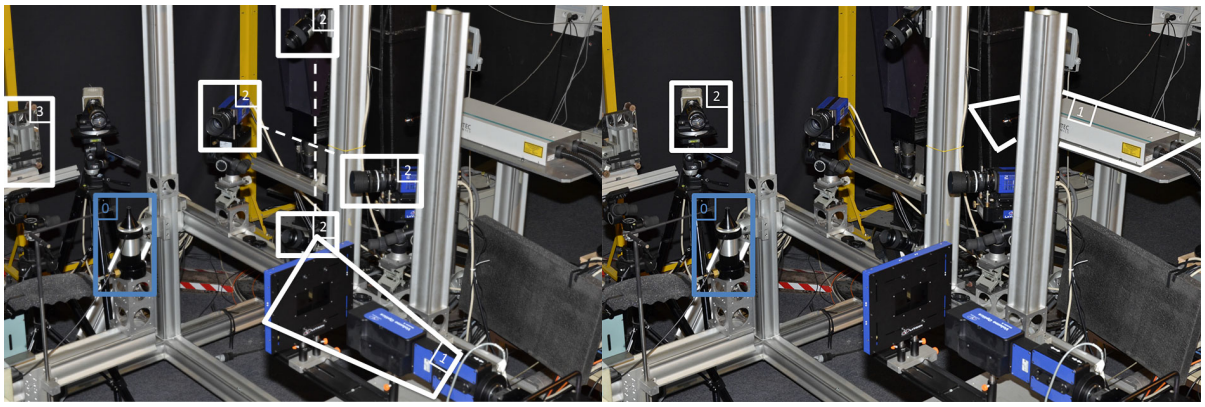

3D-PIV Setup 2D-PIV setup

Figure 5.2.2: Legend description. 3D-PIV: (0 in blue) Jet facility , (1) light volume optics and diaphragm in front of the laser which is not seen in this picture , (2) 4 cameras set in a cross-like configuration and (3) mirror to reflect the laser light. 2D-PIV : (0 in blue) Jet facility, (1) laser generator and laser optics, (2) camera.

		3D-PIV	**2D-PIV**
laser source	model	Quantel Laser Twin	Litron Laser Dual
	type	Nd-YAG	Nd-YAG
	wavelength	$\lambda = 532\ nm$	$\lambda = 532\ nm$
	pulse energy	$\approx 120\ mJ$	$\approx 200\ mJ$
	pulse length	$\approx 12\ ns$	$\approx 6 - 9\ ns$
	sheet width	$\approx 15\ mm$	$\approx 1.5\ mm$
cameras	model	2 Dantec HiSense 4M (Number **1** & **2**) 2 LaVision Imager pro X 4 M (Number **3** & **4**)	1 Dantec HiSense 11M
	sensor	CCD 2048×2048	CCD 4000×2672
	camera lens	$f = 105\ mm$	$f = 200\ mm$
	magnification	$M \approx 0.12$	$M \approx 0.23$
	camera $f_\#$	$f_\# = 8$	$f_\# = 5.6$
	pixel size	$7.4\ \mu m$	$7.4\ \mu m$
	image dynamics	**1**/**2** : 8-12 bits **3**/**4** : 14 bits	8-12 bits
acquisition	working frequency	f = 4 Hz	f = 2 Hz
	acquisition frequency	f = 2 Hz	f = 2 Hz

Table 5.2.1: Measurement systems characteristics.

5.2.3.1 3D-PIV setup

The design of a 3D-PIV setup is delicate for it directly impacts the quality of the velocity measurement. Numerous compromises have to be made so as to have the best measurement possible. We followed guidelines provided in past studies [Scarano, 2013] to choose the optical arrangement. The optical system of the 3D-PIV setup is made of 4 cameras in a cross-like configuration, see figure 5.2.3. The 2 vertical cameras are Dantec HiSense 4M, and the two horizontal ones are LaVision Imager pro X 4 M. They all have 2048×2048 pixels CCD sensors. The pixel size is 7.4 μm.

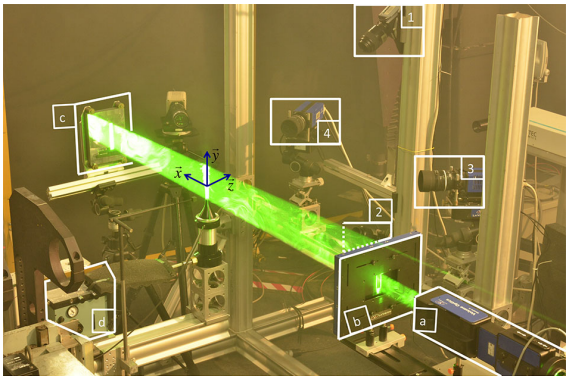

3D-PIV setup

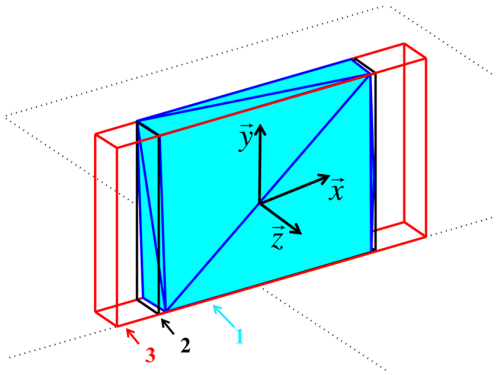

Union and Intersection Volumes

Figure 5.2.3: Legend description : **left :** *a* = Laser Volume generator, *b* = diaphragm, *c* = mirror, *d* = Inner jet stream seeding generator, {1/2/3/4} = Camera's number. **right :** *1* = Intersection polyhedron, *2* = Intersection cuboid, *3* = Union cuboid.

The cross-like configuration was chosen for two main reasons : first, this made for an easier setting of the Scheimpflug's angle for each camera. In this configuration, we only had to adjust one tilt angle for each camera, so as to have the in-focus plane as the $z = 0$ plane. The second reason was consequential to the first one : not having to tilt the cameras in another direction to account for the Scheimpflug condition meant that the intersection volume of the camera field and the laser volume of view was very close to a parallelepiped and its volume was larger. As advised in [Scarano, 2013] the aperture angle β was set to 60° in order to optimize the reconstructed shape of a particle in the depth direction.

The optical magnification for the cameras is about $M \approx 0.12$. The camera's f number ($f_\# = 8$) is set so as to have as much energy as possible (especially for the backward-scattering camera which is camera 3 in figure 5.2.3) without shrinking the camera depth of field too much. A first estimation of the cameras depth of field and the particle image diffraction spot [Raffel et al., 2007] gives :

$$\delta z = 4.88\lambda f_\#^2 (1 + \frac{1}{M})^2 \approx 14.5\ mm \quad , \quad d_{diff} = 2.44 f_\# \,(M+1)\,\lambda \approx 1.6\ pix \qquad (5.2.5)$$

Further insight into the particle image size for the tomographic setup can be found below, in section 5.2.5. The four cameras are synchronized with a Nd-YAG 532 nm laser (120 mJ). Expansion from a beam to an illuminated volume is achieved by a "LaVision Volume optics" volume generator. The resulting expanded beam passes through a rectangular section diaphragm transforming its elliptic cross-section into a rectangular cross-section. The diaphragm dimensions were found so as to have a 15 mm wide and 86 mm high laser cross-section at the jet nozzle. To account for Mie scattering, we installed

a mirror which reflects part of the incoming laser beam. This enabled us to enhance the image quality in the backward scattering cameras especially for camera number 4, but also for camera 1 and 2 as well which are set along the vertical. To further counter the effects of Mie scattering, and the loss of particles in the reconstruction, the laser optics were set to obtain a relatively narrow elliptic cross-section so as to have as much energy in the laser volume as possible. This meant that we made a choice between laser volume (width) and laser intensity, favoring intensity so as to have the highest signal-to-noise ratio in the images.

The laser volume (incoming from the laser and coming back from the mirror) was set so as to skim the jet nozzle while trying to avoid reflections as much as possible. From the cameras calibration (see 5.2.4), and the laser volume expansion estimation, we computed the Union volume and Intersection volumes (chapter 2). Figure 5.2.3 shows different volumes : the Intersection or Union of the camera's field of view and the laser volume. The camera's arrangement as well as the laser volume dictates the reconstruction volume. We show here the intersection volume, a polyhedron in blue. In black, we show the smallest cuboid containing the intersection volume and in red, the smallest cuboid containing the union volume. This is the cuboid on which the tomographic reconstruction will be performed. The ratio $\mathcal{R}_{I/U}$ is about 0.75.

5.2.3.2 2D-PIV

On the same jet facility, we installed a planar PIV measurement system which is made of one Litron Laser Dual Nd-YAG 532 nm laser and one Dantec HiSense 11M (4000×2672 pixels) camera. The laser sheet is located in the $x = 0$ plane, therefore orthogonal to the main axis of the tomographic laser as seen in figure 5.2.4. The camera's lens has a focal length of 200 mm and is set at numerical aperture $f_{\#} = 5.6$. The laser source had enough energy to allow for a relatively high f number/low aperture. The particle diameters in the images were large so as to reduce any peak-locking effects (for a particle density suited to 2D-PIV measurement). The objective magnification is $M \approx 0.23$ with a field of view of the camera of 128×86 mm yielding a resolution of 29.7 pix/mm.

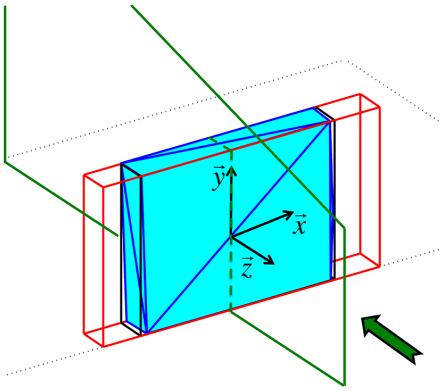

Figure 5.2.4: 2D-PIV measurement plane (yz plane) and tomographic volume.

5.2.3.3 2D-PIV and 3D-PIV synchronization

The 2D-PIV measurement system was installed to act as a reliable comparison point for the 3D tomographic PIV. The 2D-PIV measurement can be done independently (to have a precise characterization of the jet flow) or simultaneously with the 3D-PIV system

(to have a reliable velocity measurement of the same test run for the comparison). In the latter case, it was important to have the two measurement systems acquire velocity snapshots "at the same time", or as close as possible to one another time-wise. However, since the two lasers have the same wavelength, the laser pulses cannot be at the same time, for both laser sheets would disturb the illumination areas of one another. We chose to intertwine the measurements. Both systems have the same acquisition frequency (i.e. the same period between two double-pulses) but we introduced a time phase-shift in one of the systems so as to have its double pulse occur in-between the two double pulses of the other system.

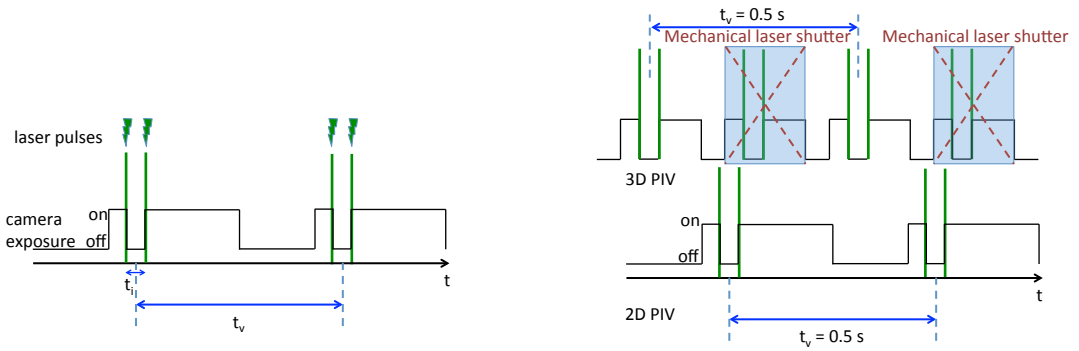

(a) single PIV system **(b)** two PIV system

Figure 5.2.5: Timing diagrams (**left :** single PIV system) (**right :** double PIV systems synchronization with mechanical laser shutter).

To do this, one must take several properties and characteristics into account and better understand how a PIV systems work, especially the synchronization between the pulsed laser and the camera. In a classical double-frame/single-exposure PIV system, the camera exposure time is synchronized with the double pulsed laser as shown in figure 5.2.5. The system has two characteristic times : t_i, the separation time between two laser pulses, and t_v the measurement acquisition period, the time in between two double pulses. One notices that the second camera exposure time is longer than the first. During this second exposure time, aside from the laser pulse, no light or laser pulse must be triggered, this would alter the second frame of the recording. This is why simply superimposing two PIV systems, with the same acquisition frequency and a simple time phase shift is not possible. The solution found (figure 5.2.5(b)) was to double the frequency of one of the systems (in our case the 3D-PIV system) and to use a mechanical shutter on that same system, that would obstruct one out of two double laser pulses so as not to disturb the images of the previous system. A good time phase shift was found to avoid any disturbances of the 2D-PIV laser on the images of the 3D-PIV that are properly illuminated by the 3D-PIV laser. The 2D-PIV system frequency was set to $f_{acquisition} = 2\ Hz$. The 3D-PIV system frequency was set to 4 Hz, but since one out of two double images are black, the resulting snapshot acquisition frequency is still 2 Hz.

5.2.4 3D and 2D Calibration

The tomographic reconstruction is based on the triangulation and intersection of line of sight of pixels in the 3D space. It is therefore necessary to proceed to a calibration of the cameras. Tomographic PIV requires a very accurate calibration since each voxel in the reconstructed space has to be projected into the images with an error lower than

0.4 pixel [Elsinga et al., 2006] and preferably less than 0.1 pixel [Wieneke, 2008].

The 3D calibration of the 4 tomographic cameras is done through an explicit pinhole model of a camera equipped with a 2-tilt angles Scheimpflug adapter. The outline and thorough description of the method can be found in [Cornic et al., 2015b]. The aim of the calibration process is to determine all extrinsic and intrinsic parameters of the camera model (6 extrinsic, 4 intrinsic, 2 tilt angles for the Scheimpflug adapter, 4 distortion parameters). To do this, we use snapshots of a "freely moving" calibration plate that can be placed at arbitrary positions in space, seen in figure 5.2.6, with 11 different positions. The goal is to minimize the sum of squared projection errors for all plate points, in all positions, for all cameras. This first optimization procedure gives us a first calibration of the cameras.

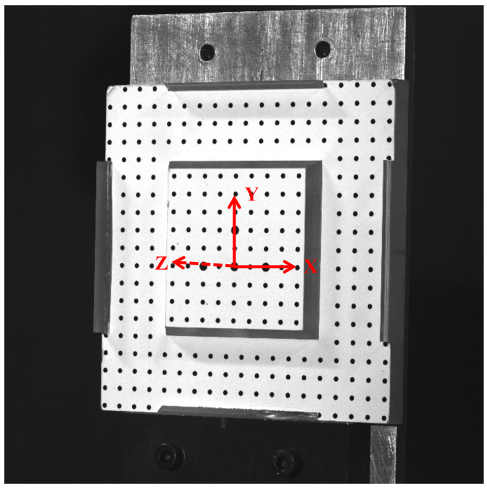

Figure 5.2.6: 3D dual plane calibration pattern and frame of reference.

The imaging system is calibrated using the dual plane calibration pattern using dot markers figure 5.2.6. The centers of the dot markers are detected in the images up to 0.05 pixel accuracy using our in-house marker detector [Le Sant and Merienne, 1995]. The optimisation is done with the camera pinhole model variables and with the observations of detected dot markers. It leads to a mean error of 0.42 pixels, a standard deviation of 0.51 pixels with a maximum error of 2.73 pixels.

As shown in [Elsinga et al., 2006], tomographic reconstruction is very sensitive to calibration errors. To minimize the calibration error and to ensure the intersection of the pixel line-of-sight, [Wieneke, 2008] introduced the self-calibration procedure. This method is based on the minimization of the system disparities. Disparity is the discrepancy between an observed particle in the camera and the projection of its triangulated position in 3D. [Cornic et al., 2015b] used this technique and implemented it in a bundle adjustment framework to obtain a globally consistent pinhole model. This technique is applied to every experimental acquisition to enhance the quality of the calibration. It leads to a mean error of 0.08 pixel, a standard deviation of 0.05 pixels with a maximum error of 0.42 pixels.

The calibration for the 2D-PIV system was done using the same calibration plate, whose top plane was positioned along the 2D-PIV laser sheet. The calibration process was done using our in-house 2D-PIV calibration code [Le Sant et al., 2007].

5.2.5 On particle image size

From the 3D-PIV camera arrangement and from the calibration step (section 5.2.4), one can have a theoretical estimate of the particle image size. Furthermore, when considering defocusing effects, one can have an estimate of the particle image size variation in the volume. Particle image size is an interesting feature for prediction of peak locking. Moreover it is a tuning for PVR-SMART algorithm which requires the PSF standard deviation for building the reconstruction weight matrix. These theoretical values of the PSF give a first crude estimate and will help us choose the PVR-SMART algorithm parameter which is the size of the reconstruction PSF (see chapter 3).

5.2.5.1 Theoretic estimation of the particle image size

When considering in-focus particles, and the physics of diffraction, the following formula can be used for an estimate of the particle image diameter [Raffel et al., 2007]

$$d_\tau = \sqrt{(Md_p)^2 + {d_{diff}}^2} \tag{5.2.6}$$

where d_p is the particle diameter, M, the magnification factor and d_{diff} the minimum image diameter due to diffraction which can be obtained from the following formula ([Raffel et al., 2007] and [Adrian and Yao, 1985])

$$d_{diff} = 2.44 f_\# \left(M + 1\right) \lambda \tag{5.2.7}$$

where $f_\#$ is the f-number, defined as the ratio between the focal length f and the aperture diameter D_a and λ the laser wavelength. In practice, the point spread function is often modeled as a normalized Gaussian function defined in 1D here by :

$$\frac{I(x)}{I_{max}} = \exp\left(-\frac{x^2}{2\sigma^2}\right) \tag{5.2.8}$$

where, $I(x)$ is the intensity in the image. In a classical PIV setup ($M \approx 0.1$, $f_\# \approx 8$ and $\lambda \approx 0.5\mu m$) in a wind tunnel using DEHS (Di-ethyl-hexyl-sebacate) particles of about $1\mu m$ diameter, diffraction effects tend to dominate over the geometric image size.

$$2.44 f_\# \left(M + 1\right) \lambda \approx 10^{-5} \gg M d_p \approx 10^{-7}. \tag{5.2.9}$$

Gaussian fitting [Raffel et al., 2007] of the diffraction shape gives the following formula linking the standard deviation of the fitting model σ to the diffraction image diameter d_{diff} :

$$\sigma = f_\# \left(M + 1\right) \lambda \sqrt{2}/\pi \approx \frac{1}{5.42} d_{diff} \tag{5.2.10}$$

This link is also verified by [Adrian and Yao, 1985]. Let us apply the formula above to evaluate the theoretical standard deviation of the PSF in our jet setup. In our setup, the cameras had the following parameters : $M \approx 0.1$, $f_\# \approx 8$, $\Delta_{pixels} = 7\mu m$ and the focal length $f = 105mm$. The laser operates at $\lambda = 532nm$. Here the standard deviation is evaluated in pixels. One thus gets

$$\sigma_{theo} \approx 0.30 \tag{5.2.11}$$

5.2.5.2 Estimation of defocusing effects

[Olsen and Adrian, 2000], introduced a model for defocusing effects, giving a formula given for of out-of-focus particles. If s_0 is the distance between the object plan (in-focus plan) and the lens, if z is the distance, projected on the lens axis, between the focus plan and the particle, D_a the aperture such as $f_\# = \frac{f}{D_a}$, then we have,

$$d_\tau = \sqrt{M^2 {d_p}^2 + 5.95\,(M+1)^2\,\lambda^2 f_\#^2 + \frac{M^2 z^2 {D_a}^2}{(s_0+z)^2}} \tag{5.2.12}$$

Considering a laser volume which is $20mm$ thick, we can have an estimate of the range of particle image diameter and therefore σ, see figure 5.2.7. The σ variation range in our laser volume is from 0.3 to 0.6 pixels.

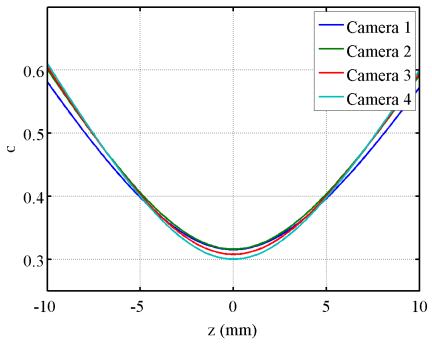

Figure 5.2.7: Theoretical image size (σ) behavior for out-of-focus particles

5.2.6 Particle density estimation

Particle density is a crucial quantity in tomographic PIV. In a classical 3D-PIV setup, where the only measurement system is the 3D-PIV system, the image density is poorly estimated from a simple particle count on the images due to overlapping. [Novara, 2013] shows that above 0.04/0.05 ppp, the overlapping issues becomes predominant. One of the possible solutions is thinning the illuminated domain. [Lynch and Scarano, 2014] used a slit region in the laser volume allowing an estimation of the *ppp* at the same time of the tomographic measurement. However, in our setup, we have synchronized the 2D-PIV setup with the 3D-PIV setup. We will use the images from 2D-PIV to estimate the particle density.

Indeed, from the 2D-PIV images of a run, one can count particles which are in the 2D-PIV thin layer sheet. This detection is based on maxima detection on a sub-region of the images and is fairly accurate as respect to particle overlapping since low densities are required for the 3D-PIV to work efficiently. Two different sub-regions were used : one is located in the middle of the jet stream, another is located outside the jet stream where the velocities are low. From the 2D laser sheet thickness estimation and the 2D-PIV camera calibration, one is thus able to estimate the particle density in the two different locations of the image sub-regions which may differ due to the two different seeding systems used. The *ppp* estimation is given by :

$$ppp = \frac{Nb_{Deteced\ Particles\ 2D}}{N_x N_y} \frac{\Delta_{Z\ Tomo}}{\Delta_{Z\ 2D}} \left(\frac{dx_{Tomo}}{dx_{2D}}\right)^2 \left(\frac{M_{2D}}{M_{Tomo}}\right)^2 \tag{5.2.13}$$

where $Nb_{Deteced\ Particles\ 2D}$ is the number of detected particles in the 2D PIV images in a subset which size is $[N_x, N_y]$.$\Delta_{Z\ Tomo}$ and $\Delta_{Z\ 2D}$ are respectively the tomographic and 2D-PIV laser sheet thickness. dx_{Tomo} and dx_{2D} are respectively the physical pixel size of one of the tomographic cameras and of the 2D-PIV camera on which the estimation is based. M_{2D} corresponds to the optical magnification of the 2D-PIV camera and M_{Tomo} refers to the optical magnification of the camera of the tomographic setup on which the density estimation is based.

In this process, the estimation error sources are multiple : First, there is an assumption of homogeneity of the particle spatial distribution inside each image subset. Overlapping of particles in the 2D-PIV images is inevitable when the density increases and is a strong limitation to the method, however, it is interesting to know from which density this phenomenon occurs and compare it to the overlapping in the tomographic images. There is an uncertainty in the particle detection due to the cameras noise. There is also an uncertainty on the estimation of both the 2D-PIV laser layer sheet and the 3D-PIV laser layer depth. Errors can also come from calibration errors but those seem negligeable in comparison to the previous ones.

For a further validation of our method, we performed synthetic tests. We created synthetic 3D-PIV images and 2D-PIV images from the same 3D particle distribution, using the calibration data from our jet setup, using a 15 mm thick laser for the tomographic experiment and a 1 mm thick laser for the 2D experiment. For the sake of simplicity, there was no camera noise in the images, and the seeding was monodisperse diameter-wise.

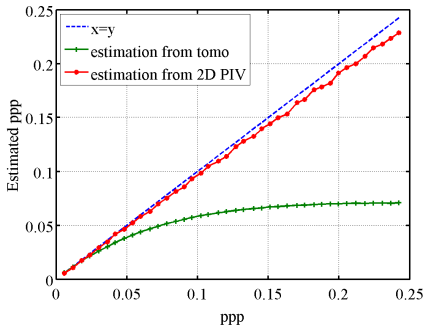

Figure 5.2.8: Estimation of ppp for 2D-PIV images or 3D-PIV images.

The results (figure 5.2.8) illustrate the estimated *ppp* when particles are counted from 3D-PIV images (tomo) or from the 2D-PIV images as a function of the real *ppp*. This shows that within the usual range of *ppp* from 0.01 to 0.2, the density estimation from the 2D-PIV images is fairly accurate and does not suffer much from errors resulting from the overlapping in the 2D-PIV images. Hence, the main sources of errors are detection errors in noisy images (false detections due to noise or missed detections due to threshold values too high to avoid noise) and laser sheet depth estimation errors for both the tomographic laser sheet and the 2D-PIV laser sheet.

However, another possible error source stems from the fact that the underlying assumption, for our particle density estimation method, is that particles detected in the 2D-PIV images, are also "visible" in the 3D-PIV images, should the two lasers hypothetically work exactly at the same time. This is not the case since the 2D laser is more powerful than the 3D tomographic laser. This means that low intensity particles

in the 2D-PIV images, which are accounted for in the ppp estimation, are not visible thus not reconstructed in the 3D volumes. This means that the ppp estimate is certainly over-estimated, but it is difficult to find an effective way to counter this effect.

5.3 Free round jet : theoretical background

In this section, we introduce and define the physical terminology and concepts used for the description of jet flows which will be used in the rest of the thesis. Jet flows are still a very active field of research for their study encompasses a wide variety of fluid dynamics concepts. We will only consider incompressible free round jet flows here.

5.3.1 The round jet : flow field description

Free jets belong to the family of free shear flows. The adjective "free" means that the flow is far away from any walls and that the turbulence appears because of mean velocity differences [Pope, 2000]. The round jet flow appears when a Newtonian fluid of viscosity ν flows through a round nozzle of diameter D, with an exit velocity profile close to a "top-hat" velocity profile (of bulk velocity denoted by V_0). The jet flows out of the nozzle into a fluid at rest, eventually entraining the receiving fluid and spreading radially with respect to the downstream distance, until the initial momentum is spread so thin that viscous effects dissipate the energy and stop the fluid motion [Ball et al., 2012], as illustrated in figure 5.3.1.

In this description, we consider the flow to be statistically stationary and axisymmetric. The adequate coordinate system to describe this flow is usually the polar coordinate system. However, later in the thesis, we will keep a cartesian coordinate system, since our 3D laser volume is a rectangle and the region on which we could have done statistics in a polar coordinate system, was not big enough to cover the whole expanding jet. In this section, we thus call V, the axial velocity of the jet on the **y** axis. U and W are the velocity field components on respectively the **x** and **w** axis.

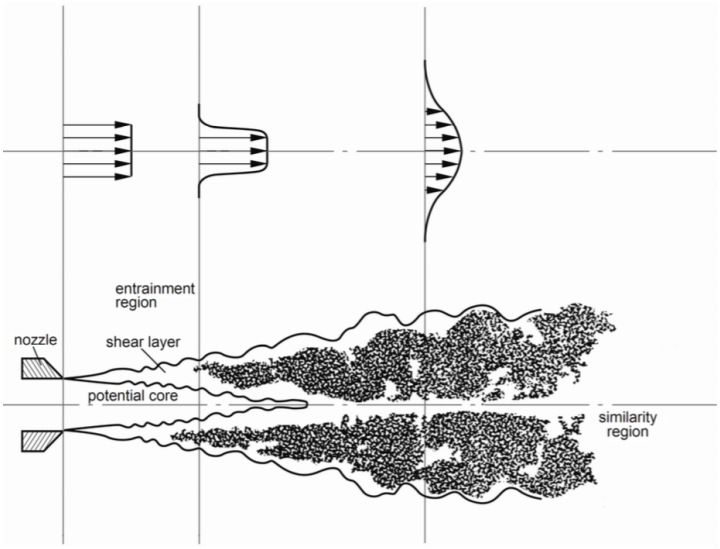

Figure 5.3.1: Sketch of the Jet flow field (bottom) with mean axial velocity profiles (top). This illustration is extracted from [Violato, 2013].

In [Bailly and Comte-Bellot, 2015], three non-dimensional parameters are considered to be the most influential in the development of the jet : two Reynolds numbers, $Re_D = V_0 D/\nu$ and $Re_{\delta_\theta} = V_0 \delta_\theta/\nu$, and the third parameter is the peak fluctuation intensity v'/V_0 at the nozzle exit. δ_θ is the momentum thickness of the exit boundary layer (equation (5.4.4) in the next section). A traditional classification of the jet flow differentiates the flow as being laminar, transitional or turbulent depending on the state

of the nozzle boundary layer which impacts the jet development. The above parameters are useful in describing the state of the exit boundary layer. However, a clear classification is difficult to establish for the jet development depends on different parameters which are ultimately all linked together. For instance, the exit velocity profile and nature of the boundary layer inside the nozzle are known to influence the mixing in the shear layer. In our case, considering to the Reynolds number ($Re_D \approx 4500$), and the inner step in the nozzle disturbing the boundary layer, it is safe to assume that our jet is either turbulent or perhaps transitioning into a turbulent jet. Furthermore, axial velocity fluctuation levels, i.e. rms axial velocity close to the exit plane of the nozzle (see next section, figure 5.4.1(a)), are close to values classically attributed to turbulent jets with a peak rms intensity of 0.11.

In any case, there are typically three main axial regions in the flow field : the near field, the intermediate field and the far field as depicted in figure 5.3.1.

The near field region is usually within $0 \leq x/D \leq 7$. Its length is defined by the length of potential core region which is flow region, where the velocity is equal to that at the nozzle exit. The interface between the jet and the fluid at rest is called the shear layer or mixing layer. Initial instabilities (Kelvin-Helmholtz) appearing between the fluid at rest and the flow existing the nozzle produces Vortices ring which are convected downstream, and will eventually pair. This leads to mass entrainment and momentum transfer through the mixing layer. The jet spreads radially while the shear layer spreads to the jet core center. This is the region on which 3D-PIV measurements will be made in the next chapter of the thesis.

The far field is where the flow is fully developed, also called the self-similar region. For [Ball et al., 2012], it is located at $x/D \geq 70$, and according to [Bailly and Comte-Bellot, 2015], the jet is fully developed at approximately $15D$. As for [Pope, 2000], the self similar region starts around $x/D \geq 30$. One sees how the definition of the self-similar region varies in the literature, however, the main properties of this region is well defined. In the so-called self-similar region and with the appropriate scaling, the radial profiles of the mean axial velocity collapse onto a single curve and an analytic solution can be found for this profile. In this region, the turbulence is fully developed, meaning that the fine scales of turbulence are present.

The intermediate region is in-between the near region and the self-similar region. This region has anisotropic turbulent structures developing and interacting with one another.

5.3.2 Coherent structures

In the previous paragraph, we described the jet flow field based on its statistical properties. Other approaches based on the concept of 'coherent structures' were developed and gave new perspective and understanding. Hussain, in [Hussain, 1986] defined it as "*a connected turbulent fluid mass with instantaneously phase-correlated vorticity over its spatial extent*". The idea is to describe the flow field in terms of velocity or vorticity structures that are born, evolve and interact. The near region of the jet is particularly well adapted to such a description. Over the years, a large amount of research has been carried out, describing jet flows with evolving orderly structures. Such work can be seen for instance in [Becker and Massaro, 1968], [Crow and Champagne, 1971], [Yule, 1978],

[Hussain, 1986] and [Liepmann and Gharib, 1992].

In the near region, the shear layer develops Kelvin-Helmholtz instabilities, the shear layer rolls up, leading to ring vortices [Becker and Massaro, 1968]. At moderate Reynolds number, the vortices grow radially in size, maintaining their axial symmetry, and the mutual induction [Crow and Champagne, 1971] between two consecutive rings makes them roll around each other and pair up. Those ring vortices can also be affected by secondary instabilities, namely azimuthal instabilities of a vortex ring, as shown in the experimental study of [Liepmann and Gharib, 1992], figure 5.3.2(a). Experimental studies as well as numerical ones [Martin and Meiburg, 1991] showed that those azimuthal perturbations can also lead to the development of streamwise vortices, organized into counter-rotating pairs in the braid region figure 5.3.2(b).

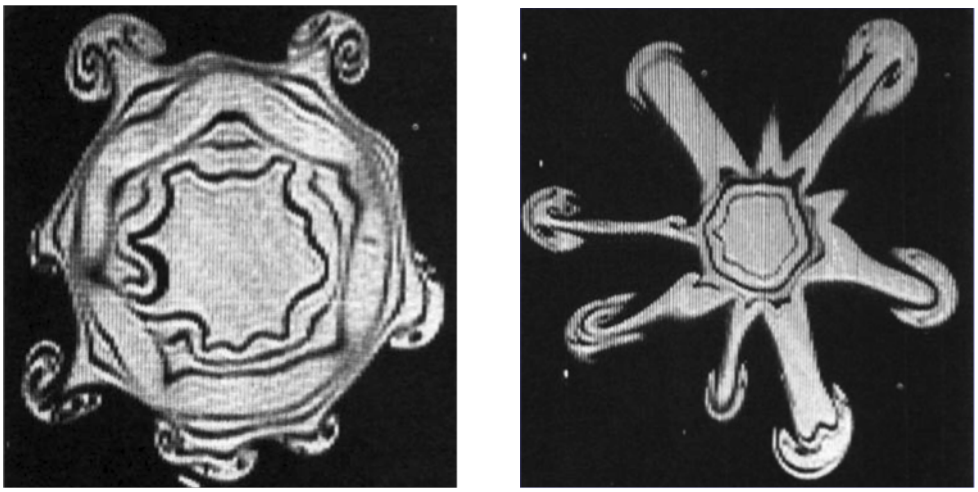

(a) jet cross-section in the middle of a ring vortex

(b) jet cross-section in the braid region

Figure 5.3.2: Dye visualization in a jet cross-section at $x/d = 3.25$ for $Re_D = 5500$ (from [Liepmann and Gharib, 1992]).

Research is still being carried out to understand how those structures interact, how they influence the mixing process in the shear layer and how initial conditions influence such structures, with different explaining scenarios being investigated [Davoust et al., 2012]. In that regard, 3D time-resolved PIV is well suited for such investigations of coherent structures [Violato and Scarano, 2011]. In the next chapter, we will investigate the near field region of our jet setup, investigating mean and rms velocity fields, as well as coherent structures.

5.4 Description of the jet flow

This section focuses on the description of the flow statistical properties using the 2D-PIV measurement system. We wish to emphasize the fact that this description was done using only the 2D-PIV setup, in optimized seeding conditions for 2D-PIV. Those conditions are very different from the conditions used in the next chapter of the thesis. The aim of this section is to experimentally assess the jet flow field which will be used for the 3D-PIV measurements later in the thesis so as to provide a reference.

5.4.1 2D-PIV settings

For the description of the jet flow field, we used the 2D-PIV measurement system. Flow field measurements were computed on 3000 snapshots at 2 Hz using a high tracer density (not fitted for 3D-PIV). The time interval between the 2 laser pulses was set to $50\mu s$. Image correlations were done with our FOLKI-PIV correlation code [Champagnat et al., 2011], using $J = 3$ levels, $N = 10$ Newton-Gauss iterations. The choice for the Interrogation Window size (IW) stemmed from a trade-off between spatial resolution and measurement noise. We chose a 31 pixels window size allowing for an estimated 20 tracer particles per interrogation window (see table 5.4.1) which is a value classically admitted in PIV literature to yield a good measurement quality. This leads to a normalized window size of 0.086 when normalized by the jet nozzle exit diameter D.

IW size (pix)	**IW size (mm)**	**IW size/D**	$\mathbf{N_{tracer\ per\ IW}}$
21	0.7	0.058	10
31	1	0.086	20
41	1.3	0.115	40
51	1.7	0.143	51

Table 5.4.1: 2D-PIV correlation window size properties : in pixels, normalized by the nozzle diameter D and the estimated number of tracer per IW.

5.4.2 Results

Considering the geometrical reference frame (see section 5.2.3.1) on our jet facility, the 2D-PIV systems measures the 2D velocity field in the $(\vec{z}, O, \vec{y})$ plane. Each measurement snapshot at a discrete time $t \in \langle t_1, t_2, ..., t_{N_s} \rangle$ corresponds to a 2D vector field $(V(\mathbf{x}, t), W(\mathbf{x}, t))$. V is the streamwise or axial velocity of the jet, W the radial velocity.

5.4.2.1 Statistical and integral quantities definitions

For any given field $\alpha(\mathbf{x}, t)$ obtained at discrete time intervals $t \in \{t_1, t_2, ..., t_{N_s}\}$,($N_s = 3000$ samples) we can compute statistical quantities such as mean, fluctuating and Root-Mean Square (rms) fields, whose definitions are respectively :

$$\langle \alpha(\mathbf{x}) \rangle = \frac{1}{N_s} \sum_{i=1}^{N_s} \alpha(\mathbf{x}, t_i) \quad , \quad \alpha'(\mathbf{x}, t) = \alpha(\mathbf{x}, t) - \langle \alpha \rangle \quad , \quad \alpha_{rms}(\mathbf{x}) = \sqrt{\frac{1}{N_s} \sum_{i=1}^{N_s} \alpha'(\mathbf{x}, t_i)^2} \tag{5.4.1}$$

The velocity fields are normalized by the jet output velocity. The definition of jet output velocity is based on the spatial integration of the mean axial velocity at $y/D = 0.46$.

$$V_0 = \frac{1}{D/4} \int_{\mathcal{L}} \langle V(z) \rangle \, dz \tag{5.4.2}$$

where $\mathcal{L}$ is the horizontal line segment of length $\mathcal{L} = D/4$, in the 2D-PIV measurement plane centered on the $\vec{y}$ axis at $y/D = 0.46$. This space location corresponds to the one that we will use in the next chapter for the 3D-PIV. The profile was extracted 5.5 mm downstream of the nozzle to avoid using unlit areas or data corrupted by the laser light reflections on the nozzle. We normalized each velocity field (V, W) with the output velocity V_0:

$$v = V/V_0 \quad , \quad w = W/V_0 \tag{5.4.3}$$

5.4.2.2 Basic flow field description

The jet facility was operated here at an output velocity $V_0 = 5.8\ m.s^{-1}$ which corresponds to a Reynolds number of $Re_D \approx 4500$ based on the nozzle exit diameter. Figure figure 5.4.1(a) shows the mean axial velocity $\langle v \rangle$ exit velocity as well as the rms streamwise velocity.

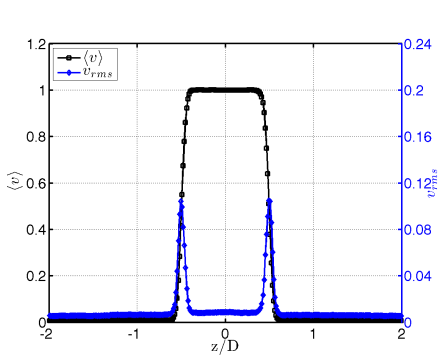

(a) Mean and rms axial velocity profiles at $y/D = 0.46$.

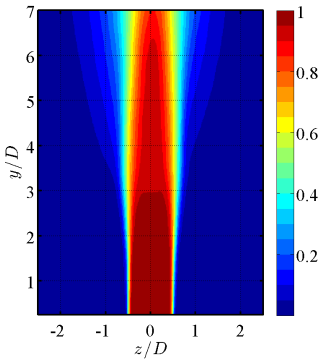

(b) Mean axial 2D velocity field.

Figure 5.4.1: Inflow conditions (a) and mean axial velocity (b).

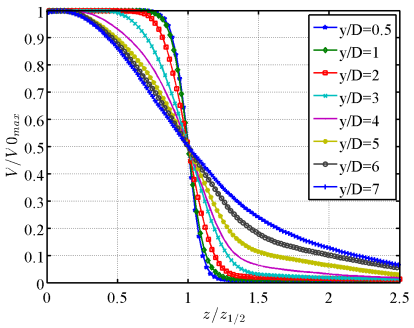

(a) Mean axial velocity profiles.

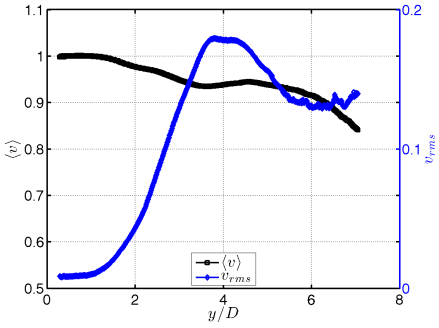

(b) Mean and rms axial centerline velocity.

Figure 5.4.2: Mean axial velocity profiles (a) where each profile is normalized by its maximum value ($V0_{max}$). Centerline mean and rms velocity (b).

From this profile we can compute the momentum thickness $\theta_e \approx 0.27\ mm$ (5.4.4) and the displacement thickness $\delta_e \approx 1.2\ mm$, which gives $\theta_e/D \approx 0.023$ and $\delta_e/D \approx 0.1$.

$$\theta_e = \int_0^\infty \frac{V}{V_0}\left(1 - \frac{V}{V_0}\right)\Big|_{y/D=0.46} dz \quad ; \quad \delta_e = \int_0^\infty \left(1 - \frac{V}{V_0}\right)\Big|_{y/D=0.46} dz \tag{5.4.4}$$

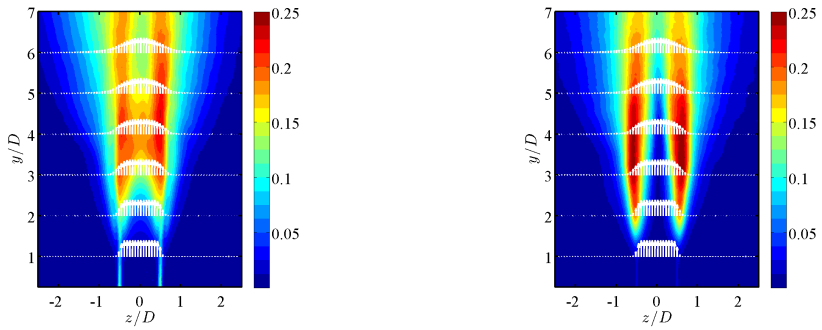

(a) Axial rms velocity field (v_{rms}). **(b)** Radial rms velocity field (w_{rms}).

Figure 5.4.3: Axial (a) and radial (b) rms velocity fields.

The mean axial velocity profile is very well fitted by hyperbolic tangent profiles [Michalke, 1984]. The level of axial velocity fluctuation v_{rms} in the jet core is less than 0.9%. A the edge of the nozzle, the rms fluctuations are about 10% of the exit velocity which are values classically attributed to turbulent jets.

The spatial enlargement and development of the jet is illustrated with 2D contours of mean axial velocity (figure 5.4.1(b)) as well as profiles of the mean axial velocity (figure 5.4.2(a)) at different locations. Each profile is normalized by its maximum value $v_{max}(y/D) = max_z(\langle v(y,z)\rangle)$ and is plotted against the radial coordinate z normalized by local jet mean velocity half-width, $z_{1/2}(y)$. The half-width is defined as the radial location at which the local jet mean velocity falls to one-half its centerline value. 95% of the exit velocity is maintained in the core of the jet till $y/D = 4$ and 90% till beyond $y/D = 6$.

One can notice that the mean velocity field does not exhibit a perfect line symmetry of axis $z/D = 0$, especially between the $y/D = 3$ and $y/D = 4$ streamwise locations. This phenomenon can be noticed in the axial rms velocity contour (figure 5.4.3(a)), the positive shear layer ($z > 0$) exhibits a higher rms intensity compared to the negative shear layer ($z < 0$). This phenomenon is less visible on the rms radial velocities (figure 5.4.3(b)). Another interesting feature of our jet flow is the behavior of the mean axial centerline velocity, displayed in figure 5.4.2(b), where the mean velocity does not decrease monotonically as classically expected between $y/D = 3$ and $y/D = 4$. It first decreases from 0 y/D to 3.5 y/D, then increases from 3.5 y/D to about 4.5 y/D before finally decreasing.

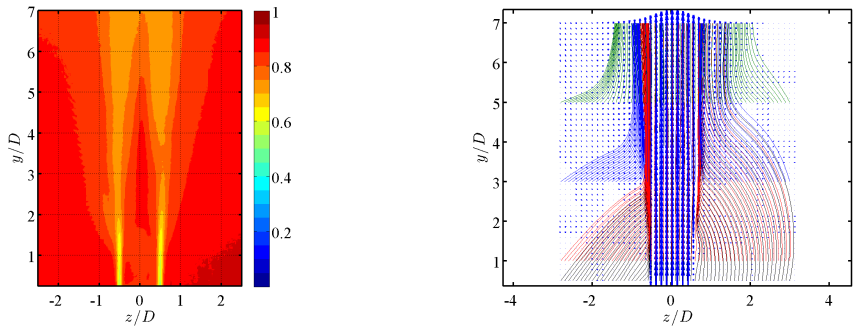

(a) Mean correlatin score **(b)** Streamlines for mean velocity field

Figure 5.4.4: Mean correlation score and streamlines

One possible interpretation of this issue could be that an outside flow is present in the flow field and jets are known to respond strongly to outside perturbations. This perturbation can be seen in the flow streamlines (figure 5.4.4(b)) in the $z > 0$ region of the jet where a left to right perturbation seems to deviate the mean flow to the right, before finally going to the left and the shear layer as expected by the entrainement of the ambient fluid to the jet core. This outside perturbation, combined with the initial output conditions of the jet will influence the jet development. However, it is difficult to know what effect is predominant and what is responsible for such and such feature of the flow. Today, numerous experimental studies [Courtier, 2015] as well as numerical research [Kim and Choi, 2009] still investigate the influence of initial conditions on the development of the jet. The issue is still not fully understood in fluid dynamics.

Another remark on the results is about the 2D-PIV measurement quality. Indeed, figure 5.4.2(b) shows that the rms centerline velocity does not seem to be fully converged yet for $y/D > 5$. This can be explained by the fact that, as the streamwise location increases, the size of the turbulent scales decreases. This means that velocity gradient in the interrogation window increases, therefore increasing the measurement noise. This is visible in the mean correlation score map figure 5.4.4(b) where the correlation score decreases for increasing y/D. The correlation score can be seen as the value of the normalized peak of the correlation map [Champagnat et al., 2011]. Values range from 0 to 1, 0 being the worst case and 1 being the best possible correlation over an interrogation window between the two pulses. In 2D-PIV, the correlation score is directly linked to the overall quality of the measurement.

5.5 Conclusion

This chapter was devoted to the description of our experimental setup which includes 2D-PIV and 3D-PIV systems synchronized together to measure the near field region of a turbulent jet.

We first described the measurement systems with their own properties and showed the synchronization was made. Then, we introduced the main feature of turbulent jets with a non-exhaustive overview of the theory of turbulent jets. Finally, we showed the 2D-PIV measurement that were performed on our jet to act as a reference. Knowing now the principle features of our jet, we will perform 3D-PIV measurements to assess the newly introduced algorithm PVR-SMART [Champagnat et al., 2014], also using classical tomo-SMART algorithm [Atkinson and Soria, 2009] to compare the two algorithms performance on experimental data. The results of this experimental assessment of PVR on our jet setup will be elaborated upon in the next chapter.

6 Experimental assessment of Particle Volume Reconstruction for 3D-PIV

6.1 Introduction

Our aim is to further the numerical work of chapter 3 by performing an experimental assessment of the PVR paradigm using PVR-SMART on experimental data.

The application is performed on the near field region of a turbulent round air jet at $Re_D \approx 4300$ whose features and characteristics were presented in the previous chapter. The tomographic setup was introduced in the previous chapter. To act as a measurement reference, a 2D-PIV system was synchronized with the 3D-PIV system. The 2D-PIV system and synchronization characteristics were also described in the previous chapter.

The idea is to compare reconstruction results and velocity fields from PVR-SMART and a classical reconstruction algorithm which we will refer to as tomo-SMART [Atkinson and Soria, 2009]. The 2D-PIV measurement will shed light on this comparison with a reference measurement while allowing for a seeding density estimation (see chapter 5).

This present chapter has two parts. In the first one, we discuss the different algorithm settings used for the experimental data. This includes the setting for both tomographic algorithms, especially thresholding methods when confronted to noisy data. The choice of the reconstruction PSF size for PVR-SMART is made through a-posteriori testing: different reconstruction PSF sizes are tested on a single snaphsot and the one which yields the best results will be kept in the remaining part of the study. Last, the choice for the correlation window volume size is explained.

In the second part of this chapter, we show the reconstruction and velocity field results for different seeding densities from both tomo-SMART and PVR-SMART algorithms. We first exhibit tomographic reconstruction intensity profiles linked to the reconstruction signal-to-noise (SNR_R). We then proceed to investigate statistical properties of the measured velocity fields, comparing for instance exit nozzle velocity conditions of the 3D-PIV and 2D-PIV measurements. The comparison of the reconstruction algorithms is extended to the flow divergence as well as to the statistical flow topology when investigating the statistical behavior of the velocity gradient tensor. Last, a final comparison is achieved through the visualization of coherent structures, using visualization of the Q criteria or iso-surfaces of vorticity components.

6.2 3D Algorithms setup

This section is devoted to the description of the algorithms and their setting parameters involved in the reconstruction and correlation step. First, we will describe the geometric parameters of the reconstruction and correlation volumes. Then, we will discuss the method used for image pre-processing and how we will use thresholds in the reconstruction algorithm when confronted with noisy images. Then, we will investigate the choice of the particle image size, or PSF size for PVR-SMART algorithm. Last, we will discuss the choice of the main parameter for the correlation step, namely the size of the Interrogation Volume (IV) for the 3D-PIV.

6.2.1 3D-PIV Volumes

From the calibration step, and an estimation of the laser illumination area, one can define the geometric characteristics of the volumes for the reconstruction and correlation step. The laser illumination area has an $x = cste$ cross section whose dimensions (height and depth) we estimated. The depth was estimated by reconstruction intensity profiles and the height was estimated on the images. The laser thickness on the $\vec{z}$ axis was found to be about 14.5 mm ($[-8\ mm\ ,\ 6.5\ mm]$) and the height on the $\vec{y}$ axis is about 86 mm ($[-36\ mm\ ,\ 50\ mm]$).

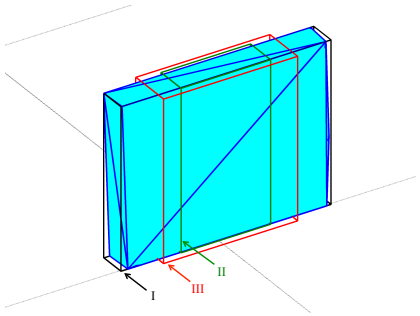

Figure 6.2.1: Tomographic volumes visualization : **Volume I** cuboid containing Intersection volume. **Volume II**: working volume for reconstruction and correlation.**Volume III**: volume used for the tomographic reconstruction intensity profiles

Here, we define 3 cuboids (see table 6.2.1) that are visualized in figure 6.2.1. They all have the same height, given by the laser height. The first volume is the smallest cuboid containing the intersection volume of the camera's field of view and the laser sheet. We will call this **Volume I**. It is the largest useful cuboid on which we can do a reconstruction. However, this volume contains a large volume of fluid at rest. This is why we restricted the extension of the volumes on the x axis to several jet diameters. The volume used for the reconstruction and correlation (**Volume II**) is the same for both steps and was chosen as the cuboid of depth $\Delta_z = [-10\ mm\ ,\ 7\ mm]$ and width $\Delta_x = [-2.D\ ,\ 2.D]$. For the computation of tomographic reconstruction intensity profiles, we chose a larger x extension $\Delta_x = [-3.D\ ,\ 3.D]$ and larger depth. This is referred to as **Volume III**. We used two depth extensions : $\Delta_z = [-12.5\ mm\ ,\ 11\ mm]$, it corresponds to a symmetric enlargement of 30% with respect to the laser thickness and $\Delta_z = [-15\ mm\ ,\ 15\ mm]$ for a larger enlargement extension. For high seeding density cases, we used the smaller extension due to computation issues.

The volumes properties are summed up in table 6.2.1. The ratio between voxel size and pixel size sets the volume discretization size. We use for tomo-SMART a $v/p = 1$ ratio and for PVR-SMART a $v/p = 1/2$. The correlation for tomo-SMART and PVR-SMART is done on a $v/p = 1$ grid. For the $v/p = 1$ grid, the resolution is 18.5 voxels/mm. For the $v/p = 1/2$ grid, the resolution increases to 37 voxels/mm.

	Volume I	**Volume II**	**Volume III**
Δx (mm) Δy (mm)	$[-56\ ,\ 56]$ $[-36\ ,\ 50]$	$[-24\ ,\ 24]$ $[-36\ ,\ 50]$	$[-36\ ,\ 36]$ $[-36\ ,\ 50]$
Δz (mm)	$[-8\ ,\ 6.5]$	$[-10\ ,\ 7]$	$[-12.5\ ,\ 11]$ $[-15\ ,\ 15]$
$v/p = 1$ (vox)	$2093 \times 1597 \times 271$	$893 \times 1597 \times 317$	$1337 \times 1597 \times 437$ $1337 \times 1597 \times 559$
$v/p = 1/2$ (vox)	$4185 \times 3195 \times 539$	$1783 \times 3195 \times 632$	$2675 \times 3195 \times 874$ $2675 \times 3195 \times 1115$

Table 6.2.1: 3D Volumes properties

6.2.2 Image Pre-Processing

This section focuses on our use of image pre-processing for the 3D-PIV images. Image pre-processing is used to enhance image contrast and consequently increase the quality of tomographic reconstruction. In real experiments, image pre-processing was shown to have a strong impact on the reconstructed volumes [Elsinga et al., 2005], [Scarano, 2013], [Thomas et al., 2010] and [Fukuchi, 2012]. Pre-processing can alter the size and shape of the particles in the images and since PVR-SMART needs the size of the PSF, it is interesting to understand which pre-processing is best suited to PVR-SMART. We will therefore investigate here the different image pre-processing that we use for tomo-SMART as well as for PVR-SMART.

As in [Lynch and Scarano, 2014], we chose a conservative behavior towards image pre-processing, selecting the pre-processing techniques that would the least alter the signal in the images. Indeed, since in PVR, the PSF size is needed, we chose the pre-processing that would not alter the PSF size. Image pre-processing consists of two steps :

1. Subtraction of historical minimum pixel-wise : the historical minimum at each pixel over 20 images is calculated for each camera. The images are then subtracted by the corresponding minimum. This was first used by [Fukuchi, 2012] and then by [Lynch and Scarano, 2014].

2. Intensity normalization, also called histogram stretching : this is done by transforming each recorded image I with intensity values in the range (Min, Max) into a new image I_N with the intensity values in the range (Min_N, Max_N). We chose a linear normalization :

$$I_N = (Max_N - Min_N)\,\frac{I - Min}{Max - Min} + Min_N \tag{6.2.1}$$

We used $(Max, Min) = (max(I), min(I))$ and $(Max_N, Min_N) = (5000, 0)$. This was done to account for the Mie scattering and the intensity difference between cameras. One may add that this will not change the signal-to-noise ratio (SNR) in the images.

Once those two operations are applied onto the images, residual noise still exists and needs to be thresholded for the reconstruction step. Indeed, keeping image noise would increase the number of ghost particles and lower the reconstruction quality. This is the subject of section 6.2.3.2 below.

6.2.3 Data Processing

6.2.3.1 Reconstruction algorithm

The reconstructions are done using a classical tomo-SMART algorithm and our PVR-SMART reconstruction algorithm (see chapter 3). Both methods are initialized with the same MLOS field. Tomo-SMART and PVR-SMART use different weigthing matrices and grid resolutions but the inversion algorithm mechanism is the same: we used a SMART (Simultaneous Multiplicative Algebraic Reconstruction Technique) algorithm [Atkinson and Soria, 2009]. We used 25 iterations with a relaxation parameter set to 1.0. We did not investigate the impact of the relaxation parameter combined with the number of iterations on the quality of the reconstruction as in [Thomas et al., 2014], however, this would be an interesting study for future work.

PVR-SMART has two tuning parameters that need to be set : the reconstruction PSF size (see) and the size of the Gaussian filtering for the "blob reconstruction". The Gaussian filtering is here to adapt the particular approach of PVR, yielding a sparse volumic representation of point particles, to a classical blob correlation paradigm used in classical 3D-PIV [Champagnat et al., 2014]. We showed in chapter 4 that our FOLKI-3D correlator was well adapted to correlate 3D Gaussian blobs of 0.6 standard deviation. We chose this value for the Gaussian filtering in PVR-SMART.

6.2.3.2 On the use of Thresholds in the reconstruction

In this section, we discuss and investigate our choice of threshold values for the images during the reconstruction step (for both MLOS initialization and SMART algorithm). For the sake of clarity, we wish to emphasize the fact that the thresholds under consideration are applied onto the images, not on any of the reconstructed volumes during the iterative steps of the reconstruction, as for instance in Fast-MART [Lynch and Scarano, 2014].

During the MLOS step : in numerous 3D-PIV reconstruction methods, the initialization is done through the MLOS step [Atkinson and Soria, 2009]. Its purpose can be seen as a pre-selection of non-zero voxels that will be used in the reconstruction algorithm. This pre-selection is done thanks to the combined effects of multiplicative lines of sight and thresholded images where the background intensity is put to zero. For the MLOS step to be effective, one thus needs to threshold the residual noise in the images.

The signal used in PIV can be seen as the sum of an effective signal (the particle image) and camera noise (see figure 6.2.2). A low threshold value will not eliminate low intensity tracer particles nor will it affect the particle shape much, but this will also keep camera noise that will generate ghost particles in the reconstructed volume, ultimately impacting the velocity estimation step (see 1D representation figure 6.2.2, Threshold 1). A high threshold value will eliminate camera noise and have fewer ghost particles but will eliminate low intensity tracers. This will also reduce the size of the

particle in the images by thresholding pixels around the particle peak which leads to reducing the size of the reconstructed particle (see 1D representation figure 6.2.2, Threshold 2). This is detrimental to the velocity estimation step which needs bloby particles.

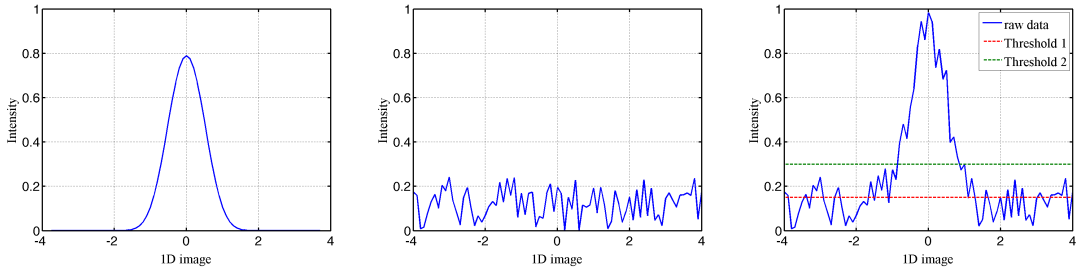

Figure 6.2.2: 1D representation of PIV images, with an ideal particle image (left), camera noise (middle), and the sum of camera noise and particle image (right). Threshold 1 and 2 illustrates the importance of the threshold for the MLOS step

To choose the threshold value, one technique is to compute the histogram of the residual noise by collecting noise sample values from non-illuminated areas in the images (should they exist) and threshold the images while knowing the noise dynamic range. This is the technique that we will consider for the rest of the thesis for the MLOS step. The threshold value is given as the percentage of thresholded noise.

During the SMART reconstruction : during the iterative steps of the reconstruction algorithm, the updated voxel projections are compared to the recorded images. A question remains whether to use the thresholded images or the non-thresholded images using the same threshold levels as in the MLOS step. To the best of our knowledge, this question has never been investigated. This question is particularly relevant since the use of thresholded images in the SMART algorithm can lead to peaked reconstructed particles and/or missed particles. Indeed, during the SMART algorithm, if the influence area of a voxel ($\boldsymbol{x_i} = W\boldsymbol{y_i}$) includes a thresholded pixel, due to the multiplicative and simultaneous nature of the algorithm, the updated voxel will be put to zero. This is detrimental when the thresolded pixel belongs to the PSF of a particle. This issue is particularly relevant when the influence area of a voxel in the weighting matrix spreads over several pixels. This is the case in PVR-SMART for large PSF size. An effective counter strategy could be to use the raw images in the SMART algorithm so as to reconstruct bigger sized particles. Non-thresholded images are hereafter call "raw" images.

We introduced the threshold issue in the MLOS step as well as the SMART algorithm. This issue is summed up in figure 6.2.3.

In the following sections, a study is carried out to understand and choose the adapted threshold levels and techniques both in the MLOS step and in the SMART algorithm. The aim is to choose the MLOS level (MLOS threshold $x\%$) and either or not to use raw or thresholded images in SMART. Here is the outline of the study : general considerations on the MLOS step and SMART regarding thresholds are given, this leads to a one-particle test case to illustrate the issue. Last, 3D synthetic tests as well as a test on experimental data are used to conclude the study. Both algorithms (tomo-SMART and PVR-SMART) will be put under consideration for this study.

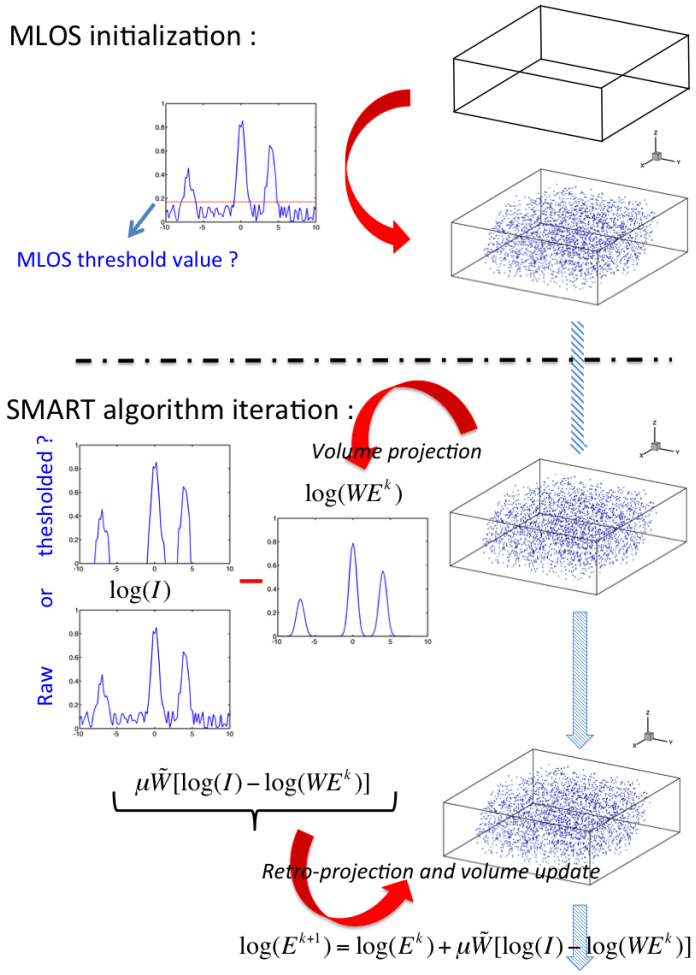

Figure 6.2.3: Representation of the threshold issue in the MLOS step and SMART algorithm

Synthetic test - One particle case : to illustrate our idea, we performed a synthetic test that involves the reconstruction of a single particle using both tomo-SMART and PVR-SMART reconstruction. The particle was at the center of the volume and four cameras (32×32 pixels) were used to reconstruct. The particle size was $\sigma_{PSF} = 0.4$ and its peak intensity in the images was 40. The camera noise was taken as a Gaussian distribution of mean 10 and of standard deviation $\sigma_{Noise} = 2$. See image in figure 6.2.4.

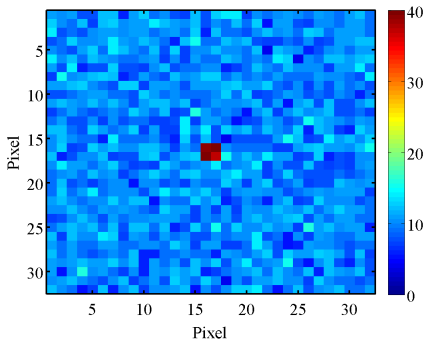

Figure 6.2.4: Image for one particle case

We used two different MLOS threshold values : 10 and 15, representing respectively 50%

and 99% of the noise thresholded. For the sake of clarity, to refer to the MLOS threshold level, we write : MLOS x %. We performed SMART reconstruction with thresholded images, hereafter denoted by "thresh" and raw images. To refer to the threhold technique in SMART, we use either "SMART raw" or "SMART thresh".

	MLOS 50%	**MLOS** 99%
tomo-SMART	raw	raw
tomo-SMART	thresh	thresh
PVR-SMART	raw	raw
PVR-SMART	thresh	thresh

Table 6.2.2: Summary of the different MLOS threshold values and threshold techniques in SMART used for the one-particle case.

Results are shown in figure 6.2.5 where we see 2D slices of the reconstructed volume. Focusing on the tomo-SMART algorithm, one sees that choosing high threshold values allows to eliminate the camera noise (figure 6.2.5(b) and figure 6.2.5(d)). When also using thresholded images in the SMART (figure 6.2.5(b)), the reconstructed particle is made of a single voxel. Using the raw images enables to recover the reconstructed particle as blob. PVR-SMART displays the same behavior as tomo-SMART towards the threshold levels and the use of raw images. The difference being that the reconstructed particles are wider than for tomo-SMART, due to the Gaussian filtering at the end of the PVR-SMART algorithm. This illustrates the idea presented in the introduction of this section. From this simple study, we clearly see that thresholds in MLOS step and in the SMART algorithm have a strong impact on the reconstruction and on the spikiness of a reconstructed particle. To understand what happens when a full set of particles is being reconstructed and how this technique behaves in light of ghost particles, one must do full 3D synthetic tests. This is the subject of our next section.

Synthetic tests-3D tests : in order to have a more realistic understanding of the thresholds techniques, we performed 3D synthetic tests. The findings will guide our decision-making process concerning the best strategy to adopt for real experiments.

We used the same setup as in our jet experimental setup. Four cameras with calibrations taken from the experimental calibrations of the jet setup were used. The laser vertical height ($\Delta_y = 86mm$) and depth ($\Delta_z = 20mm$) were matched to the ones in our experiment. The laser intensity profile was modeled as a Gaussian profile of maximum intensity $I_0 = 150$ and standard deviation $\sigma_{laser} = 5mm$. Tracer particles are uniformly distributed in the light sheet volume. The scattered light is proportional to the square of the particle diameter d_p and a polydisperse seeding was used. The particle's PSF size was taken as $\sigma_{PSF} = 0.4$, which is wider than the theoretical value $\sigma_{PSF} =\approx 0.3$ computed in chapter 5. The volumic particle density was set so as to have a $ppp = 0.05$ which gives a source density equal to $N_S = ppp.\frac{\pi}{4}.d_\tau^2 \approx 0.1$. The camera noise was taken as a Gaussian distribution of mean 10 and of standard deviation $\sigma_{Noise} = 3$ which is close to what we observe in the experiment. We used two different MLOS threshold values : 15 and 25, relatively (95% and 99% of the noise is being thresholded).

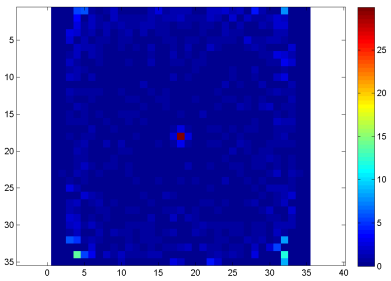

(a) tomo-SMART, MLOS 50 %, SMART raw

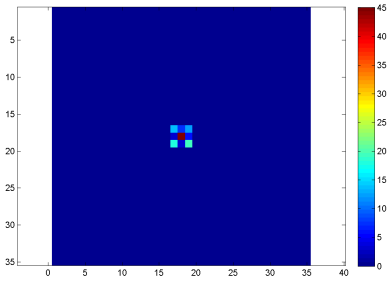

(b) tomo-SMART, MLOS 99 %, SMART raw

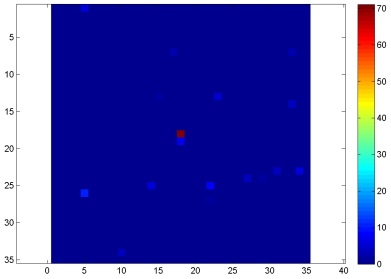

(c) tomo-SMART, MLOS 50 %, SMART thresh

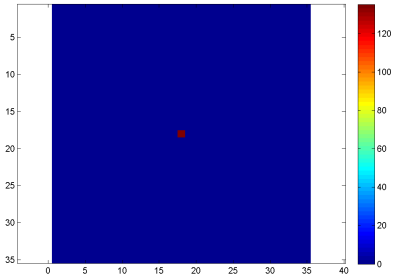

(d) tomo-SMART, MLOS 99 %, SMART thresh

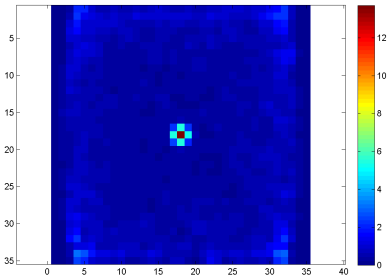

(e) PVR-SMART, MLOS 50 %, SMART raw

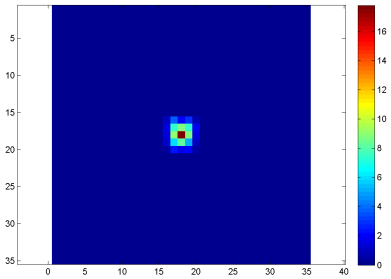

(f) PVR-SMART, MLOS 99 %, SMART raw

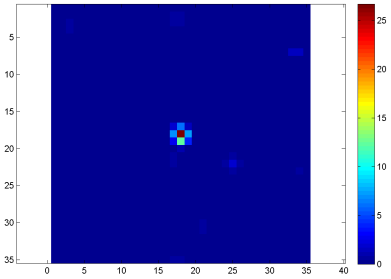

(g) PVR-SMART, MLOS 50 %, SMART thresh

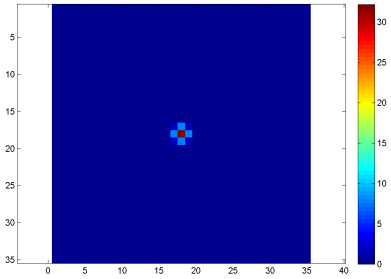

(h) PVR-SMART, MLOS 99 %, SMART thresh

Figure 6.2.5: 2D slice in the z=0 plane of the reconstructed volume for two MLOS threshold values and two threshold techniques in SMART. (left) : MLOS 50 %, (right) : MLOS 99 %

	MLOS 95%	**MLOS** 99%
tomo-SMART	raw	raw
tomo-SMART	thresh	thresh
PVR-SMART	raw	raw
PVR-SMART	thresh	thresh

Table 6.2.3: Summary of the different MLOS threshold values and threshold techniques in SMART used for the 3D synthetic tests.

Several reconstruction quality criteria were used to characterize the reconstruction. First, we used the classical Q quality factor using the ground truth built by expanding locally the physical particles to a 3D Gaussian blob. We also used metrics measuring the detection performance of the methods (TP/FP/FN) introduced in chapter 2, in table 6.2.4. We also computed the number of detected maxima and the number of voxels lit. Intensity profiles, reconstruction histograms and 2D slices of the reconstructed volumes are shown respectively in figure 6.2.6 and figure 6.2.7.

Let us first focus on the results of the **tomo-SMART** :

For **MLOS** 99%**:** SMART threshold has a strong impact on the Q factor (from 0.55 for thresh to 0.78 for raw), however for low MLOS threshold level, the impact of the SMART threshold is less significant (from 0.72 to 0.74 for Q factor). From the detection performance, one can see that for high MLOS threshold levels, using raw images in the SMART algorithm leads to increasing the number of real detected particles (from 43 649 to 65 696, an almost 50% increase) but also to increasing the number of ghost particles (from 7 601 to 865 632). One can note that the Q factor is more sensitive to the number of real particles and their shape than the number of ghost particles especially if those ghost particles intensities are low.

For **MLOS** 50%**:** the same behavior happens at the low MLOS threshold level, the only notable difference being that the number of real particles decreases slightly (from 67 839 for raw images to 66 688 for thresh images SMART). This behavior which contrasts with previous observation can be attributed to our maxima detection method based on a "low hidden" threshold value. Using a low MLOS threshold and raw images means that the reconstruction will both keep real particles and produce a lot of ghost particles. It was shown that ghost particles get their energy and intensity from the real particles [Lynch and Scarano, 2014], and therefore decrease the energy of the real particles. Some real particles have lower intensities than our maxima detection threshold, and are counted as missing. This is why we can observe a decrease in TP when using raw images in the SMART. The number of ghost particles increases (from 112 693 to 3 185 090) which is the same behavior as in the case of a high MLOS threshold.

The increase in the number of ghost is always associated with a decrease in the Reconstruction Signal-to-Noise Ratio (SNR_R, [Lynch and Scarano, 2014]), this can be seen in the reconstruction intensity profiles since ghost particles lower the intensity of real particles (see figure 6.2.6). For the high MLOS threshold and raw SMART threshold case, the Q factor is the highest and the SNR is high enough for a good reconstruction quality (the empirical rule being that a reconstruction is good enough for the velocity estimation step for $SNR \geq 2$). Furthermore, when looking at the reconstruction histograms (see figure 6.2.6), ones sees that in this case the real particle and ghosts histogram are the furthest apart. This method will there-

fore be the one that we use in a real 3D-PIV experiment for the tomo-SMART algorithm.

Algorithm	**MLOS Threshold 15** 95%	**MLOS Threshold 25** 99%
MLOS	Q = 0.3045, P = 0.009, R = 0.92 TP = 79502, FP = 8 633 079 FN = 6 687	Q = 0.5542 P = 0.07, R = 0.77 TP = 67 070, FP =836 255 FN = 19 119
tomo-SMART raw	Q = 0.74, P = 0.02, R = 0.77 TP = 66 688, FP = 3 185 090 FN = 19 501	Q = 0.78, P= 0.07, R = 0.76 TP = 65 696, FP = 865 632 FN = 20 493
tomo-SMART thresh	Q = 0.7214, P = 0.37, R = 0.78 TP = 67 839, FP = 112 693 FN = 18 350	Q = 0.55, P = 0.85, R = 0.51 TP = 43 649, FP = 7 601 FN = 42 540
PVR-SMART raw	Q = 0.86, P = 0.17, R = 0.66 TP = 57 172, FP = 280 973 FN = 29 017	Q = 0.85, P = 0.11, R = 0.77 TP = 66 739, FP = 510 719 FN = 19 450
PVR-SMART thresh	Q = 0.8800, P= 0.71, R = 0.71 TP = 61 721, FP = 25 390 FN = 24 468	Q = 0.65, P = 0.67, R = 0.32 TP = 27 809, FP = 13 513 FN = 58 380

Table 6.2.4: Synthetic Tests Results

Let us now focus on the results for the **PVR-SMART** algorithm :

For the **MLOS** 99% **:** the use of raw or thresh SMART has a strong impact on the reconstruction. When using raw images, the number of TP dramatically increases (from 27809 for thresh to 66739 for raw). The Q factor also increases (from 0.65 for thresh to 0.86 for raw).

For the **MLOS** 95% **:** the impact of the SMART threshold is less significant (from 0.88 to 0.86 for Q factor). Using raw images in the SMART algorithm always leads to an increase in the number of ghost particles and therefore a decrease in SNR, seen in both FP detections and intensity profiles figure 6.2.7. Unlike tomo-SMART algorithm, the highest Q factors for PVR-SMART are met for the low MLOS threshold levels. This is due to the fact that even if fewer real particles are being reconstructed (about 60000 for PVR instead of 67000 for tomo-SMART), their reconstructed shape is better because of the Gaussian smoothing in PVR and significantly fewer ghost particles are being reconstructed. It is important to notice that in a real experiment, calibration errors are unavoidable and using the thresholded images in SMART may cause real particles not to be reconstructed.

Based on the Q factor and the number of ghost particles, it is difficult to select a method that is the best, there is a doubt between the MLOS 50% / SMART thresh (highest $Q = 0.88$, lowest $FP = 25\ 390$ number) and MLOS 90% /raw SMART (high $Q = 0.85$ factor highest $TP = 66\ 739$ but also the highest number of ghost particles $FP = 510\ 719$). Since synthetic criteria do not appear to be discriminating enough to determine what is the best possible method for PVR-SMART between these two cases, we will do an "a-posteriori" choice : on a real 3D-PIV experiment snapshot, both methods will be applied to make a decision based on velocity field and reconstruction criteria. This is the topic of the next section.

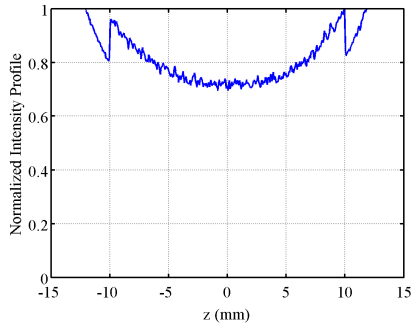

(a) tomo-SMART, MLOS 95%, SMART raw

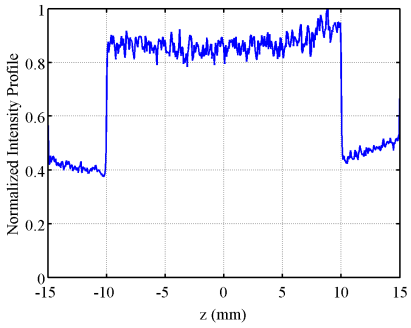

(b) tomo-SMART, MLOS 99%, SMART raw

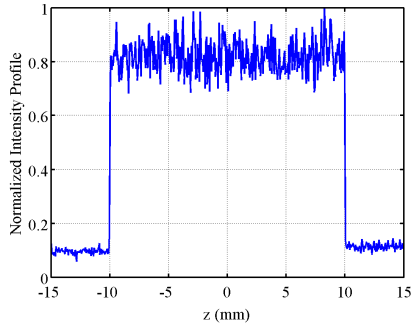

(c) tomo-SMART, MLOS 95%, SMART thresh

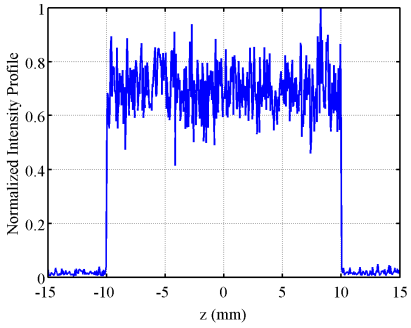

(d) tomo-SMART, MLOS 99%, SMART thresh

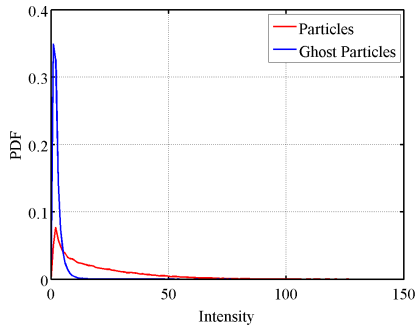

(e) tomo-SMART, MLOS 95%, SMART raw

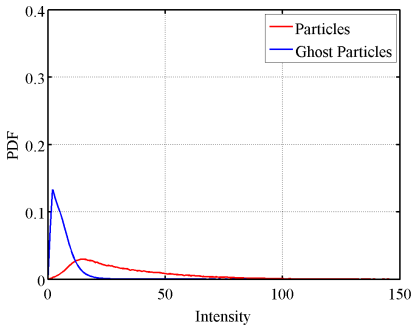

(f) tomo-SMART, MLOS 99%, SMART raw

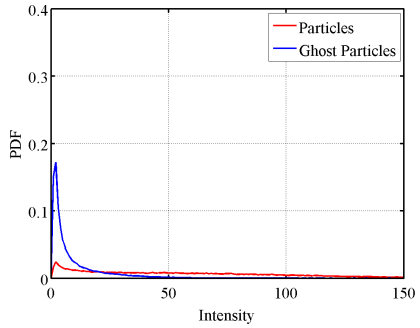

(g) tomo-SMART, MLOS 95%, SMART thresh

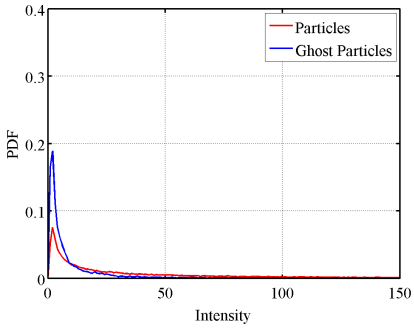

(h) tomo-SMART, MLOS 99%, SMART thresh

Figure 6.2.6: 3D tests: Intensity profiles and Reconstruction histograms for tomo-SMART.

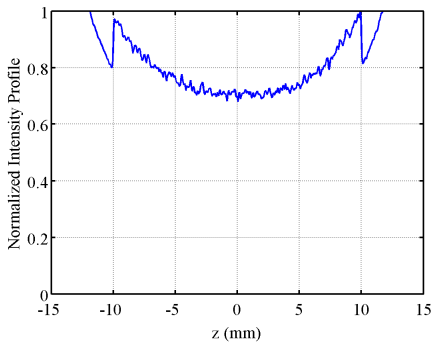

(a) PVR-SMART, MLOS 95%, SMART raw

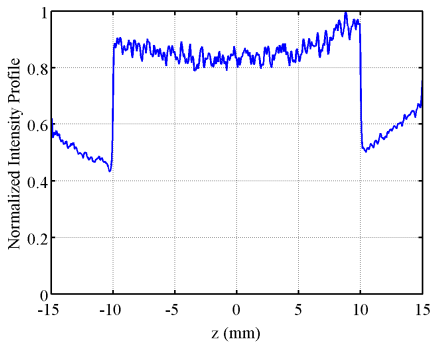

(b) PVR-SMART, MLOS 99%, SMART raw

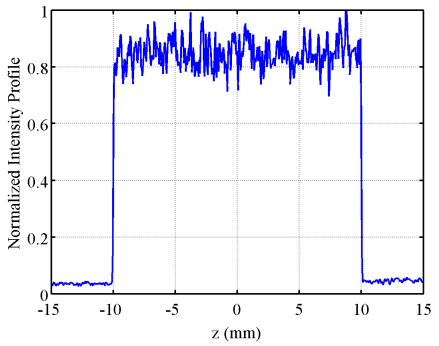

(c) PVR-SMART, MLOS 95%, SMART thresh

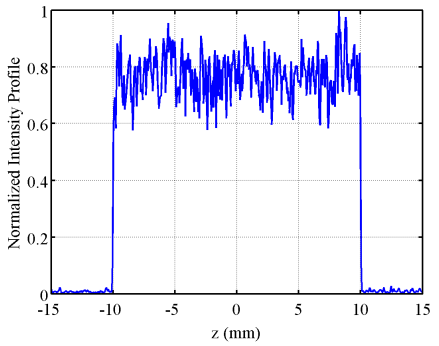

(d) PVR-SMART, MLOS 99%, SMART thresh

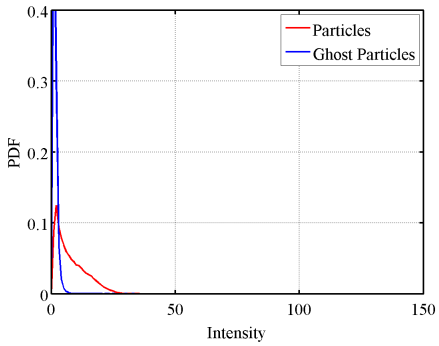

(e) PVR-SMART, MLOS 95%, SMART raw

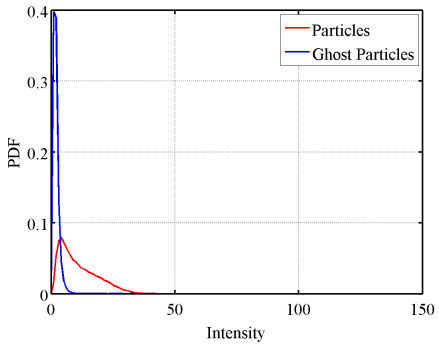

(f) PVR-SMART, MLOS 99%, SMART raw

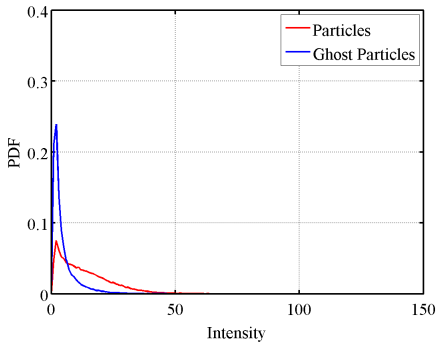

(g) PVR-SMART, MLOS 95%, SMART thresh

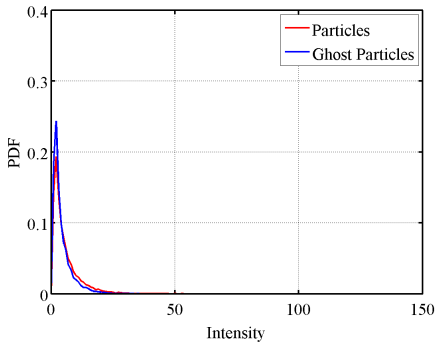

(h) PVR-SMART, MLOS 99%, SMART thresh

Figure 6.2.7: 3D tests: Intensity profiles and Reconstruction histograms for PVR-SMART.

Experimental Realization : in this section we put in practice image pre-processing and thresholding methods on real 3D-PIV measurement. We must choose for PVR-SMART between a low MLOS threshold/SMART thresh method and a high MLOS threshold/ SMART raw method. To do so, we will perform both methods on a 3D-PIV snapshot and look at the reconstruction and velocity fields.

Investigations are undertaken in the near field region of the jet. The exit nozzle diameter of the jet is $12mm$, and its exit velocity is 6 $m.s^{-1}$ ($Re_D \approx 4800$). Reconstructions were done on the same image set, with an estimated particle density $ppp \approx 0.05$. As mentioned in section 6.2.2, the first step in the pre-processing process is to subtract the historical minimum (which is computed over 20 images) and then do a re-normalization since the 2 camera systems have different dynamical ranges. Then, in order to have a good estimation of the noise distribution in the images, probability density functions of the noise in unlit areas over 20 images are computed (see figure 6.2.8). The noise distribution is computed here for camera 1 (Dantec) and camera 3 (LaVision). For every camera and every pulse, the MLOS threshold value is computed according to the percentage of noise that we want to threshold in the images. As previously, we chose two types of thresholds : a "low" 95 % of noise threshold and a "high" 99 % of noise threshold.

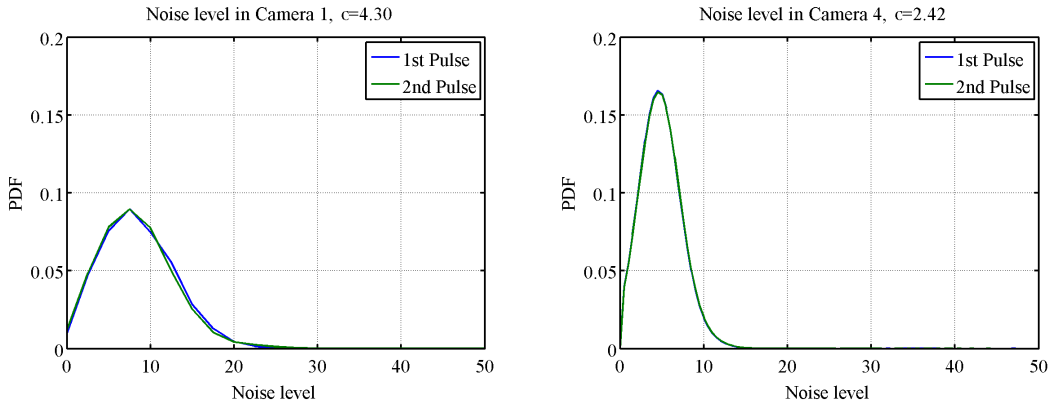

Figure 6.2.8: Camera noise distribution for camera 1 (left) and camera 3 (right)

Since the choice of threshold technique is clear for tomo-SMART, we only performed reconstructions and correlations with the PVR-SMART algorithm on our jet setup. For this reconstruction algorithm, the PSF function modeled as an integrated Gaussian function of width σ_{PSF} is unknown to the experimentalist. One can have a theoretical estimation of this function (see chapter 5). Also, as suggested recently by [Champagnat et al., 2014], PSF calibration techniques can be applied to obtain the desired information. This can lead to spatially varying PSF due to defocussing and astigmatism. The choice of PSF size is the subject of next our section. To ensure that the choice of the threshold method is not affected by the choice of PSF size so that settings can be done separately, we performed PVR-SMART reconstruction with different PSF size ($\sigma_{PSF} = \{0.2\ ,\ 0.4\ ,\ 0.6\}$). Regarding the other settings of the reconstruction algorithm, the number of iterations was set to $N_{iter} = 25$, relaxation parameter to $\mu = 1.0$. For the correlation step, we used our FOLKI-3D in-house code using a Gaussian interrogation volume of size $IV_{size} = 41$, and standard deviation of the weighting function $\frac{\sigma_{IV}}{IV_{size}} = 4$, we used $J_{Level} = 3$ for the multi-grid approach and $N_{Iteration} = 7$ for the number of Gauss-Newton iterations. For more on the choice of the correlation algorithm settings, see section 6.2.4.

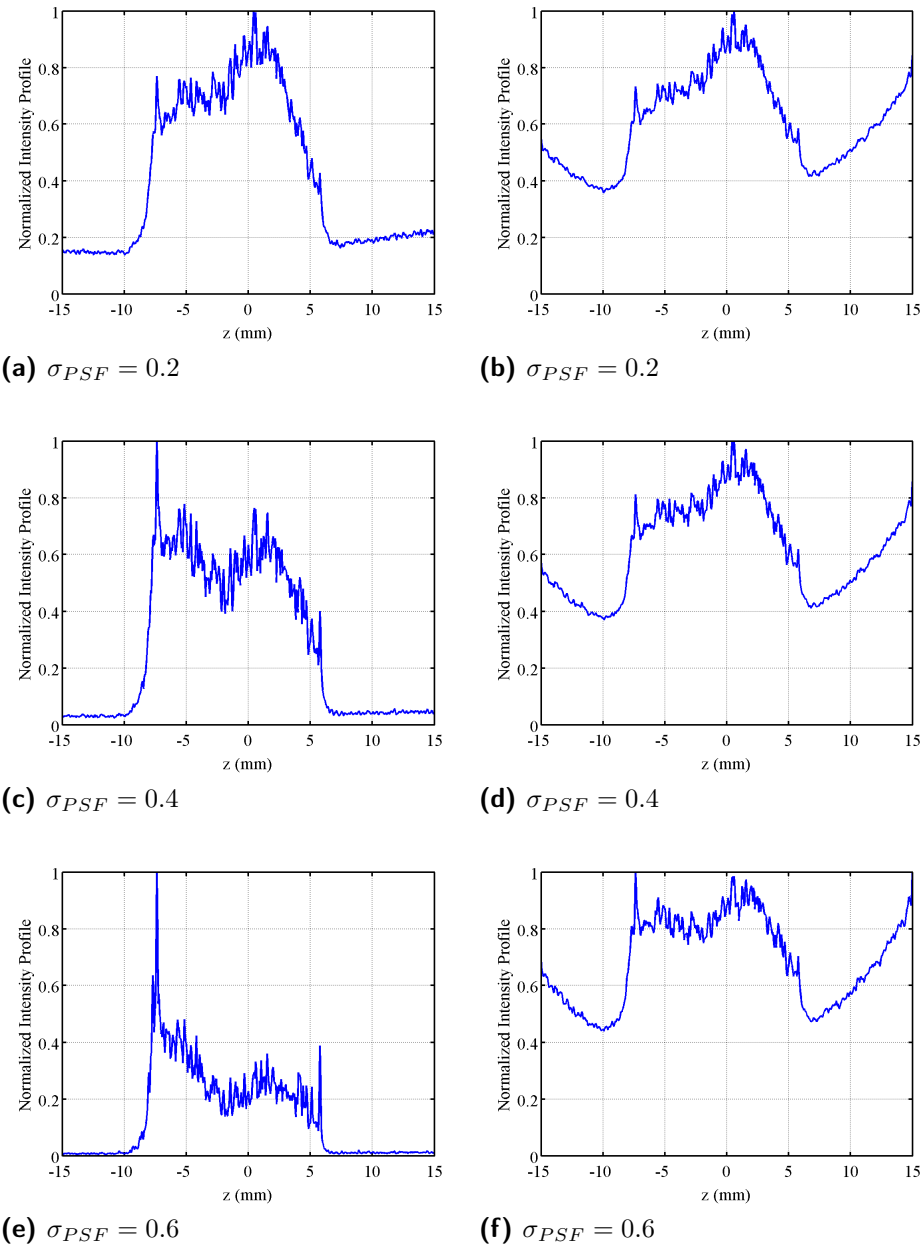

Figure 6.2.9: PVR-SMART reconstruction intensity profiles for different reconstruction PSF sizes (σ_{PSF}): **left** MLOS 95% , SMART thresh, **right** MLOS 99%, SMART raw

Figure 6.2.9 shows the reconstruction intensity profiles of the PVR-SMART reconstruction for different σ_{PSF}. One sees that for the low MLOS threshold/SMART thresh method, the SNR_R is strongly impacted by the σ_{PSF} with a dramatic decrease in quality when σ_{PSF} increases. This is expected since the bigger the σ_{PSF} is, the more likely a thresholded pixel in the near vicinity of a particle is to appear in the images, which leads to the elimination of the particle in the iteration process of the SMART algorithm. The low MLOS threshold/SMART thresh method is not robust enough to σ_{PSF}, especially when the particle PSF size is over-estimated. However, high MLOS threshold/SMART raw method is not significantly impacted by σ_{PSF} and seems robust to different σ_{PSF}. The intensity profiles are roughly identical compared to the dramatic difference of the previous method. The difference between those SNR_R is to

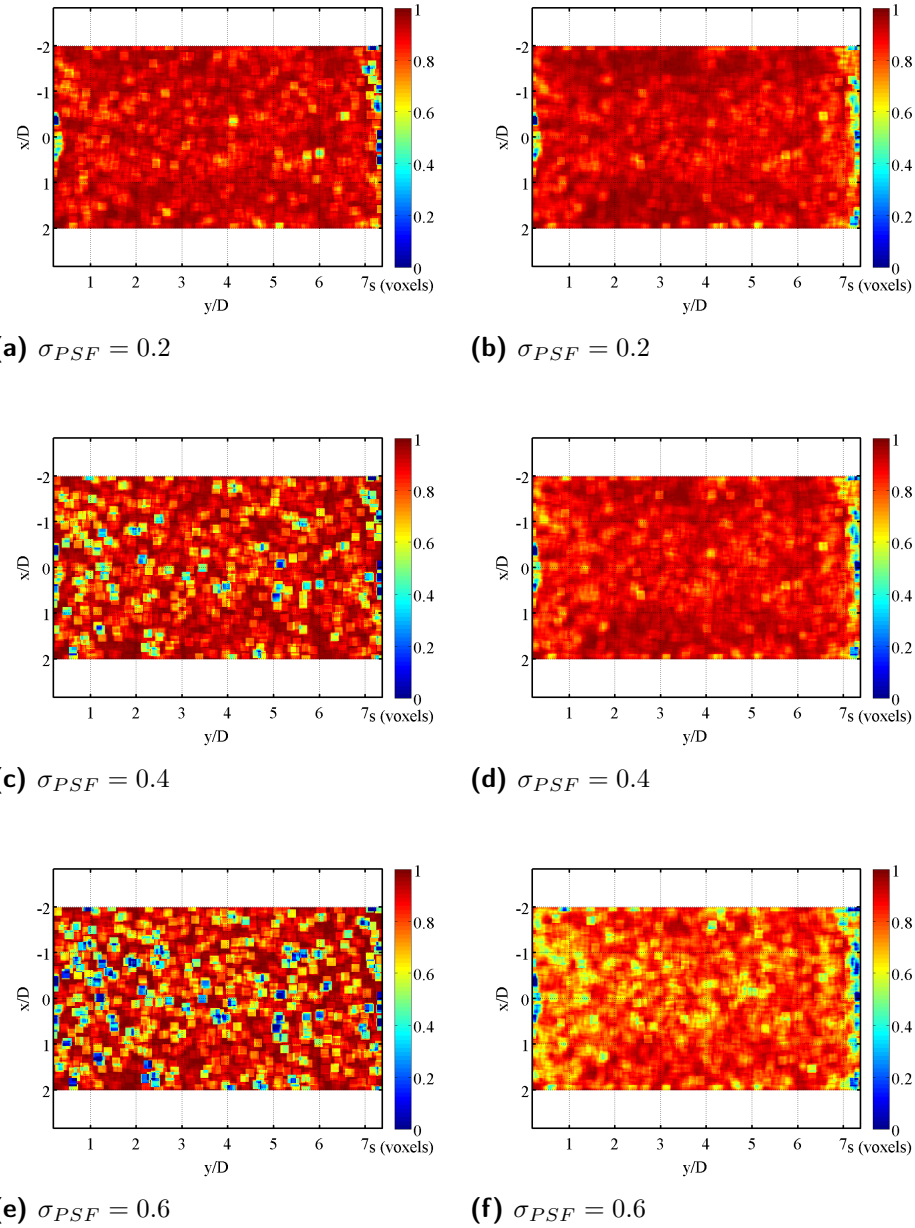

(a) $\sigma_{PSF} = 0.2$ **(b)** $\sigma_{PSF} = 0.2$

(c) $\sigma_{PSF} = 0.4$ **(d)** $\sigma_{PSF} = 0.4$

(e) $\sigma_{PSF} = 0.6$ **(f)** $\sigma_{PSF} = 0.6$

Figure 6.2.10: PVR-SMART Correlation score map in $z = 0$ plane for different reconstruction PSF sizes (σ_{PSF}): **left** MLOS 95% , SMART thresh, **right** MLOS 99%, SMART raw

be investigated in the next section on the choice of σ_{PSF}.

To get a clearer understanding of how the correlation step is impacted by the threshold methods, we show the correlation score map in the $z = 0$ plane (see figure 6.2.10). As previously, the correlation score map is strongly impacted for the low MLOS threshold/SMART thresh method. The more the PSF size increases, the more noisy the map is, with low score appearing in the map down to 0 or 0.1 values, with patchy windows of low score which is the proof that there are not enough particles reconstructed for a good correlation. For the high MLOS threshold/SMART raw method, the same trend appears but its magnitude is far less noticeable than previously, since even for the $\sigma_{PSF} = 0.6$, the lowest score values in the jet stream are about 0.5 to

0.6. As a conclusion, the high MLOS threshold/SMART raw method is way more robust and gives better SNR_R and correlation map than the low MLOS threshold/SMART thresh method. Whatever the reconstruction σ_{PSF} is, we will choose from now on, and for the rest of the study, to use the high MLOS threshold (99%)/SMART raw method for PVR-SMART.

Preliminary conclusion : the purpose of our study in 6.2.3.2 was to choose the method of thresholds in the MLOS step and the SMART algorithm for both tomo-SMART and PVR-SMART algorithms.

To do so, we illustrated the issue with the reconstruction of one single particle, we performed 3D synthetic test with a fixed image source density ($ppp \approx 0.05$ and $\sigma_{PSF} = 0.4$). From those synthetic tests, a preferred method emerged for the tomo-SMART algorithm. We will first use a high MLOS threshold value : this eliminates a large amount of noise in the images and avoids numerous ghost particles in the reconstruction. For the SMART algorithm, we will use raw images : this prevents the real reconstruction particles from shrinking in size and from reconstructing them as blobs of the same size as their images.

The experimental validation for PVR-SMART was done on a single 3D-PIV snapshot at a particle image density estimated at 0.05. Results showed us that the same threshold method as for tomo-SMART was more robust and gave good results. This is why we will use this method also.

We will now focus on two other paramters : the choice of reconstruction PSF size for PVR-SMART and finally the choice of correlation Interrogation Volume size.

6.2.3.3 On the choice of the reconstruction PSF size for PVR-SMART

PVR-SMART reconstruction algorithm requires the user to give a PSF size (σ_{PSF}) for the weight matrix. The theoretical estimation of the PSF size in chapter 5 showed that the standard deviation of the PSF in the focus plane was about 0.3, with a variation in the laser volume which led to 0.6 σ_{PSF} on the edge of the laser volume. As mentioned in [Champagnat et al., 2014], the algorithm provides a principled approach for dealing with spatially varying PSF. Since PVR builds the weight matrix from samples of the PSF, PSF calibration techniques can be used as suggested by [Reichenbach et al., 1991] or more recently by [Delbracio et al., 2012] and [Schanz et al., 2010]. However, since it is the first time that PVR is being tested on an experimental setup, our goal here is to use PVR with a single fixed PSF size for each camera. The use of PSF calibration and varying PSF and the gain obtained from a non-varying PSF reconstruction is a valuable perspective for future work.

To estimate the PSF size as in [Schanz et al., 2013a] we choose a least-square estimation of the PSF size in the images. To do so, we assume an "optics+pixel" PSF made of a Gaussian function $h(x, y)$ with standard deviation σ_{PSF} averaged on the pixel surface, assuming a 100 % fill factor. See chapter 3 for extensive model description. On the pixel array of the CCD camera, noise is present and can be modeled as an added function. Considering a particle at $\mathbf{X}$ in 3D space, F the geometric projection function in the image, and h the Point Spread Function, the intensity in the pixel $\mathbf{k}$ is then :

$$I(\mathbf{k}) = I_0.h(\mathbf{k} - F(\mathbf{X})) + \beta_{Noise}(\mathbf{k}) \tag{6.2.2}$$

β_{Noise} represents the camera noise which can be seen as a random variable. Its probability density distribution is a function of the camera's optics and sensor. To estimate the size of the PSF, a peak-finding algorithm tracks local maxima in the image and collect PSF samples. A PSF sample is 5×5 pixel array. To avoid any overlapping in the PSF samples, we eliminated PSF samples that were adjacent to one another and/or overlapping. Then, on each PSF sample, shape fitting was achieved through 2D non-linear least-square fitting to find the 5 unknowns $(I_0, x, y, \sigma_{PSF}, \beta_{Noise})$. β_{Noise} is modeled as a single constant over the whole PSF sample, even if it is a function of pixel $\mathbf{k}$.

The fit was done after the images were pre-processed (section 6.2.2). Results on a 3D-PIV snapshots at an estimated $ppp \approx 0.05$ are shown in figure 6.2.11. The PDFs are not converged, this is due to the relatively low number of samples on which the fit is done. Furthermore, in all 4 cameras the estimated distribution of σ_{PSF} are bi-modal with two peaks : a sharp one around 0.15 and a large one around $0.3 - 0.4$. A further study, that lies outside the scope of this manuscript, suggests that the bi-modality appears for small σ_{PSF} combined with camera noise, especially when the noise standard deviation becomes important. The mean values of the estimated σ_{PSF} distribution are 0.34, 0.30, 0.22, 0.27 for respectively camera 1, 2, 3 and 4. Those values seem physical and agree rather well with what we can see in the recorded images and with the theoretical estimation (see chapter 5). However, the bi-modal distribution means that our fitting method is not reliable enough and not robust-to-noise enough for us to use the values of estimated PSF size in PVR-SMART, let alone use this fitting method in the calibration process of a varying PSF function. Further work should be done to understand how such a critical situation can avoided to ensure a more reliable estimation of the PSF size.

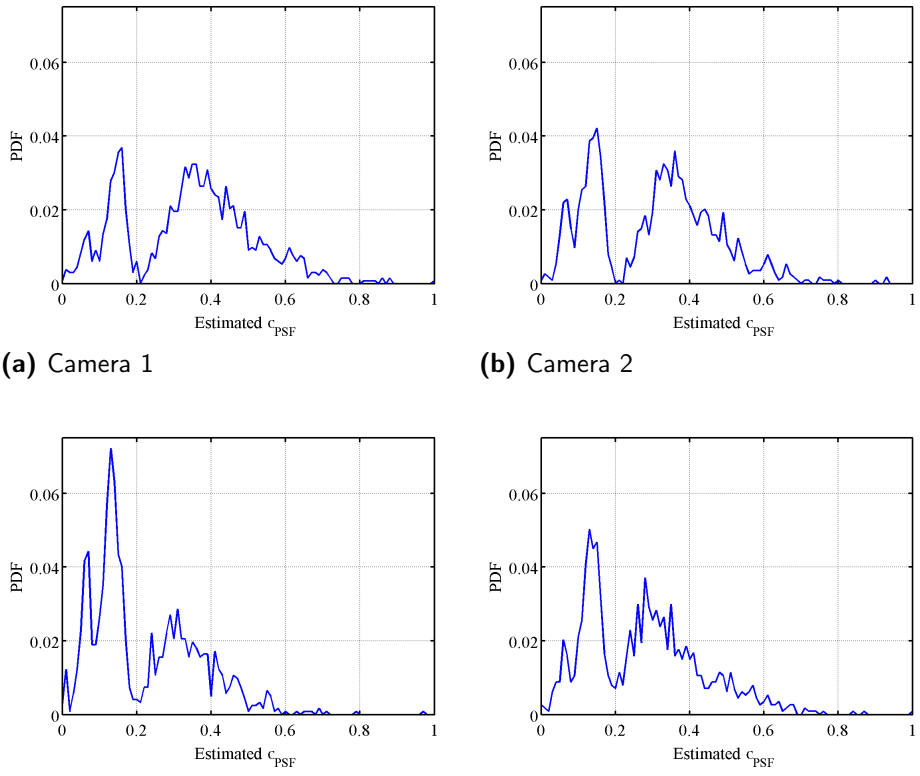

(a) Camera 1 **(b)** Camera 2

(c) Camera 3 **(d)** Camera 4

Figure 6.2.11: PDF of estimated σ_{PSF}. The non-linear least-square fit was done on 1327 PSF samples for camera 1, 1138 for camera 2, 1219 for camera 3, 1133 for camera 4

For the choice of the reconstruction σ_{PSF} we chose to do an a-posteriori choice. On the same snapshot as 6.2.3.2, we reconstructed the particle volumes using PVR-SMART with different σ_{PSF}. We will choose the reconstruction σ_{PSF} as the one which overall gives the most physical results. For the sake of simplicity, the same reconstruction σ_{PSF} was used for every camera. The reconstruction algorithm settings were the same as in 6.2.3.2 as well as the settings of the correlation algorithm.

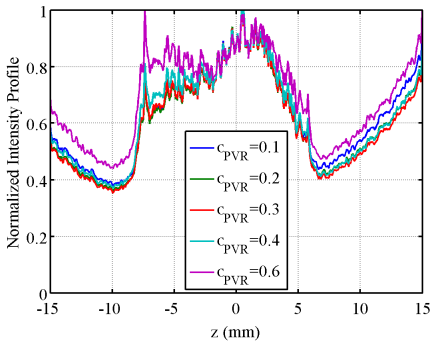

Figure 6.2.12: Normalized Intensity Profiles for different reconstruction $\sigma_{PSF} = \{0.1, 0.2, 0.3, 0.4, 0.6\}$

The results of the tomographic reconstruction are summed up in the intensity profiles in figure 6.2.12. The different σ_{PSF} tested were $\{0.1\ ,\ 0.2\ ,\ 0.3\ ,\ 0.4\ ,\ 0.6\}$. Following Lynch 2014 we can compute the different SNR_R. It is defined as the ratio of reconstructed intensity inside the illuminated area (E_I) and that outside (E_o). We considered the illuminated region as the area in between $-7\ mm$ and $5\ mm$. E_I was defined as the mean intensity over this area. For E_o, we defined it as the mean value of the two local minima of the profile located at the extremity of the laser sheet. The respective SNR_R are $\{1.88\ ,\ 1.97\ ,\ 2.02\ ,\ 2.01\ ,\ 1.82\}$. From the theoretical estimation and the recorded image investigation, we are inclined to select a PSF size of 0.2/0.3 standard deviation. The computation of SNR_R suggests that the reconstruction volumes with $\sigma_{PSF} = 0.2/0.3/0.4$ are fairly similar. To further distinguish those 3 candidates, we will look at the results of the displacement estimation step using those 3 reconstruction parameters.

Using a 41 voxels IV size, we computed the displacement fields for $\sigma_{PSF} = \{0.2, 0.3, 0.4\}$. Results are shown in figure 6.2.13 in the $z = 0$ cross-section, where we investigate the correlation score and the displacement in the $\vec{x}$ direction, u. One sees that the results are fairly similar and the differences are minimal. However, one can notice that the best results are obtained for $\sigma_{PSF} = 0.2$ with scores closer to 1 and fewer patchy areas of low score than the other results, which means that the correlation quality is higher for $\sigma_{PSF} = 0.2$. Displacement-wise, this means that the displacement field should less noisy for $\sigma_{PSF} = 0.2$ than for the other values. This is indeed noticeable in the u cross-section, in areas of the jet where the displacement is supposed to be null. Indeed, the larger the size of the reconstruction σ_{PSF} is, the noisier the displacement field is. This is why we finally chose the reconstruction parameter $\sigma_{PSF} = 0.2$.

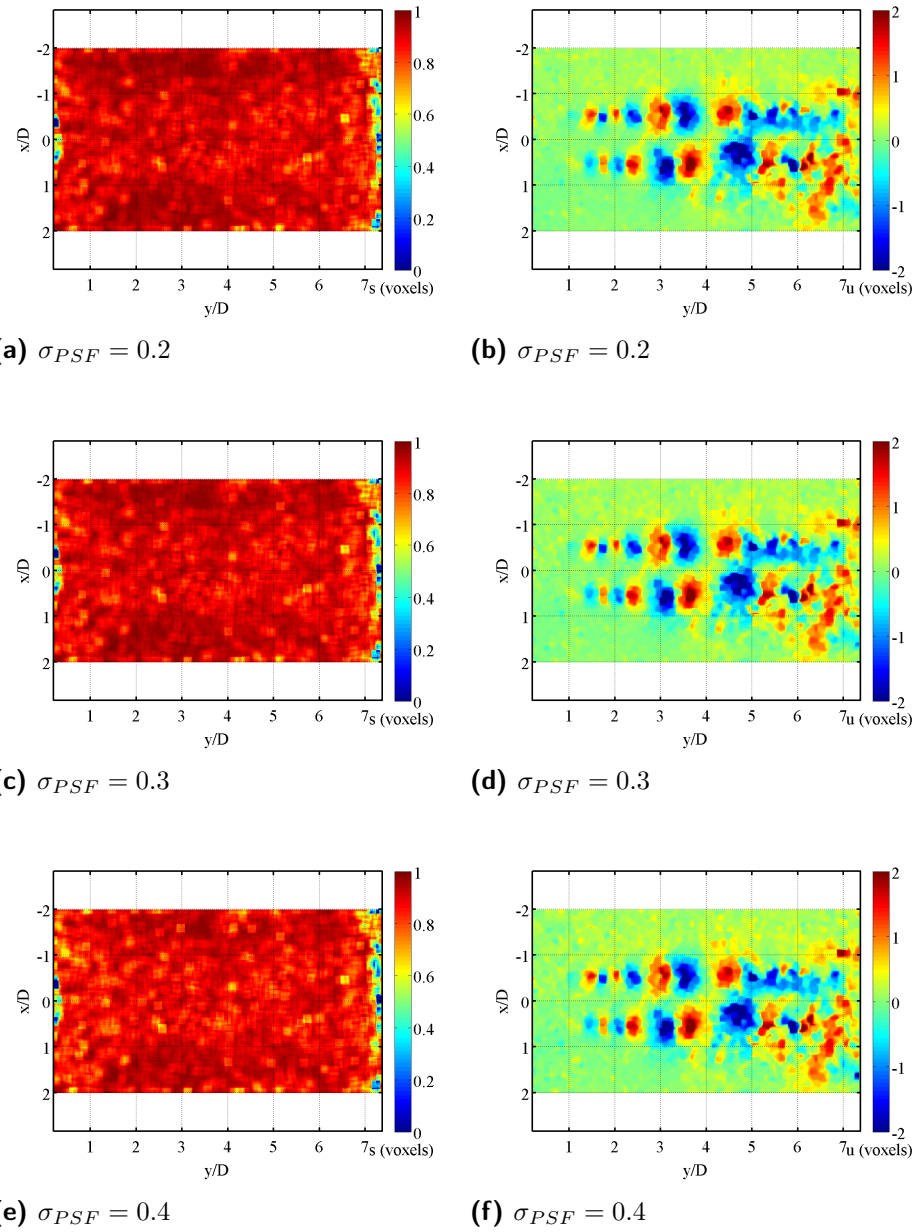

(a) $\sigma_{PSF} = 0.2$ **(b)** $\sigma_{PSF} = 0.2$

(c) $\sigma_{PSF} = 0.3$ **(d)** $\sigma_{PSF} = 0.3$

(e) $\sigma_{PSF} = 0.4$ **(f)** $\sigma_{PSF} = 0.4$

Figure 6.2.13: $z = 0$ Cross-sections of (left) correlation score and (right) u displacement field in voxel unity for different reconstruction PSF sizes (σ_{PSF}) using PVR-SMART

6.2.4 Displacement Estimation : choice of 3D Interrogation Volume size

The final algorithm's parameter that we will discuss for the 3D-PIV is the size of the Interrogation Volume for our FOLKI-3D cross-correlation code. The choice of this parameter in 3D tomographic PIV is always delicate and most of the following results will depend on the choice we make. Indeed, like in a classical 2D-PIV framework, a trade-off has to be made between measurement spatial resolution and measurement noise levels. Knowing precisely the density of tracer is therefore of paramount importance. In chapter 5, we showed our density estimation method. However, as shown in section 6.3.4.4 below, this estimation method is not quite as accurate as we hoped it would be. To have a clearer idea, we performed tests on the experimental data, investigating correlation score map and the velocity results from an experimental snapshot at

$ppp \approx 0.05$. Results are shown in figure 6.2.14. The reconstruction algorithm used here is tomo-SMART. We used a Gaussian Interrogation Volume which standard deviation is $\sigma_{IV} = IV_{size}/4$, $J = 3$ levels, and $N = 7$ Newton-Gauss iterations.

For IV sizes of 21 and 31 voxels, the score map is very patchy and with low score values, yielding a noisy displacement field. For 41 and 51 voxels IV sizes, the displacement field is smoother, especially for 51 voxels where the small spatial gradients of the flow field are filtered out by the correlation window. We chose a 41 voxels IV size as a good compromise between spatial resolution and measurement noise.

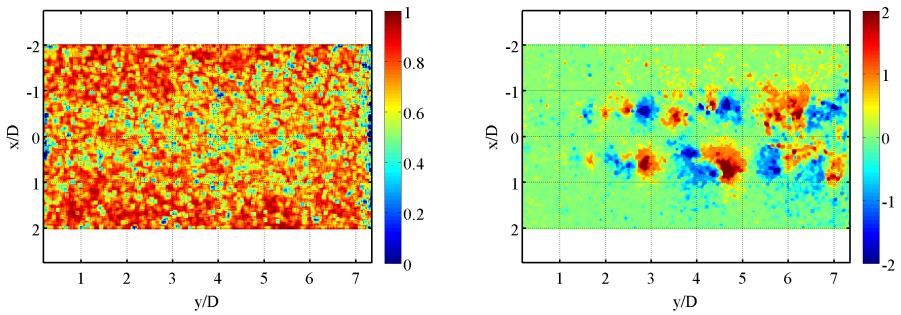

(a) 21 voxels IV **(b)** 21 voxels IV

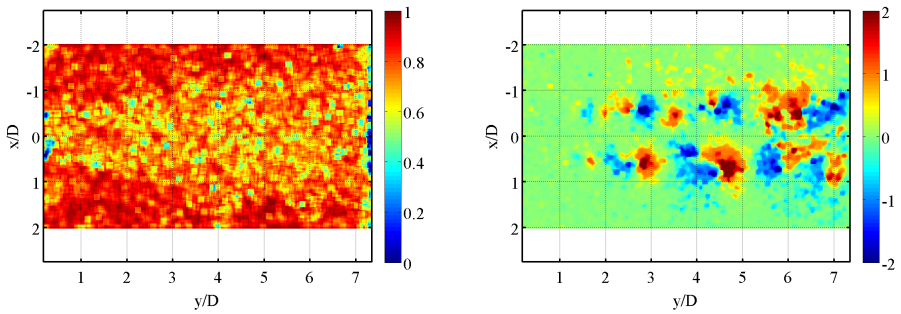

(c) 31 voxels IV **(d)** 31 voxels IV

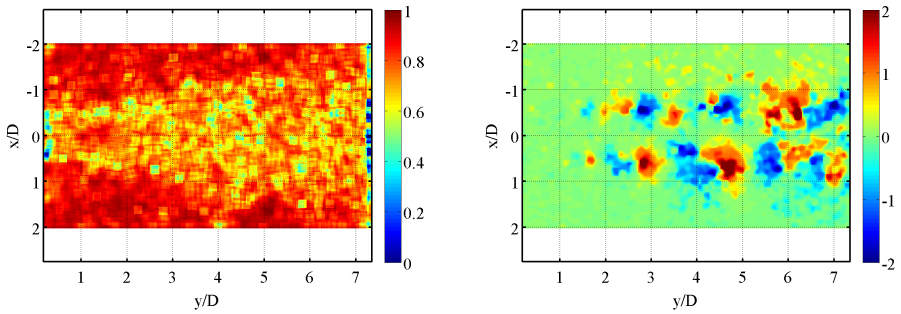

(e) 41 voxels IV **(f)** 41 voxels IV

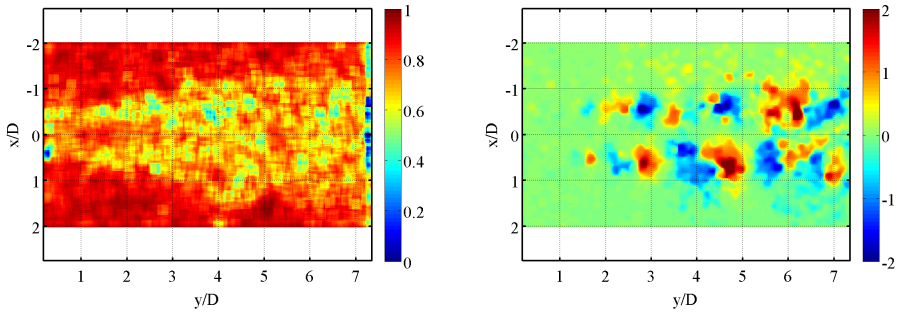

(g) 51 voxels IV **(h)** 51 voxels IV

Figure 6.2.14: $z = 0$ cross-sections of (left) correlation score map and (right) u displacement field in voxels for different IV sizes using tomo-SMART

6.3 Reconstructions algorithms comparison on a turbulent jet

This section focuses on the comparison of tomographic reconstruction algorithms on experimental measurements. This comparison consists in a thorough investigation of 3D measurement velocity fields in the near regions of a round free jet. 3D velocity fields are produced from the same data set but with two different tomographic reconstruction algorithms : 1- a classical tomo-SMART algorithm [Atkinson and Soria, 2009] which we implemented in a GPU framework. 2- PVR-SMART, our in-house reconstruction model (see chapter 3). Furthermore, the 2D-PIV measurement system synchronized with the 3D-PIV system will bring additional comparison points.

6.3.1 Comparison data set

The purpose of this work is to compare tomo-SMART and PVR-SMART and to see their dependence on different experimental conditions, especially the seeding density. This is why several image data sets were acquired with different tracer particles densities on the near region of the jet facility. Each image data set consists of $N_{acquisition} = 1000$ double snapshots. Figure 6.3.1 shows the estimated density from the 2D-PIV for two different acquisitions (**I** and **II**). During every acquisition, the external seeding density decays which enables us to have a great range of seeding density. From the two acquisitions, we selected four subsets of $N_{3D\ PIV} = 300$ images. Each subset can be seen as a density case.

Density **Case 1** has an external seeding ranging from 0.3 to 0.15, and an internal jet seeding of $ppp \approx 0.2$. **Case 2** has the same internal seeding density but with a lower external density ranging from 0.13 to 0.10. **Case 3** has a lower external and internal seeding density ranging from 0.09 to 0.04 ppp. As for **Case 4**, the internal density is stable around 0.05 *ppp* and the external seeding density decreases to 0.03.

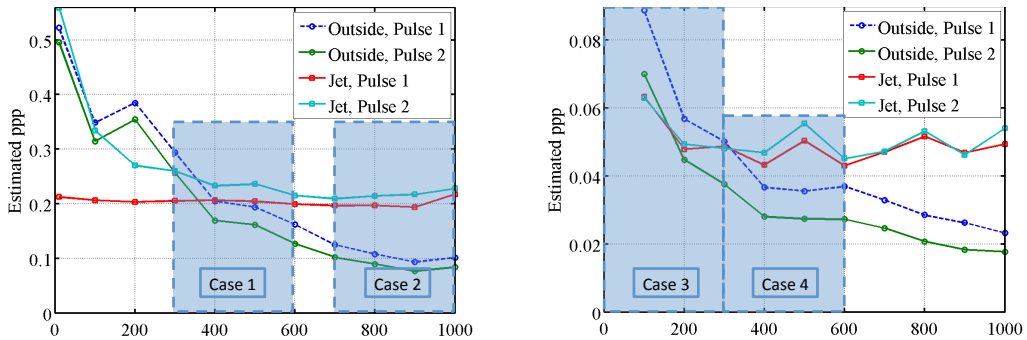

(a) Acquisition **I** **(b)** Acquisition **II**

Figure 6.3.1: 3D-PIV ppp estimation for Acquisition **I** and **II**. The 2 pulses in the figure's legend refer to the 2 pulses of the 2D-PIV laser. The pulse 1 was more powerful than pulse 2, hence detecting more particles

6.3.2 On the comparison between 2D-PIV and 3D-PIV

The comparison to 2D-PIV raises several issues. There is obviously a timing issue (the two measurement systems acquiring data at separate times), and a spatial measurement discrepancy since the 2D-PIV measures the velocity field in the $(\mathbf{y}, O, \mathbf{z})$ plane, (V and

W velocity) and not the full 3D field. However, the main issue is the spatial resolution of both measurement systems. The size of IV for the 3D-PIV system was chosen in previous section 6.2.4. For the 2D-PIV measurement to be a reference measurement, the size of its IW must be comparable or smaller than the size of IV to have the same or a smaller spatial filtering. Additionally, the number of tracers per IW in the 2D-PIV plane must be large enough (around 10) to avoid measurement noise.

The IV tomo size is such that $IW_{size}/D = 0.18$. We have to choose the size of the IW for the 2D-PIV measurement. Table 6.3.1 shows the measurement characteristics such as IW size and number of tracers per IW (N_{tracer}/IW_{size}) for different 3D-PIV image density for the 3D IW size and for several 2D-PIV IW sizes.

	3D-PIV	2D-PIV			
IW size	41 (vox)	21 (pix)	31 (pix)	41 (pix)	51 (pix)
IW size/D	0.18	0.06	0.08	0.11	0.14
ppp	N_{tracer}/IW_{size}				
0.03	7	0.3	0.7	1.2	1.9
0.05	11	0.5	1.1	1.9	3
0.07	16	0.7	1.6	2.8	4.4
0.1	22	1	2.3	4	6
0.15	34	1.5	3.4	6	9
0.2	45	2	4.5	8	12

Table 6.3.1: 2D-PIV IW and 3D-PIV IV characteristics : estimation of the number of tracers per IV or IW as a function of seeding density.

One can think of two strategies to adopt in order to choose the 2D-PIC IW size. The first one is to choose the IW size so as to have the same number of tracers per IW as in the tomographic case, but this would impact the high frequency scales that would be filtered out. The 2D-PIV IW size must therefore be $IW\text{size} = 97\ (pix)$, $IWsize/D = 0.27$. The second strategy is to consider same sized IW for 2D-PIV and 3D-PIV. The properties are summed up in table 6.3.2.

	2D-PIV				
	Same number of tracers		$IW\text{size} = IV\text{size}$		
ppp	IW size (pix)	$IW\text{size}/D$	$N_{tracer}/IW\text{size}$	IW size (pix)	$IW\text{size}/D$
0.03	97	0.27	3.1	65.6	0.18
0.05	97	0.27	5	65.6	0.18
0.07	97	0.27	7	65.6	0.18
0.1	97	0.27	10	65.6	0.18
0.15	97	0.27	15	65.6	0.18
0.2	97	0.27	20	65.6	0.18

Table 6.3.2: 2D-PIV IW characteristics : estimation of the number of tracers per IV or IW as a function of seeding density considering two options : either choosing the IW size with the same number of tracers as in the tomo case, or choosing the same size as in the 3D-PIV case.

A criterion that would help the choice is the average correlation score map over the same snapshots sequence (over all **acquisition I** snapshots) for different IW sizes. The results suggest that the tracer density is too small in **acquisition II** for a reliable displacement estimation, as foreseen by the tracer density estimation in table 6.3.1.

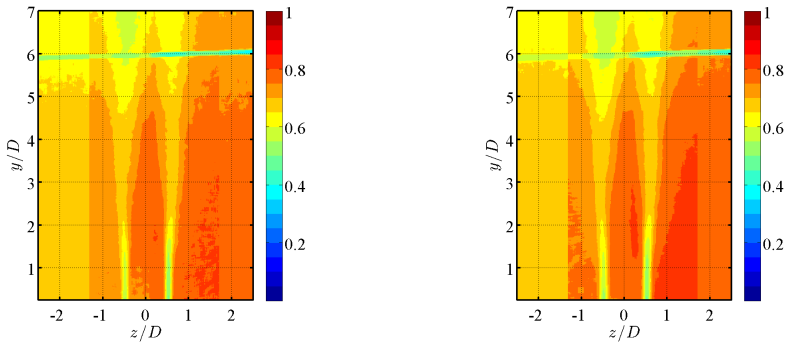

(a) IW size 41 **(b)** IW size 51

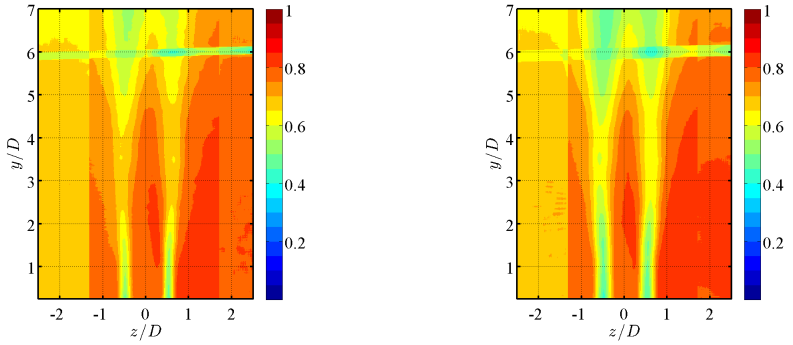

(c) IW size 65 **(d)** IW size 97

Figure 6.3.2: Mean correlation score map for 2D-PIV, **acquisition I**

We show here the mean correlation score for **acquisition I** in figure 6.3.2. One notices that there is a vertical discontinuity at $z/D \approx -1.25$. The camera sensor noise becomes noticeable when the tracer densities are low. The CCD camera is made of two different sensor pixel subsets which are assembled. Each subset has its own characteristic noise signature. This is what we see in figure 6.3.2. Furthermore, the tracer density is not homogeneous because the source of the external seeding is located in the $z > 0$ side of the room. The $z > 0$ side of the experimental room has more particles than the $z < 0$ side. For **acquisition I**, we will choose the IW size with 51 pixels for it seems a good compromise between spatial resolution and measurement noise, as well as having a smaller resolution than 3D-PIV.

6.3.3 Tomographic reconstruction analysis

The 3D-PIV method is based on two steps. Each step yields an output field on which an accuracy analysis can be based. A-posteriori analysis of the tomographic reconstruction can be done through several methods based on the reconstructed intensity distribution. [Lynch and Scarano, 2014] investigated three main criteria: Reconstruction Signal-to-Noise (SNR_R), relative Quality factor (Q^*) and normalized Intensity variance (σ_{E^*}). We will especially focus here on the SNR_R.

To compare the tomographic reconstructions, we selected 4 cases from the experimental data set (**acquisition I & II**) which represent 4 different tracer particle densities (table 6.3.3). For each case, we computed tomographic reconstruction for five consecutive images. We wish to emphasize the fact that we ranked the cases in an increasing density order as shown in table 6.3.3.

	Acquisition II		**Acquisition I**	
	Case 4	**Case 3**	**Case 2**	**Case 1**
Image number	$300-304$	$100-104$	$700-704$	$400-404$
ppp inside Jet	0.05	0.06	0.20	0.22
ppp outside Jet	0.04	0.08	0.11	0.18

Table 6.3.3: Density estimation

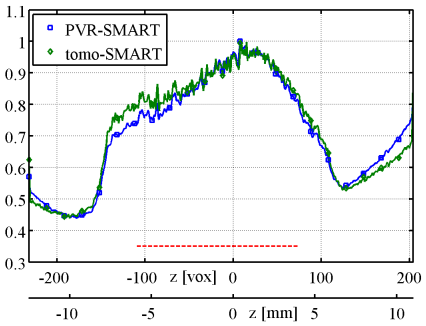

(a) Case 4. Tomo-SMART, $SNR_R = 1.81$, PVR-SMART, $SNR_R = 1.78$

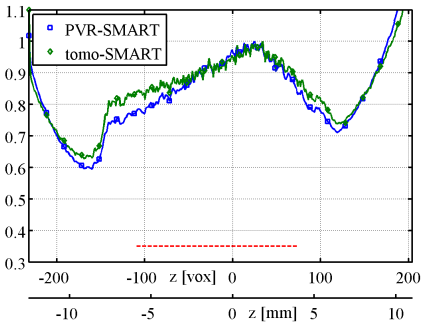

(b) Case 3. Tomo-SMART, $SNR_R = 1.32$, PVR-SMART, $SNR_R = 1.36$

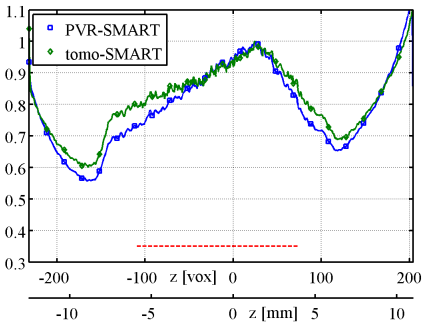

(c) Case 2. Tomo-SMART, $SNR_R = 1.38$, PVR-SMART, $SNR_R = 1.44$

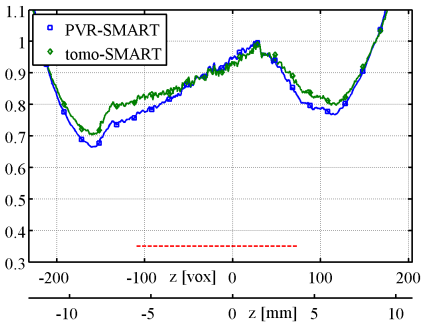

(d) Case 1. Tomo-SMART, $SNR_R = 1.19$, PVR-SMART, $SNR_R = 1.23$

Figure 6.3.3: Z intensity profiles of four density cases, ranked in a increasing seeding density order

The main quality factor assessed here is the SNR_R [Scarano, 2013], [Lynch and Scarano, 2014] which represents the reconstructed intensity profiles along the volume depth in figure 6.3.3. For each case, the intensity profile was done from an average of five consecutive snapshots. The intensity profile was then normalized by its maximum in the illuminated region. The laser illuminated region formed a "plateau" at the center of the intensity profile. In this region, both ghost particles and real particles were reconstructed. We see that at the edges of the laser volume, the reconstructed intensity decreases abruptly. Outside of the illuminated region, only ghost particles are reconstructed. As observed in [Thomas et al., 2014] for SMART reconstructions, the intensity profile outside the illuminated area increases till the edges of the tomographic volume. For the SMART algorithm, reconstruction artifacts, i.e. ghost particles tend to agglomerate at the very edges of the volume on which the reconstruction is done. [Thomas et al., 2014] showed that this phenomenon appears when dealing with noisy images and affects the quality of the reconstruction if the reconstructed volume is too small compared to the illuminated area.

Results show that as the particle tracer density increases, the intensity at the edges of the laser volume increases. When comparing tomo-SMART and PVR-SMART, one notices that for small tracer density (**Case 4**) the intensity at the edges of the laser volume are similar for both algorithms. When the density increases, the algorithms differences increase, PVR-SMART always having lower intensity levels outside the laser sheet, which means that ghost particles intensity are lower for PVR-SMART than tomo-SMART. This can be seen in SNR_R. Following [Lynch and Scarano, 2014] the SNR_R was defined as the ratio of reconstructed intensity inside the illuminated area (E_I) and that outside (E_o). The illuminated region is illustrated by the red line in every intensity profile plot. E_I was defined as the mean intensity over this area. As for E_o, we chose to define it as the mean value of the two local minima of the profile located at the extremity of the laser sheet. The intensity profiles were computed on a 30% volume enlargement. The comparison of the SNR_R is not straightforward. Results (figure 6.3.3) show that PVR-SMART has a better SNR_R than tomo-SMART for **Case 1** to **Case 3** which have higher densities. tomo-SMART has a better SNR_R for the low density case. One can also notice that the SNR_R are significantly lower than the 2.0 reference value recommended by [Scarano, 2013] for a good quality reconstruction.

6.3.4 Velocity field investigation

6.3.4.1 Preliminary remarks and definitions

In this section, 3D velocity fields obtained using both tomo-SMART and PVR-SMART algorithms, are investigated. We computed 3D velocity fields for two different density cases/image sequences : for **Acquisition I**, case 2, and for **Acquisition II**, case 4. As mentioned above, 2D-PIV fields were only computed for **Acquisition I** since the low tracer particle density in **Acquisition II** did not allow for a satisfying spatial resolution without too much compromise on the measurement noise.

For each 3D-PIV case, statistical quantities of the velocity field are computed on a set of $N = 300$ velocity snapshots.

On the other hand, since we use the 2D-PIV measurement as a reference point for the comparison of the 3D-PIV algorithms, we decided to compute 2D statistical quantities over the entire acquisition sequence, i. e. $N_{2D-PIV} = 996$ snapshots, in order to ensure a better convergence.

In the following we will consider mean and root mean square (rms) quantities, defined for any component α as:

$$\langle\alpha(\mathbf{x})\rangle = \frac{1}{N}\sum_{i=1}^{N}\alpha(\mathbf{x},t_i) \quad , \quad \alpha'(\mathbf{x},t) = \alpha(\mathbf{x},t) - \langle u\rangle \quad , \quad \alpha_{rms}(\mathbf{x}) = \sqrt{\frac{1}{N}\sum_{i=1}^{N}\alpha'(\mathbf{x},t_i)^2} \tag{6.3.1}$$

In order to use normalized physical quantities, we will normalize velocity fields by a characteristic velocity of the flow (the exit nozzle velocity) and lengths will be normalized by a characteristic length of the flow (the nozzle diameter). For the 2D-PIV measurements, the exit velocity is computed as shown in section 5.4. For the 3D measurements, the exit velocity is computed by integrating the mean axial velocity at $y/D = 0.46$:

$$V_0 = \frac{1}{\pi D^2/4}\iint_{\mathcal{D}}\langle V(X,Z)\rangle\, dXdZ \tag{6.3.2}$$

where $\mathcal{D}$ is the disk area of diameter $\mathcal{D} = D/4$, centered on the $\vec{y}$ axis at $y/D = 0.46$.

6.3.4.2 Inflow conditions

Figure 6.3.4 shows the inflow conditions of the jet, namely $\langle v\rangle$ at $z = 0$ and $y = 0.46$ for **Case 2** and **Case 4**. Integral quantities that serve as a description of the mean axial velocity profile at the exit of the jet nozzle, found by both 3D-PIV algorithms and when available by 2D-PIV, are summed up in table 6.3.4. Results show that for the quantities based on the mean profile, tomo-SMART and PVR-SMART have relatively similar results. When comparing with the 2D-PIV for the estimation of V_0, PVR-SMART tends to over-estimate it by 0.03 $m.s^{-1}$ as tomo-SMART underestimates it by 0.04 $m.s^{-1}$. The behaviors of tomo-SMART and PVR-SMART are similar for θ_e, δ_e as well as δ_ω (see chapter 5 for definitions) which does not seem to be impacted by any of the measurement methods (2D-PIV or 3D-PIV). However, when focusing on rms quantities, a strong discrepancy exists between tomo-SMART and PVR-SMART. $\tilde{v}_{rms}$ in table 6.3.4 is here a spatial integral of axial rms velocity over the jet core velocity. $\tilde{v}_{rms} = \int_{-D/4}^{D/4} v_{rms}dx$. In the jet core center, tomo-SMART has a greater rms velocity

than PVR-SMART by nearly an order of magnitude (0.1353 compared to 0.0469).

The comparison with the 2D-PIV measurement which was made over a greater number of snapshots confirms that tomo-SMART has indeed a greater rms error than PVR-SMART. The same behavior is visible for low velocity values, outside of the jet where there is entrainement velocity : 2D-PIV and tomo-SMART measurement are similar and tomo-SMART has higher values. Inside the shear layer where velocity gradients are stronger and measurement noise error is expected to be higher, rms behaviors of tomo-SMART and PVR-SMART are similar, both higher than 2D-PIV rms velocity with values up to 20% of V_0. This comes from the fact 2D-PIV measurement has a smaller IW size as well as more snapshots on which the rms values can converge.

One can also notice that the 2D-PIV rms profile is not fully symmetrical. This comes from the fact that the 2D-PIV measurement is highly sensitive to tracer density which is not totally homogeneous at this density. Indeed, external seeding comes from a seeding generator located 5 meters back of the jet in the z direction as explained in chapter 5. The trends are similar with lower density **Case 4**, with overall higher rms values which is synonymous with higher measurement noise due to lower seeding density. Despite having in between 7 to 11 tracers per IV, if those tracers are partially or badly reconstructed due to low intensity levels in the tomographic images and Mie scattering or calibration errors, there is a lower number of reconstructed tracers in the IV. This increases the measurement noise.

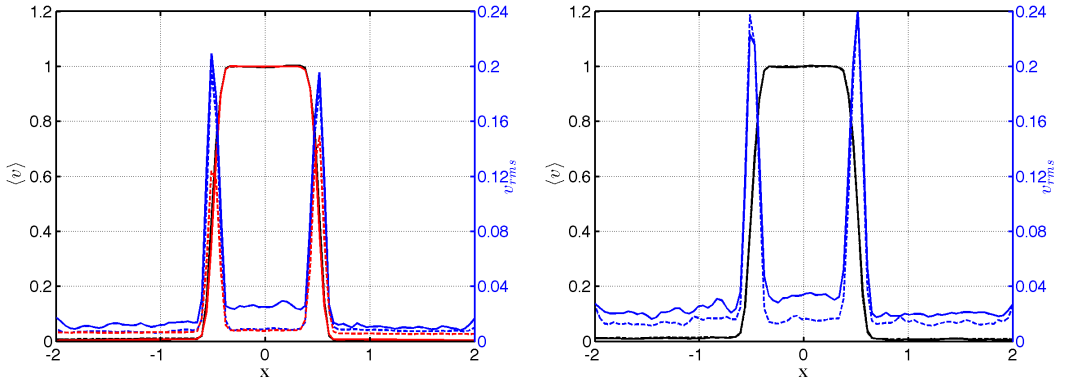

(a) Case 2 **(b) Case 4**

Figure 6.3.4: Axial Mean and rms velocities at z=0 and y=0.46 for the two density cases : **Case 2** and **Case 4**. The legend is the same as in figure 6.3.5.

	Case 2			Case 4	
	2D-PIV	tomo-SMART	PVR-SMART	tomo-SMART	PVR-SMART
$V_0\ m/s$	5.63	5.58	5.65	5.59	5.61
$\tilde{v}_{rms}$	0.0455	0.1353	0.0469	0.1634	0.0865
θ_e	$3.4e-04$	$3.9e-04$	$3.38e-04$	$3.71e-04$	$3.63e-04$
δ_e	0.0012	$9.3e-04$	$9.42e-04$	$9.38e-04$	$9.43e-04$
δ_ω	0.0015	0.0014	0.0014	0.0014	0.014

Table 6.3.4: Inflow conditions and shear layer description.

6.3.4.3 Mean and rms centerline evolution

The mean and rms axial velocity centerline profiles (figure 6.3.5) exhibit a rather similar behavior as shown previously. For low y, tomo-SMART, PVR-SMART and 2D-PIV show a similar mean axial velocity evolution but for $y > 3$, PVR-SMART seems to have a lower mean axial velocity centerline profile. PVR-SMART has almost constantly lower rms values than tomo-SMART, much closer to the 2D-PIV measurement for low y but also for higher y, which means that PVR-SMART measurement velocity is less noisy than the tomo-SMART case. This trend is confirmed in the low density case, where both rms and mean velocity for PVR-SMART are constantly lower than the tomo-SMART algorithm.

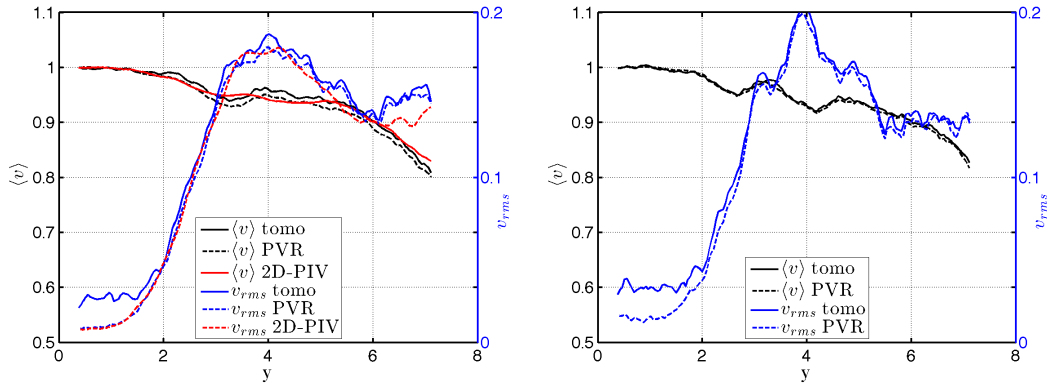

(a) Case 2 **(b)** Case 4

Figure 6.3.5: Axial centerline mean and rms velocities.

6.3.4.4 Jet development

The evolution of mean axial velocity in the $z = 0$ cross-section (figure 6.3.6) shows that PVR-SMART and tomo-SMART have relatively similar behaviors, both exhibiting a dissymmetry of the jet with the right shear layer ($x > 0$) wider than the left ($x < 0$). Tomo-SMART has a longer jet core with velocities of 95% V_0 up to $y = 5$. Moreover, when looking at the $y = 2$ cross-section, the spherical structure of the mean axial velocity is more visible for tomo-SMART than for PVR-SMART. PVR-SMART seems to be more affected by side effects due to ghost particles which tend to be gathered on the sides of the reconstructed volume. However, when looking at the rms cross-sections, one notices that PVR-SMART has significantly less noise than tomo-SMART especially in areas with low mean velocity levels.
To illustrate this more quantitatively, we computed local means of u,v and w rms velocities in the $z = 0$ cross sections outside the jet where the is only entrainement velocity ($-2 < x < -1$ and $0 < y < 3$). The rectangle, on which the rms computation is done, is represented by a white rectangle in the $z = 0$ cross-sections, displayed in v rms cross-sections in figure 6.3.7. Results (table 6.3.5) show that for both tomo-SMART and PVR-SMART w velocity is noisier than u and v which means that more measurement error is done on the reconstructed w component than on the (u, v) plane. This is true for both density cases. This is an expected result since the w component of the flow is the one which is reconstructed, and is the one along the line-of-sight of the camera pixels. Due to the camera setup, the particles are elongated in the $\vec{z}$ axis [Scarano, 2013], thus increasing the measurement noise on this component. For **Case 2**, comparing tomo-SMART and PVR-SMART shows that noise levels have a similar ratio 1.51

but this ratio increases for the w component 1.55. PVR-SMART is about 50% less noisy than tomo-SMART. For the lower density **Case 4**, the ratio also increases for the w component 1.55. However, one notices that the ratio of the u and v component are not the same as previously with **Case 2**.

	Case 2			**Case 4**		
	tomo-SMART	PVR-SMART	ratio	tomo-SMART	PVR-SMART	ratio
$\hat{u}_{rms}$	0.0181	0.0120	1.51	0.0220	0.0154	1.42
$\hat{v}_{rms}$	0.0128	0.0085	1.51	0.0202	0.0133	1.52
$\hat{w}_{rms}$	0.0256	0.0165	1.55	0.0360	0.0232	1.55
$\hat{u}_{rms}[vox]$	0.101	0.067	1.51	0.123	0.086	1.42
$\hat{v}_{rms}[vox]$	0.071	0.047	1.51	0.113	0.074	1.52
$\hat{w}_{rms}[vox]$	0.143	0.092	1.55	0.201	0.129	1.55

Table 6.3.5: Mean rms values of a low velocity area on the outskirts of the jet at $z = 0$, $-2 < x < -1$ and $0 < y < 3$. In figure 6.3.7, the area is visualized by a white rectangle.

When comparing the two density cases, the trend previously exhibited is confirmed : **Case 4** has higher rms values than **Case 2**. More precisely, for tomo-SMART, the rms values are respectively 22 %, 59 % and 40 % higher for **Case 4** than **Case 2**, on respectively u,v and w component. For PVR-SMART, the rms values are respectively 28 %, 57 % and 40 % higher for **Case 4** than **Case 2**, on respectively u,v and w component. The velocity fields from **Case 4** are noisier with statistics being less converged than **Case 2**. Our interpretation so far has been that the increased measurement noise comes from a lack of tracer in the correlation window, despite the fact that we previously estimated the number of tracers per IW to about 7 to 11 in table 6.3.1. However, this estimation was done through the use of 2D-PIV images, with a 200 mJ laser, much powerful than the 3D-PIV laser (120 mJ). This means that some particles seen by the 2D-PIV setup, are not seen from the 3D-PIV setup therefore not reconstructed, due to the lower illumination and also Mie scattering. Adding calibration errors, discretisation errors and image pre-processing thresholds, fewer tracers are actually reconstructed by the tomographic step than estimated by the 2D-PIV images. It would be very interesting to have an actual estimation of the reconstructed tracer density, based for instance on tracer tracking from a pulse to the following. This would help choose the IW size for the 3D correlation step. This will undoubtedly be the subject of future research.

For the sake of clarity, from now on and for the rest of the study, we will focus on results from **Case 2**, since the main difference between **Case 2** and **Case 4** is the measurement noise stemming from the difference in the number of tracers per IV.

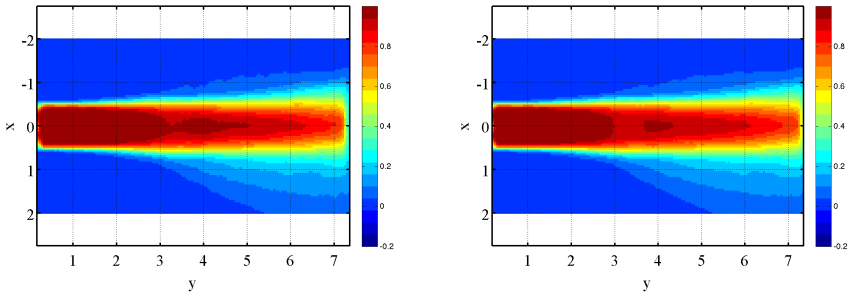

(a) tomo-SMART, **Case 2**, z=0

(b) PVR-SMART, **Case 2**, z=0

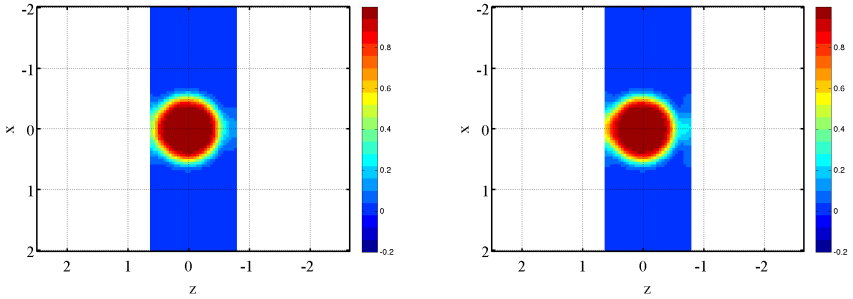

(c) tomo-SMART, **Case 2**, y=2

(d) PVR-SMART, **Case 2**, y=2

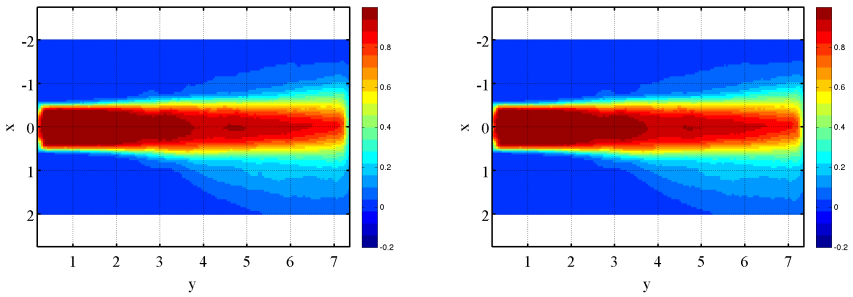

(e) tomo-SMART, **Case 4**, z=0

(f) PVR-SMART, **Case 4**, z=0

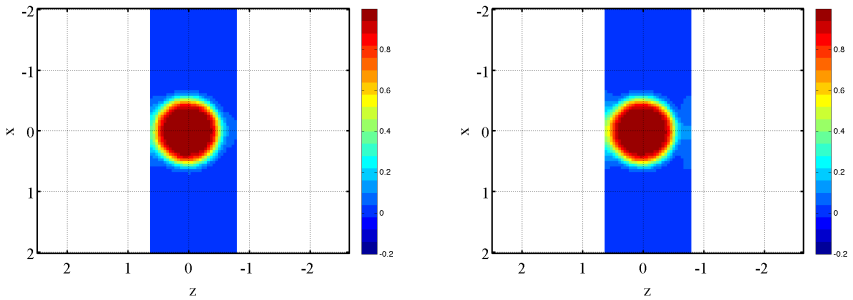

(g) tomo-SMART, **Case 4**, y=2

(h) PVR-SMART, **Case 4**, y=2

Figure 6.3.6: Mean axial velocity $\langle v \rangle$ for the two density cases, (a,b,c,d) **Case 2**, (e,f,g,h): **Case 4**.

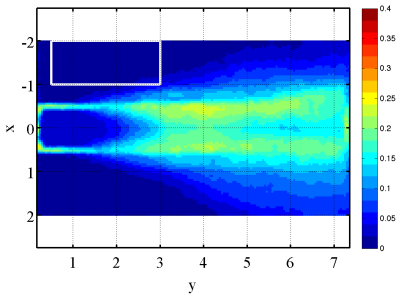

(a) tomo-SMART, **Case 2**, z=0

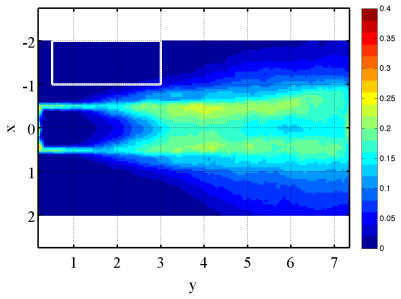

(b) PVR-SMART, **Case 2**, z=0

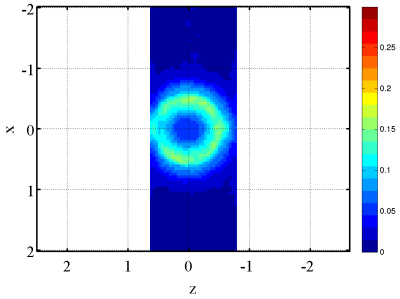

(c) tomo-SMART, **Case 2**, y=2

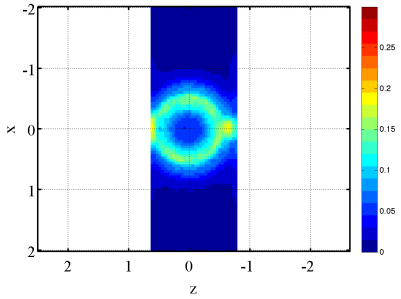

(d) PVR-SMART, **Case 2**, y=2

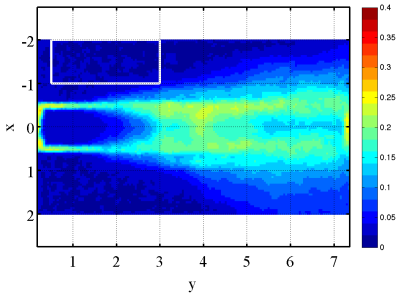

(e) tomo-SMART, **Case 4**, z=0

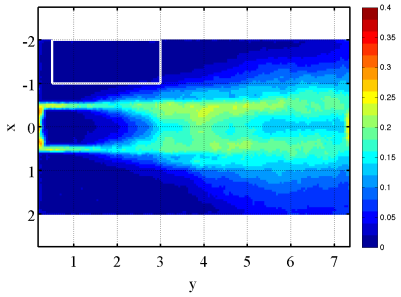

(f) PVR-SMART, **Case 4**, z=0

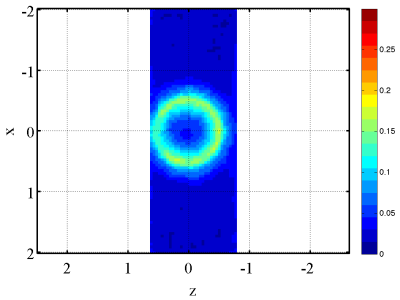

(g) tomo-SMART, **Case 4**, y=2

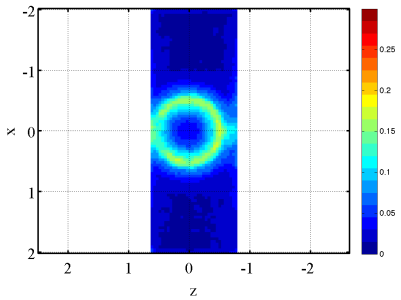

(h) PVR-SMART, **Case 4**, y=2

Figure 6.3.7: Axial rms velocity v'_{rms} for the two density cases, (a,b,c,d) **Case 2**, (e,f,g,h): **Case 4**.

6.3.4.5 Score map and peak-locking analysis

There is a discrepancy in the level of noise between PVR-SMART and tomo-SMART. Investigating the score map could help understand this high noise levels in tomo-SMART. The correlation score is a good indication of how good the correlation was. In 2D-PIV, the correlation score can be directly linked to the overall quality of the measurement. For 3D-PIV, the link is less obvious : the score still indicates how well the matching was done, but there is no evidence that all the tracers in the Interrogation Volume, that were 'matched', are indeed real particles. [Elsinga et al., 2011] showed that in some cases, ghost particles are coherent and disturb the correlation of the real particles. Nonetheless, the correlation score gives a good insight on the correlation step. To do so, we visualized a cross-section at $z = 0$ of the mean correlation score map for **Case 2** (the mean was computed over the 300 snapshots of **Case 2**) for PVR-SMART and tomo-SMART. Results are shown in figure 6.3.8. The jet topology is visible in both score maps. The score decreases in the mixing layer, where spatial gradients are strong and with decreasing lengthscales are convected streamwise. The score is closer to 1 in the jet potential core where velocity gradients are less strong. PVR-SMART has an overall higher score with mean scores ranging from 0.8 to 1, and tomo-SMART has mean scores ranging from 0.65 to 0.95. PVR-SMART intensity field yields better 3D correlations than tomo-SMART reconstruction. Therefore, we can expect the tomo-SMART velocity fields to be more noisy than the PVR-SMART velocity fields.

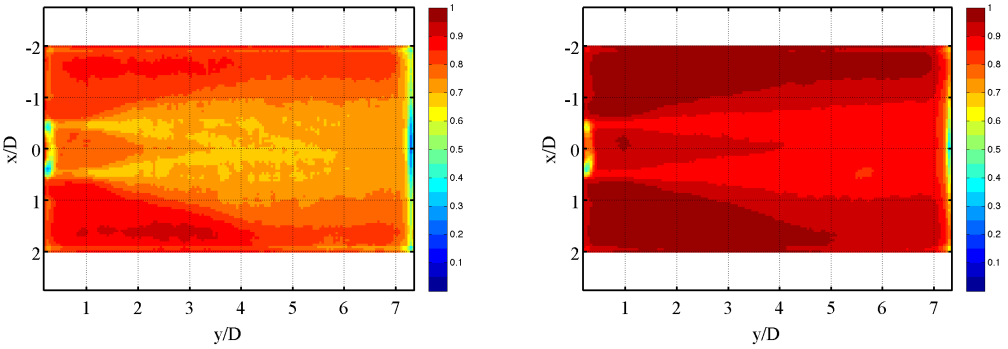

(a) tomo-SMART, z=0 **(b)** PVR-SMART, z=0

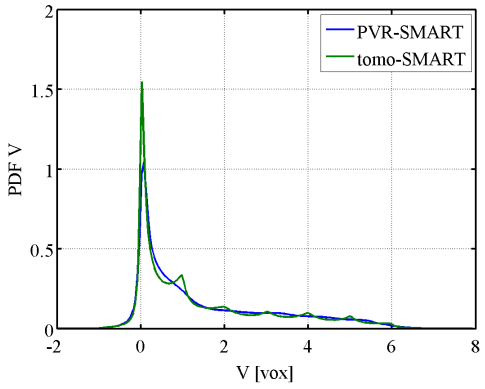

(c) PDF of the v component for tomo-SMART

Figure 6.3.8: Mean correlation score for tomo-SMART and PVR-SMART (up) and (down) Velocity PDF of the v component for tomo-SMART, in $x \in [-1.5\ ,\ 1.5]$, $y \in [3\ ,\ 6.5]$, $z \in [-0.45\ ,\ 0.45]$, over 300 samples.

Several explanations can account for these results. In [Champagnat et al., 2014], PVR-SMART was shown to out-perform tomo-SMART for several reconstruction quality criteria. This was shown for different imaging σ_{PSF}, tracer density and we also investigated PVR-SMART robustness w.r.t. inaccurate PSF knowledge. PVR-SMART was especially shown to have a better Recall than tomo-SMART, which means that PVR-SMART has more tracers for the correlation step, leading to a better correlation score. Despite the fact that, in the article we did not investigate such small σ_{PSF} imaging conditions and how PVR-SMART compares to tomo-SMART in these conditions, the SNR_R shown in section 6.3.3 allows us to think that a better reconstruction quality is the cause of this score difference.

Another interesting result, could partially explain the score difference. It can be found in a PDF of the v displacement (figure 6.3.8). This clearly shows that tomo-SMART suffers from peak-locking compared to PVR-SMART. The explanation is that the size of the reconstructed particles by tomo-SMART is the same as the particles in the images. Considering the type of image pre-processing used, the size of the PSF in the images (0.3 σ_{PSF} in the theoretical estimation), the high value threshold, discretization and calibration errors, all those properties lead to relatively small reconstructed particles, sometimes to only a few voxels. This is why peak-locking appears for tomo-SMART. A solution to this problem for tomo-SMART is the use in pre-processing of Gaussian filtering which artificially increases the size of the particle in the images. However, as mentioned in [Scarano, 2013], this can be detrimental to high density by increasing the Image Source density. Since we wanted to compare the algorithms with the same input, the same images, a Gaussian filtering for image pre-processing was not done. It would be valuable to see its effects on the results of tomo-SMART.

6.3.4.6 Reynolds tensor investigation

3D-PIV gives access to the full 3D Reynolds tensor which we investigate here. We will take a closer look at the behavior of the diagonal components of the Reynolds stress (whose sum forms the Turbulent Kinetic Energy, TKE) along the centerline jet axis and $\vec{x}$ axis as well as the shear stress component of the Reynold stress tensor which is available for the 2D-PIV measurement. These quantities are defined as :

$$\mathcal{R}_{i,j}(\mathbf{x}) = \left\langle u_i'(\mathbf{x},t)u_j'(\mathbf{x},t)\right\rangle \qquad \forall\{i,j\}\in\{1,2,3\}^2 \qquad , \qquad TKE(\mathbf{x}) = \frac{1}{2}\mathcal{R}_{i,i}(\mathbf{x}) \tag{6.3.3}$$

The evolution of TKE along the centerline of the jet is illustrated in figure 6.3.9(a). The sudden growth of TKE takes place at $y = 2$, then fluctuates on a plateau for $y = 4$ to $y = 6$ before finally increasing downstream. Both tomo-SMART and PVR-SMART follow the same trend that we just described, but PVR-SMART TKE values are always lower than tomo-SMART, which can again be interpreted as the fact that PVR-SMART is less noisy than tomo-SMART, therefore having a lower TKE. The TKE measurement is a representation of the level of fluctuations in the signal, that can come from the dynamics of the flow but also from the measurement own erroneous noise. When looking at the radial behavior of TKE in figure 6.3.9(b), the same conclusion can be drawn regarding the difference in the levels of noise between tomo-SMART and PVR-SMART. The TKE reaches a local maximum in the shear layer at $x = 0.5$ which is expected, reaching up to 0.05 at $y = 4$. We also investigated a non-diagonal component of the Reynods Stress tensor, the shear stress. For the 3D PIV, this shear stress was computed

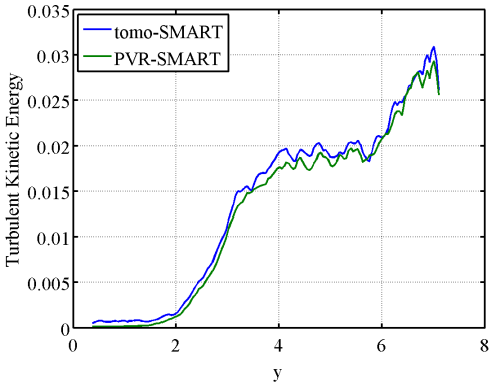

(a) TKE on the centerline

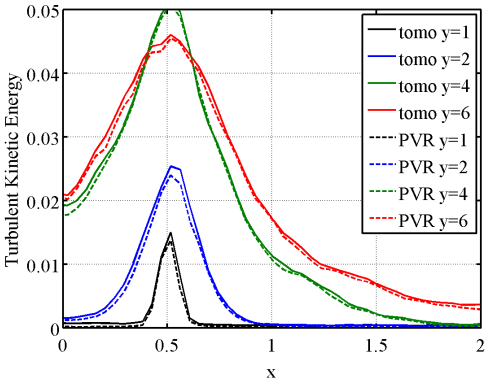

(b) TKE radial behavior

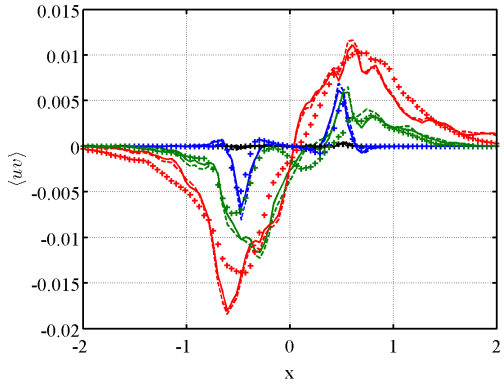

(c) Turbulent Shear stress radial behavior

Figure 6.3.9: Reynolds tensor investigation.

in the $z = 0$ plane. Assuming axisymmetry of the jet, the shear stress of the 3D-PIV in the $z = 0$ plane should be comparable to the 2D-PIV shear stress, computed in the $x = 0$ plane. Figure 6.3.9(c) shows the shear stress of both tomo-SMART and PVR-SMART in the $z = 0$ plane and the 2D-PIV shear stress in $x = 0$ for different downstream locations. The comparison of 2D-PIV and 3D-PIV is not straightforward. Several reasons might account for such a difference between 3D-PIV and 2D-PIV. As mentioned in chapter 5, the streamlines of the jet in the 2D-PIV plane show that the jet is not perfectly axisymmetrical and the jet might be disturbed by an outside flow. The rms cross-sections from 3D-PIV further confirm this trend. The shear stress and fluctuated quantities are sensitive to such a perturbation. This may lead to such a difference in the shear stress profiles.

6.3.4.7 Flow Divergence

Since 3D-PIV enables us to capture the full 3D velocity field, we can investigate the full 3D gradient of the velocity field. We started by investigating the divergence of the flow field (which is the trace of the gradient tensor). In our case, considering the low velocities and the low Reynolds number, compressible effects are negligible, therefore the divergence of the flow is supposed to be null at any point and time in the flow. In this case, flow divergence is well suited to estimate the measurement error on the spatial derivatives of the flow [Violato and Scarano, 2011]. We investigated two quantities : the divergence $\nabla.u$ and the normalized divergence ξ:

$$\nabla.\mathbf{u} = \frac{\partial u}{\partial x} + \frac{\partial v}{\partial y} + \frac{\partial w}{\partial z} \quad , \quad \xi = \frac{(\frac{\partial u}{\partial x} + \frac{\partial v}{\partial y} + \frac{\partial w}{\partial z})^2}{(\frac{\partial u}{\partial x})^2 + (\frac{\partial v}{\partial y})^2 + (\frac{\partial w}{\partial z})^2} \tag{6.3.4}$$

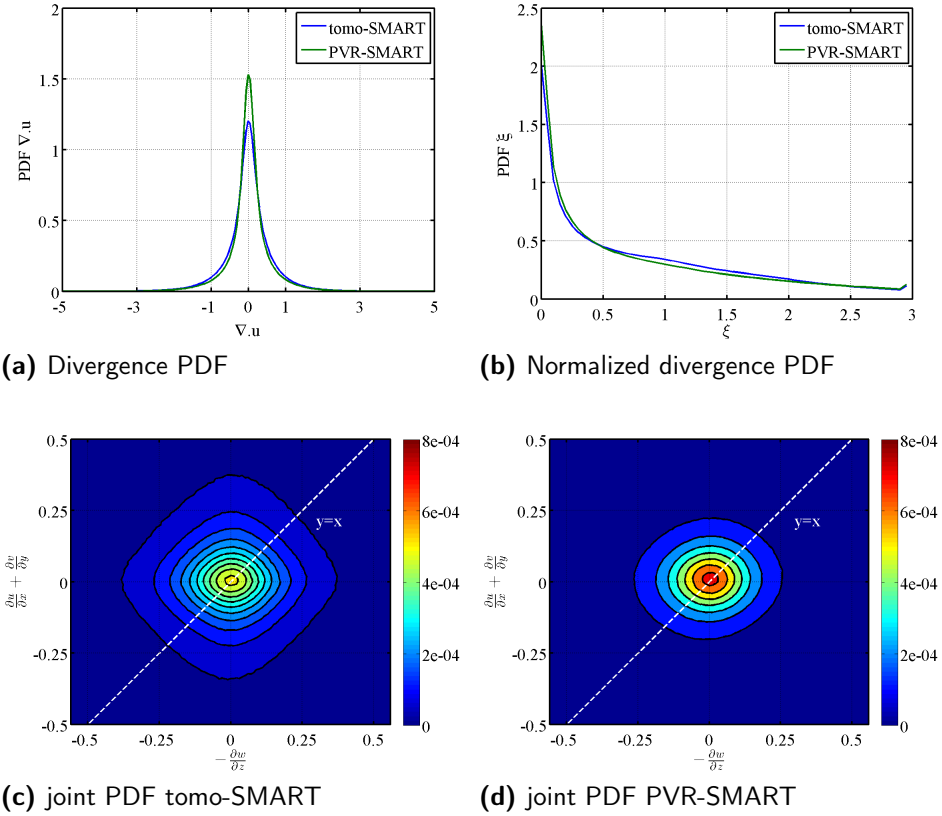

(a) Divergence PDF **(b)** Normalized divergence PDF

(c) joint PDF tomo-SMART **(d)** joint PDF PVR-SMART

Figure 6.3.10: Divergence investigation : PDF of the divergence (a) and the normalized divergence (b). Joint probability between $\frac{\partial u}{\partial x} + \frac{\partial v}{\partial y}$ and $-\frac{\partial w}{\partial z}$ of respectively tomo-SMART (c) and PVR-SMART (d). Those statistical quantities were collected over the whole measurement domain on $N = 300$ samples.

To estimate the spatial derivatives of the measurement field, we used a Savitzky–Golay 2nd order filter with 5 points stencil, also known in the PIV literature as a 'least square' filter [Raffel et al., 2007]. One could argue that numerical truncation due to the spatial discretisation of the velocity field could impact the numerical evaluation of the divergence from the experimental data. However, the large overlap factor (75%) between neighboring interrogation boxes ensures that truncation errors are negligible

with respect to the effect of the finite size of the Interrogation Volume [Scarano and Poelma, 2009].

Figure 6.3.10(a) illustrates the probability density of $\nabla.\mathbf{u}$ over the entire **Case 2** data set. The distribution is symmetrical around zero with a standard deviation of 0.60 and 0.66 in dimensionless quantities for PVR-SMART and tomo-SMART respectively, which is respectively 0.0151 and 0.0166 in $[vox/vox]$. Figure 6.3.10(b) shows the normalized divergence probability density function. PVR-SMART has a distribution closer to zero than tomo-SMART. Figure 6.3.10(c) and figure 6.3.10(d) show the joint probability between $\frac{\partial u}{\partial x} + \frac{\partial v}{\partial y}$ and $-\frac{\partial w}{\partial z}$ of respectively tomo-SMART and PVR-SMART. Tomo-SMART's joint PDF is more spread in the 2D plane than PVR-SMART which distribution is closer to the origin $(0, 0)$. One can notice that neither tomo-SMART nor PVR-SMART distribution is aligned on the divergence free $y = x$ line. Tomo-SMART distribution has a square shape and PVR-SMART has an elliptical shape which seems to indicate that even if the overall divergence tends to zero, the velocity components do not seem constrained by the mass conservation and are rather independent. We also computed the same results using a 2nd order central finite difference scheme for the spatial derivatives, to see whether or not the findings concerning the divergence depended on the derivation method. The behaviors of tomo-SMART and PVR-SMART were found similar.

6.3.4.8 Statistical flow topology

We further investigated the 3D velocity gradient by studying the strain field and the topology of the velocity tensor invariants. In 1990, [Chong et al., 1990] showed that one can study the local evolution and topology of an incompressible flow field by investigating the second and third invariant of the velocity gradient tensor. Additional details and further understanding of the topological methodology can be found in [Chong et al., 1990], [Soria et al., 1994], [Hugh M. Blackburn and Cantwell, 1996] among others. We will only present here a short summary of the physical quantities on which the analysis is based. [Chong et al., 1990] recalled that the velocity tensor $\mathcal{A}_{ij} = \partial u_i/\partial x_j$ has the following charateristic equation :

$$\lambda_i^3 + P_\mathcal{A}\lambda_i^2 + Q_\mathcal{A}\lambda_i + R_\mathcal{A} = 0 \tag{6.3.5}$$

where λ_i are the eigenvalues of $\mathcal{A}_{ij}$, with $P_\mathcal{A}$,$Q_\mathcal{A}$ and $R_\mathcal{A}$ being the first, second and third tensor invariants. For incompressible flows, one can compute the invariants such as :

$$\begin{aligned} P_\mathcal{A} &= -\mathcal{A}_{ii} = 0 \\ Q_\mathcal{A} &= -\frac{1}{2}\mathcal{A}_{ij}\mathcal{A}_{ji} \\ R_\mathcal{A} &= -\frac{1}{3}\mathcal{A}_{ij}\mathcal{A}_{jk}\mathcal{A}_{ki} \end{aligned} \tag{6.3.6}$$

For incompressible flows, the first tensor invariants is null due to the flow being divergence-free. Therefore, the local characteristics of the flow depends on the values of $Q_\mathcal{A}$ and $R_\mathcal{A}$. These two quantities define the category to which the local flow topology belongs. One can see the local topology of the flow as the local streamline characteristics in the vicinity of the point where the velocity gradient is computed. [Chong et al., 1990] showed that for incompressible flows, using the joint-PDF of $Q_\mathcal{A}$ and $R_\mathcal{A}$ one can distinguish 4 regions of different non-generate flow typologies : stable-focus/stretching, unstable-focus/compressing, stable-node/saddle/saddle and unstable-node/saddle/saddle. The four regions are separated by the Q axis and the tent-like curve

($D_{\mathcal{A}} = 0$), line representing the discriminant of $\mathcal{A}_{ij}$ given by the equation :

$$D_{\mathcal{A}} = \frac{27}{4} R_{\mathcal{A}}^2 + Q_{\mathcal{A}}^3 \tag{6.3.7}$$

Furthermore, the velocity gradient tensor $\mathcal{A}_{ij}$ can be split into a symmetric part $\mathcal{S}_{ij}$ (rate-of-strain tensor) and an antisymmetric part $\mathcal{W}_{ij}$ (rate-of-rotation tensor) such that,

$$\mathcal{A}_{ij} = \mathcal{S}_{ij} + \mathcal{W}_{ij} \tag{6.3.8}$$

Similarly, one can define the invariants of the rate-of-strain tensor, (R_s,Q_s), and the rate-of-rotation tensor, (R_w,Q_w), from by their own characteristic equation. In the rest of the study and for the sake of simplicity, when referring to the invariants of the velocity tensor $\mathcal{A}$, we will use the notations (P, Q, R).

Numerous studies show the scatter plot of the joint-PDF of Q and R, also called the '$Q - R$' plot. DNS studies of isotropic homogeneous turbulence of incompressible flows have shown that the joint PDF of Q and R is skewed towards the $D_{\mathcal{A}}$ line as well as towards the second quadrant ($+Q$ and $-R$), such a shape is called the teardrop shape (e.g., [Chong et al., 1998], [Nomura and Post, 1998], [Martin et al., 1998], [Ooi et al., 1999], Lüthi et al. [2009]). This trend also occurs in experiments [Tsinober et al., 1992], [Gulotski et al., 2007], [Elsinga and Marusic, 2010] suggesting it is an universal characteristic of small-scale turbulence. More details and a thorough review of the research being carried out on this topic can be found in the work of [Meneveau, 2011]. With the rise of 3D-PIV, this kind of investigation has become popular in PIV literature. [Khashehchi et al., 2012] studied the evolution of the invariants (Q and R) in the developing region of a turbulent round jet ($R_D \approx 5600$, based on the jet nozzle diameter). Gan et al. [2012] compared two tomographic reconstruction algorithms by investigating velocity and velocity gradients statistics obtained from 3D PIV measurements of locally isotropic turbulence produced in a large mixing tank at high-Reynolds numbers.

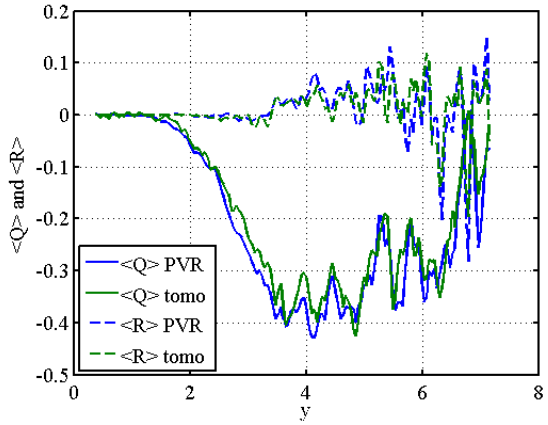

Figure 6.3.11: $\langle Q \rangle$ and $\langle R \rangle$ centerline evolution.

Our study here is inspired by these two studies. We will compare tomo-SMART and PVR-SMART by investigating the evolution of the two velocity gradient invariants (Q, R) in the near region of our jet. figure 6.3.11 illustrates the evolution of the mean profiles of the two invariants ($\langle Q \rangle$ and $\langle R \rangle$) along the jet centerline. Here, Q and R are computed from dimensionless velocity fields. The evolution of both quantities is similar

to [Khashehchi et al., 2012]. At the exit of the nozzle, both quantities are zero. The rate of change of Q is much greater than of R, as shown in [Khashehchi et al., 2012] Q invariants decays from $y = 1$ to $y = 4$, then fluctuates before increasing towards zero. R stays at zero until $x = 3$, then also fluctuates also. The comparison between tomo-SMART and PVR-SMART is difficult since both $\langle Q \rangle$ and $\langle R \rangle$ plots seem quite hectic. A possible reason is the propagation of uncertainty from the noisy velocity field to the spatial derivatives and thus to the Q criteria. Considering the error propagation, the plots are possibly not converged enough, since as mentioned in section 6.3.4.1, there are only 300 samples at each measurement point. At the beginning of the jet, for $0 < y < 4$, $\langle Q \rangle$ from PVR-SMART seems less noisy than tomo-SMART. However, for the rest of the jet, the comparison does not seem to be relevant.

The evolution of the $Q - R$ plot along the jet development axis can be seen in figure 6.3.12 and figure 6.3.13. Each $Q - R$ plot is a scatter of the values of Q and R in the planes $y = \{0.5, 1, 2\}$ in figure 6.3.12 and $y = \{3, 6\}$ in figure 6.3.13, over the 300 velocity fields of the data set **Case 2**. For every $Q - R$ plot, Q and R values were normalized using Q_w. The same general behavior of the $Q - R$ plot as shown in [Khashehchi et al., 2012] is observed here. Near the nozzle exit, the $Q - R$ plot is a vertical ellipse, which is expected since the velocity is mostly composed of the v component. In that case, the velocity gradient is said to be degenerate, Q and R are close to zero, and as presented in [Khashehchi et al., 2012], Q is of the order of $|\mathcal{A}|^2$ and R is of the order of $|\mathcal{A}|^3$. Considering noise in the results, this leads to a vertical ellipse. After $y = 3$, the teardrop shape appears and is even more visible for larger y positions, while the flow increasingly tends to be skewed along the $D_{\mathcal{A}}$ line in the second quadrant of the plot where the flow is said to be unstable-node/saddle/saddle (lower right of the plot).

When comparing the $Q - R$ plot of PVR-SMART and tomo-SMART algorithm, one can notice that the plots are rather similar, and their individual behavior along the jet centerline axis are the same. However, little differences can be noticed when paying close attention, especially from $y = 2$. At $y = 2$, the $Q - R$ plot is stretched along the Q axis, and is thinned out at the center of the plot. PVR-SMART distribution seems to be more attached to the $D_{\mathcal{A}}$ discriminant curve than tomo-SMART. Such a difference is also seen at $y = 3$ and further away from the exit nozzle at $y = 6$ where the teardrop shape for PVR-SMART is closer attached to or hugging the discriminant line than tomo-SMART. Those differences are admittedly small, as the $Q - R$ plot seems to smooth out the differences between the two algorithms.

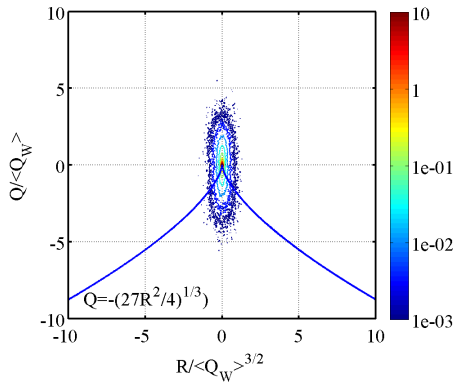

(a) tomo-SMART y = 0.5

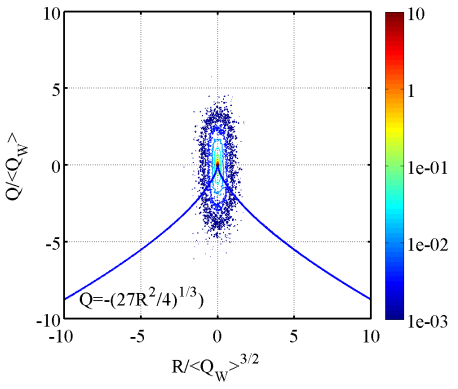

(b) PVR-SMART y = 0.5

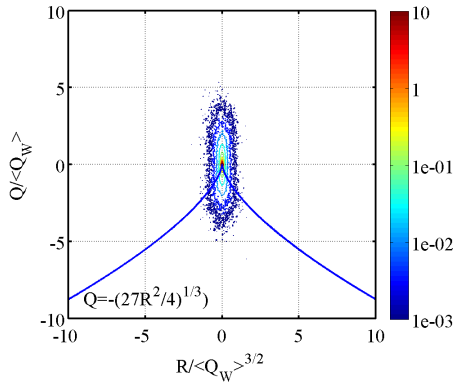

(c) tomo-SMART y = 1

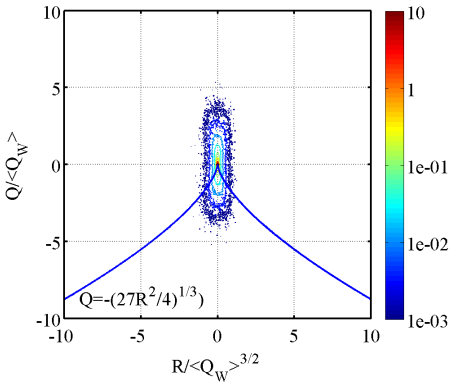

(d) PVR-SMART y = 1

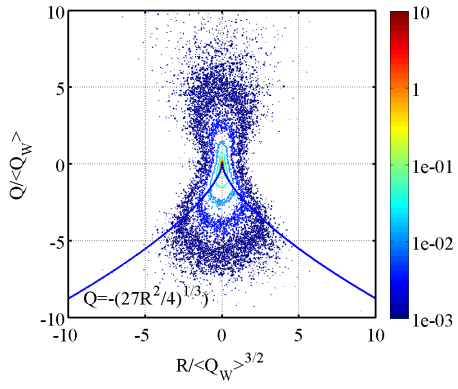

(e) tomo-SMART y = 2

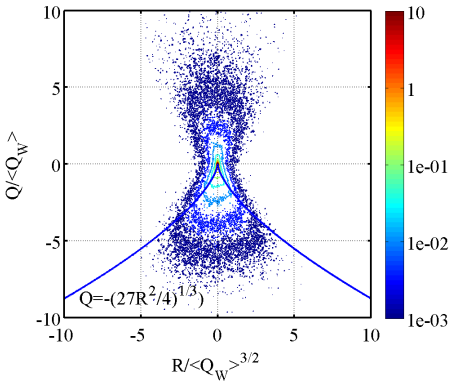

(f) PVR-SMART y = 2

Figure 6.3.12: 'Q-R' Joint PDF for $y = \{0.5, 1, 2\}$.

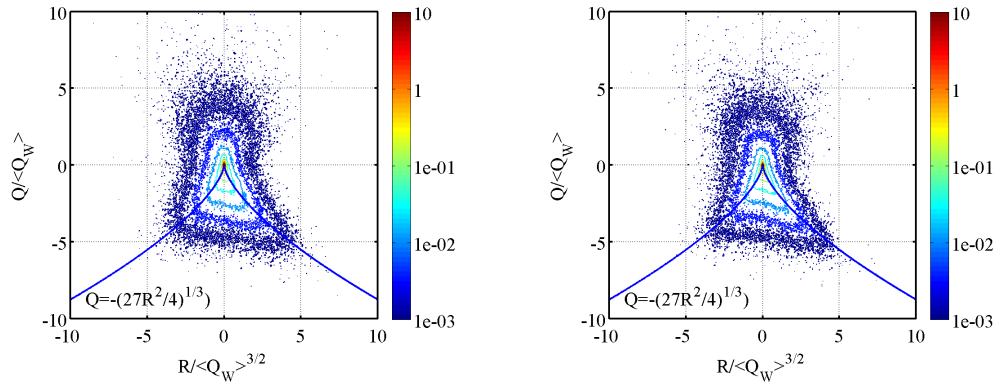

(a) tomo-SMART y = 3 **(b)** PVR-SMART y = 3

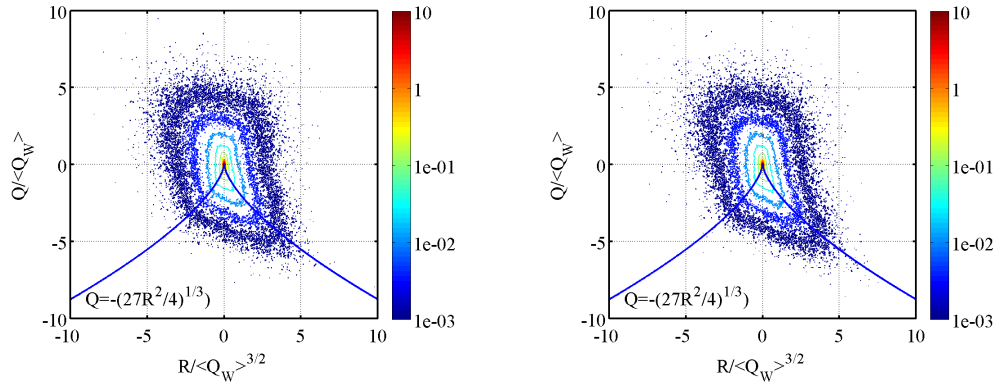

(c) tomo-SMART y = 6 **(d)** PVR-SMART y = 6

Figure 6.3.13: 'Q-R' Joint PDF for $y = \{3, 6\}$.

6.3.4.9 Comparison of the jet 3D structure

In this section, we compare tomo-SMART and PVR-SMART by investigating the instantaneous 3D flow organization, or 3D structures of the jet. [Violato and Scarano, 2011] did an extensive study of the 3D structure organization and evolution of a turbulent jet at $Re_D = 5000$ using 3D-PIV. The 3D flow visualizations presented in their work are well adapted for this study.

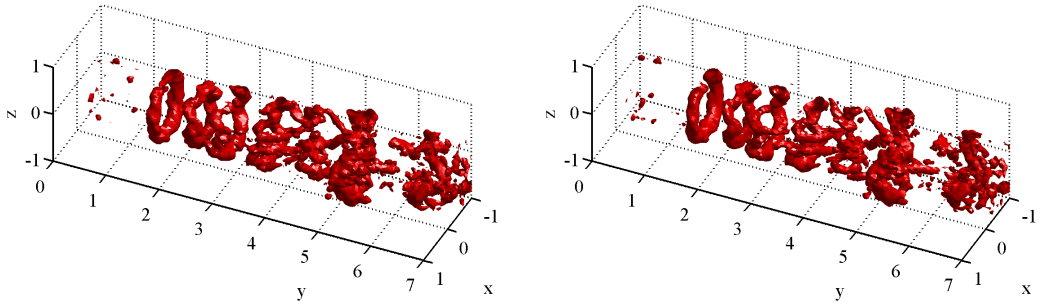

(a) tomo-SMART **(b)** PVR-SMART

Figure 6.3.14: Isovalue of Q criterion, Q = 2.

The first 3D visualization is the Q criterion (see equation (6.3.6)) which is one of many criteria to visualize vortices. figure 6.3.14 illustrates iso-surfaces of $Q = 2$ criterion. One can notice that the vortices rings are not completed for the laser sheet was not wide enough to encompass the whole 3D vortex ring. This visualization enables us to see vortex rings being convected in the streamwise direction. They are the result of the growth of Kelvin-Helmholtz instabilities. The vortex shedding seems to happen between $y = 1.5$ and $y = 2$.

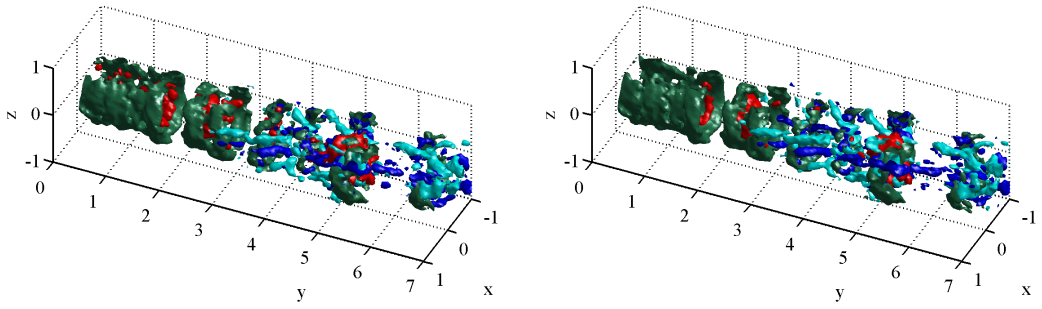

(a) tomo-SMART **(b)** PVR-SMART

Figure 6.3.15: Isovalue of axial velocity 1.05 V_0 (red), Isovalue of vorticity components $\omega_\theta = 2$ (green), $\omega_z = 1.2$ (cyan) and -1.2 (blue).

In this snapshots, one can see that the vortex rings are unstable and while convected are being torn and later destroyed once the flow has become fully three-dimensional.

This is a well-known feature of this flow ([Yule, 1978], [Liepmann and Gharib, 1992], Violato and Scarano [2011] among others). Indeed, vortex rings are pairing while being convected, and during this pairing phase the flow shows a growth of azimuthal instabilities. These lead to a further stretching of vortices. Azimuthal instabilities of the ring vortices also lead to the growth of secondary streamwise vortices appearing in between vortex rings. In a numerical study, [Martin and Meiburg, 1991] showed that initial azimuthal perturbations also lead to the development of streamwise vortices, organized into pairs in the braid region which is the region in between two subsequent spanwise rollers. [Liepmann and Gharib, 1992], in an experimental study, confirmed this organization in a low Reynolds number round jet.

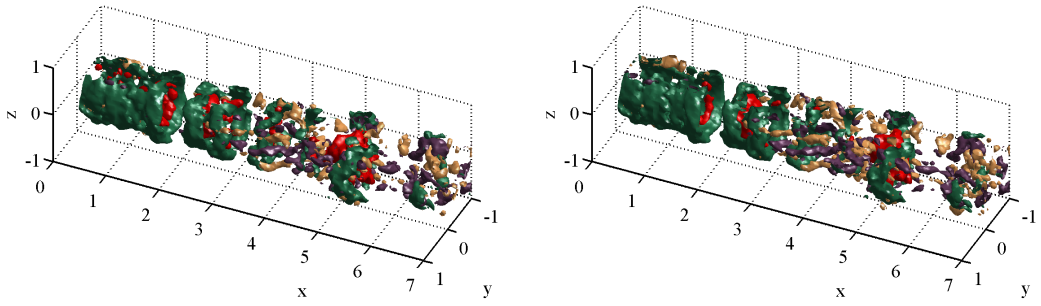

(a) tomo-SMART **(b)** PVR-SMART

Figure 6.3.16: Isovalue of axial velocity 1.05 V_0 (red), isovalue of vorticity components $\omega_\theta = 2$ (cyan), $\omega_r = 1.2$ (ocher) and -1.2 (purple).

For a better understanding of the flow organization, we separated the physical phenomena and plotted visualizations of the azimuthal, the radial, and the axial components of the vorticity vector as in [Violato and Scarano, 2011]. This allows an easier investigation of the flow, especially in the three-dimensional part of the jet where streamwise vortices are created and interact with azimuthal vortices. Figure 6.3.15 illustrates the behavior of azimuthal and axial vorticity and figure 6.3.16 illustrates the behavior of radial and axial vorticity.

The flow organization described previously can be seen in those visualizations, with the shedding of vortex ring (represented by ring of azimuthal vorticity in green), the growth of azimuthal instability combined with the appearance of streamwise vortices. These streamwise structures are inclined at an angle of about $30° - 40°$ relatively to the jet axis. This inclination is responsible for both axial and radial vorticity (seen in figure 6.3.15 and figure 6.3.16). The visualization of axial vorticity shows that the pair of streamwise vortices is indeed a counter rotating pair. Further downstream, the vortex ring is now completely distorted (at $y = 5$), the flow becoming fully 3D and turbulent.

A zoomed visualization of Q criterion for $y = [1.5\ 2.5]$ in figure 6.3.17 shows the azimuthal instability of the vortex ring.figure 6.3.18 illustrates the growth of counter-rotating streamwise structures, visible among features in the axial vorticity instability in the braid region. This zoomed 3D visualization is better suited for the comparison of the flow structures from tomo-SMART and PVR-SMART. The two algorithms display the same features previously explained and their differences are minimal. However,

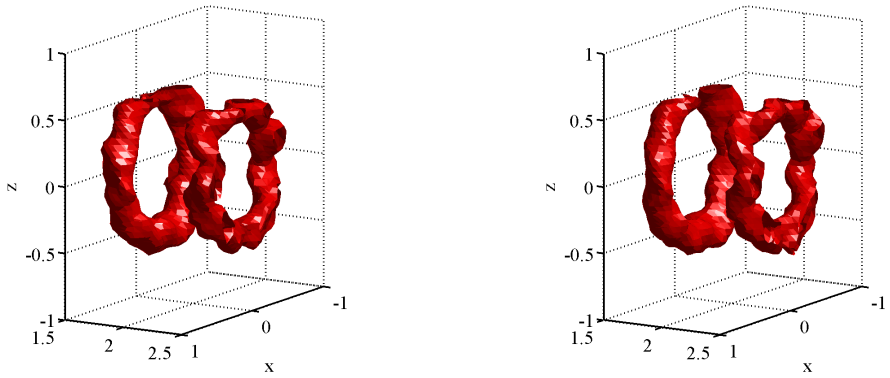

(a) tomo-SMART **(b)** PVR-SMART

Figure 6.3.17: Isovalue of Q=2 criterion for $y = 1.5$ to $y = 2.5$.

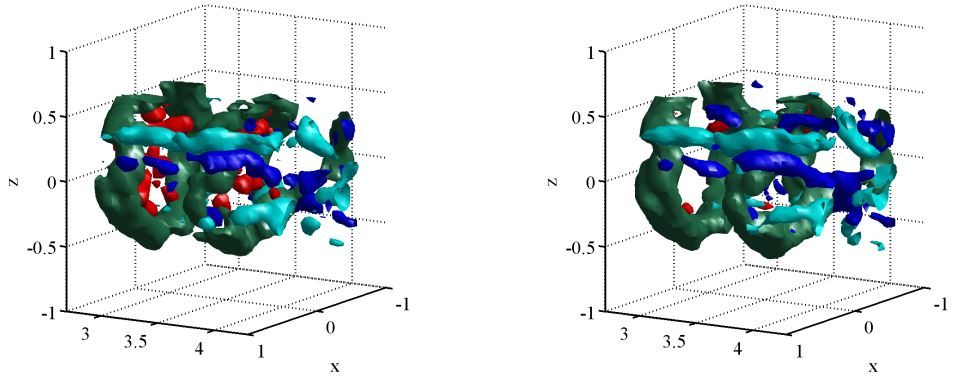

(a) tomo-SMART **(b)** PVR-SMART

Figure 6.3.18: Isovalue of axial velocity 1.05 V_0 (red), isovalue of vorticity components $\omega_\theta = 2$ (green), $\omega_z = 1.2$ (cyan) and -1.2 (blue) for $y = 2.5$ to $y = 4.5$.

upon closer look and thanks to the zoom enhancement, one notices differences. For the comparison of the Q criterion, PVR-SMART seems to have a smoother initial vortex ring than tomo-SMART. The distorted vortex ring looks rather similar for both algorithms. When looking at azimuthal vorticity and axial vorticity, the differences are more visible. PVR-SMART has rounder and smoother ring vortex - even if distorted and twisted - than tomo-SMART (in green), the counter-rotating streamwise vortex are longer, smoother, and bigger for PVR-SMART than for tomo-SMART.

6.4 Conclusion

The first part of this chapter was devoted to the parameter settings of the reconstruction algorithm as well as the correlation algorithm. A full study on the use of threshold methods in the reconstruction led to choose two parameter settings : the MLOS threshold value (set so as to threshold 99% of the image noise) and the use of this same threshold in the images when performing the iterative reconstruction. This issue is critical when noise is present in the images. The method using a MLOS 99% threhold and raw images in the SMART algorithm was shown to be the more robust and yield more physical results than other methods, and was thus chosen. The choice of the PVR reconstruction PSF size was made doing a-posteriori tests. The IV size for FOLKI-3D was also chosen by a-posteriori tests.

PVR-SMART and tomo-SMART were finally compared on the near field region of a turbulent air jet. Several seeding density conditions were used to compare the performances of both algorithms. The analysis of the reconstruction signal-to-noise ratio confirmed the trend obtained in the simulations regarding the comparison between tomo-SMART and PVR-SMART. With the given image pre-processing, PVR-SMART was found to yield velocity fields that are about 50 % less noisy than tomo-SMART. An analysis of the mean correlation score showed that indeed, the correlation score for tomo-SMART was significantly less than for PVR-SAMRT. This was further investigated by a peak-locking analysis which showed that tomo-SMART does suffer from peak-locking, due to the image pre-processing and the size of the particles in the images. But, based on a different reconstruction paradigm, PVR-SMART does not suffer from this phenomenon, since its very definition makes it less impacted by difficult imaging conditions such as small particle image sizes. The velocity field comparison includes velocity field statistical properties, flow divergence analysis, velocity gradient tensor and coherent structures exploration. These results on experimental data confirm the gains obtained by PVR in the numerical study.

7 Conclusion

In this final chapter, we will summarize the main results and conclusions of this thesis before finally putting this work into perspective with regards to the future and evolution of tomographic PIV.

7.1 On the simulation of experimental factors in 3D-PIV

The second chapter of this thesis was dedicated to the study of experimental factors impacting the quality of the tomographic reconstruction. This study was carried out with numerical simulation of 3D-PIV. Numerical simulation is particularly well suited for the study of reconstruction accuracy since it requires the knowledge of the ground truth, i.e. the particle space location and intensity. In our synthetic images, different noises, or imaging deterioration were generated to assess their impact on the reconstruction quality. We focused on imaging conditions generally found in incompressible air flow fields.

The first aspect of image degradation we focused on, can be seen as additional noise in the images. Geometric considerations were used to quantify the impact of "added particles" lying in the Union volume of the camera fields of view and the illumination area. From this, a geometrical factor was deduced, quantifying the level of noise introduced in the reconstruction, which is the ratio between the Intersection and the Union volume defined by the cameras field of view and the illumination area, called $R_{I/U}$. The main impact on the reconstruction is the increase in the number and intensity of ghost particles. Performing numerical simulation of tomo-PIV without accounting for this effects was shown to drastically overestimate the reconstruction algorithm accuracy.

The other aspect of image deterioration investigated was the decrease in signal-to-noise ratio in the image, especially Mie scattering and defocusing effects. Results suggest that the main impact of particle image defocusing on the reconstruction is the loss of real particles due to the peak intensity decrease when the PSF size increases, (when the particles increasingly become out of focus). As for Mie scattering, the main impact is also the loss of real particles due to the polydisperse nature of the seeding, leading to dispersion of the particle intensity.

Those simulation refinements increased simulation realism and emphasized the importance of imaging conditions for tomo-PIV, especially when the signal-to-noise ratio in the images is low, as it is for instance when using time-resolved 3D-PIV in the air. We showed that in a real experiment, once the cameras positions were set, optimizing their orientation did not have a significant impact on the $R_{I/U}$ factor,

and thus on the geometrically added particles. However, this noise source has to be accounted for in a simulation when for instance assessing the accuracy of reconstruction algorithm.

7.2 Lucas-Kanade based correlation method for 3D-PIV

We introduced a cross-correlation technique for 3D-PIV (FOLKI-3D) as an extension to 3D of the algorithm FOLKI-PIV [Champagnat et al., 2011]. As in the planar context, the displacement is searched as the minimizer of a sum of squared differences, which is solved iteratively by using volume deformation. In a GPU implementation, the latter can be performed using a simple, linear scheme or a higher-order, cubic B-Spline scheme.

Numerical tests performed on synthetic 3D particle distributions have confirmed that the spatial frequency response is similar to that of standard iterative deformation algorithms, for both top-hat and Gaussian weightings, while similar gains as reported in the literature are obtained by choosing the cubic B-Spline interpolation rather than the linear one.

Tests on volumes reconstructed from projected images have then allowed us to characterize the robustness of the algorithm to specific tomographic noise (i.e. ghost particles), as well as the gain brought by the higher-order interpolation in a more realistic configuration. FOLKI-3D has been found in particular more robust to coherent ghosts than a standard iterative deformation algorithm, while the gain in accuracy of the high-order deformation has been confirmed for various quantities of ghosts in the reconstructions, and various shapes of the reconstructed particles.

7.3 Particle Volume Reconstruction

An alternative approach to the classical tomographic reconstruction was introduced. It seeks to recover nearly single voxel particles rather than blobs of extended size using a particle-based representation of image data. We refer to this approach as Particle Volume Reconstruction (PVR). PVR underlies a sparse volumic representation of point particles, which lives halfway between infinitely small particles - which they physically are - and larger two to three voxel diameter blobs usually used in tomo-PIV. From that representation, it is possible to use it to perform PTV or to smooth it to the 2 voxel diameter blob, which is the gold standard of correlation for PIV. We focus here on the 3D-PIV use of PVR, by incorporating the PVR paradigm in a SMART algorithm (PVR-SMART).

The performances of the PVR-SMART reconstruction method was assessed by means of 3D simulations of reconstruction and displacement estimation. PVR-SMART has been shown to outperform tomo-SMART ([Atkinson and Soria, 2009]) on a large domain of generating conditions and a variety of metrics on volume reconstruction and displacement estimation, especially in the case of seeding density greater than 0.06 *ppp* and of PSFs characterized by a standard deviation larger than 0.8 pixel. Robustness to inaccurate knowledge of the PSF size has also been checked. Tests showed that the performance gains on displacement fields with PVR are systematically obtained

whatever the value of the PSF in the case of underestimation, and they persist in the case of an overestimation of up to 10% of the PSF value.

The application and assessment of PVR-SMART on experimental data was performed on a turbulent round air jet at $Re_D \approx 4300$, with D the nozzle diameter. An extensive study was carried out to determine the proper use of thresholds in the reconstruction algorithm in the presence noisy images. The choice of the reconstruction PSF size for PVR was done through a-posteriori testing. Several seeding density conditions were used to compare the performance of tomo-SMART and PVR-SMART. Furthermore, an additional 2D-PIV system synchronized with the tomo-PIV setup was used as a measurement reference for this comparison. The analysis of the reconstruction signal-to-noise ratio confirmed the trend obtained in the simulations regarding the comparison between tomo-SMART and PVR-SMART. Velocity fields of the near field region obtained by tomo-SMART and PVR-SMART were compared. With the given image pre-processing, PVR-SMART was found to yield velocity fields that are about 50 % less noisy than tomo-SMART. The velocity field comparison included velocity field statistical properties, peak-locking study, flow divergence analysis, velocity gradient tensor and coherent structures exploration. These results on experimental data confirm the gains obtained by PVR in the numerical study.

7.4 Perspectives

The main finding in this dissertation is the introduction of PVR approach for reconstructing particle volumes. This approach was implemented in a tomoPIV context, and was shown to exhibit performance gains compared to a classical reconstruction algorithm [Atkinson and Soria, 2009] on both numerical and experimental data. In this paradigm, the PSF size is needed to reconstruct the volume. For the sake of clarity, we used a-posteriori tests to choose the PSF size. However, a calibration process such as [Reichenbach et al., 1991] or [Delbracio et al., 2012] could yield the knowledge of a varying defocusing PSF function for all cameras. This implementation and use in PVR could lead to increased performances and will be an interesting follow up of this research. Furthermore, following the investigation of Mie scattering and its effects on the tomographic reconstruction in chapter 2, it would be valuable to investigate the effects of an adjusting coefficient on the back-scattering images.

Because of its specific particle representation, PVR is well adapted for sparse reconstruction algorithms such as [Barbu et al., 2011], [Cornic et al., 2013], with the final aim of estimating the displacement by PTV tracking. [Cornic et al., 2015a] used the PVR approach with a CoSaMP algorithm (Compressed Sampling Matching Pursuit [Needell and Tropp, 2009]) providing an excellent initial guess for PTV, which can be refined to subvoxel accuracy and then used for tracking for the displacement estimation. Furthermore, in a time-resolved context, where a criterion can be found to discriminate ghost particles from real particles - very much like [Schanz et al., 2013b] - this development could show great potential for measuring turbulent flows.

[Yegavian et al., 2015] recently introduced a new method for estimating fluid trajectories in a time-resolved PIV context. It also relies on a Lucas-Kanade paradigm and consists in a simple and direct extension of a two-frame estimation proposed in the context of FOLKI-PIV where so-called Lucas-Kanade Fluid Trajectories (LKFT) are assumed to be polynomial in time. This method could be extended to 3D to improve

the displacement estimation of FOLKI-3D for time-resolved 3D-PIV in air flows where noise levels are high in the reconstruction volumes due to the relative low energy of the high repetition rate laser and the low signal-to-noise ratio in the images. Moreover, such techniques enable researchers to directly access velocity material derivatives.

Finally, in the context of time-resolved PIV applied on a turbulent jet at DAFE (ONERA), and after the works [Davoust et al., 2014] and [Courtier, 2015], we believe that our 3D measurements methods will be powerful tools to investigate coherent structures and their developments.

Bibliography

Adrian, R. J. and Yao, C.-S. (1985). Pulsed laser technique application to liquid and gaseous flows and the scattering power of seed materials. *Applied Optics*, 24(1).

Albrecht, H.-E., Damaschke, N., Borys, M., and Tropea, C. (2003). *Laser Doppler and Phase Doppler Measurement Techniques*. Springer-Verlag Berlin Heidelberg, 1st edition.

Arroyo, M. and Greated, C. (1991). Stereoscopic particles image velocimetry. *Measurement Science and Technology*, 2(12).

Astarita, T. and Cardone, G. (2005). Analysis of interpolation schemes for image deformation methods in piv. *Experiments in Fluids*, 38.

Atkinson, C. and Soria, J. (2009). An efficient simultaneous reconstruction technique for tomographicparticle image velocimetry. *Experiments in Fluids*, 47:553–568.

Bailly, C. and Comte-Bellot, G. (2015). *Turbulence*. Springer, 2nd edition.

Baker, S. and Matthews, I. (2004). Lucas-Kanade 20 years on: a unifying framework. *Int. J. Comput. Vis.*, 16(4).

Ball, C., Fellouah, H., and Pollard, A. (2012). The flow field in turbulent round free jets. *Progress in Aerospace Sciences*, 50:1 – 26.

Barbu, I. (2014). *Tridimensional Estimation of Turbulent Fluid Velocity*. PhD thesis, Université Rennes 1.

Barbu, I., Herzet, C., and Memin, E. (2011). Sparse models and pursuit algorithms for PIV Tomography. In *Forum on Volumic Reconstruction 2011*.

Becker, B. H. A. and Massaro, T. A. (1968). Vortex evolution in a round jet. *Journal of Fluid Mechanics*, 31:435–448.

Bohren, C. F. and Huffman, D. R. (1983). *Absorption and scattering of light by small particles*. Wiley.

Borys, M., Strunck, V., Muller, H., and Dopheide, D. (2002). Simultaneous measurement of velocity and particle size profiles with the reference beam technique. *Laser Techniques for Fluid Mechanics*, pages 251–268.

Brucker, C. (1995). Digital-Particle-Image-Velocimetry (dpiv) in a scanning light-sheet: 3D starting flow around a short cylinder. *Experiments in Fluids*, 19:255–263.

Byrne, C. L. (2008). *Applied Iterative Methods*. AK Peters.

Champagnat, F., Cornic, P., Cheminet, A., Leclaire, B., Besnerais, G. L., and Plyer, A. (2014). Tomographic PIV: particles versus blobs. *Measurement Science and Technology*, 25(8):084002.

Champagnat, F. and Le Sant, Y. (2013). Efficient cubic B-Spline image interpolation on a GPU. *Journal of Graphics Tools*, 16(2).

Champagnat, F., Plyer, A., Le Besnerais, G., Leclaire, B., Davoust, S., and Le Sant, Y. (2011). Fast and accurate PIV computation using highly parallel iterative correlation maximization. *Experiments in Fluids*, 50:1169–1182.

Cheminet, A., Leclaire, B., Champagnat, F., Cornic, P., and Le Besnerais, G. (2013). On factors affecting the quality of tomographic reconstruction. In *Proceedings of PIV13*.

Chong, M. S., Perry, A. E., and Cantwell, B. J. (1990). A general classification of three dimensional flow fields. *Physics of Fluids*, 2(5):765–777.

Chong, M. S., Soria, J., Perry, A. E., Chacin, J., Cantwell, B. J., and Na, Y. (1998). Turbulence structures of wall-bounded shear flows found using DNS data. *Journal of Fluid Mechanics*, 357:225–247.

Cornic, P., Champagnat, F., Cheminet, A., Leclaire, B., and Besnerais, G. L. (2013). Computationally efficient sparse algorithms for tomographic PIV Reconstruction. In *Proceedings of PIV13*.

Cornic, P., Champagnat, F., Cheminet, A., Leclaire, B., and Besnerais, G. L. (2015a). Fast and efficient particle reconstruction on a 3d grid using sparsity. *Experiments in Fluids*, 56(3).

Cornic, P., Illoul, C., Sant, Y. L., Cheminet, A., Besnerais, G. L., and Champagnat, F. (2015b). Calibration drift within a Tomo-PIV setup and Self-Calibration. In *Proceedings of PIV15*.

Courtier, R. (2015). *Influence des conditions initiales et dynamique des grandes échelles dans les jets turbulents*. PhD thesis, Ecole Polytechnique.

Crow, S. and Champagne, F. (1971). Orderly structure in jet turbulence. *Journal of Fluid Mechanics*, 48:547–591.

Davoust, S. (2011). *Dynamique des grandes echelles dans les jets turbulents avec ou sans effets de rotation*. PhD thesis, Ecole Polytechnique.

Davoust, S., Jacquin, L., and Leclaire, B. (2012). Dynamics of m = 0 and m = 1 modes and of streamwise vortices in a turbulent axisymmetric mixing layer. *Journal of Fluid Mechanics*, 709:408–444.

Davoust, S., Jacquin, L., and Leclaire, B. (2014). New results on the structure of turbulence in a mixing layer with and without swirl. *International Journal of Heat and Fluid Flow*, 49:11–17.

De Silva, C. M., Baidya, R., Khashehchi, M., and Marusic, I. (2012). Assessment of tomographic PIV in wall-bounded turbulence using direct numerical simulation data. *Experiments in Fluids*, 52:425–440.

Delbracio, M., Muse, P., Almansa, A., and Morel, J. M. (2012). The Non-parametric sub-pixel local point spread function estimation is a well posed problem. *Int J. Comput. Vis.*, 96:175–94.

Dyke, M. V. (1982). *An Album of Fluid Motion*. THE PARABOLIC PRESS.

Elsinga, G., Wieneke, B., Scarano, F., and van Oudheusden, B. (2005). Assessment of Tomo-PIV for three-dimensional flows. In *6th International Symposium on Particle Image Velocimetry, PIV 05*, Pasadena, California, USA,.

Elsinga, G. E. (2008). *Tomographic particle image velocimetry and its application to turbulent boundary layers*. PhD thesis, TU Delft.

Elsinga, G. E. and Marusic, I. (2010). Evolution and lifetimes of flow topology in a turbulent boundary layer. *Physics of Fluids*, 22(1).

Elsinga, G. E., Scarano, F., Wieneke, B., and van Oudheusden, B. (2006). Tomographic particle image velocimetry. *Experiments in Fluids*, 41:933–947.

Elsinga, G. E., Westerweel, J., Scarano, F., and Novara, M. (2011). On the velocity of ghost particles and the bias errors in tomographic-piv. *Exp. Fluids*, 50:825–838.

Fukuchi, Y. (2012). Influence of number of cameras and preprocessing for thick volume Tomographic PIV. In *16th Int. Symp. on Applications of Laser Techniques to Fluid Mechanics, Lisbon*, Lisbon, Portugal, USA,.

Gan, L., Cardesa-Duenas, J. I., Michaelis, D., and Dawson1, J. (2012). Comparison of Tomographic PIV algorithms on resolving coherent structures in locally isotropic turbulence. In *16th Int Symp on Applications of Laser Techniques to Fluid Mechanics, Lisbon*, Lisbon, Portugal.

Gulotski, G., Kholmyansky, M., Kinzelbach, W., Luthi, B., Tsinober, A., and Yorish, S. (2007). Velocity and temperature derivatives in high-reynolds-number turbulent flows in the atmospheric surface layer. part 1. Facilities, methods and some general results. *Journal of Fluid Mechanics*, 589:57–81.

Hecht, E. and Zajac, A. (2001). *Optics*. Addison-Wesley Pub. Company, Massachusetts.

Herman, G. T. and Lent, A. (1976). Iterative reconstruction algorithms. *Computers in Biology and Medicine*, 6(4):273 – 294.

Hinsch, K. (2002). Holographic particle image velocimetry. *Measurement Science and Technology*, 13:61–72.

Hugh M. Blackburn, N. N. M. and Cantwell, B. J. (1996). Topology of fine-scale motions in turbulent channel flow. *Journal of Fluid Mechanics*, 310:269–292.

Hussain, A. K. M. F. (1986). Coherent structures and turbulence. *Journal of Fluid Mechanics*, 173:303–356.

Khashehchi, M., Elsinga, G. E., Hooman, K., Ooi, A., Soria, J., and Marusic, I. (2012). Tomographic PIV Assessment of Turbulence Characteristics in the Developing Region of a Turbulent Round Jet. In *16th Int Symp on Applications of Laser Techniques to Fluid Mechanics, Lisbon*, Lisbon, Portugal.

Kim, J. and Choi, H. (2009). Large eddy simulation of a circular jet: effect of inflow conditions on the near field. *Journal of Fluid Mechanics*, 620:383–411.

Lamarche, F. and Leroy, C. (1990). Evaluation of the volume of intersection of a shpere with a cyinder by elliptic integras. *Computer Physics Communications*, 59:359–369.

Le Sant, Y., Gardarin, B., Leclaire, B., Geffroy, P., and Soulevant, D. (2007). Polynomial calibration vs. pinhole calibration. In *In 7th International Symposium on Particle Image Velocimetry*, Roma, Italy.

Le Sant, Y. and Merienne, M.-C. (1995). An image resection method applied to mapping techniques. In *ICIASF'95*, Dayton, OH.

Leclaire, B., Sant, Y. L., Besnerais, G. L., and Champagnat, F. (2011). On the stability and spatial resolution of image deformation PIV methods. In *9th Int Symp on Particle Image Velocimetry - Kobe, Japan*.

Liepmann, D. and Gharib, M. (1992). The role of streamwise vorticity in the near-field entrainment of round jets. *Journal of Fluid Mechanics*, 245:643–668.

Lynch, K. P. and Scarano, F. (2014). Experimental determination of tomographic PIV accuracy by a 12-camera system. *Measurement Science and Technology*, 25(8):084003.

Lynch, K. P. and Scarano, F. (2015). An efficient and accurate approach to mte-mart for time-resolved tomographic piv. *Experiments in Fluids*, 56(3):1–16.

Lüthi, B., Holzner, M., and Tsinober, A. (2009). Expanding the Q–R space to three dimensions. *Journal of Fluid Mechanics*, 641:497–507.

Maas, H. G., Gruen, A., and Papantoniou, D. (1993). Particle tracking velocimetry in three-dimensional flows. part 1. photogrammetric determination of particle coordinates. *Experiments in Fluids*, 15:133–146.

Malik, N. A., Dracos, T., and Papantoniou, D. (1993). Particle tracking velocimetry in three-dimensional flows. *Experiments in Fluids*, 15(4-5):279–294.

Martin, J., Ooi, A., Chong, M. S., and Soria, J. (1998). Dynamics of the velocity gradient tensor invariants in isotropic turbulence. *Physics of Fluids*, 10(9):2336–2346.

Martin, J. E. and Meiburg, E. (1991). Numerical investigation of three-dimensionally evolving jets subject to axisymmetric and azimuthal perturbations. *Journal of Fluid Mechanics*, 230:271–318.

Meneveau, C. (2011). Lagrangian Dynamics and Models of the Velocity Gradient Tensor in Turbulent Flows. *Annual Review of Fluid Mechanics*, 43(1):219–245.

Meng, H., Pan, G., Pu, Y., and Woordward, S. (2004). Holographic particle image velocimetry: from film to digital recording. *Measurement Science and Technology*, 15(4).

Michalke, A. (1984). Survey on jet instability theory. *Progress in Aerospace Sciences*, 21:159 – 199.

Needell, D. and Tropp, J. (2009). Cosamp: Iterative signal recovery from incomplete and inaccurate samples. *Applied and Computational Harmonic Analysis*, 26(3):301 – 321.

Nomura, K. K. and Post, G. K. (1998). The structure and dynamics of vorticity and rate of strain in incompressible homogeneous turbulence. *Journal of Fluid Mechanics*, 377:65–97.

Novara, M. (2013). *Advances in tomographic PIV*. PhD thesis, TU Delft.

Novara, M., Batenburg, K. J., and Scarano, F. (2010). Motion tracking-enhanced mart for tomographic piv. *Measurement Science and Technology*, 21(3):035401.

Olsen, M. G. and Adrian, R. J. (2000). Out-of-focus effects on particle image visibility and correlation in microscopic particle image velocimetry. *Experiments in Fluids*, 29(1):S166–S174.

Ooi, A., Martin, J., julio Soria, and Chong, M. S. (1999). A study of the evolution and characteristics of the invariants of the velocity-gradient tensor in isotropic turbulence. *Journal of Fluid Mechanics*, 381:141–174.

Pereira, F., Gharib, M., Dabiri, D., and Modaress, D. (2000). Defocusing digital particle image velocimetry: a 3-component 3-dimensional dpiv measurement technique. application to bubbly flows. *Experiments in Fluids*, S:78–84.

Petra, S. and Schnörr, C. (2009). TomoPIV meets compressed sensing. *Pure Mathematics and Applications*, 20(1-2):49 – 76.

Pope, S. B. (2000). *Turbulent flows*. Cambridge University Press, Cambridge.

Raffel, M., Willert, C. E., Wereley, S. T., and Kompenhans, J. (2007). *Particle Image Velocimetry. A practical guide*. Springer Verlag, 2nd edition.

Reichenbach, S. E., Park, S. K., and Narayanswamy, R. (1991). Characterizing digital image acquisition devices. *Opt. Eng.*, 30:170–7.

Reynolds, O. (1895). On the Dynamical Theory of Incompressible Viscous Fluids and the Determination of the Criterion. *Philosophical Transactions of the Royal Society of London A: Mathematical, Physical and Engineering Sciences*, 186:123–164.

Scarano, F. (2002). Iterative image deformation methods in PIV. *Measurement Science and Technology*, 13:1–19.

Scarano, F. (2013). Tomographic PIV: principles and practice. *Measurement Science and Technology*, 24(1):012001.

Scarano, F. and Poelma, C. (2009). Three-dimensional vorticity patterns of cylinder wakes. *Experiments in Fluids*, 47(1):69–83.

Scarano, F. and Riethmuller, M. L. (2000). Advances in iterative multigrid PIV image processing. *Experiments in Fluids*, 29(1).

Schanz, D., Gesemann, S., Schreder, A., Wieneke, B., and Novara, M. (2013a). Non-uniform optical transfer functions in particle imaging: calibration and application to tomographic reconstruction. *Meas. Sci. Technol.*, 24:1–15.

Schanz, D., Gesemann, S., and Schröder, A. (2016). Shake-the-box: Lagrangian particle tracking at high particle image densities. *Experiments in Fluids*, 57(5):1–27.

Schanz, D., Gesemann, S., Schroder, A., Wieneke, B., and Michaelis, D. (2010). Tomographic reconstruction with non-uniform optical transfer functions (OTF). In *15th Int Symp on Applications of Laser Techniques to Fluid Mechanics Lisbon, Portugal, 05-08 July*.

Schanz, D., Schreder, A., Gesemann, S., Michaelis, D., and Wieneke, B. (2013b). Shake The Box: A highly efficient and accurate Tomographic Particle Tracking Velocimetry (TOMO-PTV) method using prediction of particle positions. In *Proceedings of PIV13*.

Schrijer, F. F. J. and Scarano, F. (2008). Effect of predictor–corrector filtering on the stability and spatial resolution of iterative PIV interrogation. *Experiments in Fluids*, 45:927–941.

Schröder, A., Schanz, D., Michaelis, D., Cierpka, C., Scharnowski, S., and Kähler, C. (2015). Advances of PIV and 4D-PTV "Shake-The-Box" for Turbulent Flow Analysis -the Flow over Periodic Hills. *Flow, Turbulence and Combustion*, 95(2):193–209.

Soloff, S. M., Adrian, R. J., and Liu, Z.-C. (1997). Distortion compensation for generalized stereoscopic particle image velocimetry. *Measurement Science and Technology*, 8:1441–1454.

Soria, J., Sondergaard, R., Cantwell, B. J., Chong, M. S., and Perry, A. E. (1994). A study of the fine-scale motions of incompressible time-developing mixing layers. *Physics of Fluids*, 6(2):871–884.

Thomas, L., Tremblais, B., and David, L. (2014). Optimization of the volume reconstruction for classical Tomo-PIV algorithms (MART, BIMART and SMART): synthetic and experimental studies. *Measurement Science and Technology*, 25(3):035303.

Thomas, L., Vernet, R., Tremblais, B., and David, L. (2010). Influence of geometric parameters and image preprocessing on tomoPIV results. In *Proceedings 15th Int Symp on Applications of Laser Techniques to Fluid Mechanics Lisbon, Portugal, 05-08 July*.

Tsinober, A., Kit, E., and Dracos, T. (1992). Experimental investigation of the field of velocity gradients in turbulent flows. *Journal of Fluid Mechanics*, 242:169–192.

Violato, D. (2013). *3D flow organization and dynamics in subsonic jets : Aeroacoustic source analysis by tomographic PIV*. PhD thesis, TU Delft.

Violato, D. and Scarano, F. (2011). Three-dimensional evolution of flow structures in transitional circular and chevron jets. *Physics of Fluids*, 23(12).

Westerweel, J. and Scarano, F. (2005). Universal outlier detection for PIV data. *Experiments in Fluids*, 39:1096–1110.

Wieneke, B. (2008). Volume self-calibration for 3D particle image velocimetry. *Experiments in Fluids*, 45:549–556.

Wieneke, B. (2013). Iterative reconstruction of volumetric particle distribution. *Measurement Science and Technology*, 24(2):024008.

Willert, C. (1997). Stereoscopic digital particle image velocimetry for application in wind tunnel flows. *Measurement Science and Technology*, 12.

Worth, N. A. and Nickels, T. B. (2008). Acceleration of Tomo-PIV by estimating the initial volume intensity distribution. *Exp. Fluids*, 45:847–856.

Yegavian, R., Leclaire, B., and Champagnat, F. (2015). Lucas-Kanade Fluid Trajectories for time-resolved PIV. In *Proceedings of PIV15*.

Yule, A. J. (1978). Large-scale structure in the mixing layer of a round jet. *Journal of Fluid Mechanics*, 89:413–432.

Zhang, J., Tao, B., and Katz, J. (1997). Turbulent flow measurement in a square duct with hybrid holographic PIV. *Experiments in Fluids*, 3:373–381.

université PARIS-SACLAY
ÉCOLE DOCTORALE
Sciences mécaniques et énergétiques, matériaux et géosciences (SMEMAG)

Titre : Développement de la PIV tomographique pour l'étude d'écoulements turbulents

Mots clés : Turbulence, Métrologie, PIV, Reconstruction tomographique

Résumé : Cette thèse porte sur le développement de la PIV tomographique pour la mesure d'écoulements turbulents. Elle se fonde sur la reconstruction tomographique d'une distribution volumique d'intensité de particules, à partir de projections enregistrées par des caméras. La principale difficulté est le bruit dit tomographique (particules fantômes) qui croît exponentiellement avec la forte densité de traceur, requise pour obtenir une résolution spatiale fine de la mesure.
Une étude sur les conditions optiques nous a permis de proposer une approche alternative à la reconstruction tomographique classique : Reconstruction Volumique de Particules (PVR). Des simulations numériques ont montré qu'utiliser PVR-SMART permettait des gains de performance par rapport à un algorithme classique comme tomo-SMART (Atkinson 2009).
L'aspect vélocimétrie par corrélation de la méthode a aussi été pris en compte avec une extension à la 3D (FOLKI-3D) de l'algorithme FOLKI-PIV (Champagnat et al. 2011). Des simulations numériques de reconstruction tomographique ont permis de caractériser la robustesse de l'algorithme au bruit spécifique de la tomographie. Nous avons montré que FOLKI-3D était plus robuste aux particules fantômes cohérentes que les algorithmes classiques de déformation volumique. L'application de PVR-SMART sur des données expérimentales a été effectuée sur un jet d'air turbulent. Différentes densités de particules ont été utilisées pour comparer les performances de PVR-SMART avec tomo-SMART sur la région proche buse du jet. Nous montrons que les champs de vitesse de PVR-SMART sont près de 50 % moins bruités que ceux de tomo-SMART.

Title : Development of tomographic PIV for the study of turbulent flows

Keywords : Turbulence, Metrology, PIV, Tomographic reconstruction

Abstract : This research dissertation focuses on the developments of tomographic PIV (tomo-PIV) for the measurement of turbulent flows (Elsinga et al. 2006). It is based on the tomographic reconstruction of a volumic intensity distribution of tracer particles from projections recorded on cameras. Its main limitation is the appearance of *ghost particles*, *ie* reconstruction noise, which occurs when high tracer concentrations are required for high spatial resolution measurements.
A study on the imaging conditions for tomo-PIV led us to propose an alternative approach to classical tomographic reconstruction: Particle Volume Reconstruction (PVR). PVR underlies a more physical, sparse representation of point particles, which lives halfway between infinitely small particles, and voxel blobs commonly used in tomo-PIV, which smoothed, can be used in 3D-PIV.
Numerical simulations showed that PVR-SMART outperforms tomo-SMART (Atkinson et al. 2009) especially in the case of seeding density greater than 0.06 ppp. We introduce a cross-correlation technique for 3D-PIV (FOLKI-3D) as an extension to 3D of the FOLKI-PIV algorithm (Champagnat et al. 2011). Numerical simulations of tomographic reconstruction characterized the robustness of the algorithm to specific tomographic noise. FOLKI-3D was found more robust to coherent ghosts than standard deformation algorithms. Experimental validation of PVR-SMART was performed on a turbulent air jet. Several seeding density conditions were used to compare the performance of tomo-SMART and PVR-SMART on the near field region of the jet. With the given image pre-processing, PVR-SMART was found to yield velocity fields that are 50 % less noisy than tomo-SMART.

Université Paris-Saclay
Espace Technologique / Immeuble Discovery
Route de l'Orme aux Merisiers RD 128 / 91190 Saint-Aubin, France